Corrosion of Bolted Joints – Analysis and Smart Monitoring

by

Soroosh HAKIMIAN

MANUSCRIPT-BASED THESIS PRESENTED TO ÉCOLE DE TECHNOLOGIE SUPÉRIEURE IN PARTIAL FULFILLEMENT FOR THE DEGREE OF DOCTOR OF PHILOSOPHY
Ph.D.

MONTREAL, JANUARY 14, 2025

ÉCOLE DE TECHNOLOGIE SUPÉRIEURE
UNIVERSITÉ DU QUÉBEC

BOARD OF EXAMINERS (THESIS PH.D.)

THIS THESIS HAS BEEN EVALUATED

BY THE FOLLOWING BOARD OF EXAMINERS

Mr. Lucas A. Hof, Thesis Supervisor
Department of Mechanical Engineering at École de technologie supérieure

Mr. Abdel-Hakim Bouzid, Thesis Co-supervisor
Department of Mechanical Engineering at École de technologie supérieure

Mr. Amin Chaabane, President of the Board of Examiners
Department of Systems Engineering at École de technologie supérieure

Mr. Mohammad Jahazi, Member of the jury
Department of Mechanical Engineering at École de technologie supérieure

Mr. Axel Homborg, External Evaluator
Faculty of Military Sciences at the Netherlands Defence Academy

Mr. Sasha Omanovic, Independent External Evaluator
Department of Chemical Engineering at McGill University

THIS THESIS WAS PRENSENTED AND DEFENDED

IN THE PRESENCE OF A BOARD OF EXAMINERS AND PUBLIC

JANUARY 10, 2025

AT ÉCOLE DE TECHNOLOGIE SUPÉRIEURE

ACKNOWLEDGMENT

First and foremost, I wish to express my gratitude to my supervisors, Professor Lucas A. Hof and Professor Hakim A. Bouzid, for their unconditional support, invaluable guidance, and encouragement throughout my PhD journey. I am deeply thankful for their understanding, patience, wisdom, and contributions that greatly fostered my professional development. I extend my appreciation to all members of the LFIC group for creating a positive research environment and offering their assistance during my studies.

I am especially grateful to Mr. Michel Drouin for his expertise and assistance in designing the electrical boards. I would also like to thank Mr. Serge Plamondon for his training and helpful guidance in using equipment, and Dr. Mohammad Saadati for providing training and insightful advice on characterizations.

I owe my deepest thanks to my beautiful wife, Shamim, for her unwavering love, support, and patience throughout my academic journey. Her intelligence, kindness, and perseverance continue to inspire me, and I am truly blessed to have her by my side. I am also thankful to my parents, my siblings, and my in-laws for their unconditional love and support. Finally, I want to acknowledge my friends for their emotional support over the years.

I would like to express my gratitude to the Natural Sciences and Engineering Research Council of Canada for their continuous support, as well as to the Réseau de recherche en économie circulaire du Québec, Mitacs, ÉTS SUBSTANCE, and Centre interdisciplinaire de recherche en opérationnailsation du développement durable for their funding contributions during my PhD research.

CORROSION DES ASSEMBLAGES BOULONNÉS – ANALYSE ET SURVEILLANCE INTELLIGENTE

Soroosh HAKIMIAN

RESUME

Cette étude examine la corrosion des faces de brides des assemblages boulonnés utilisés dans des applications industrielles telles que les réservoirs et tuyauterie sous pression, les éoliennes et les ponts. Un banc d'essai simulant un montage de brides a été développé pour simuler les conditions réelles, permettant un suivi continu des facteurs influençant la corrosion, comme la température, le débit de fluide, la pression, la conductivité, le pH, la différence de potentiel et l'intensité du courant. Des techniques électrochimiques, incluant les polarisations potentiodynamique et potentiostatique, la spectroscopie d'impédance électrochimique (EIS) et la mesure de bruit électrochimique (ENM), ont été employées pour caractériser la corrosion. Les résultats montrent que la corrosion par crevasse débute dans l'espace entre les rayons intérieurs du joint et la bride, avec les joints en graphite causant plus de corrosion sur les surfaces en acier inoxydable ASTM A182 F321 que les joints en PTFE. L'effet des dimensions de l'espace de crevasse sur la corrosion a également été étudié, révélant qu'une augmentation de l'épaisseur de l'espace de 1,58 à 6,35 mm accroît les taux de corrosion générale, tandis qu'une réduction de la profondeur de crevasse les diminue. Des algorithmes d'apprentissage automatique (arbre de décision, SVM, forêt aléatoire et classificateur par bagging) ont été comparés pour la prédiction du comportement de corrosion, le classificateur par bagging atteignant une précision de 94,4 %. De plus, des réseaux neuronaux récurrents (RNNs), et en particulier les modèles LSTM, ont été utilisés pour classifier les types de corrosion via les données de bruit électrochimique, atteignant une précision de 93,62 %, avec une approche hybride RF-LSTM atteignant 97,85 %. Un modèle LSTM non supervisé, combiné à l'analyse en composantes principales (PCA) et au regroupement K-means, montre un potentiel pour la surveillance en ligne de la corrosion. Ce travail fait progresser le domaine en démontrant l'efficacité des modèles d'apprentissage automatique et d'apprentissage profond pour la prédiction et la classification du comportement de corrosion, offrant une alternative plus

efficace aux tests de corrosion traditionnels. Les connaissances acquises en matière de sélection de matériaux, de conception de joints et de dimensions des interstices contribuent à des conceptions de brides plus sûres et plus fiables dans les applications industrielles, réduisant potentiellement les coûts liés à la maintenance et aux défaillances imprévues. Ces résultats ouvrent la voie à des systèmes de surveillance en temps réel capables de gérer proactivement les risques de corrosion, améliorant ainsi la sécurité et la continuité opérationnelle.

Mots-clés : Assemblages à brides boulonnées avec et sans joints d'étanchéité ; Corrosion par crevasse ; Corrosion par piqûres ; Surveillance de la corrosion ; Sélection des matériaux ; Analyse microscopique ; Géométrie de crevasse ; Tests électrochimiques ; Apprentissage automatique ; Apprentissage profond

CORROSION OF BOLTED JOINTS – ANALYSIS AND SMART MONITORING

Soroosh HAKIMIAN

ABSTRACT

This study examines corrosion of flange faces in bolted joints with and without gaskets used in industrial applications like pressure vessels and piping, wind turbines, and bridges. A test rig based on a bolted joint fixture were developed to simulate real-world conditions, allowing continuous monitoring of factors influencing corrosion, such as temperature, fluid flow, pressure, conductivity, pH, current, and potential. Electrochemical techniques, including potentiostatic and potentiodynamic polarization, electrochemical impedance spectroscopy, and electrochemical noise measurement, were used to characterize corrosion.

The results show that graphite gaskets increase the susceptibility to localized corrosion on ASTM A182 F321 stainless steel flange surfaces under the same working conditions, compared to graphite gaskets with metal foil inserts and virgin polytetrafluoroethylene (PTFE) gaskets. The mechanism of flange face corrosion is that, for PTFE gaskets, corrosion propagation mainly occurs at the gasket inner diameter and propagates through the depth of the flange while, for graphite gaskets, corrosion occurs on the whole contact surface of the flange and the gasket. This study also examined the effect of gap dimensions between the gasket and flanges, which influence crevice thickness and depth, on corrosion behavior. It was found that increasing the gap thickness from 1.58 to 6.35 mm raises the general corrosion rate of the flange surface from 0.09 to 1.03 mm. y^{-1}, and crevice corrosion initiation time increases from 0.23 to 3.12 h.

Machine learning algorithms, including decision tree, support vector machine, random forest (RF), and bagging classifier, were compared for corrosion behavior prediction. Among these algorithms, bagging classifier achieved the highest accuracy of 94.4%. Additionally, recurrent neural networks, particularly long short-term memory (LSTM) models, were used to classify corrosion types using electrochemical noise data, achieving 93.62% accuracy, with a hybrid RF-LSTM approach reaching 97.85%. An unsupervised LSTM model with principal component analysis and k-means clustering offers potential for real-time corrosion monitoring.

This work advances the field by demonstrating the effectiveness of machine learning and deep learning models in predicting and classifying corrosion behavior, offering a more efficient alternative to traditional corrosion testing. The insights gained on material selection, gasket design, and gap dimensions contribute to safer and more reliable flange designs in industrial applications, potentially reducing costs associated with maintenance and unexpected failures. These findings pave the way for real-time monitoring systems that can proactively manage corrosion risks, improving overall safety and operational continuity.

Keywords: Flanged joints with or without gaskets; Crevice corrosion; Pitting corrosion; Corrosion monitoring; Materials selection; Microscopic analysis; Crevice geometry; Electrochemical tests; Machine learning; Deep learning

TABLE OF CONTENTS

Page

LIST OF TABLES

Page

LIST OF FIGURES

Page

LIST OF ABREVIATIONS

ML	Machine Learning
AI	Artificial Intelligence
DL	Deep Learning
RF	Random Forest
SVM	Support Vector Machine
DT	Decision Tree
RNN	Recurrent Neural Network
ANN	Artificial Neural Network
CNN	Convolutional Neural Network
KNN	K-nearest neighbors
LSTM	Long Short-Term Memory
GRU	Gated Recurrent Unit
UNS	Unified Numbering System
RTJ	Ring Type Joint
SCC	Stress Corrosion Cracking
PREN	Pitting Resistance Equivalent Number
PTFE	Polytetrafluoroethylene
RO	Reverse Osmosis
MIC	Microbiologically Induced Corrosion
CPT	Critical Pitting Temperature
CCT	Critical Crevice Temperature
CRA	Corrosion Resistant Alloy

XXX

ZRA	Zero Resistance Amperemeter
SS	Stainless Steel
DSS	Duplex Stainless Steel
SDSS	Super Duplex Stainless Steel
EPDM	Ethylene Propylene Diene Monomer
XRD	X-Ray Diffraction
EDX	Energy-dispersive X-ray
FT-IR	Fourier Transform Infrared Spectroscopy
SEM	Scanning Electron Microscope
OCP	Open Circuit Potential
MR	Mass Loss Rate
NPS	Nominal Pipe Size
ASTM	American Society for Testing and Materials
ASME	American Society of Mechanical Engineers

LIST OF SYMBOLS

E	Electrode potential
E^o	Standard electrode potential
E_{corr}	Corrosion potential
i	Current density
i_{corr}	Corrosion current density
η	Overpotential
R_{ct}	Charge transfer resistance
R_p	Polarization resistance
A	Surface area
σ	Conductivity
I	Current
I_{corr}	Corrosion current
IR	Potential drop
CPE	Constant phase element
R	Resistance
C	Capacitance
pH	Measure of the acidity or alkalinity of a solution
F	Faraday constant
z	Charge number of ions
M	Molecular weight
n	Number of electrons transferred in a reaction
h_t	Hidden state at time step t

x_t	Input vector at time step t
W_h	Weight matrix for hidden state
W_x	Weight matrix for input
W_y	Weight matrix for output
y_t	Output at time step t
c_t	Cell state in Long Short-Term Memory (LSTM) network
f_t	Forget gate activation in LSTM
i_t	Input gate activation in LSTM
o_t	Output gate activation in LSTM
σ_f	Activation function for forget gates
σ_i	Activation function for input gates
σ_o	Activation function for output gates
tanh (x)	Hyperbolic tangent activation function

INTRODUCTION

Corrosion is an electrochemical process occurring between a material and its surrounding environment, with material susceptibility to corrosion influenced by its composition, application, and exposure conditions. Corrosion poses a significant risk to the structural integrity of engineering systems. Bolted flanged joints are among the most commonly used engineering structures in industrial applications, serving as essential connections in pipelines, pressure vessels, oil and gas facilities, nuclear plants, and wind turbine towers. Corrosion within these joints can lead to catastrophic failures, resulting in substantial financial losses, shut-downs, safety and health hazards for humans, and harmful environmental damage.

This thesis focuses on corrosion in bolted flanged joints, specifically on flange faces in contact with gaskets working under harsh conditions, where corrosion often leads to leakage failures. Detecting flange face corrosion is challenging and, in many cases, impossible until leakage has already occurred. Localized corrosion, particularly crevice corrosion, is the most prevalent type in these joints. Several factors influence the initiation and progression of localized corrosion, all of which should be studied to improve design standards and material selection for flanges and gaskets, ultimately aiming to prevent failures.

To accurately assess the corrosion behavior of materials, testing should ideally replicate real-world industrial conditions. Typically, corrosion measurement studies employ small specimens in standardized cells according to ASTM guidelines; however, these cells are insufficient for evaluating corrosion in bolted flanged gasketed joints as they lack critical parameters such as gasket presence, fluid pressure, gasket contact stress, and fluid flow. As a result, a specialized setup is required to simulate actual conditions in bolted flanged joints, enabling a comprehensive study of how working conditions and material selection affect flange corrosion behavior. This research introduces a novel test bench setup that allows for a detailed investigation of material selection and design impacts on flange corrosion, enhanced by advanced analytical techniques, including machine learning (ML) and deep learning (DL).

Corrosion in bolted flanged joints necessitates a real-time monitoring system to detect localized corrosion, predict failures, and support preventive measures. This thesis proposes a novel approach that combines electrochemical techniques with DL to identify corrosion types

on flange faces without requiring system shutdown or joint disassembly, significantly reducing maintenance and repair costs.

This is an article-based thesis composed of six journal articles: five are published, and one has been submitted for publication. The structure of this thesis is as follows:

Chapter 1 provides a detailed literature review through a published review article:

Soroosh Hakimian, Abdel-Hakim Bouzid, Lucas A. Hof, Corrosion failures of flanged gasketed joints: A review, *Journal of Advanced Joining Processes*, Volume 9, 2024, 100200, ISSN 2666-3309, https://doi.org/10.1016/j.jajp.2024.100200.

Chapter 2 reviews the application of ML in corrosion science. This is followed by Chapter 3, which defines the research objectives and strategy.

Chapter 4 introduces the novel rig and fixture developed to characterize corrosion in flanged gasketed joints, presented in the published article:

Soroosh Hakimian, Abdel-Hakim Bouzid, Lucas A. Hof, An improved fixture to quantify corrosion in bolted flanged gasketed joints, ASME. *Journal of Pressure Vessel Technology* Volume 146, 2024, 011302, https://doi.org/10.1115/1.4063975.

Chapter 5 examines the impact of gasket material on flange face corrosion, as detailed in:

Soroosh Hakimian, Abdel-Hakim Bouzid, Lucas A. Hof, Effect of gasket material on flange face corrosion, *International Journal of Pressure Vessels and Piping*, Volume 209, 2024, 105207, ISSN 0308-0161, https://doi.org/10.1016/j.ijpvp.2024.105207.

Chapter 6 investigates how gap size affects corrosion on flange faces:

Soroosh Hakimian, Abdel-Hakim Bouzid, Lucas A. Hof, Effect of gap size on flange face corrosion, *Materials and Corrosion*, 2024, Pages 1–18, ISSN 0947-5117 https://doi.org/10.1002/maco.202414367.

Chapter 7 explores the application of ML to classify corrosion behaviors for material selection, as published in:

Soroosh Hakimian, Shamim Pourrahimi, Abdel-Hakim Bouzid, Lucas A. Hof, Application of machine learning for the classification of corrosion behavior in different environments for material selection of stainless steels, *Computational Materials Science*, Volume 228, 2023, 112352, ISSN 0927-0256, https://doi.org/10.1016/j.commatsci.2023.112352.

Chapter 8 focuses on the use of DL, specifically recurrent neural networks (RNNs), to identify types of corrosion on flange faces. This article has been submitted for publication in the *Engineering Applications of Artificial Intelligence* journal.

Soroosh Hakimian, Abdel-Hakim Bouzid, Lucas A. Hof, Corrosion type identification in flanged joints using a novel recurrent neural network technique applied to electrochemical noise measurements, *Engineering Applications of Artificial Intelligence*.

Finally, the thesis concludes with conclusions and recommendations for future research.

CHAPTER 1

CORROSION FAILURES OF FLANGED GASKETED JOINTS: A REVIEW

Soroosh Hakimian [a], Abdel-Hakim Bouzid [a], Lucas A. Hof [a]

[a] Department of Mechanical Engineering, École de technologie supérieure, 1100 Notre-Dame Ouest, Montréal, QC H3C 1K3, Canada

Paper published in: *Journal of Advanced Joining Processes*, Volume 9, June 2024, 100200.
https://doi.org/10.1016/j.jajp.2024.100200

Abstract

Corrosion-induced leakage in flanged gasketed joints is a critical issue in various industries, with implications for safety, environmental compliance, and economic sustainability. This review paper examines the mechanisms and factors contributing to corrosion-related failures in these joints, clarifying the diverse range of materials, operating conditions, and gasket types that influence their susceptibility to degradation. The paper investigates the key corrosion processes, such as pitting, crevice, and galvanic corrosion, that can initiate and propagate in the joint's critical areas. It explores the role of environmental factors, including microorganisms, temperature, flow, and chlorination, in accelerating the corrosion process. Additionally, the influence of gasket materials and design on corrosion susceptibility is investigated, highlighting the importance of selecting appropriate materials and sealing technologies. Furthermore, it reviews various corrosion monitoring techniques that can help identify corrosion early, ensuring the integrity and reliability of flanged gasketed joints.

1.1 Introduction

A bolted flanged joint is a widely employed method for connecting piping systems and pressure vessels that handle fluids at elevated pressures and temperatures. These joints find

frequent use in industries such as seawater handling, hydrocarbons, petrochemical and nuclear applications. Their primary advantage lies in the ease of assembly and disassembly, distinguishing them from welded joints (Nechache & Bouzid, 2007). In applications where these joints are used for holding or transferring fluids, there is a risk of metal-to-metal contact between the flanges causing leakage due to surface irregularities. In order to establish a secure and leak-free connection, gaskets made of comparatively softer materials are placed between the mating surfaces of the flanges. Gaskets in flange joints typically have lower stiffness compared to other joint components. They deform easily when subjected to a compressive load, filling in surface irregularities and leakage paths (Nelson et al., 2023). Gaskets play a significant role in preventing leakage in such joints. A schematic illustration of bolted flanged gasketed joints can be seen in Figure 1.1. Gaskets must have specific characteristics to be suitable for use. These characteristics include sealability, chemical resistance to the media, and tolerance toward pressure changes, temperature exposure, and creep (Nurhadiyanto, 2014a; Rice & Waterland, 2014). The most crucial concern in bolted flanged gasketed joints is the potential leakage of the enclosed fluid (Abid & Nash, 2003; A. H. Bouzid, 2009).

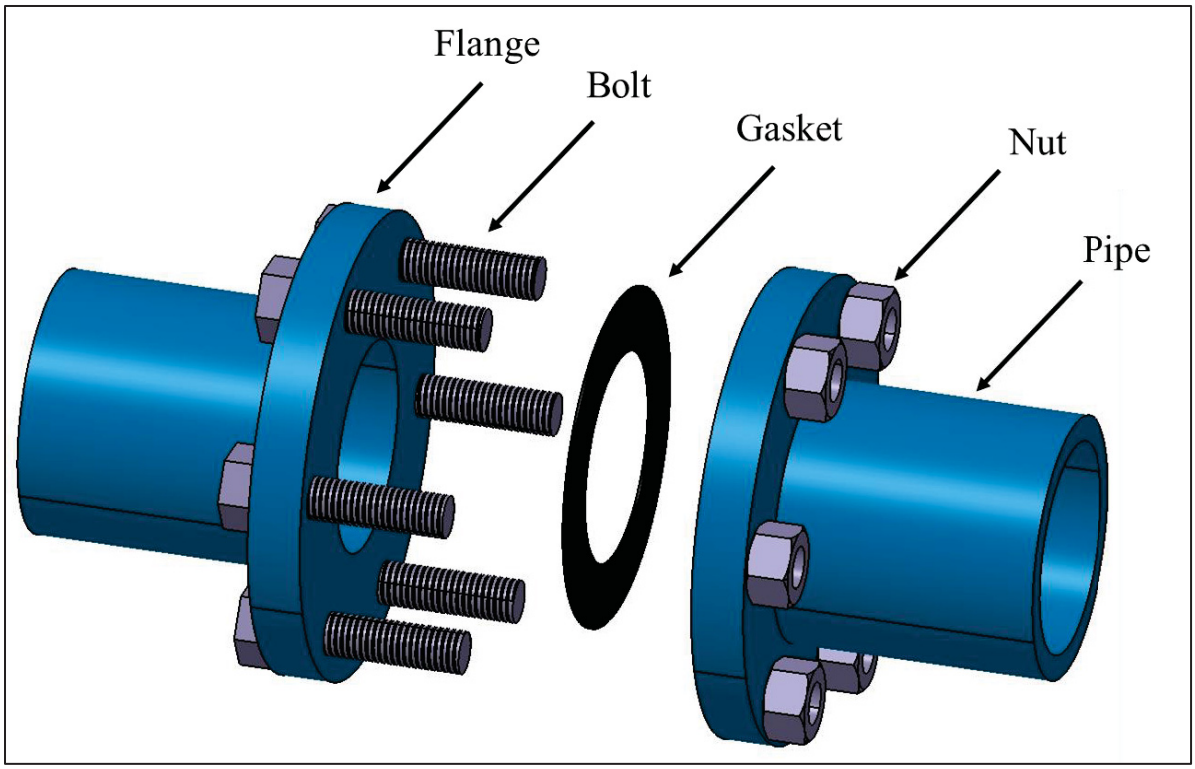

Figure 1.1 Schematic of a bolted flanged joint with a gasket placed between two flanges, and tightened by bolts

Throughout history, numerous accidents involving pipelines have been documented, with a significant portion attributed to fluid leaks during the transportation of substances like water, crude oil, steam, natural gas, and hazardous chemicals to different destinations. The use of pipelines has experienced notable growth over the past two decades, and pipeline accidents have been reported across the globe, with Canada and the United States ranking highest in incident frequency. Some of these incidents have even resulted in explosions, leading to tragic fatalities. Effective pipeline and joint design can play a key role in reducing such incidents (Nelson et al., 2023).

In seawater and hydrocarbon services, bolted flanged joints are susceptible to corrosion, especially at the interface between the gasket and the flange. Detecting corrosion at the flange interface before leakage occurs is also challenging, which can lead to costly consequences (Bond et al., 2018). Remedial or replacement work often results in unscheduled downtime, unplanned costs, and loss of revenue (Kazeminia & Bouzid, 2016). Flange face corrosion is a significant threat to the integrity of bolted flanged gasketed joints and can lead to potentially

severe leakage issues. It has been repeatedly observed that bolted flanged joints suffer premature failure due to corrosion, highlighting the necessity for an analysis of the root causes and the development of preventive strategies (Farrel J. Martin; Paul M. Natishan; Steven H. Lawrence; Elizabeth A. Hogan; Keith E. Lucas; Elvin Dail Thomas, 2004; Kain, 1998b; Kölblinger et al., 2022; Nicolas Larché; Dominique Thierry; Pauline Boillot; Thierry Cassagne; Jéréme Blanc; Philippe Dézerville; Elisabeth Johansson; Jean Marc Lardon, 2016; Takahiro Tsuda; Nozomi Satake; Manabu Itoki, 2021; Tavares et al., 2018). When the flange faces, where the gasket is seated, are exposed to corrosive substances of the transported fluids or to marine environment, they can deteriorate over time. Pitting and crevice corrosion damage the quality of the faces of the flanges, compromising the evenness and smoothness required for an effective seal. As the flange faces corrode, they lose their ability to maintain uniform pressure distribution across the gasket, making it difficult to retain fluid pressure (Fischer & Zitter, 1960; Tavares et al., 2018). This corrosion-induced degradation can result in gaps, irregularities, or pitting on the flange face, rendering the gasket sealing task complex and ultimately allowing fluid to leak.

Over the last six decades, extensive research has been conducted on the corrosion of bolted flanged joints. Various studies in the literature have documented instances of premature failures attributed to galvanic (Hu et al., 2020) and crevice corrosion (Kölblinger et al., 2022; Long et al., 2022; Nicolas Larché; Dominique Thierry; Pauline Boillot; Thierry Cassagne; Jéréme Blanc; Philippe Dézerville; Elisabeth Johansson; Jean Marc Lardon, 2016; Troels Mathiesen; Henrik Bang, 2011) occurring between the gaskets and flange faces. Due to its relatively high corrosion currents, galvanic corrosion accelerates the flange surface corrosion in cases where graphite is used in sheet gaskets, in metallic gaskets, or in semi metallic gaskets (R. Francis; G. Byrne, 2007). Gaps or crevices between flanges due to the presence of the gasket are potential locations for crevice corrosion to take place. Flange face corrosion occurs due to fluid penetration through gaps created at the flange-gasket interface. These gaps are created by material loss due to corrosion and aging and facilitated by the loosening of the joint due to the creep-relaxation of the joint (A. Bouzid et al., 1995; Nechache & Bouzid, 2007, 2008), rotation on the flange (Bouzid A.; Chaaban A.; Bazergui A., 1994; A. H. Bouzid et al., 2004), and waviness and misalignment (Worden, 2014a). The corrosion behavior of the flange

is influenced by metallurgical factors, environmental conditions, and the flange and gasket materials (Kain, 1998b; Troels Mathiesen; Henrik Bang, 2011).

In summary, the corrosion-related failures of flanged gasketed joints can be attributed to a variety of factors. Contributing factors include the flange and gasket material compatibility, the presence of corrosive agents such as O_2, SO_2, and CO_2, stagnant zones, chemical compatibility, temperature, and metallurgical factors. Despite the recurring incidents of flanged gasketed joint failures due to corrosion, there is a lack of predictive rules or methodologies to prevent such failures. Identifying the precise reasons for corrosion-related failures in flanged gasketed joints during operation is a complex task. Therefore, given the frequent occurrence of these failures and the existing literature, there is a significant demand for a comprehensive study on the factors causing these failures, preventative measures, and corrosion inspection techniques, with a particular focus on the corrosion occurring on the flange face. The purpose of the work presented in this paper is to explore the failure mechanisms associated with corrosion in flanged gasketed joints, the factors that influence such failures, preventive measures, and techniques for monitoring corrosion.

After introducing the relevance of corrosion failures of flanged gasketed joints in this section, section 1.2 highlights the review methodology, discussing the procedures employed for data collection and literature review. The subsequent section 1.3, includes an analysis of failure cases and identifies root failure causes, revealing primary corrosion mechanisms and influential factors. Following this failure analysis, the corrosion mechanisms on the flange faces in flanged gasketed joints are explored in section 1.4, presenting a detailed examination of each mechanism and the corresponding evaluation techniques. Section 1.5 introduces corrosion-contributing factors aligned with the identified failure cases. Then, section 1.6 addresses corrosion monitoring techniques, offering an insight into effective monitoring practices. Section 1.7 concludes the analysis of flange face corrosion based on collected data and root cause analysis. The discussion section (1.8) utilizes a diagram to illustrate the contribution of each factor to flange corrosion, drawing upon historical data. Finally, section 1.9 concludes the review study highlighting its most important findings.

1.2 Review methodology

The review methodology is structured into four distinct sections, each of which is crucial in guiding the approach and analysis employed in this study. These four sections are outlined in the flowchart presented in Figure 1.2, which provides a visual overview of the methodology organization.

1.2.1 Search strategy and criteria

The primary method employed to identify relevant literature for this review involved using the Engineering Village search engine, a comprehensive database that predominantly focuses on peer-reviewed journals and conference papers. The keywords used in this review are 'Flange,' 'Gasket,' 'Corrosion,' 'Crevice corrosion,' 'Pitting corrosion,' and 'Galvanic corrosion.' These keywords were selected to explore various aspects of corrosion mechanisms, including crevice, pitting, and galvanic corrosion, as well as the influential factors.

1.2.2 Selection criteria

After conducting a search using the keywords 'Flange,' 'Gasket,' and 'Corrosion,' 106 records directly relevant to corrosion in flanged gasketed joints are identified. However, a large number of records (more than 50,000) are found for other keywords mentioned in the initial search. To ensure relevance and focus on the most recent developments, the most recent papers to clarify corrosion mechanisms, influential factors, and monitoring methods are selected.

1.2.3 Data extraction and reviewing

After the initial selection of relevant papers, a secondary screening process was applied, resulting in 42 articles that primarily focus on flanged gasketed joint corrosion. These 42 articles were thoroughly reviewed and analyzed to form the basis of this review paper.

Additionally, 50 articles were included for the analysis of corrosion mechanisms and influential factors.

1.2.4 Research gaps and conclusion

In this step, the research limitations as well as future steps are identified aimed at predicting corrosion in flanged joints and protecting them from it and ultimately preventing leakage. These critical aspects have been included in the concluding section of the review.

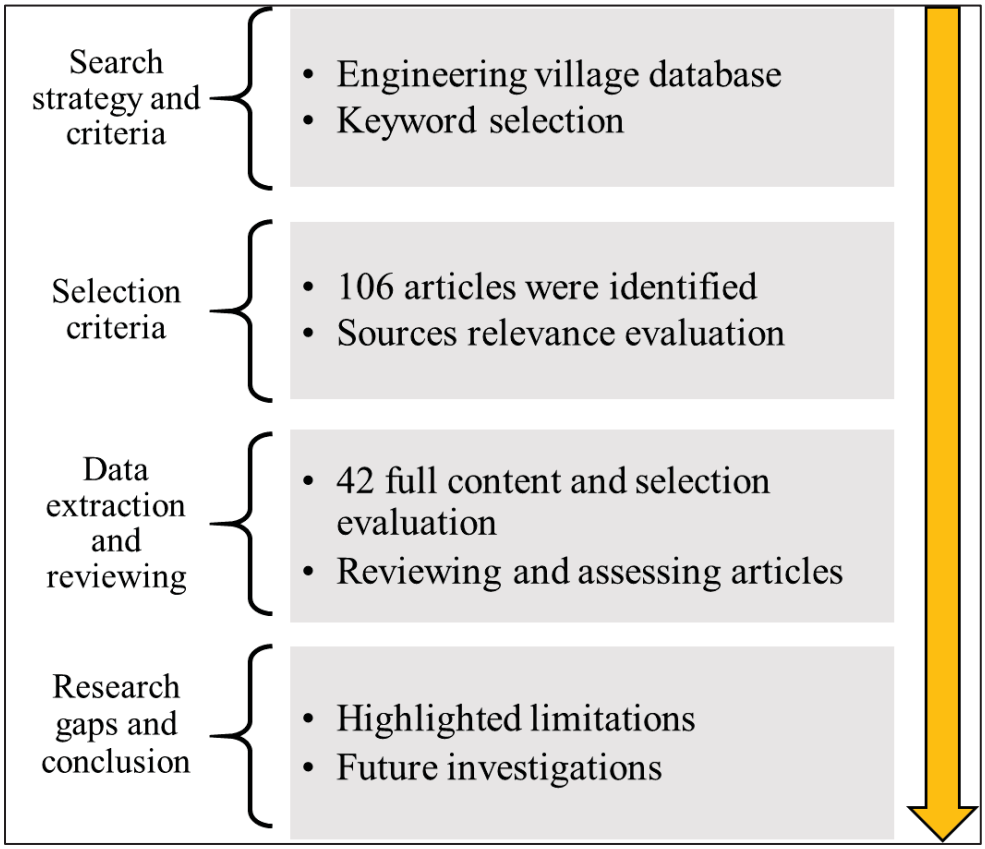

Figure 1.2 Flowchart of the deployed review methodology including four steps: search strategy and criteria, selection criteria, data extraction and reviewing, and research gaps and conclusion

Figure 1.3 shows the results of the documented literature search, which reports that 42 papers directly examined flange and gasket corrosion in bolted flanged joints between 1960 and 2023.

Flange failure due to corrosion was the subject of at least one publication every year from 2014 to 2023.

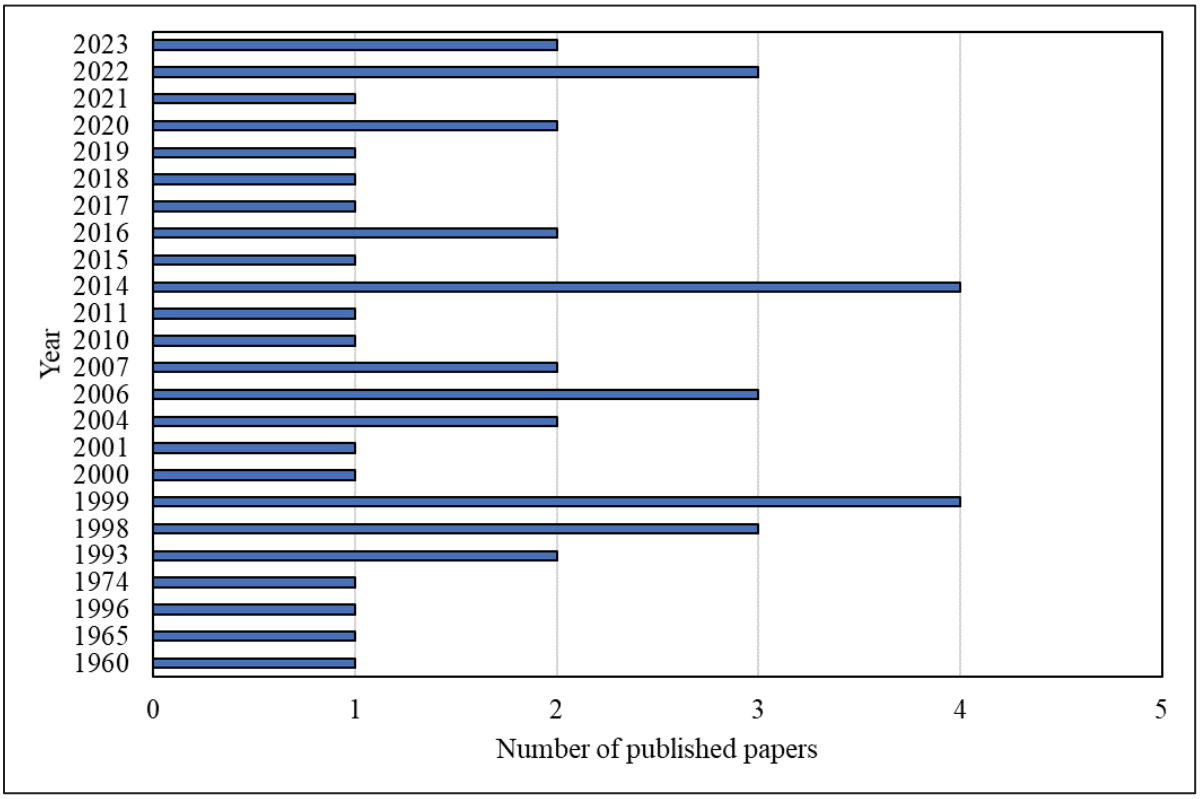

Figure 1.3 The number of papers directly studied flange corrosion in bolted flanged joints from 1960 to 2023

1.3 Failure cases

Numerous studies have examined the corrosion of bolted flanged gasketed joints specially over the past sixty years. Different types of premature failures have been reported in the literature due to crevice, pitting, and galvanic corrosions. Mathiessen et al. (Troels Mathiesen; Henrik Bang, 2011) reported severe crevice corrosion and subsequent leakages in flange joints within firewater systems on offshore oil and gas production platforms, as well as in chemical plants with bolted flanged connections operating in harsh environments. The affected firewater systems contain stagnant seawater at ambient temperature. The analysis conducted in these studies revealed that UNS31254 stainless steel (SS) flange faces experienced corrosion when

used in conjunction with graphite-filled spiral wound gaskets. In another case, crevice corrosion occurred on the face of the UNS S32760 super duplex stainless steel (SDSS) that was in contact with the gasket (Figure 1.4). There has been five years of operation of the flange line, running under a pressure of 1.14 MPa on the top side of an oil platform with seawater at 28°C on average (Kölblinger et al., 2022). Tavares et al. (Tavares et al., 2018) reported premature failure of a SS (UNS S32750) flange due to pitting corrosion and cracking (Figure 1.5), which was operated with seawater at 40°C and 0.1 MPa of pressure in a discharge water line of an offshore platform.

Figure 1.4 Crevice corrosion observed on the UNS S32760 SDSS flange face in the gasket region
Adapted from Kölblinger et al. (2022)

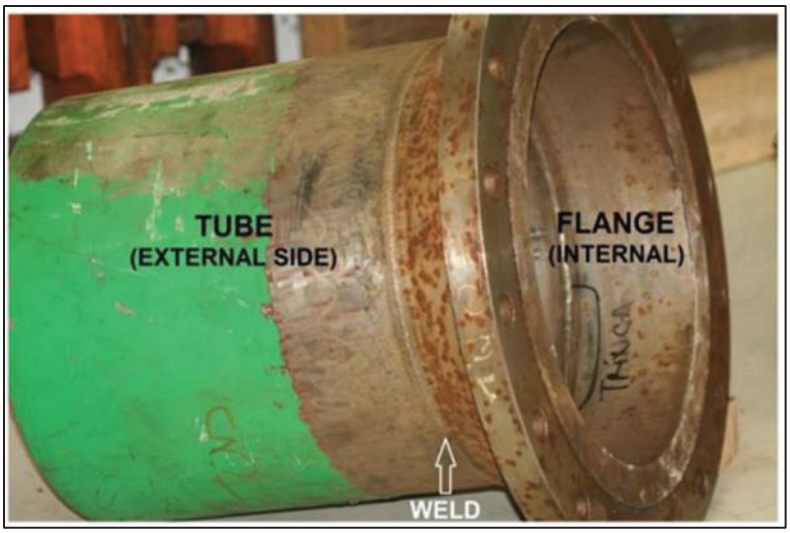

Figure 1.5 Flange failure due to severe internal pitting corrosion and circumferential crack, visibly marked by a black line on the internal side of the flange
Adapted from Tavares et al. (2018)

Poorwa Gore et al. (Gore et al., 2014) studied the failure of a flange used with ring type joint (RTJ) that was part of the reactor pipeline of a hydrocracker unit. Following a periodic shut-down of the unit, cracks were observed on the flange grooves and RTJ gaskets (Figure 1.6). At the time of failure, the hydrocracker had been in service for approximately 11 years. RTJ gaskets were manufactured from stabilized grades of austenitic SS, specifically type 321 and type 347. Further investigations revealed that the RTJ gaskets failed due to trans-granular stress corrosion cracking (SCC). This cracking was initiated by the formation of polythionic acid resulting from the presence of H_2S in the process gas, combined with the presence of H_2O within the system. Based on empirical evidence, it was suggested that the hydrocracker unit was improperly shut down during the last maintenance, which allowed O_2 and H_2O to enter the system.

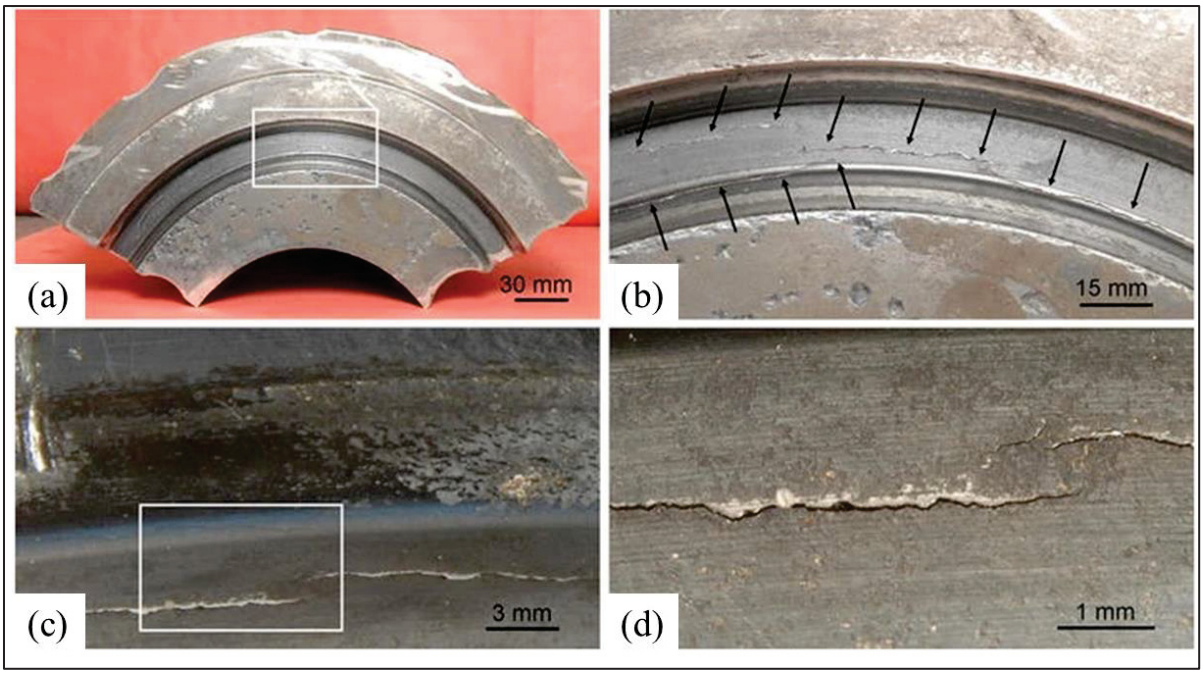

Figure 1.6 SCC on the flange RTJ (a) An area of the flange RTJ with a crack, (b) a magnified image (a) where multiple cracks are shown, (c) multiple cracks joining together, and (d) a close-up view of (c)
Adapted from Gore et al. (2014)

Tsuda et al. (Takahiro Tsuda; Nozomi Satake; Manabu Itoki, 2021) reported severe corrosion on ASTM A 105 flange surface in a modular plant construction. According to a root cause analysis, the extended construction period during modular construction has resulted in significant corrosion of flange faces due to water ingress into tightly fastened flanges. The modules were transported via sea from fabrication yards to the plant site for assembly. Upon arrival at the plant site, it was observed that the flange faces, including the surfaces in contact with the gaskets, exhibited severe corrosion, despite the flanges having been tightened at the module fabrication yards.

Bengtsson (Bengtsson, 2015a) focused on corrosion of flange faces in a backup diesel cooling system that uses brackish water which caused drips and leaks. It was believed that the graphite gasket used with UNS S31254 SS flanges could cause galvanic corrosion in the presence of brackish water. UNS S31254 SS is a noble material, and the graphite gasket is more noble than UNS S31254 with a potential difference of 0.3 V. The analysis results indicated that several factors contributed to the corrosion acceleration of the SS flange surface. These factors

included the presence of a crevice between the flange and gasket, inadequate placement of the weld, and the presence of chlorides in the water. Furthermore, the galvanic current had a synergistic effect on the corrosion of the flange face, leading to increased damage from corrosion.

Hu et al. (Hu et al., 2020) investigated a corroded copper flange that caused leakage in a diesel engine cooling system in less than one year of service. A Monel spiral wound gasket filled with PTFE was used with the copper flange. The chemical composition analysis showed that the base material of the flange contained 69.7% Cu and 28% Zn. As shown in Figure 1.7, the corroded surface of the flange has a red ochre color (area A), and a yellow ochre area (area B). The authors took samples from these two areas and did a chemical analysis. Based on the results, in the red ochre area, the content was 86% Cu, and 3.61% Zn, while in the yellow ochre area, the content was 55.27% Cu and 39.20% Zn. This indicates that dezincification corrosion occurred more in the area A than area B. Due to the dezincification corrosion, pores are formed on the flange surface, the PTFE coating on the Monel insert is not enough thick to fill in the pores due to the limited deformation; consequently, the fluid leaked through the pores.

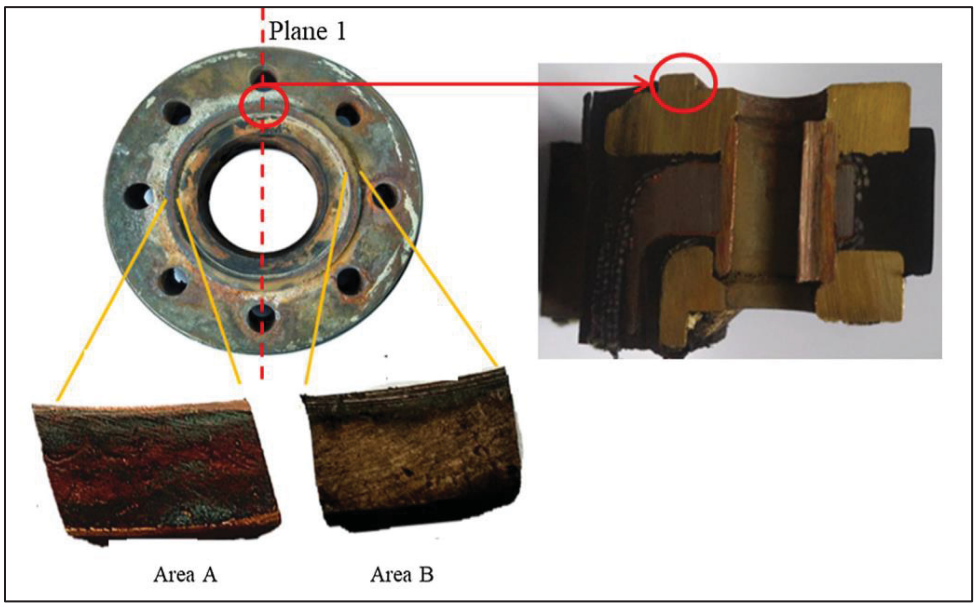

Figure 1.7 Corroded surface of a copper flange highlighting two distinct corroded areas labeled A and B. The red dashed line indicates the position of the convex flange's cross section
Adapted from Hu et al. (2020)

In a study by Ji et al. (Ji et al., 2023), it was noted that corrosion was identified on the inner wall and sealing groove end face of a surface pipeline flange after a year of operation in a western Chinese oilfield. Failure analyses indicated that the flange's chemical composition and mechanical properties complied with the specified parameters. The primary reason for the corrosion observed was attributed to CO_2-induced corrosion. Furthermore, the elevated temperature and the high flow rate of the medium significantly accelerated the corrosion process. The corrosion of the sealing groove end face, on the other hand, was a result of galvanic corrosion, with the difference in corrosion potential between the flange and gasket being the principal factor driving this phenomenon. The corroded sealing groove of an ASTM A105 carbon steel flange is depicted in Figure 1.8 (a), while Figure 1.8 (b) displays a magnified image of the corroded area.

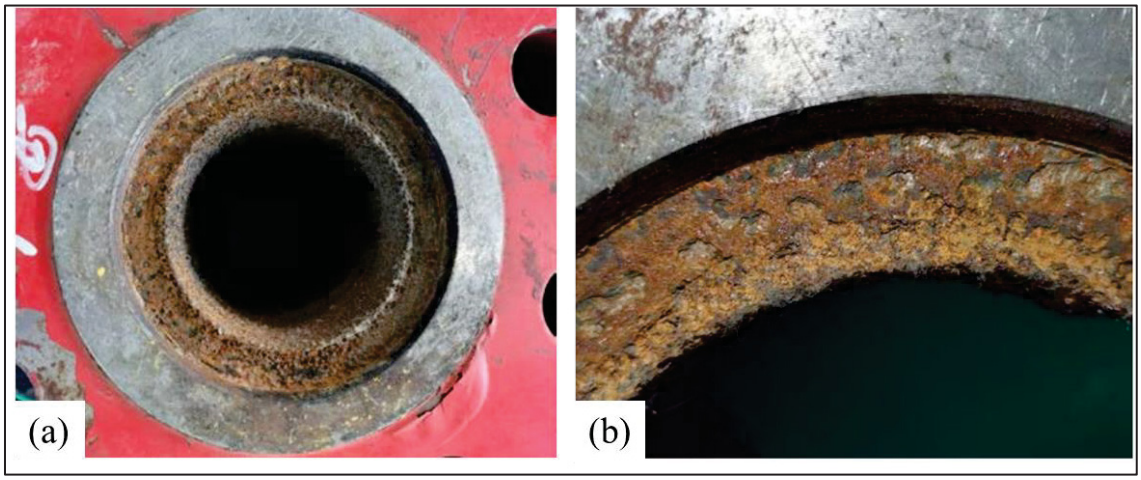

Figure 1.8 Macroscopic image of the corroded ASTM A105 flange; (a) corroded sealing groove; (b) magnified corroded sealing groove
Adapted from Ji et al. (2023)

Al-Abbadi et al. (Al-Abbadi et al., 2017) reported corrosion failure of Inconel 625 flange faces were designed for 30 years operation, but failed after two years in the cooling system containing elevated temperature seawater. The investigation determined that the utilization of Inconel gaskets coated with graphite resulted in galvanic corrosion on the flange surfaces in a seawater environment. Consequently, it was advised to substitute the Inconel 625 gaskets

coated with PTFE (Polytetrafluoroethylene). Additionally, for the flange surfaces, the recommended course of action was to restore them by applying a weld overlay with the same Inconel 625 metallurgy, and then they were reintroduced into service. Nevertheless, in under two years since the leakage episode, the cooler channel underwent removal from service for a nozzle inspection. The inspection report revealed distinct evidence of pitting at multiple flange surfaces. Notably, this pitting corrosion was exclusively observed in the gasket seating areas of the flange connections, with no signs of corrosion present on any other Inconel 625 surfaces exposed to seawater.

In summary, the cases analyzed in this section have enabled us to identify the specific types of corrosion responsible for flange failures in real applications and the critical factors contributing to the resulting incidents. Refer to Table 1.1 for a comprehensive overview of the contextual conditions leading to these failures. Subsequently, the following sections of this paper investigate these corrosion types, their underlying mechanisms, the key influencing factors, and the latest monitoring techniques to mitigate and manage these corrosion challenges.

Table 1.1 Details of corrosion failures of bolted flanged joints

Gasket material	Flange material	Service Period (years)	Type of corrosion	Medium	Root causes	Application	Preventive measures	Ref.
Duplex stainless steel (DSS) spiral wound graphite gaskets	UNS31254 SS flange	1	Crevice	Seawater	- Less resistant duplex grade for the spiral than the flange material - Chlorination of water	A firewater system located on a production platform for offshore oil and gas in the North Sea.	Using polymer gaskets	(Troels Mathiesen; Henrik Bang, 2011)
Graphite gaskets	UNS31254 SS flange	-	Crevice and Galvanic	Brackish water	- Existence of a crevice between the gasket and flange	A cooling system to the backup diesels	- Using casted flanges - Using non-conductive gaskets	(Bengtsson, 2015a)

Gasket material	Flange material	Service Period (years)	Type of corrosion	Medium	Root causes	Application	Preventive measures	Ref.
					- Inadequate positioning of a weld with the presence of chlorides in water - Galvanic currents might have contributed to crevice corrosion along with a synergistic impact			
Monel alloy gasket in the middle winded by polytetrafluoroethylene (PTFE)	Copper alloy flange	<1	Galvanic and dezincification	Seawater	- Dezincification of the copper flange - Polytetrafluoroethylene on the Monel gasket cannot penetrate into pores formed by dezincification corrosion within copper alloys, so water penetrated to the pores and	Diesel engine cooling system of a ship	Replacing the using flange with aluminum bronze	(Hu et al., 2020)

Gasket material	Flange material	Service Period (years)	Type of corrosion	Medium	Root causes	Application	Preventive measures	Ref.
					corrosion occurred			
Not mentioned	UNS32760 SS flange	5	Crevice	Seawater	- Crevice microbiologically induced corrosion (MIC) occurred on the flange surface	Top side of an oil platform	-	(Köllbinger et al., 2022)
Not mentioned	UNS32760 SS flange	-	Pitting and cracking	Seawater	- Using cast flange instead of forged flange - Chemical composition and microstructure were inadequate for seawater application	A discharge water line of an offshore platform	-	(Tavares et al., 2018)
Ring gasket austenitic SS type 321 and 347	Austenitic SS type 321 and 347	11	Trans granular SCC	H_2S	- The initiation of SCC in RTJ components was attributed to the formation of polythionic acid, which occurred as a result of the	Reactor pipeline of a hydrocracker unit	-	(Gore et al., 2014)

Gasket material	Flange material	Service Period (years)	Type of corrosion	Medium	Root causes	Application	Preventive measures	Ref.
					presence of H_2S in the process gas and H_2O in the system			
Inconel 625 gasket coated with PTFE	Inconel 625 (UNS N06625)	<2	Crevice and pitting	Hydrocar-bon and Seawater	- Susceptibility of Inconel 625 to crevice corrosion when it is used in high-temperature service with high chloride content	Inlet gas cooler	Using alloys with higher CCT, e.g., Hastelloy C-276 instead of Inconel 625	(Al-Abbadi et al., 2017)
304 SS	ASTM A105	1	Galvanic corrosion and erosion	CO_2	- Galvanic corrosion resulting from the contact between the gasket and the flange material - The fluid's average flow velocity within the pipeline exceeded the critical erosion velocity. Consequently, the fluid flow inside	Oilfield production well	-	(Ji et al., 2023)

Gasket material	Flange material	Service Period (years)	Type of corrosion	Medium	Root causes	Application	Preventive measures	Ref.
					the pipeline caused erosion to the inner wall of the flange			
-	UNS S42000 martensitic SS	~ 2	Pitting and crack propagation from the pit along the delta ferrite/martensite interfaces	CO_2	- The presence of chromium-rich carbides within the structure diminished the resistance against pitting corrosion. - Delta ferrite component weakened the crack resistance - The stress level within the sealing structure of the flange played a significant role in influencing the behavior of crack propagation	Ultra deep high-pressure and high-temperature gas well	Optimizing the forging process to reduce the delta ferrite content	(Long et al., 2022)
Corrugated metallic 304 SS	304SS	<1	Pitting corrosion on the gasket	Demineralized water	- Contamination of the water by chloride ions,	Hydrocarbon transfer pipeline in polyethylene plant and piping system	-	(Tawancy, 2019)

Gasket material	Flange material	Service Period (years)	Type of corrosion	Medium	Root causes	Application	Preventive measures	Ref.
					and excessive compressive preload			

1.4 Corrosion mechanisms on the flange faces in flanged gasketed joints

Corrosion is a natural process that occurs when certain materials, particularly metals, react with their environment and undergo deterioration. It is an electrochemical process that involves the gradual degradation and loss of material. For a corrosion reaction to occur, several components are typically involved. These components are essential in creating the necessary electrochemical reactions that drive the corrosion process. The key components are as follows: anode (the site on the metal where oxidation occurs), cathode (the site on the metal where reduction reactions take place), electrolyte (a conducting medium that allows the movement of ions between the anode and cathode), and electron transfer path (for the flow of electrons generated at the anode to the cathode) (Bradford, 2003). These components are all present in bolted flanged gasketed joints.

In the case of bolted flanged joints, the flange serves as the anode, which is the site that will undergo corrosion. The cathode can either be the flange itself or the gasket that is in contact with the flange. The fluid that flows in the pipeline acts as the electrolyte, facilitating the movement of ions between the anode and cathode. The direct contact between the flange and gasket forms the electron transfer path, enabling the flow of electrons from the anode to the cathode. There are different forms of corrosion based on the morphology of the corroded part. However, a few types of corrosion have been observed in bolted flanged joints. According to the literature Table 1.1, crevice, pitting, and galvanic corrosion do widely occur on the flange faces in bolted flanged joints in industrial installations. The mechanisms of the mentioned types of corrosion will be discussed hereafter.

1.4.1 Crevice corrosion

Crevice corrosion, a common type of corrosion failure in corrosion resistant alloys (CRAs), is regarded as more hazardous than pitting corrosion due to its occurrence in concealed areas that are typically inaccessible and not visible (Costa et al., 2023). This type of corrosion occurs in the crevices, which are wide enough to allow liquid entry but sufficiently narrow to maintain a stagnant zone (Kruger & Begum, 2016). Metals with passive behavior (e.g., SS) suffer more from crevice corrosion because of the passive layer breakdown (Hu et al., 2011a). Crevice corrosion primarily occurs in systems containing oxygen, and it becomes more severe when aggressive ions, typically chloride, are present (Luo et al., 2022). This type of corrosion is commonly observed in bolted flanged gasketed joints. The gap within the joint near the gasket area becomes oxygen-depleted and acts as the anodic site. In the presence of seawater, corrosion is exacerbated as negatively charged chloride ions migrate into the crevice. These ions not only counterbalance the accumulation of positive charges around the crevice but also serve as a catalyst, expediting the metal's dissolution. This gradual process leads to the formation of deep pits (Brondel et al., 1994).

Two mechanisms of crevice corrosion are identified in the literature; these are critical crevice solution (CCS) theory and IR drop theory (Kennell et al., 2008; Shojaei et al., 2019). According to the CCS theory, the crevice corrosion mechanism constitutes of two stages; in the first stage, anodic and cathodic reactions occur according to Equation (1.1) and Equation (1.2), respectively. In Equation (1.1), the metal *M* (e.g., iron) is dissolved in aerated seawater and oxygen will be reduced to hydroxide ion, as shown in Equation (1.2). Figure 1.9 shows a schematic illustrating the components involved in crevice corrosion. These components include the crevice former, responsible for creating a specific crevice gap on the metal surface. Each equation corresponding to the reactions is indicated by numbers in Figure 1.9. Number (1) indicates the occurrence of oxidation as per Equation (1.1) taking place on the metal surface within the crevice, while number (2) indicates the occurrence of reduction as per Equation (1.2) taking place on the metal surface outside the crevice.

$$\text{Oxidation: } M \rightarrow M^{n+} + ne^{-} \qquad (1.1)$$

$$\text{Reduction: } O_2 + 2H_2O + 4e \rightarrow 4OH^- \quad (1.2)$$

In the second stage, oxygen concentration decreases over time since species exchange is restricted in the crevice. According to Figure 1.9, the absence of oxygen in the crevice gap causes chloride ions to move to the crevice (shown by arrows on the Cl^- ion) to react with an excess positive charge of M^{n+} and balance the electric charge. Afterwards, the metal chloride (MCl_n) hydrolysis in water (as stated by Equation (1.3)) reacts to give undissolved metal hydroxide and acid. In Figure 1.9, number (3) indicates that the reaction as per Equation (1.3) taking place within the crevice. Rising the concentration of hydrogen ions and chloride ions accelerates the corrosion rate of metal; furthermore, the higher corrosion rate provides more M^{n+} ions, and consequently, the amount of acid increases, so this process is autocatalytic. In cases where a passive layer forms on the metal surface, high H^+ and Cl^- concentrations damage the passive layer and drastically increase the corrosion rate. Crevice corrosion is a localized corrosion, since during the time that the metal is being corroded aggressively, the reduction reaction constantly occurs on the exterior surface, so the outer surface of the crevice is protected (Costa et al., 2023) .

$$MCl_n + nH_2O \rightarrow M(OH)_n + nH^+ + nCl^- \quad (1.3)$$

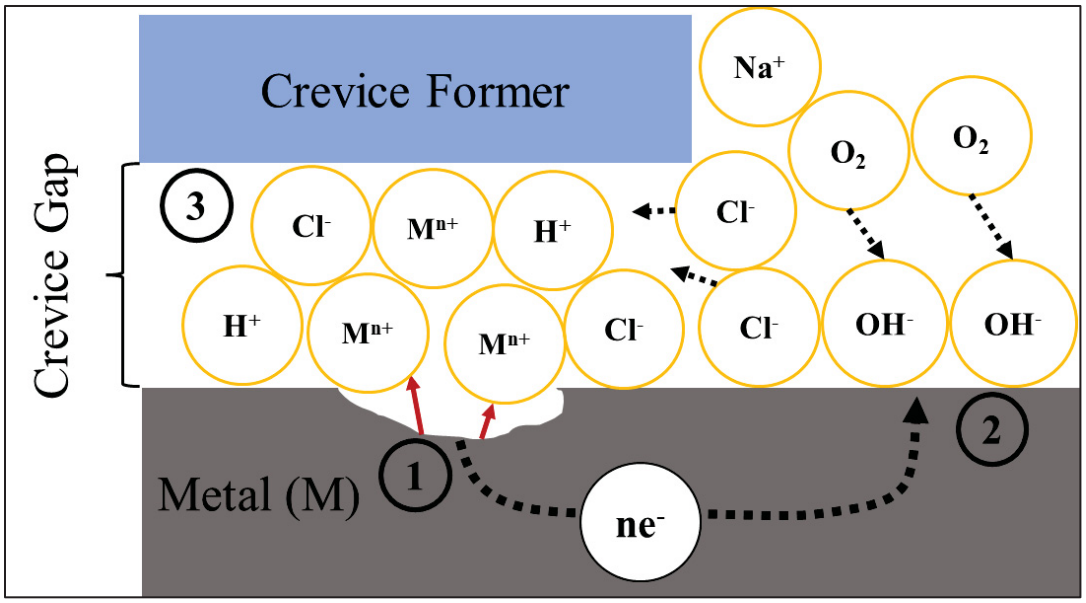

Figure 1.9 Illustration of the crevice corrosion, depicting oxygen depletion and acid formation within the crevice in three steps according to CCS theory: 1- the metal (M) is oxidized to (M^{n+}), 2- oxygen (O_2) is reduced to hydroxide ion (OH^-), 3- the metal chloride (MCl_n) hydrolysis in seawater and forms metal hydroxide ($M(OH)_n$), hydrogen ions (H^+), and chloride ions (Cl^-)

In IR drop theory, I refers to the current and R refers to the resistance (Pickering, 1989). According to the IR-drop theory, several factors, including the crevice's geometry, composition, and concentration gradients, contribute to the establishment of a potential difference between the crevice and its surrounding environment. This potential difference, driven by the resistance to electric current flow in the crevice, is known as the IR drop (Kelly & Lee, 2018). In areas where the electric potential decreases to a critical level, denoted as critical potential (E_{crit}), the current density experiences a significant surge. This occurs because the protective passive film loses its stability, causing a shift to active dissolution. The IR-drop mechanism has been gaining attention because it offers insights into corrosion mechanisms in environments containing chloride and those without it, a capability not shared by the CCS model. However, it is important to note that the IR drop model is particularly suitable for metal/electrolyte systems that exhibit both active and passive behavior within the crevice solution (Betts & Boulton, 1993).

Crevice corrosion evaluation involves a range of techniques designed to assess the susceptibility and severity of this localized form of corrosion. These techniques can be broadly

categorized into three groups: non-electrochemical or immersion methods, electrochemical methods at open circuit potential, and electrochemical methods with applied signals (Kelly & Lee, 2018; Oldfield, 1987). Table 1.2 illustrates techniques that are used to evaluate localized corrosion.

Table 1.2 Techniques to quantify localized corrosion

Technique	Description	Alloy	Electrolyte	Temperature	Time	Results	Limitations	Ref.
Non-electrochemical or immersion methods	ASTM G48 standard test method	SSs and related alloys	Methods A and B: 6 wt.% ferric chloride ($FeCl_3$) Methods C, D, E, and F: 6 wt.% ferric chloride ($FeCl_3$) + 1 % HCl	Methods A and B: 22°C or 50°C Methods C, D, E, and F: between 0°C and 85°C	Methods A, B, and C: 72h	Mass-loss, maximum penetration depth, attack area, critical crevice temperature (CCT), critical pitting temperature (CPT)	The test methods and their acceptance criteria differ among various oil companies, and each of the outlined methods involves leaving certain details to the test laboratory. These details could have a crucial influence on the final result (Mathiesen & Andersen, 2013).	(ASTM International, 2020c)
	ASTM G78 standard test method	Iron-base, Nickel-base	Seawater	Ambient	At least 30 days	Mass-loss, maximum penetrat	-	(ASTM International

Technique	Description	Alloy	Electrolyte	Temperature	Time	Results	Limitations	Ref.
		stainless alloys				ion depth, attack area		, 2020e)
Electrochemical methods at open circuit	Monitoring open circuit potential	-	-	-	-	Corrosion potential (E_{corr}), initiation of crevice corrosion	Open-circuit measurements cannot provide any data on reaction rate because there is no current flow between the crevice and the reference electrode	(Kelly & Lee, 2018)
	ASTM G71 standard test method	-	-	-	-	Current flow between anode (creviced) and cathode (non-creviced) using ZRA method	This method must be supplemented by weight loss or other techniques, as ZRA only measures net current.	(ASTM International, 2019)
Electrochemical methods with applied signal	ASTM G61-Cyclic potentiodynamic polarization	Iron-, Nickel-, or Cobalt-based alloys	Appropriate electrolyte that simulates the expected service environment	The temperature should represent the service environment	-	Pitting or crevice potential (E_{pit}, E_{crev}), re-passivation potentia	E_{rep} are not highly reproducible particularly when the alloy is not very susceptible to crevice corrosion or	(ASTM International, 2018c) (Esmailzadeh et al.,

Technique	Description	Alloy	Electrolyte	Temperature	Time	Results	Limitations	Ref.
						l (E_{rep}), corrosion potential (E_{corr}), passive current density (i_{pass})	when the environment is not highly aggressive.	2018)(Sridhar & Cragnolino, 1993)
	Potentiostatic test	-	-	-	-	Current vs. time curve provides information about crevice corrosion initiation time and propagation	This method may produce cathodic currents exceeding what a local cathode could provide. Consequently, reaction rates are frequently overestimated when compared to open circuit exposures limited by either anodic or cathodic reactions.	(Kelly & Lee, 2018)
	ASTM G192-standard test method	Corrosion-resistant alloys	Any electrolyte Standard: 1 M NaCl	90°C or lower	-	Crevice re-passivation potential	This technique tends to be slow and requires a significant amount of time due to	(ASTM International, 2020f)

Technique	Description	Alloy	Electrolyte	Temperature	Time	Results	Limitations	Ref.
							the typical occurrence of E_{rep} at low potentials.	

1.4.2 Pitting Corrosion

Pitting corrosion, which shares similar mechanisms with crevice corrosion, represents another form of localized corrosion. In both of these corrosion types, a distinct alteration in the local environment is a prerequisite for significant damage to occur. The onset of crevice corrosion is marked by the formation of pits within enclosed areas. The primary differentiation between crevice corrosion and pitting corrosion lies in the fact that crevice corrosion necessitates the presence of a physically confined space for initiation. Pitting corrosion, on the other hand, can manifest on exposed surfaces, although some studies have suggested that pitting may also commence at the interface between an inclusion and the matrix (Guo et al., 2021). Pitting corrosion is characterized as an autocatalytic reaction, wherein the dissolved metal converts into metal ions, creating a highly acidic environment that accelerates the local corrosion rate and deepens the pits. In the context of bolted flanged joints, pitting corrosion has been observed predominantly on the inner side (as depicted in Figure 1.10) and on flange faces (Al-Abbadi et al., 2017; Tavares et al., 2018). The pitting corrosion resistance can be evaluated using electrochemical methods. The pitting potential (E_{pit}) and the re-passivation potential (E_{rep}) of alloys in different environments are obtained by cyclic potentiodynamic polarization measurements based on the ASTM G61 standard test method. Another standard test method, ASTM G150 (ASTM International, 2018e), introduces a procedure for obtaining the critical pitting temperature (CPT). This CPT is the highest temperature below which pitting corrosion does not occur. As such, a high material CPT value indicates a good pitting resistance compared to materials possessing lower CPT values.

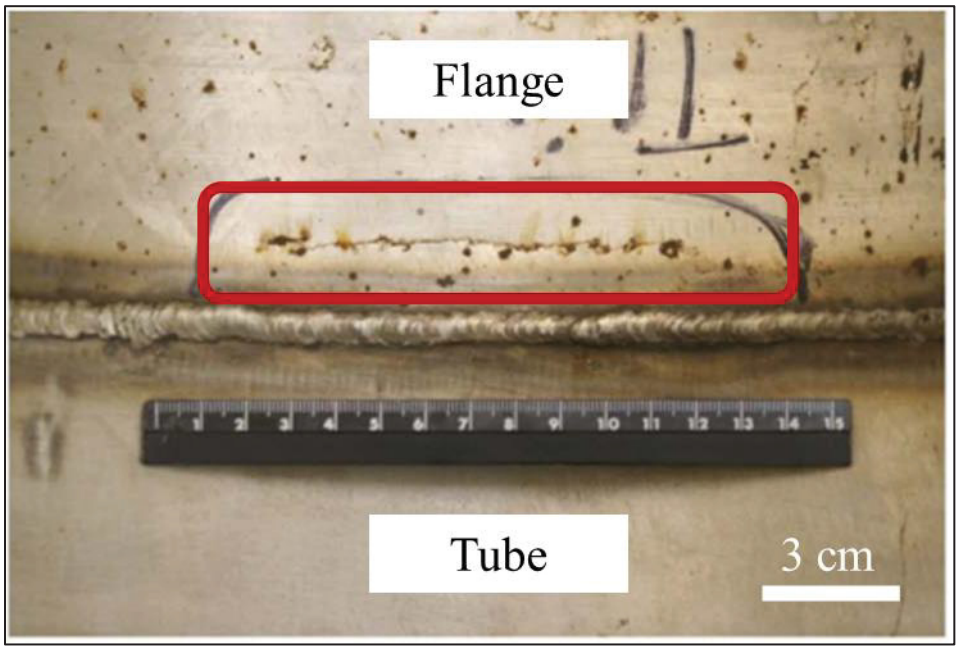

Figure 1.10 Severe pitting corrosion observed on the internal side of the SDSS flange near the flange and tube connection, highlighted by the red rectangle
Adapted from Tavares et al. (2018)

1.4.3 Galvanic corrosion

When two dissimilar metals are in contact with each other and immersed in a corrosive solution, the metal having a higher potential behaves as a cathode, and the other metal acts as an anode, resulting in the flow of electrons between them (Hack, 2016). Galvanic corrosion, due to its relatively high corrosion currents, could accelerate the flange surface corrosion in cases where graphite containing gaskets are used in combination with flanges (R. Francis; G. Byrne, 2007). Graphite exhibits a high level of nobility compared to most metals when exposed to seawater (Francis, 1994a). Consequently, it has the potential to induce corrosion, even in the case of high-alloy materials, particularly within crevices. Sheet-type gaskets, such as flexible graphite, are frequently employed in situations involving smaller diameters, low pressures, or lower temperatures. However, as the diameter, pressure, or temperature rises, sheet gaskets become less appropriate due to the heightened risk of blowout. In such cases, semi metallic or metallic gaskets are employed as a solution (A.-H. Bouzid & Das, 2023).

Bengtsson et al. (Bengtsson, 2015a) reported flange face corrosion in brackish water inside a cooling system of backup diesel generators. The flange material used in this system was UNS31254 SS, and a graphite-containing gasket was used to seal the joint. The high potential difference between the gasket and flange material accelerated the crevice corrosion on the flange surface, as is illustrated in Figure 1.11.

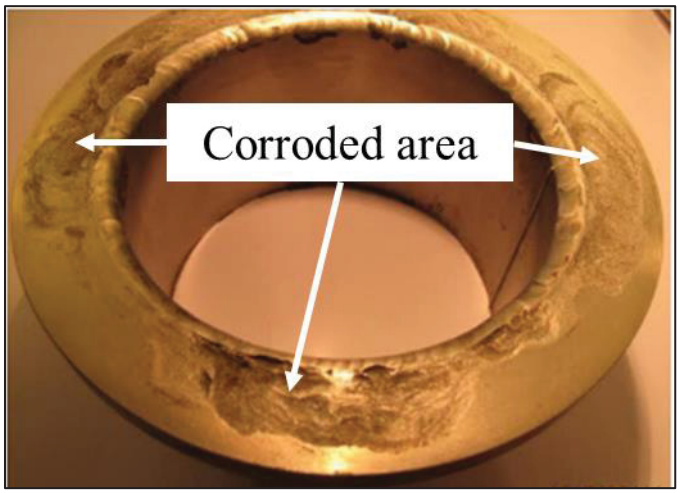

Figure 1.11 Crevice corrosion (locations indicated by the arrows) on the face of a UNS31254 SS flange
Adapted from Bengtsson (2015a)

Ji et al. (Ji et al., 2023) conducted an analysis of the corrosion issue observed in a pipeline flange that exhibited corrosion on the inner wall and sealing groove end face after one year of service. The study findings revealed that the main cause of flange face corrosion was galvanic corrosion resulting from the contact between the gasket (made of 304 SS) and the flange material, which had different materials and a potential difference of 0.67 V. Galvanic corrosion depends not just on the potential difference but also critically on the polarization behavior. Therefore, graphite and an alloy that has a passive behavior (e.g., Alloy C-276) may exhibit a significant difference, but the corrosion rate may not be significant.

The ASTM G71 standard method proposes another method for conducting and evaluating galvanic corrosion tests in different electrolytes (ASTM International, 2019). The galvanic current is measured with a “zero resistance” amperemeter (ZRA), practically having a very low resistance. Such instrument measures the current between two electrodes by short-

circuiting them. Figure 1.12 presents a schematic illustration of a galvanic current measurement by using electrodes (anode and cathode) partially immersed in an electrolyte and short-circuited by a ZRA. Typically, a coating is applied on both electrodes to ensure a well-defined electrode surface area exposed to the electrolyte. It should be noted that ZRA measurements of galvanic corrosion must be supplemented by weight loss or other techniques because ZRA only measures net current. It does not specify whether the cathode also corrode at a high rate. This can be a problem for some alloys that exhibit a significant active-passive peak, where ZRA measurements can indicate a small galvanic current, but they corrode at a rapid rate (Okonkwo et al., 2021).

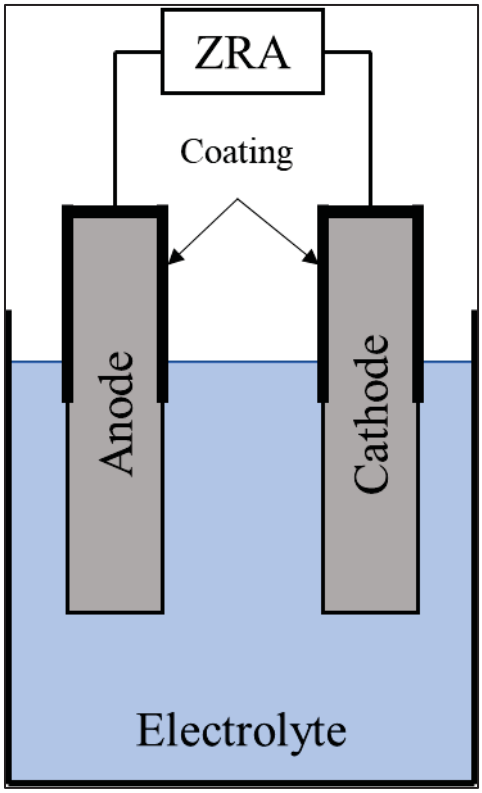

Figure 1.12 Schematic of the galvanic corrosion test setup to measure the galvanic current between a partially coated anode and cathode, connected to each other by a zero resistance amperemeter (ZRA) and immersed in an electrolyte

In this section, the mechanisms of corrosion types that commonly occur in bolted flanged joints are introduced, along with widely known test techniques. However, it is important to consider the limitations of these methods when evaluating crevice corrosion, pitting corrosion, or

galvanic corrosion in bolted flanged joints. Standards such as ASTM G71, G78, and G150 provide standardized test methods with simplified geometric configurations that may not fully represent the complex geometries and conditions encountered in the actual complex structures such as bolted flanged joints. Consequently, the test results may not accurately reflect the actual corrosion behavior in practical applications. Furthermore, these standards do not encompass the wide range of environmental conditions that bolted flanged joints can be exposed to. Factors such as varying temperatures, different corrosive media, and fluctuating exposure durations may not be adequately captured in the testing protocols, limiting the applicability and representativeness of the results. It is important to note that these ASTM standards primarily focus on corrosion evaluation and do not incorporate mechanical loading or stress conditions present in operational bolted flanged joints. The absence of mechanical loading may result in an incomplete understanding of the overall corrosion behavior of the joint under realistic working conditions. For instance, the mechanical loading affects the thickness of the gasket in the joint which determines the size of the crevice and has a strong relationship with the initiation and development of crevice corrosion (Luo et al., 2022; Shojaei et al., 2019). In recent years, researchers have been working on the development of fixtures for measuring flange face corrosion under conditions that closely mimic actual working conditions (Hakimian, Bouzid, et al., 2023; Hakimian et al., 2022).

1.5 Corrosion contributing factors

Analysis of corrosion-related failures in the literature reveals that certain factors can accelerate corrosion in bolted flanged joints. This section presents the most critical factors, drawing upon failure analysis and technical research.

1.5.1 Flange material and microstructure

Material selection is one of the most important steps in designing industrial structures (Hakimian, Pourrahimi, et al., 2023). Flanges are manufactured using a variety of materials, including carbon steels, low alloy steels, SSs, and nickel-based alloys. Table 1.3 provides a list

of the most commonly used flange materials, chosen according to the necessary mechanical properties and operational considerations, such as temperature, pressure, and pH, in bolted flanged gasketed systems. Nadarajah's study (Nadarajah, 2004) focuses on determining the maximum level of corrosion that a weld neck flange face could withstand without compromising its structural integrity, ensuring its suitability for service. The investigation involves a parametric analysis using the finite element method, which encompasses all weld neck flanges specified in the ASME B16.5 Code for Pipe Flanges and Flanged Fittings. This analysis results in the creation of several tables that set limits on corrosion for different classes and sizes of flanges. It is important to note that this research specifically considers the A105, A182 Cl 70, and A350 LF2 flange materials and addresses general corrosion on the flange face, taking into account a maximum temperature of 38°C. It is worth mentioning that although general corrosion can affect carbon steels like A105, the most problematic form of corrosion for flange faces is crevice or pitting corrosion, which spreads rapidly within a localized area.

Table 1.3 Materials frequently used in flange fabrication

Name	Grade	Specification
Carbon steel	ASTM A105 (ASTM International, 2018a), ASTM A350 (ASTM International, 2018b)	Carbon steel forgings for piping applications
Low alloy steels	ASTM A182 (ASTM International, 2020a)	Forged or rolled alloy and SS pipe flanges
Stainless steels	ASTM A182	Forged or rolled alloy and SS pipe flanges
Nickel alloys	ASTM B462 (*Standard Specification for Forged or Rolled*	Forged or rolled nickel alloy pipe flanges, forged fittings, and valves and parts for corrosive high-temperature service

Name	Grade	Specification
	Nickel Alloy Pipe Flanges, Forged Fittings, and Valves and Parts for Corrosive High-Temperature Service, n.d.)	

While there are standard specifications for flange chemical compositions and manufacturing processes, corrosion failures are sometimes observed as a result of discrepancies with the standards. SS flanges used in the oil and gas sector are typically required to be manufactured through forging, as per the ASTM A 182 standard. Nevertheless, it is common to encounter cast flanges on offshore oil and gas platforms, and these cast flanges frequently experience failures within a short timeframe, often within hours or days of being put into service (Kölblinger et al., 2022). Laboratory experiments have demonstrated that crevice corrosion propagates more significantly in cast SDSSs than in wrought SDSSs in seawater ranging from 15°C to 40°C (Larché & Dézerville, 2012). In a specific case documented by Tavares et al. (Tavares et al., 2018), a cast flange was supplied with significant amounts of sigma phase, likely due to the absence of a proper solution treatment. Consequently, the flange failed due to brittleness and pitting corrosion. Following a polarization test, optical microscopy and scanning electron microscopy (SEM) were employed to analyze the material. The analysis revealed that pits nucleated within intermetallic phases and non-metallic inclusions. Figure 1.13 (a) and (b) depict the existence of non-metallic inclusions within the flange material structure, leading to the formation of intermetallic phases. These inclusions and intermetallic

phases serve as preferential sites for pit nucleation, consequently reducing the pitting corrosion resistance of the flange material.

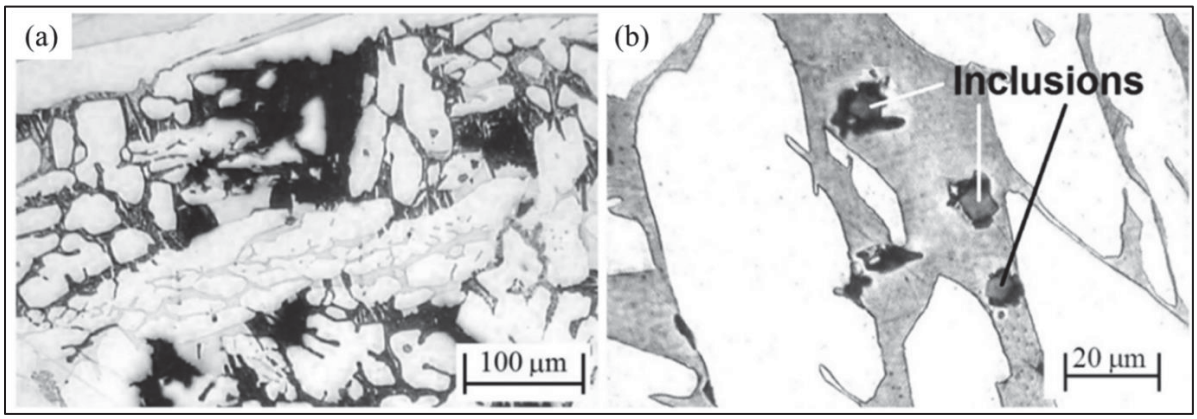

Figure 1.13 Observation of pitting after polarization testing (a) region of the high density of σ phase (b) pit nucleation in non-metallic phase from
Adapted from Tavares et al. (2018)

In a study conducted by Long et al. (Long et al., 2022), it was observed that UNS S42000 SS(13Cr) pipe flange exhibited leakage after being in service for 23 months in an ultra-deep high-pressure and high-temperature gas well. This leakage was attributed to pitting corrosion on the inner wall of the flange, leading to the propagation of a crack towards the ring groove. The corresponding illustrations, Figure 1.14 (a) and (b), depict this situation. Additionally, Figure 1.14 (c) shows the cross-sectional appearance of the pitting and cracking area near the flange end, while Figure 1.14 (d) shows that the crack propagated alongside the banded phase. The banded phase is known as delta ferrite, which forms during the forging process at higher temperatures than the austenitizing temperature. The presence of this delta ferrite proved to be a significant factor in the failure of the system. The presence of a significant amount of delta ferrite promoted the formation of chromium-rich carbides, leading to a decrease in pitting resistance. Additionally, the delta ferrite compromised crack resistance, causing cracks to form along the interfaces of delta ferrite and martensite.

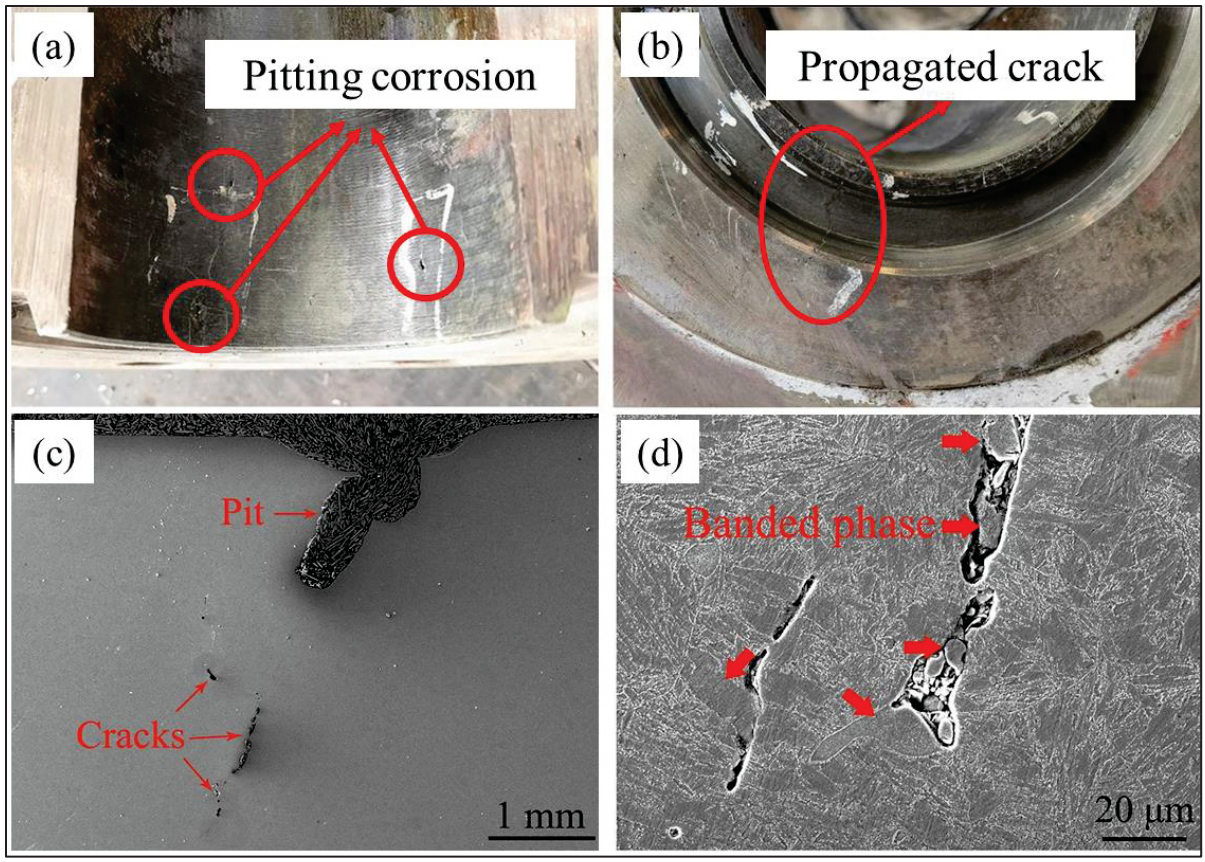

Figure 1.14 Corrosion and propagation of cracks on the surface of the pipe flange can be observed as follows: (a) pitting corrosion occurring near the flange end on the inner surface; (b) crack propagation originating from the pit located in the ring groove; (c) the detailed cross-sectional morphology of the region affected by pitting and cracking; (d) a closer examination at a higher magnification
Adapted from Long et al. (2022)

SSs in seawater are highly vulnerable to crevice and pitting corrosion originating from the presence of gaps and crevices in bolted flanged joints (R. Francis; G. Byrne, 2007). In order to mitigate degradation by these corrosion types, it is recommended to use SSs with a Pitting Resistance Equivalent Number (*PREN*) higher than 40 to reduce the probability of crevice and pitting corrosion. This *PREN* is defined by Eq.(1.4), and involves chromium, molybdenum, and nitrogen weight percentages, as these elements stabilize the passive film on SS surfaces (Kang & Lee, 2013; Westin & Hertzman, 2014).

$$PREN = \%Cr + 3.3 \times \%Mo + 16 \times \%N \quad (1.4)$$

For example, UNS S32750, UNS S31254, and UNS S31266 are high-grade SSs with a *PREN* greater than 40 (Nicolas Larché; Dominique Thierry; Pauline Boillot; Thierry Cassagne; Jéréme Blanc; Philippe Dézerville; Elisabeth Johansson; Jean Marc Lardon, 2016) and typically suggested as flange material in corrosive environments. Rogne et al. (Rogne et al., 1998) used the ASTM G48 test method to compare the crevice corrosion properties of weld overlays of Ni-based alloys to UNS S31254 SSs for seawater applications. Their investigations showed that only alloy 59 is beneficial for use with respect to crevice corrosion initiation compared to UNS S31254 SSs, while all alloys C-22, C-276, 625, and C-4 weld overlays have lower critical crevice temperature (CCT) than the UNS S31254 base material. F.J Martin et al. (Farrel J. Martin; Paul M. Natishan; Steven H. Lawrence; Elizabeth A. Hogan; Keith E. Lucas; Elvin Dail Thomas, 2004) ranked the corrosion susceptibility of Ni-Cr-Mo alloys in elevated temperature seawater in combination with gaskets. In their study, a potentiostat controlled the potential at a constant value of 0.3 $V_{Ag/AgCl}$, and the solution temperature was kept constant at 65ºC. As shown in Table 1.4, it was found that alloy 625, which had the lowest *PREN* among the studied alloys, exhibited crevice corrosion initiation at a lower exposure time (t_{init} = 2.9 hours).

Table 1.4 Crevice corrosion initiation time (t_{init}) for Ni-Cr-Mo alloys in 65ºC seawater Adapted from Martin, Natishan, et al. (2004)

Alloy	**PREN**	**t_{init} (hr)**
625	51	2.9
276	73	9.5
59	74	16
2000	76	20
686	77	>120

Al-Abbadi et al. (Al-Abbadi et al., 2017) investigated the crevice corrosion failure of alloy 625 flange in seawater service at an elevated temperature and proposed an alternative in alloy 686 with a CCT of up to 85°C. Larché et al. (Nicolas Larché; Dominique Thierry; Pauline Boillot; Thierry Cassagne; Jéréme Blanc; Philippe Dézerville; Elisabeth Johansson; Jean Marc Lardon,

2016) studied the crevice corrosion performance of several SS and nickel alloys at various temperatures in both natural seawater and chlorinated seawater. In their tests, flanged joints were immersed in seawater for three months, including natural seawater at 30°C, chlorinated seawater at 30°C, and chlorinated seawater at 50°C. They reported that among the tested alloys, flanges made of UNS N06022 and UNS S31266 exhibited resistance to crevice corrosion.

Even high *PREN* SSs are susceptible to crevice corrosion in seawater. Indeed, the *PREN* does not consider significant factors that affect corrosion resistance (e.g., metallurgy, product form, service conditions, geometrical configuration of the confined zones, and etc.); for example, cast alloys have less resistance to crevice corrosion than wrought alloys because of more heterogeneous metallurgical composition (Larché & Dézerville, 2012; Nicolas Larché; Dominique Thierry; Pauline Boillot; Thierry Cassagne; Jéréme Blanc; Philippe Dézerville; Elisabeth Johansson; Jean Marc Lardon, 2016). In addition, the validity of *PREN* as a universal method has been questioned in a number of papers (Sridhar, 2022).

Although high-grade SSs with a high *PREN* value were used in aggressive environments, other factors, including metallurgical and environmental factors, caused the failure of the flanges. The *PREN* does not consider the negative influence of impurities, such as sulfur and carbon or the effect of microstructure. In fact, it is possible for DSS, and SDSS to have drastically reduced corrosion resistance if the microstructure consists of small amounts of deleterious phases (such as sigma phases) (Fargas et al., 2009). Table 1.5 summarizes the chemical composition of CRAs that are used in the literature as a flange material.

Table 1.5 Chemical composition of the materials used as a flange material in the literature

Material	UNS No.	Other designations	Cr	Ni	Mo	N	Other	PREN	Type	Corrosion failure reported
Stainless steels	S32750	2507	24-26	6-8	3-5	0.24-0.32	Cu <0.5	38-47	Super duplex	Yes
	S42000	420	12-14	<0.5	<0.5	-	Cu <0.5	-	Martensitic	Yes
	S31254	254 SMO	19.5-20.5	17.5-18.5	6-6.5	0.18-0.22	Cu 0.5-1	42-45	Super austenitic	Yes

Material	UNS No.	Other designations	Cr	Ni	Mo	N	Other	PREN	Type	Corrosion failure reported
	S31266	B66	23-25	21-24	5.2-6.2	0.35-0.6	Cu 1-2.5 W 1.5-2.5	46-54	Super austenitic	No
	N08367	Al6XN	20-22	23.5-25.5	6-7	0.18-0.25	Cu 0.75	43-49	Super austenitic	Yes
	S32205	-	22-23	4.5-6.5	3-3.5	0.14-0.2	-	34-38	Duplex	Yes
Nickel alloys	N06625	Inconel alloy 625	20-23	>58	8-10	-	-	40.2-41.3	-	Yes
	N06022	Hastelloy alloy C-22	20-22.5	>58	12.5-14.5	-	W 2.8-3.2	45.5-45.7	-	No
	N06686	Inconel alloy 686	20-23	>58	15-17	-	3-4.4	47-55.1	-	No

1.5.2 Gasket material

In bolted flanged joints, the gasket acts as a crevice former; therefore, the gasket material or the type of gasket affects the crevice corrosion on the flange surface. The primary purpose of a gasket in a flanged joint is to prevent leakage from the connection. However, many factors need to be considered in selecting the appropriate type of gasket, including the bolting, the media inside the pipeline, the pressure of the media, the temperature, and any cyclic or vibrational behavior of the joint (Bond & Yi Li., 2020). There are numerous types of gaskets, which can be classified into three categories: 1- metallic, 2- non-metallic, 3- semi-metallic (Shorts, 2017).

Kain et al. (Kain, 1998b) have studied the effect of gasket material on the crevice corrosion of a 316 SS flange in seawater, and, according to Table 1.6, it was reported that carbon fiber, aramid fiber, PTFE, glass-filled PTFE, and graphite/SS gaskets caused severe crevice corrosion. However, the reason for such behavior was not discussed in this work. Indeed,

corrosion was only evaluated visually and quantified by measuring the corroded surfaces depth.

Table 1.6 Crevice corrosion initiation and propagation on 316 SS flange in combination with various gaskets
Adapted from Kain (1998b)

Gasket material	No. of flanges attacked	Maximum depth (mm)
Fluoroelastomer	0/2	0.00
Red rubber	1/2	0.01
Carbon Fiber + Nitrile	2/2	0.77
Aramid Fiber + Nitrile	2/2	2.1
PTFE	2/2	1.05
Glass Filled PTFE	1/2	1.4
Graphite/SS	1/2	0.69

Turnbull (Turnbull, 1998, 1999) stated that the use of a graphite gasket, which is more noble than DSS, results in an increase in pH within the crevice, thereby preventing crevice corrosion. Flexible graphite gasket is frequently chosen as a sealing material because it offers extensive chemical resistance, a broad temperature range, affordability, outstanding sealing performance, and the ability to provide fire safety. This noble gasket has a higher corrosion potential than the DSS in their used 0.6 M NaCl solution, hence the reaction on the graphite will be net cathodic, and indeed the hydrogen ions (H^+) will be reduced in the crevice. This result is contradictory to Kain findings (Kain, 1998b), which concluded that graphite gaskets caused severe crevice corrosion. Turnbull's studies indicate that the corrosion potential of graphite in acidic solutions is expected to be more noble than that of DSS in seawater when biofilm formation occurs. Consequently, graphite will act as a cathode within the crevice of this system. This suggests that coupling DSS with a graphite gasket has the potential to mitigate the pH decline within the crevice. Thus, graphite gaskets could help prevent the initiation of crevice corrosion in systems where acidification of the crevice solution serves as a precursor to crevice attack. Turnbull's experiments confirmed this concept by demonstrating that significant acidification within the crevice can be prevented for potentials up to approximately 0.4 V_{SCE}. However, in Kein's experiments, where the applied potential was 0.6 V_{SCE}, the

reactions on the graphite surface become net anodic, potentially contributing to the initiation of crevice attack

Rogne et al. (Rogne et al., 1998) also studied the impact of gasket material on CCT. Tests were carried out by PTFE and rubber bonded aramid gaskets. The CCT of the setup using a PTFE gasket was measured to be 35°C, whereas the CCT of the setup using an aramid gasket was 42°C. This indicates that the aramid gasket enhanced the resistance to crevice corrosion. This study uncovered that the porous structure of aramid gaskets facilitated the absorption of seawater, thereby providing the necessary oxygen for the cathodic reaction within the crevice formed between the gasket and flange. Consequently, the acidification of the crevice and the subsequent crevice corrosion were delayed. However, there exists a contradiction between the findings of Rogne and Kain. According to Kain's results (Table 1.6), aramid fiber gaskets actually accelerated crevice corrosion of the flange. In contrast, Rogne's work identified aramid as a suitable gasket material capable of preventing corrosion. Hence, it appears that other factors, such as the material composition of the flange, may influence the corrosion propagation. Furthermore, discrepancies in the behavior of 316 SS and weld overlays with Ni-based alloys in seawater could contribute to the divergent outcomes observed in these studies.

Martin et al. (Farrel J. Martin; Paul M. Natishan; Steven H. Lawrence; Elizabeth A. Hogan; Keith E. Lucas; Elvin Dail Thomas, 2004) determined the sensitivity of several Ni-Cr-Mo alloys to crevice corrosion in seawater at 65^{o}C and at 0.3 V_{SCE}. Their results showed that fluoroelastomeric gaskets enhanced the resistance of alloys to crevice corrosion, even at higher potentials (0.6 V_{SCE}) and longer exposure times (60 hours). X-ray diffraction (XRD), energy-dispersive X-ray spectroscopy (EDX), and Fourier transform infrared spectroscopy (FT-IR) analysis of gasket material and residues on metals revealed that a layer of tac deposited on the surface of the metal prevents the metal from corroding. The tac-related layer originates from the mold release agent used to process fluoroelastomeric gaskets. In agreement with Kein’s results (Table 1.6), this research claims that fluoroelastomeric gaskets could be suitable for sealing.

Literature mainly discusses low-pressure applications for corrosion studies. However, in industrial applications with higher pressures, typically ranging from 65 to 100 bars, metal gaskets or spirally wound gaskets are used due to the risk of blowout in sheet gaskets (A.-H.

Bouzid & Das, 2023). The material of these gaskets should be compatible with the flange material to reduce the risk of galvanic corrosion in seawater (R. Francis; G. Byrne, 2007). Mathiesen et al. (Troels Mathiesen; Henrik Bang, 2011) compared crevice corrosion initiation and propagation in a UNS S31254 flange using graphite gaskets, spiral wound gaskets, and polymer gaskets. The results of the polarization tests revealed that the initiation potential for the graphite gasket was lower than for the others, and, in addition, crevice corrosion propagated after initiation with the graphite gasket, while causing repassivation in the cases of polymer and spiral wound gaskets. Stress corrosion cracking (SCC) in a ring type joint (RTJ) caused failure of reactor pipeline of a hydrocracker unit; the ring gasket was made of 347 SS. Examinations showed that the ring gasket had developed a number of discrete cracks as shown in Figure 1.15 (a), (b), and(c). Figure 1.15 (d) depicts the corrosion products firmly adhering to the fracture surfaces. (Gore et al., 2014). Simonton et al. (J. Simonton & Barry, 2006; J. L. Simonton & Barry, 2006) embarked on the development of an innovative gasket design that distinct from the traditional spiral wound gasket, which typically consists of Monel windings, PTFE filler, and an outer carbon steel ring. Their primary objective was to address a range of critical concerns, which encompassed reducing flange face corrosion, improving handling limitations, and enhancing sealing performance. The researchers observed that the standard spiral wound gasket configuration with a Monel inner ring proved ineffective in preventing corrosion across the entire flange face. They modified the design by adding machined serrations to the ring faces, similar to the kammprofile or serrated metal gasket type. The final design features Monel windings, flexible graphite as the filler material, and a serrated inner ring coated with PTFE. Hamblin et al. (Hamblin & Finch, 2001) reported severe corrosion on the outer rings of spiral wound gaskets made from carbon steel, resulting in corrosion-induced removal of the outer ring, which poses a potential risk of diminishing the blowout resistance of the sealing component. Additionally, the expansion of corrosion products had the potential to exert pressure on the flanges, potentially releasing the compressive stress on the sealing element. They stated that replacing the gasket with corrosion-resistant alternatives was not feasible immediately, as it was necessary for the system to remain operational. In addition, implementing individual remedial measures for each flange, such as sealant injection, was also less desirable due to the extensive number of flanges involved. However, after conducting

physical testing, theoretical modeling, industrial investigations, and risk assessments, the decision was made to continue the system operation. Table 1.7 summarizes the details of the corrosion failures due to inappropriate gasket material or design.

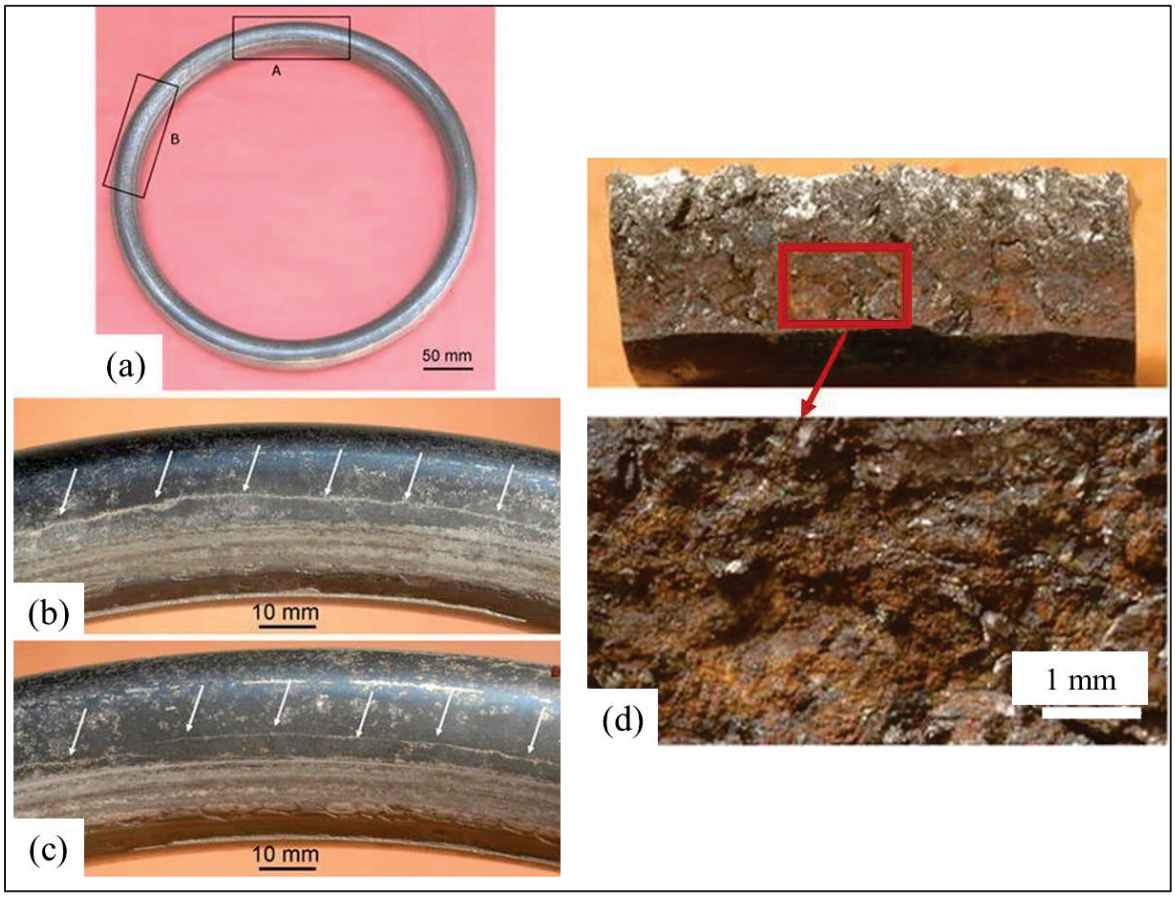

Figure 1.15 Ring gasket: (a) overall view of the failed gasket; (b) and (c) close-up views of regions A and B, which reveal cracks; (d) fracture surface of the ring gasket displaying a thick layer of oxides and/or corrosion products
Adapted from (Gore et al. (2014)

Table 1.7 Details of the corrosion failures due to inappropriate gasket material or design

Type of gasket	Gasket material	Medium	Location of corrosion	Root cause	Mitigation method	Ref.
Spiral wound	DSS 2205 windings, graphite filler	Seawater	Crevice corrosion on the flange face	Gasket material	Using polymeric gaskets instead of spiral wound	(Troels Mathie sen; Henrik

Type of gasket	Gasket material	Medium	Location of corrosion	Root cause	Mitigation method	Ref.
						Bang, 2011)
Sheet	Graphite, and PTFE	Seawater	Crevice corrosion on the flange face	Gasket material	Using elastomer-type gaskets instead of graphite and PTFE gaskets	(Kain, 1998b)
Spiral wound	316L SS inner ring, carbon steel outer ring, 316L SS hoop, expanded graphite filler	Marine humidity	Flange surface on the contact area with gasket	Water ingress in tightened flanges in modular construction	- Rust preventive coating - Special spiral wound gasket made by vermiculite instead of expanded graphite filler	(Takahiro Tsuda; Nozomi Satake; Manabu Itoki, 2021)
Spiral wound	Monel windings, PTFE filler, and carbon steel ring	Hydrofluoric acid	Flange face	Gasket design	Designed a new customized gasket that prevents the direct contact of the process with the flange face	(J. Simonton & Barry, 2006; J. L. Simonton & Barry, 2006)
Sheet	Graphite	Seawater	Crevice corrosion on the flange face	Gasket material	Using non-graphite gasket	(Francis, 1994b)
Spiral wound	Carbon steel outer ring	-	Severe corrosion on the outer ring	-	Field tests and risk assessment provided confidence that it was acceptable to continue operation	(Hamblin & Finch, 2001)

1.5.3 Microorganisms

Microbiological species are another factor that may influence corrosion when present in the environment. Corrosion influenced by microbiological activity is known as microbiologically influenced corrosion (MIC). As a result of a microorganism rich environment, pitting and crevice corrosion, selective de-alloying, and differential aeration may occur (Little et al., 2000). Kolblinger et al. (Kölblinger et al., 2022) reported the failure of a UNS S32760 SDSS (*PREN* ≥ 40) flange, although the chemical composition and microstructure of the material were based on the ASTM A182 standard. Here, in the crevice of the gasket, the flange material suffered preferential corrosion of the ferrite phase. Figure 1.16 shows peaks relating to sulfur (S) and chlorine (Cl). In addition to deposits of organic materials that form during stagnant conditions or when there is a low or intermittent liquid flow, resulting in the creation of crevices and differential aeration cells, sulfur is also a characteristic of corrosion induced by microorganisms (i.e., microbiologically influenced corrosion). Furthermore, the service conditions, which involve exposure to 28°C seawater and the specific geometry and size of the crevice between the gasket and flange, promote the proliferation of bacteria and expedite the corrosion process. In seawater, microorganisms present in water can adhere to surfaces and form biofilms. Biofilms are thin layers of microorganisms that adhere to each other and to surfaces. Mathiesen et al. (Troels Mathiesen; Henrik Bang, 2011) stated that the presence of biofilms in seawater below 40 °C leads to flange material ennoblement, elevating the potential of UNS S31254 to 350 to 450 $mV_{Ag/AgCl}$. This elevation contributes to the initiation and propagation of crevice corrosion, especially when graphite is used in spiral wound gaskets.

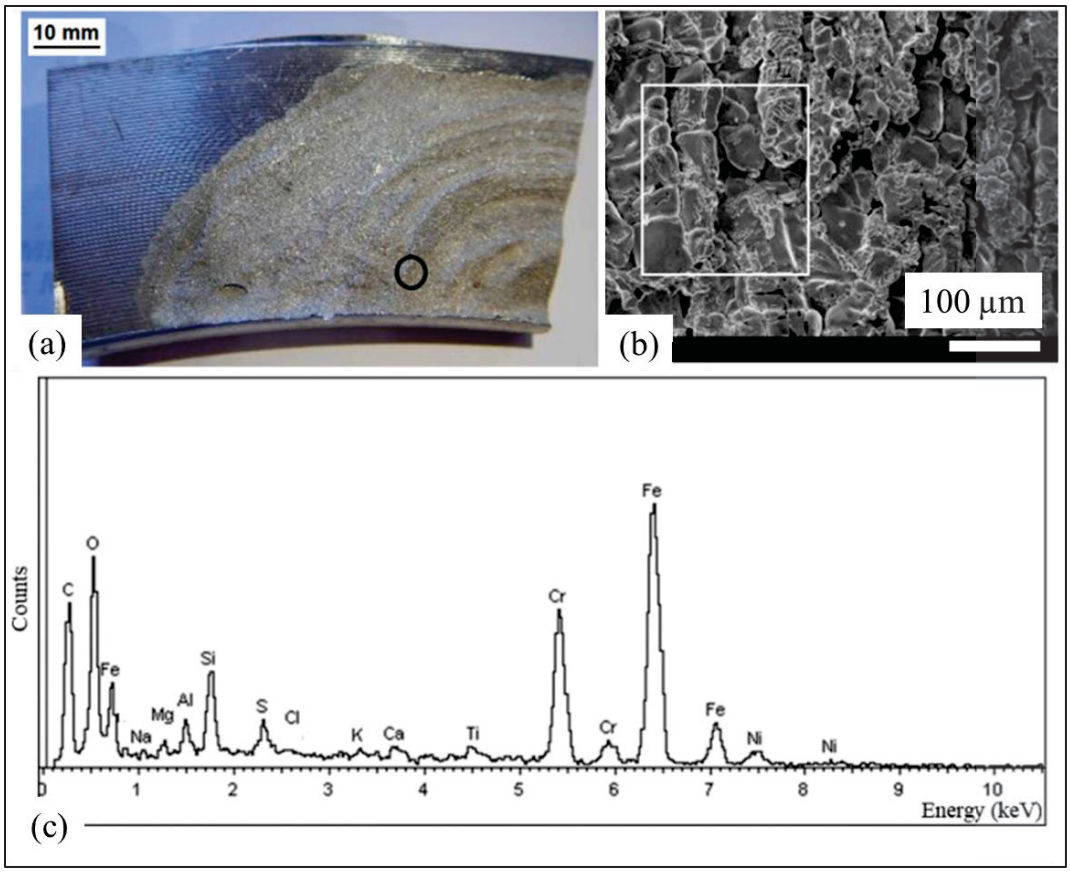

Figure 1.16 Analysis of the corroded flange face: (a) the selected region of the corroded surface for SEM analysis; (b) SEM image of the circled region; (c) EDS analysis
Adapted from Kölblinger et al. (2022)

1.5.4 Temperature

Larche et al. (Nicolas Larché; Dominique Thierry; Pauline Boillot; Thierry Cassagne; Jéréme Blanc; Philippe Dézerville; Elisabeth Johansson; Jean Marc Lardon, 2016), revealed that the temperature affects the electrochemical potentials and kinetics of the corrosion initiation and propagation. This work studies the effect of temperature on six types of flanges, including UNS S32205, S32750, N08367, S31266, N06625, and N06022, for three months in both natural and chlorinated seawater. In the seawater solutions at 30°C, only the surface of the less alloyed S32205 was corroded, but in the solution at 50°C, corrosion was observed on the surfaces of N08367, S32750, and N06625 flanges. Upon visual examination of the corrosion results, it was observed that the corrosion on the surface of the UNS S32750 flanges was notably severe.

In contrast, the propagation of crevice corrosion on the UNS N06625 flanges was relatively limited. Remarkably, the surfaces of the UNS S31266 and UNS N06022 flanges exhibited resistance to crevice corrosion even after three months of exposure to chlorinated seawater at 50°C.

Rogne et al. (Rogne et al., 1998) specified CCT for weld overlays of different Ni alloys by increasing the temperature in steps of 5°C from 20°C to 100°C. It was found that the more resistant the alloy, the higher the CCT temperature. In addition, at higher temperatures, the time of corrosion initiation diminished drastically.

1.5.5 Chloride concentration

Chloride concentration is another major influential factor in the crevice corrosion behavior of SSs. Hydrolysis occurs in chlorinated solutions in crevices, causing an increased concentration of acid and chloride in occluded volumes, ultimately resulting in passive film breakdown (Oldfield & Sutton, 1978a, 1978b). An increment in chloride concentration decreases the corrosion resistivity of SSs to localized corrosion. This factor affects the passivity breakdown potential and makes the SS vulnerable to localized corrosion (Dastgerdi et al., 2019b; Ibrahim et al., 2009). Tawancy et al. (Tawancy, 2019) reported a leakage failure of a 304 SS gasket used as a seal in bolted flanged joints of a hydrocarbon transfer pipeline in a polyethylene plant, as well as in a piping system employed for demineralized water distribution in a polypropylene plant. Root cause analysis indicated that contamination of the water by chloride ions, and excessive compressive preload were the main reasons for the leakage. In some cases, chlorination is carried out in seawater systems to avoid the formation of marine biofilms on the surface of the metal (Troels Mathiesen; Henrik Bang, 2011). Larche et al. (Nicolas Larché; Dominique Thierry; Pauline Boillot; Thierry Cassagne; Jéréme Blanc; Philippe Dézerville; Elisabeth Johansson; Jean Marc Lardon, 2016) reported an open circuit potential (OCP) difference of SS materials in chlorinated and non-chlorinated seawater of about 300 mV. Still, for Ni-based alloys, the increment of OCP in chlorinated seawater was less than 100 mV. This clearly demonstrates that the effect of chlorination is more pronounced in SSs compared to Ni-based alloys. Generally, it has been observed that an increase in chloride concentration in the

bulk solution leads to a decrease in the crevice initiation potential for Ni-based alloys (Odahara et al., 2020).

1.5.6 Flow

The effect of fluid flow velocity on the corrosion between gaskets and flanges is considered by the study of Mameri et al. (Mameri et al., 2000). Their study results showed that increasing the fluid velocity from 1.4 cm. s^{-1} to 4.5 cm. s^{-1} slightly increased the corrosion rate of carbon steel XC38. Based on this work, it can be hypothesized that the main cathodic reaction is the reduction of oxygen, which is diffusion controlled. Therefore, by increasing the flow rate, the amount of oxygen on the surface of the cathode can be increased, and as a result, the corrosion rate will then rise. Additionally, flow conditions can influence corrosion by either conveying corrosive substances toward the metal surface or carrying away corrosion products from the metal surface. Ji et al. (Ji et al., 2023) examined the impact of flow velocity on the corrosion of the inner wall of an ASTM A105 carbon steel flange after one year of service. Figure 1.17 (a) and (b) demonstrate visible fluid erosion marks on the inner wall surface. Based on their analysis, it was determined that the average flow velocity of the fluid within the pipeline surpassed the critical erosion velocity. Consequently, the fluid flow inside the pipeline caused erosion to the inner wall of the flange. In seawater applications, CRAs often experience heightened corrosion aggressiveness during shutdown periods, leading to stagnant seawater in contact with the flange surface. Seawater stagnation can easily give rise to the formation of differential aeration cells and/or deposits, ultimately compromising the passivity and causing a dramatic propagation of localized corrosion (Larché & Dézerville, 2012).

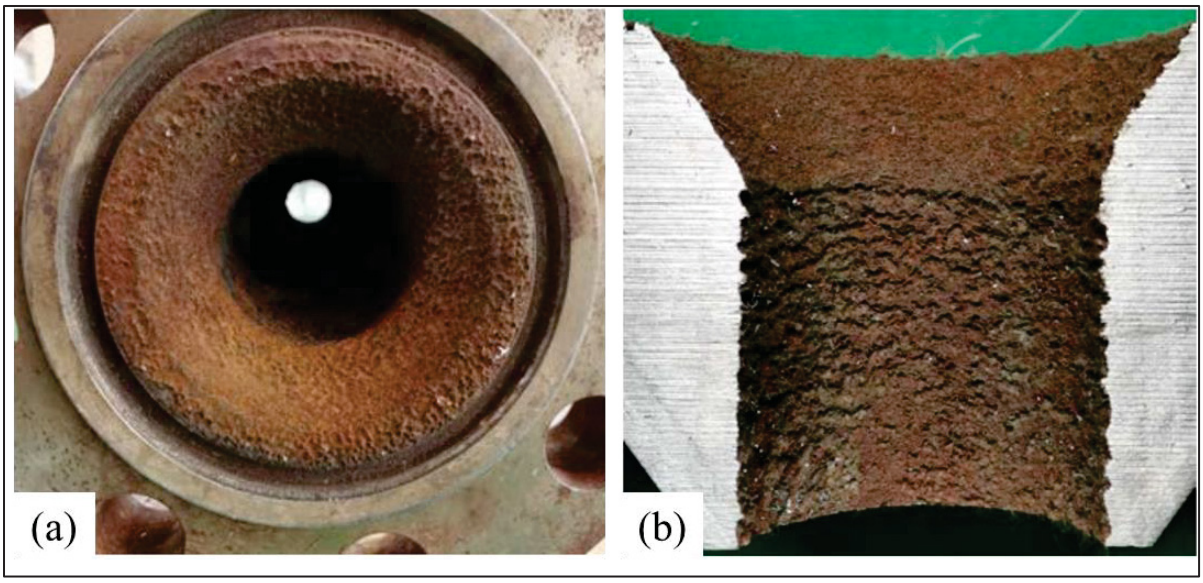

Figure 1.17 Macroscopic image of the corroded ASTM A105 flange; (a) corroded sealing groove and inner wall; (b) cross section of the corroded flange
Adapted from Ji et al. (2023)

1.6 Corrosion monitoring techniques

Corrosion monitoring and detection methods can be categorized into two groups: offline detection and online monitoring. Offline detection suffers from extended testing cycles and the inability to conduct continuous assessments (Hussein Khalaf et al., 2024). Online corrosion monitoring techniques are valuable for detecting and assessing corrosion in various forms, including localized corrosion. However, traditional corrosion monitoring methods face specific challenges and limitations that can complicate the detection of localized corrosion. Various methods have been introduced in the literature for monitoring pitting corrosion (Orlikowski et al., 2017). However, only a few publications have discussed the monitoring of crevice corrosion (Schmitt et al., 2004; X. Sun & Yang, 2006). Given the similarity between pitting corrosion and crevice corrosion, and considering that crevice corrosion often initiates with the formation of pits in the occluded regions (Costa et al., 2023), the advantages and disadvantages of monitoring methods for pitting corrosion are also applicable to crevice corrosion. Non-destructive testing methods find extensive use in industrial settings, with the ultrasonic technique (UT) being particularly notable for its ability to observe the dimensions and configurations of pits. Regrettably, this method exhibits low sensitivity, limiting its

efficacy to detecting only advanced stages of pitting corrosion. The localized nature of damage necessitates a considerable number of measurements for precise diagnosis (D. Sun et al., 2009). Another prevalent technique for monitoring pitting corrosion is the acoustic emission method, where acoustic signals are produced by the evolution of hydrogen bubbles or the cracking of passive layers. This method key advantage lies in its capability to capture the early stages of pitting corrosion, attributed to the degradation process of passive layers. Optimal outcomes are achieved for materials featuring thick passive layers, such as aluminum and magnesium alloys (Orlikowski & Darowicki, 2011). Despite its numerous advantages, the acoustic emission method is seldom integrated into online corrosion monitoring systems due to its heightened sensitivity to external noise, a common occurrence in industrial environments (Mazille et al., 1995; Xu et al., 2011). Corrosion monitoring through electrochemical techniques is not without drawbacks and limitations, primarily tied to the generation of corrosion products and variations in the conductivity of the corrosion medium, which can impact measurement accuracy (Cox & Lyon, 1994). Moreover, employing electrochemical methods in the investigation of metal corrosion may distort the actual corrosion reactions of the samples under study due to the necessity for additional interference. Additionally, these methods fall short in precisely identifying localized corrosion or effectively assessing cumulative corrosion processes, as they can only deliver average electrochemical data for a specific region at a specified time (Arellano-Pérez et al., 2018).The most commonly used electrochemical techniques for corrosion monitoring include the corrosion coupon technique, electrochemical resistance probes (ER), linear polarization resistance (LPR), electrochemical impedance spectroscopy (EIS), and electrochemical noise (EN). Various electrochemical techniques for corrosion monitoring are compared in Table 1.8 (Ma et al., 2019b). Artificial intelligence (AI) has recently been used in the field of corrosion monitoring, enhancing precision, speed, and efficacy in the detection and protection against corrosion (Pourrahimi et al., 2023). It is important to remember, nevertheless, that effective data processing and analysis skills are required for the successful application of these strategies, as are dependable communication technologies for sending data from remote locations. (Hussein Khalaf et al., 2024).

Table 1.8 Comparison of electrochemical techniques for corrosion monitoring
Adapted from Ma et al. (2019b)

Method	ER	LPR	EIS	EN	Coupon
Quantitative localized corrosion	×	×	-	×	✓
Qualitative localized corrosion	×	×	-	✓	✓
General corrosion	✓	✓	✓	✓	✓
Field monitoring use	✓	✓	✓	✓	✓
Response time	2h to days	Instant	Instant	Instant	10-365 days

1.7 Analysis of the flange face corrosion

Gaps or crevices between flanges due to the presence of the gasket are potential places for crevice corrosion to take place. Figure 1.18 indicates potential locations for crevice corrosion when using spiral wound and sheet gaskets. There is a gap between the inner ring and the pipe bore Figure 1.18 (a) and (b)), and the upper and lower zones of the inner ring of spiral wound gaskets which are susceptible to crevice corrosion (Figure 1.18 (a)) (Worden, 2014a). Figure 1.18 (c) illustrates the distribution of bolt load along the outer diameter (OD) of the flange, resulting in bending around the bolt circle and causing the flange to lift off from the inner diameter (ID) of the gasket. This phenomenon creates potential gaps that can facilitate the occurrence of crevice corrosion. The zones described with a circle in the flange face near the gasket inside diameter are crevices containing small amounts of stagnant fluid. A high rate of metal dissolution occurs in these crevice regions according to the mechanism discussed in section 1.4.1. After a period of time, enough mass loss occurs enlarging the crevice zone toward the outside causing failure by creating a leak path in the flange facing (as shown in Figure 1.19). Creep in bolted flanged joints is a phenomenon where the bolts and the flange components deform over time due to the influence of mechanical loads and elevated temperatures (Kanthabhabha Jeya et al., 2020; Sawa et al., 2015). The deformation caused by the gasket and bolt creep can result in the formation of crevices or gaps at the flange facings (Efremov, 2005).

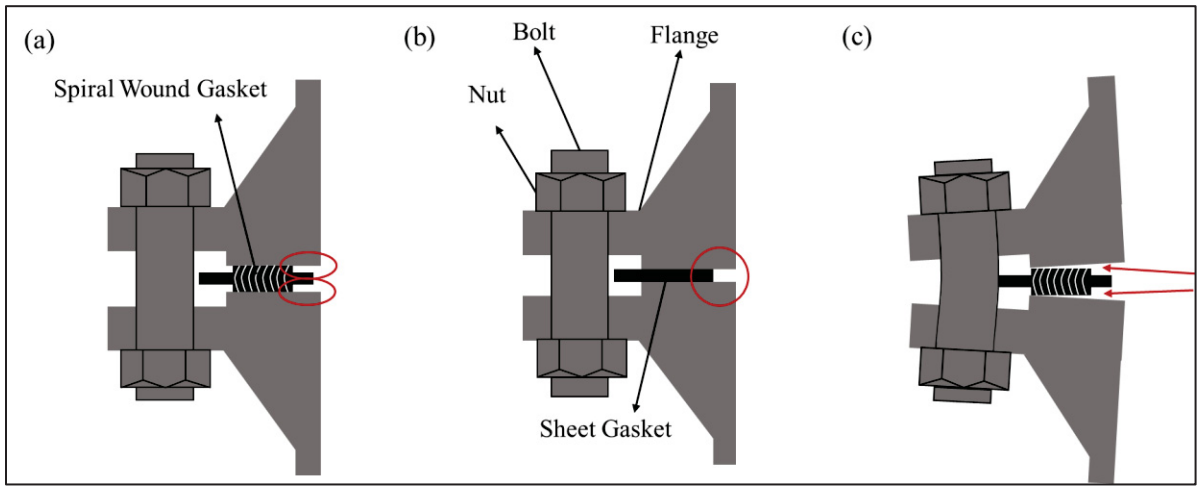

Figure 1.18 Schematic of vulnerable places for crevice corrosion between gaskets and flanges: (a) standard spiral wound with inner ring-crevice at ID; (b) standard cut-sheet gasket-crevice at ID; (c) crevices above and below spiral wound inner ring
Adapted from Worden (2014a)

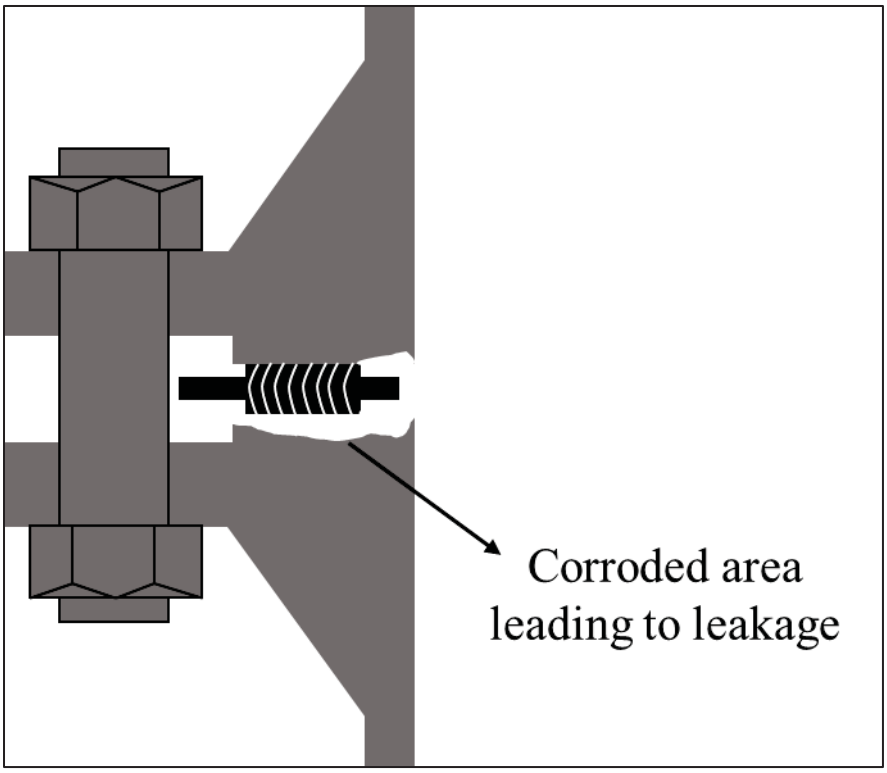

Figure 1.19 Schematic illustration depicting crevice corrosion on the flange face at the interface between the flange and the standard spiral wound gasket, resulting in leakage Adapted from Worden (2014a)

Corrosion on the flange surface or gasket can result in surface irregularities and inadequate compression force, thereby increasing the risk of leakage. In Figure 1.20, the diagram illustrates the forces acting on gaskets in a bolted flanged joint (Tawancy, 2019). Prior to pressurizing the system, the gasket experiences a compressive force (F_b) generated by tightening the bolts, effectively compressing the gasket into the flange to establish a seal and prevent fluid leakage between the flanges. Once the system is pressurized, opposing forces come into play: the hydrostatic force (F_h), which seeks to separate the flanges, and the blowout force (F_p), which aims to displace the gasket. To counteract the combined impact of the hydrostatic force and the blowout force, additional bolt tightening is required to maintain the gasket in position. However, excessive compression force, beyond what is necessary to counteract these opposing forces, may eventually lead to gasket deformation. Furthermore, non-uniform preload can introduce localized variations in gasket stresses. Taking these forces into consideration, the corrosion process can intensify the hydrostatic and blowout forces,

leading to the unloading of the preload and, ultimately, causing leakage. As per the literature, corrosion affecting the outer ring of the spiral wound gasket (made of carbon steel) can diminish the gasket resistance to blowout forces. Furthermore, the corrosion of carbon steel flange faces may induce the expansion of corrosion products, potentially opening the flanges apart and relieving the compressive stress on the sealing element, ultimately resulting in leakage (Hamblin & Finch, 2001).

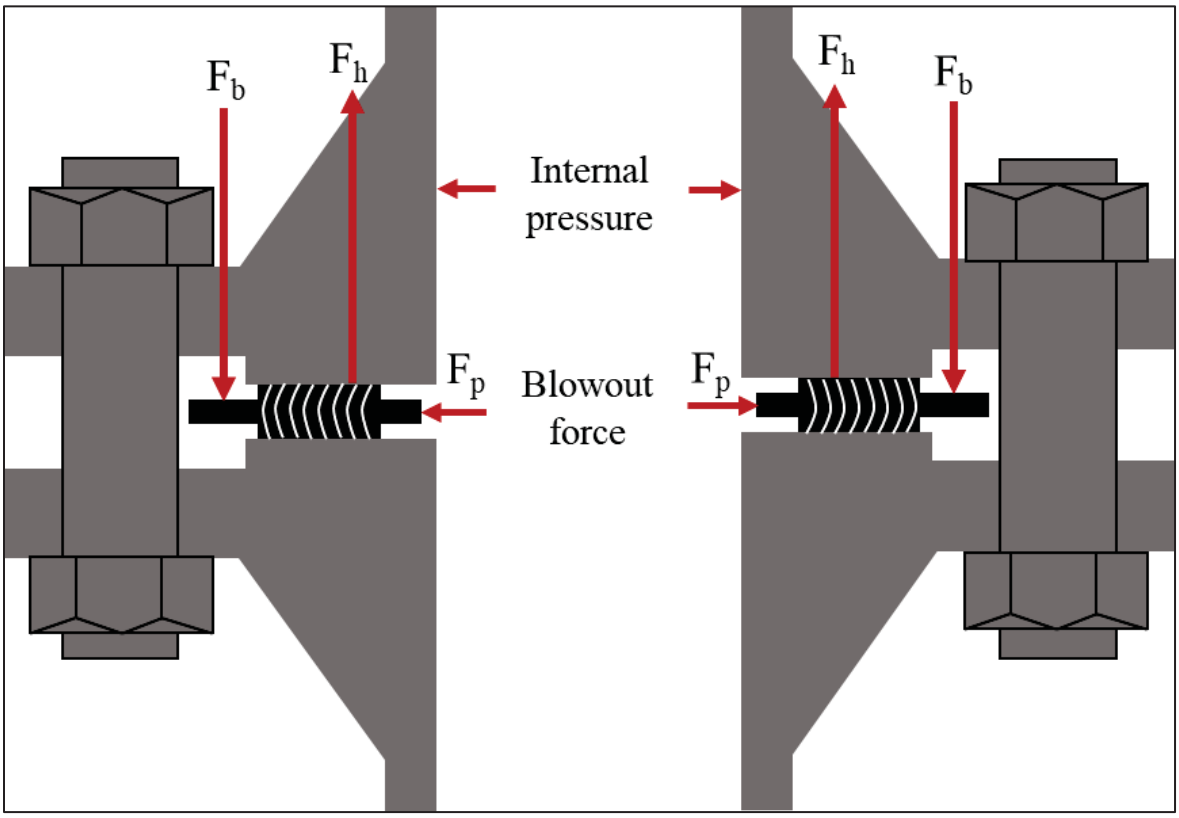

Figure 1.20 Illustrative diagram depicting the mechanical forces applied on the gasket in action. The red arrows identify each force, including the compressive force generated by tightening the bolts (F_b), the hydrostatic force (F_h), and the blow out force (F_p)

As shown in Figure 1.21, in flanged joints, there are two surfaces: the occluded face, which is the surface facing the gasketed joint, and the open surface. The occluded face typically acts as an anode for those alloys that are passive, while the open surface acts as a cathode, except in cases where the gasket is a nobler material (e.g., graphite). The extent of oxidant presence and its accessibility to the open flange surface are critical factors influencing the anodic dissolution

reaction within the crevice, ultimately leading to an increased rate of crevice corrosion. What makes crevice corrosion notably challenging is the contrasting availability of oxygen, or other oxidants. Oxygen is often more abundant on the open flange surface, where it can facilitate the formation of a protective oxide layer.

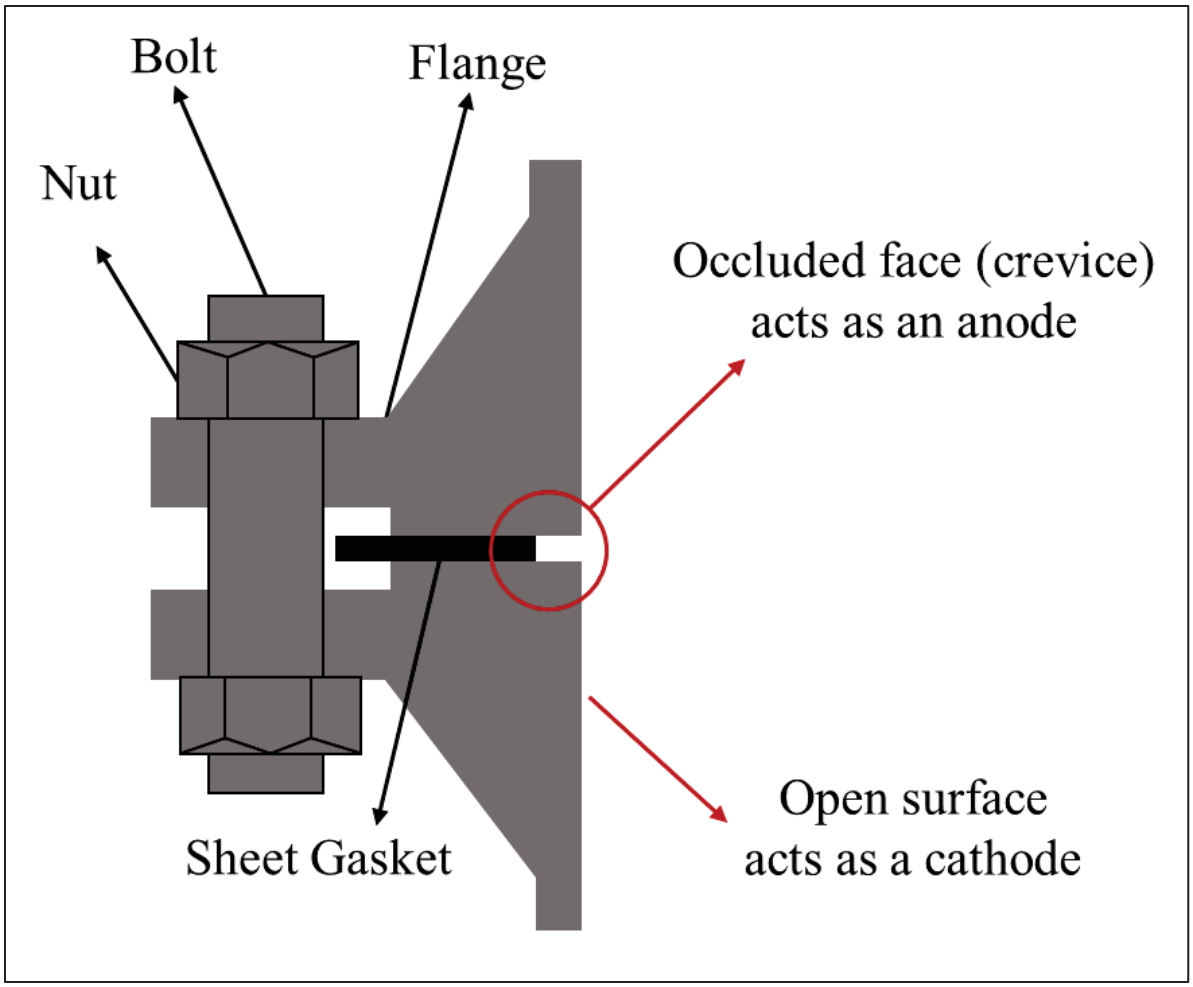

Figure 1.21 Illustration of crevice corrosion in bolted flanged gasketed joints, highlighting the anode and cathode regions

1.8 Discussion

The distribution and fraction of the studied factors in the field of corrosion phenomena in bolted flanged systems are presented in Figure 1.22 to better understand the most important failure factors and the factors that are understudied in the literature. Most of these studies

investigated the material of the flange and the type of gasket. As well, it can be concluded that SSs and nickel-based alloys dominated the studied flange materials in most cases. It was reported that the *PREN* value could be used to compare corrosion resistance of flange materials to pitting and crevice corrosion, with higher values of *PREN* indicating greater resistance. However, environmental factors and specific microstructures resulted in corrosion failure of alloys with a high *PREN*. Temperature, chloride concentration, roughness, fluid flow, stress, microorganisms, and pH are all factors that may influence flange corrosion, but very few studies have addressed them. The primary function of a gasket is to provide a leak-tight seal and to provide electrical insulation at the same time. Most of the gaskets used for critical services are semi metallic, such as spiral wound gaskets, Kammprofiles, etc. While these products can provide leak-tight seals when well designed, their metallic nature allows electrons flow between flanges, which may induce galvanic corrosion. Graphite gaskets are commonly considered inappropriate for use in seawater systems because the noble galvanic properties of the material lead to accelerated corrosion of the anodic flange material. However, such gaskets are useful for systems that operate at high temperatures.

There is a substantial amount of research on crevice and galvanic corrosion, which are among the main corrosion mechanisms on the flange surface, however, the majority of these studies are solely focused on experiments carried out by conditions which are not close to industrial applications. In these documented experiments, the assessment of materials occurs under conditions that deviate from those commonly encountered in industrial applications. For instance, these experiments neglect factors such as crevice geometry, the presence of fluid flow, and gasket contact stress. None of the studied papers and existing standards (e.g., ASTM, ISO) have proposed a scientific approach to analyze and predict the corrosion behavior of the flange in the presence of specific service conditions and different gasket materials.

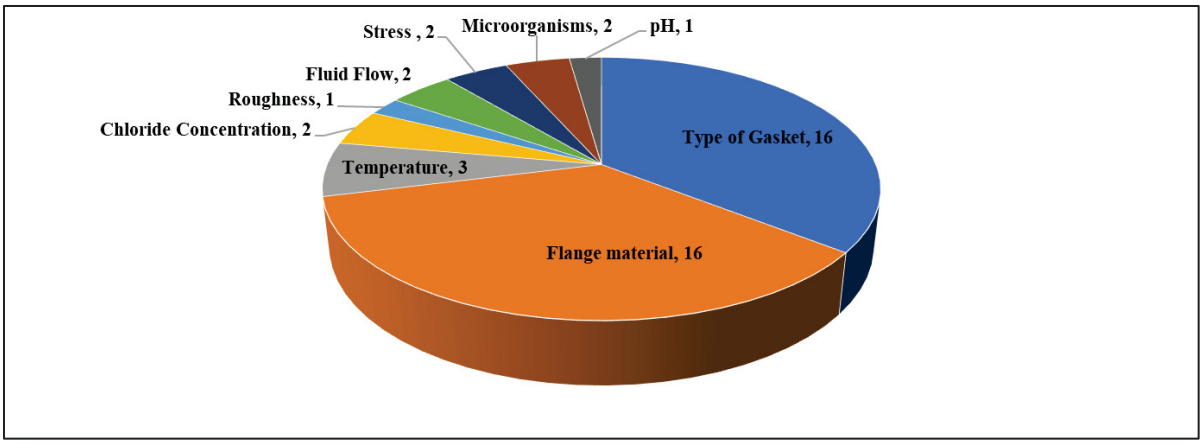

Figure 1.22 Studied factors in papers examined flange corrosion in bolted flanged joints

1.9 Conclusion

This review study documents failures in bolted flanged gasketed joints due to flange face corrosion and discusses the influence of the crucial factors on degradation by corrosion in these cases.

- Corrosion may occur on the inner side of the flange and the flange surface between gaskets and flanges. The gaps or crevices between gaskets and flanges are potential places for crevice corrosion which can be accelerated by the significant potential difference between the gasket and flange material, i.e., galvanic corrosion, sensitization due to welding on the flange surface, and the presence of deleterious phases in the flange material.
- Based on the conducted literature review, it was concluded that most studies reveal that the flange and gasket materials are the most problematic factors for flange face corrosion. Only a few studies discuss the influence of environmental factors, such as temperature, chlorination, and flow on corrosion behavior of bolted flanged systems.
- Indeed, the majority of the reviewed literature focused on investigating the consequences of corrosion following the occurrence of failure, while limited attention was given to preventive analysis of such failures or corrosion monitoring systems in this specific case. As a result, it can be inferred that there is currently a lack of studies

that examine the factors influencing corrosion phenomena in bolted flanged joints and that provide predictions regarding the corrosion behavior of flanges prior to failure.

- Most corrosion mitigation methods identified in the literature focus on flange and gasket material selection or altering gasket design. The literature reveals a limited number of studies proposing the implementation of coating and cathodic protection methods for corrosion prevention.
- Emerging AI techniques might be promising in the field of corrosion monitoring for flanged gasketed joints, and there is a gap in research within this field, highlighting the need for further exploration and investigation.

CHAPTER 2

LITREATURE REVIEW ON THE APPLICATION OF MACHINE LEARNING IN CORROSION SCIENCE

2.1 Introduction

The corrosion process is highly influenced by chemical composition and multiple environmental or operating factors. Therefore, it is difficult to establish causal relationships between individual environmental factors and corrosion processes based on physics-based corrosion laws or predict the corrosion life of materials. Corrosion behaviour prediction of materials in any environmental condition is important because testing materials under every one of them is time-consuming and expensive (Jiménez-Come et al., 2019). Accordingly, analyzing corrosion data and, subsequently, predicting corrosion behaviour needs advanced data mining methods (Pei et al., 2020; Yan et al., 2020). Recently, machine learning (ML) methods have been extensively used in materials research thanks to their powerful data mining capabilities. It automates searching for knowledge by learning from example data and experience without relying on predetermined equations. In corrosion research, ML algorithms such as random forest, support vector regression, and artificial neural networks have been used to study the corrosion behaviour (Y. Diao et al., 2021; Jiménez-Come et al., 2019; Lv et al., 2020; Pei et al., 2020).

2.2 Basic concepts of ML

Before going into details, it is essential to introduce some concepts related to ML methods. As shown in Figure 2.1, there are four steps in ML modelling that should be followed. In the first step, the appropriate data are extracted according to the application, and the database needs to be authentic to obtain reliable results. The second step is related to data pre-processing in which the outlier, repeated, or missing data are treated. In some cases, feature reduction or feature creation is beneficial. Completing data selection and pre-processing, different models are fitted

to the data, and the accuracy of each model is evaluated to find the best model. For model selection, the data are separated into two sections: train and test data. The model is fitted to the train data and will be evaluated on the test data, unseen data for the model. The best model is selected using K-fold cross-validation and hyperparameter search approaches. Industrial applications may change over time, so it is important to prevent model degradation. The last step, model maintenance, aims to keep the model compatible with changes over time (Carvalho et al., 2019; Y. Diao et al., 2021).

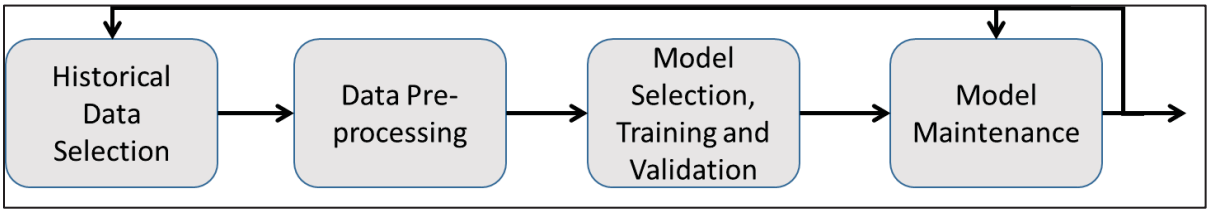

Figure 2.1 The main steps for the design of a ML model
Adapted from Carvalho et al. (2019)

ML algorithms are divided into two categories, namely unsupervised learning and supervised learning (Figure 2.2). The data are without labels in unsupervised learning, so the model must make sense of the inputs without outside help. In the supervised process, the network is provided with the desired output. For a proper use of the supervised learning process, the output of specific inputs is made available to train the model and find the mapping function, and then the model can be used to predict the output of new inputs (A. Y. T. Wang et al., 2020).

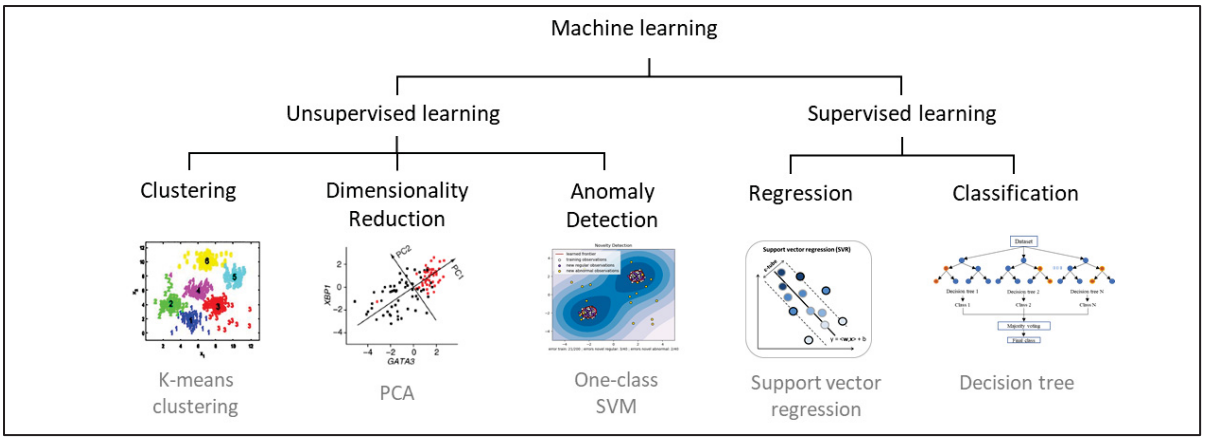

Figure 2.2 Categorizing ML algorithms
Adapted from One-Class SVM with Non-Linear Kernel (RBF) — Scikit-Learn 1.5.2 Documentation (n.d.) Pourrahimi et al. (2023) Rodríguez-Pérez & Bajorath (2022) Ringnér (2008)

2.3 Applications of ML in corrosion

Supervised ML algorithms are mainly used for modelling corrosion processes. Chemical composition of the alloy and environmental factors are considered input features, and corrosion rate is considered as output to establish corrosion rate prediction model with ML methods (Y. Diao et al., 2021; Pei et al., 2020; Yan et al., 2020). In the literature, ML was used in corrosion researches for several purposes, namely, prediction of corrosion rate (Y. Diao et al., 2021; Kamrunnahar & Urquidi-Macdonald, 2010; Lv et al., 2020; Pei et al., 2020; Wen et al., 2009; Yan et al., 2020), prediction of pitting corrosion behaviour (Jiménez-Come et al., 2019), and modelling maximum pit dimensions (Cavanaugh et al., 2010a). In the following, the results of related studies are elaborately discussed.

Ya-jun et al. (Lv et al., 2020) studied steel corrosion prediction using support vector machine (SVM) algorithm for embedded steel bars in concrete. The authors tried to establish a relationship between the geometrical parameters and corrosion rate, which is not linear. To do so, data related to 3D coordinate of the rebar corrosion condition was converted to the seven numerical parameters by mathematical calculations. These seven parameters were used to characterize the cross-section morphology of rusted steel bars. After pre-processing the data, they found that the most precise corrosion rate prediction models (for this application) are particle swarm optimization support vector machine (PSO-SVM) and grid search support

vector machine (GS-SVM) models with an accuracy of R^2=0.98 and R^2=0.92, respectively (As shown in Figure 2.3).

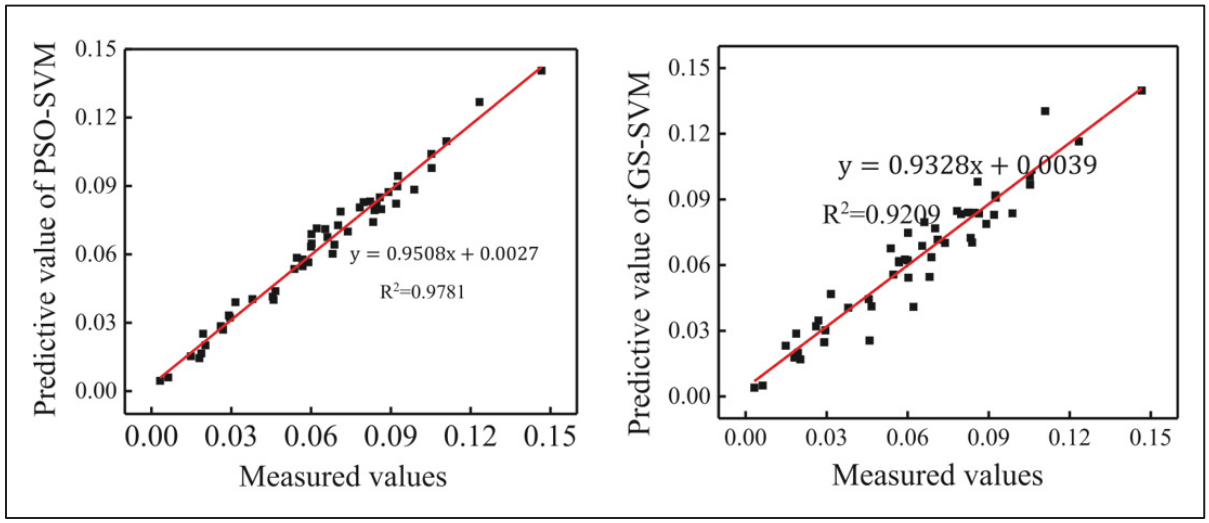

Figure 2.3 Relations between the predicted value and the actual (measured) value for PSO-SVM and GS-SVM models
Adapted from Lv et al. (2020)

Diao et al. (Y. Diao et al., 2021) studied the possibility of predicting marine corrosion of low alloy steels by ML algorithms. The authors used marine corrosion data of low alloy steels to create a model. Such data includes material and environmental descriptions, as shown in Table 2.1. Material contents, environmental factors, and time are input features, and corrosion rate is the output feature. The accuracies of several algorithms were compared in this research. It was found that random forest (R.F.) had the best prediction accuracy among the tested algorithms. This study employed three feature reduction methods: gradient boosting decision tree (GBDT), Kendall correlation analysis, and principal component analysis (PCA) to improve the model accuracy.

Table 2.1 List of features used in the corrosion rate prediction models
Adapted from Y. Diao et al. (2021)

Features		**Unit**	**Descriptions**
Material	Elements {i}	wt%	C content S content P content Mn content Si content Cr content Mo content Al content V content Ti content Cu content Nb content
Environmental	T_max/T_mean/T_min pH_max/pH_mean/pH_min O_2_max/O_2_mean/O_2_min S_max/S_mean/S_min	^oC $ml.L^{-1}$ %	Maximum/mean/minimum temperature value; pH value; dissolved oxygen content; salinity value of the seawater
Time	t	year	Immersion time
Corrosion rate	v	$mm.a^{-1}$	Annual corrosion depth, milimeter per year

Such feature reduction methods remove the least influential features on the corrosion behaviour of the steel. By doing so, the feature importance process is established and used to select relevant features to build the corrosion behaviour model. Figure 2.4 shows the feature importance plot used to predict corrosion rate, according to the results of GBDT method. All features with a relative importance higher than five were used to adjust the model.

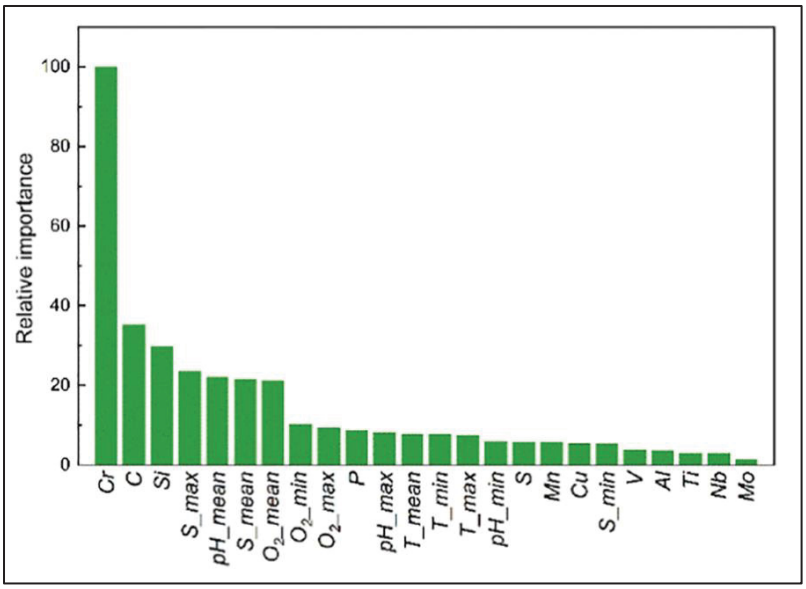

Figure 2.4 The importance sequence of input features to the corrosion rate measured by gradient boosting decision tree method
Adapted from Y. Diao et al. (2021)

The obtained ML model can show the influence of alloy interactions on the corrosion rate. Figure 2.5 shows that the corrosion rate decreases with either Cr and Cu element increase, and no significant interaction was observed. The authors used a novel method to convert the chemical composition features to the set of atomic and physical property features; as a result, the model could be generalized to materials with different chemical compositions.

ML algorithms are also applied to predict atmospheric corrosion of carbon steels. Environmental factors are considered input features. According to the accuracy of the prediction models, the random forest-based ML method possessed the highest accuracy compared to the artificial neural network (ANN) and support vector regression (SVR) (Pei et al., 2020).

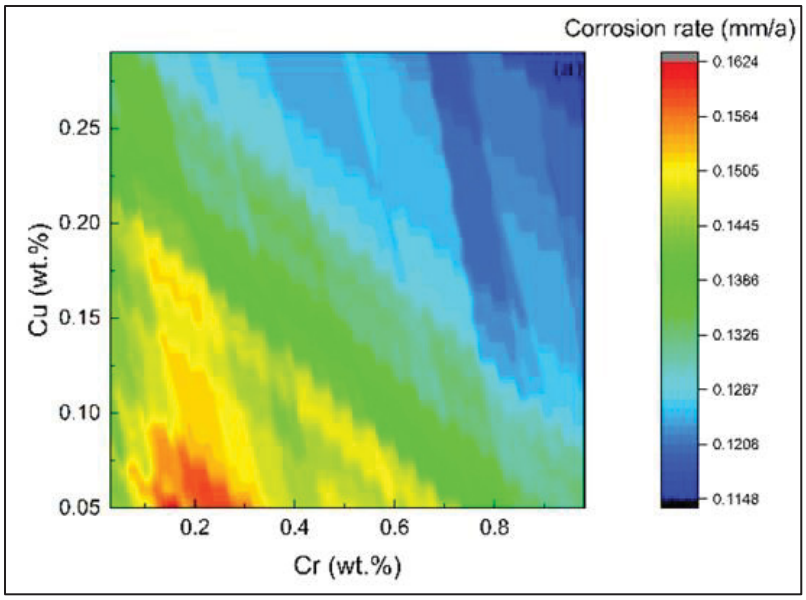

Figure 2.5 Simulation results of interaction between elements Cr and Cu, and their influence on steel's corrosion rate
Adapted from Y. Diao et al. (2021)

Jiménez-Come et al. (Jiménez-Come et al., 2019) state that many researchers use ANN for corrosion modelling, but there are some disadvantages in using this method. Slow convergence speed, less generalizing performance, arriving at local minimum, and overfitting problems are to name a few. As a result, they propose to use support vector machine (SVM) algorithms as an alternative method for modelling the corrosion. The authors studied the pitting corrosion behaviour of EN 1.4404 stainless steel as a function of temperature, acidity, and Cl^- ion concentration using support vector machine-based ensemble algorithm. The study primary goal was to develop an SVM ensemble model to predict pitting corrosion behaviour of EN 1.4404 stainless steel. Two pre-processing approaches were applied to improve the prediction performance, PCA (principal component analysis) and LDA (linear discriminant analysis). According to the results, PCA pre-processing method improves the accuracy of the pitting corrosion prediction to 96.7%.

The most challenging issue in applying ML techniques is the size of the data set. Therefore, it is crucial that the latter is large enough and includes most examples of the combinations of the material compositions. Generally, increasing the number of training samples helps improve the generalization ability of the model (Wen et al., 2009). The data set size will almost always

determine the available choices of ML models. Classical and statistical ML approaches (e.g., regression, support vector machines, k-means, and decision trees) are more suitable for smaller data set sizes. In contrast, neural networks require more significant amounts of data and usually it is needed in the order of thousands or more (A. Y. T. Wang et al., 2020).

2.4 Conclusion

Based on the literature, ML techniques are recognized as effective method for analyzing corrosion data and assessing the impact of various factors on corrosion behavior. However, challenges remain in applying ML to corrosion science, particularly the need for large datasets to train ML models and ensuring the validity and consistency of the procedures used to obtain experimental data for training. Corrosion in flanged joints typically initiates from the inside of the pipeline, remaining undetectable until it leads to unexpected leakage failures. Localized corrosion, which propagates rapidly, often goes unnoticed in periodic inspections. Even continuous monitoring systems generate massive datasets that require sophisticated data mining techniques to detect localized corrosion. Current methods, as highlighted in the literature, have not demonstrated adequate efficacy in addressing this critical challenge.

CHAPTER 3

RESEARCH OBJECTIVES AND STRATEGY

3.1 Introduction

The literature review highlighted gaps in research on the corrosion of flanges in bolted flanged joints. This research area was mainly developed in response to failures occurring in industry. Despite existing failure analyses, new cases continue to be reported, highlighting the need for an in-depth study and analysis of corrosion mechanisms. Furthermore, traditional monitoring and inspection methods are inadequate for detecting corrosion before failure occurs. In the following, the research objectives, and the overview of the research strategy are discussed.

3.2 Research objectives

Based on the literature review, material selection, service conditions and design factors are all influencing corrosion parameters. There is a lot of interest in developing an intelligent framework capable of predicting the corrosion behavior of bolted flanged joints based on electrochemical measurements that are processed using ML and DL models. Therefore, the main objective of this thesis is to propose a novel test bench to study flange corrosion behavior and conduct real-time monitoring coupled to intelligent approaches and strategies to analyze, identify and predict the corrosion types in service. The sub-objectives encompass the design and construction of the test bench, conducting experiments, and performing data analysis, as detailed below:

- Sub-objective 1

  The first sub-objective is to develop a new corrosion quantification test bench capable of replicating the real conditions under which flanges operate, particularly in the presence of gaskets and applied stress while enabling electrochemical corrosion characterizations.

- Sub-objective 2

  Assess the influence of Graphite and PTFE gasket materials on the corrosion behavior of flanges.

- Sub-objective 3

  Investigate the influence of the gap or crevice size on the initiation and propagation of the crevice corrosion.

- Sub-objective 4

  Propose a practical approach for materials selection by analyzing and identifying the most critical factors in corrosion data obtained from databases.

- Sub-objective 5

  Establish an automated and intelligent framework for identifying corrosion types in the real-time corrosion monitoring of flanged gasketed joints.

3.3 Research strategy

To achieve the research objectives, the strategy of this thesis research work is divided into the following overarching steps:

- Study cases of flange failures and review papers that treats corrosion of bolted joints to identify the research gaps.
- Design and construct a test bench to study flange face corrosion under realistic service conditions.
- Conduct corrosion characterization tests to assess the impact of materials and design on corrosion behavior.
- Apply ML algorithms for material selection based on corrosion performance.
- Automate corrosion type identification using deep learning techniques.

In the following sub-sections, these steps are discussed generally and the details of each specific methodology to achieve the research sub-objectives are presented in chapters (4 to 8)

where each chapter represents a peer-reviewed research paper. Figure 3.1 shows a schematic overview of the proposed research strategy to address the research objectives.

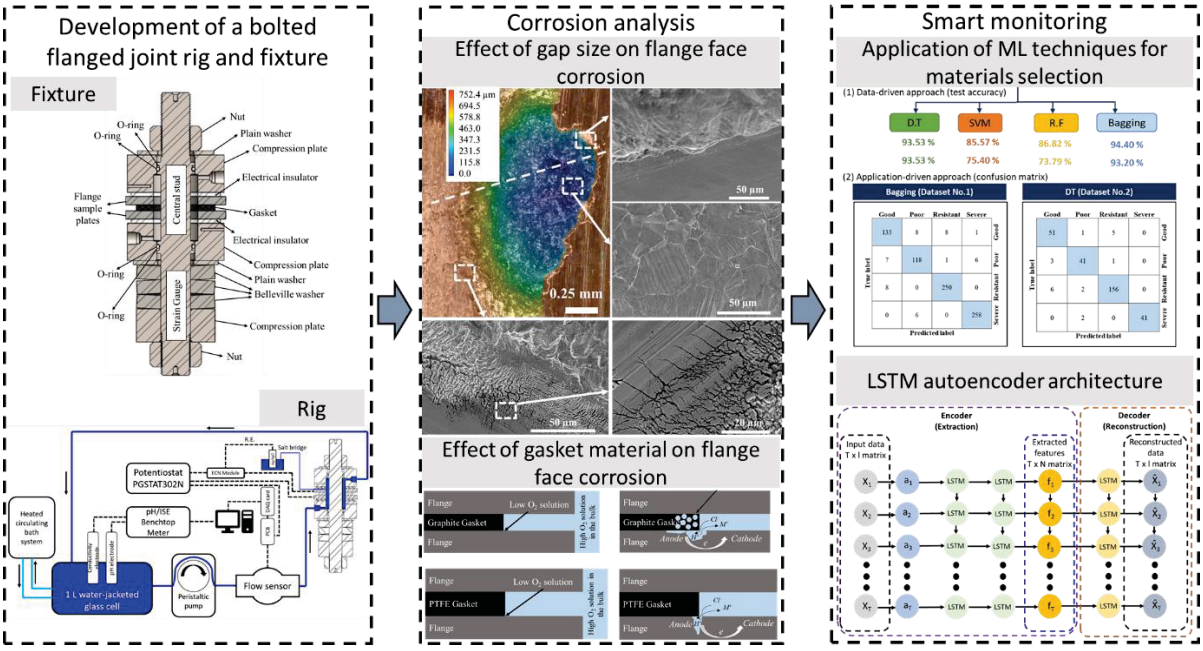

Figure 3.1 Overview of the research strategy addressing the research objectives

3.3.1 Review of the literature to identify research gaps

The first step in the methodology for this research is to review current failure cases, corrosion mechanisms on flange faces, contributing factors, and corrosion monitoring techniques to understand the challenges, identify areas for improvement, and define the research objectives. This step is divided into four distinct sections as follows:

- Define the search strategy and criteria
- Select articles and reports from relevant sources
- Review the literature, extracting data, and assessing the articles
- Highlight research gaps, limitations, and areas for future investigation

This step is a prerequisite for achieving all the research objectives outlined in this thesis.

3.3.2 Design and construct a corrosion test bench

To achieve the first sub-objective, a test rig that replicate the characteristics of real-world bolted flanged gasketed joints, enhancing the accuracy of corrosion characterizations and measurements is designed. The following steps are undertaken to address this sub-objective:

- Conduct a more focused literature review on the topic
- Develop a novel test bench setup, including the test rig and fixture
- Establish a procedure for mounting the fixture and applying load using a hydraulic tensioner
- Improve and refine the rig by incorporating additional sensors
- Design a data acquisition system and programming the LabVIEW environment
- Conduct preliminary electrochemical tests and resolving any issues that arise

3.3.3 Conduct corrosion characterizations tests

To achieve the second and third research objectives, experimental tests using the developed test rig are conducted to evaluate the impact of gasket and flange materials and geometry on the corrosion behavior of flanges. The following steps are followed to conduct corrosion characterization testing:

- Select gasket and flange materials and corrosion solutions for experimental tests
- Assemble the test rig and conduct checkdown testing
- Design and plan experiments based on the literature and objective
- Conduct electrochemical tests, including potentiodynamic polarization, potentiostatic polarization, electrochemical impedance spectroscopy
- Analyze the data obtained from the electrochemical tests
- Characterize sample surfaces using microscopy before and after the electrochemical tests

3.3.4 Apply ML algorithms for material selection based on corrosion performance

To address the fourth sub-objective, a database containing the chemical composition of 34 different grades of stainless steel (SS), as well as the type, concentration, and temperature of various corrosive environments, is selected. ML techniques are applied to map these features to the corresponding corrosion behavior. The procedure for developing the ML models includes the following steps:

- Preprocess and clean the data obtained from the database and create features
- Select appropriate ML models for training on the database
- Tune hyperparameters of the ML models
- Conduct feature importance analysis to find the most influential factors contributing to the corrosion behavior
- Evaluate the models to identify the best-performing model

3.3.5 Automate corrosion type identification using deep learning techniques

To achieve the fifth sub-objective, deep learning methods, including the application of recurrent neural networks (RNNs), are employed to process electrochemical noise current and potential data for identifying the type of corrosion during online monitoring. The following methodology is used to address this sub-objective:

- Select materials and solutions for the experiments
- Design and planning each test
- Conduct electrochemical noise measurement tests
- Preprocess the data obtained from the experiments
- Characterize the sample surfaces using microscopy to verify the type of corrosion
- Train deep learning and ML models using three approaches: supervised learning, hybrid learning, and unsupervised learning
- Tune hyperparameters of the models
- Evaluating model performance using various metrics

3.4 Conclusion

In conclusion, this chapter describes the research gaps and challenges through a literature review and discussions with experts in the field. The research objectives and the overarching research strategy to achieve these objectives are also presented. Finally, Figure 3.2 outlines the sub-objectives and their associations with publications in scientific journals. These publications form the subsequent chapters of this thesis, as indicated in Figure 3.2.

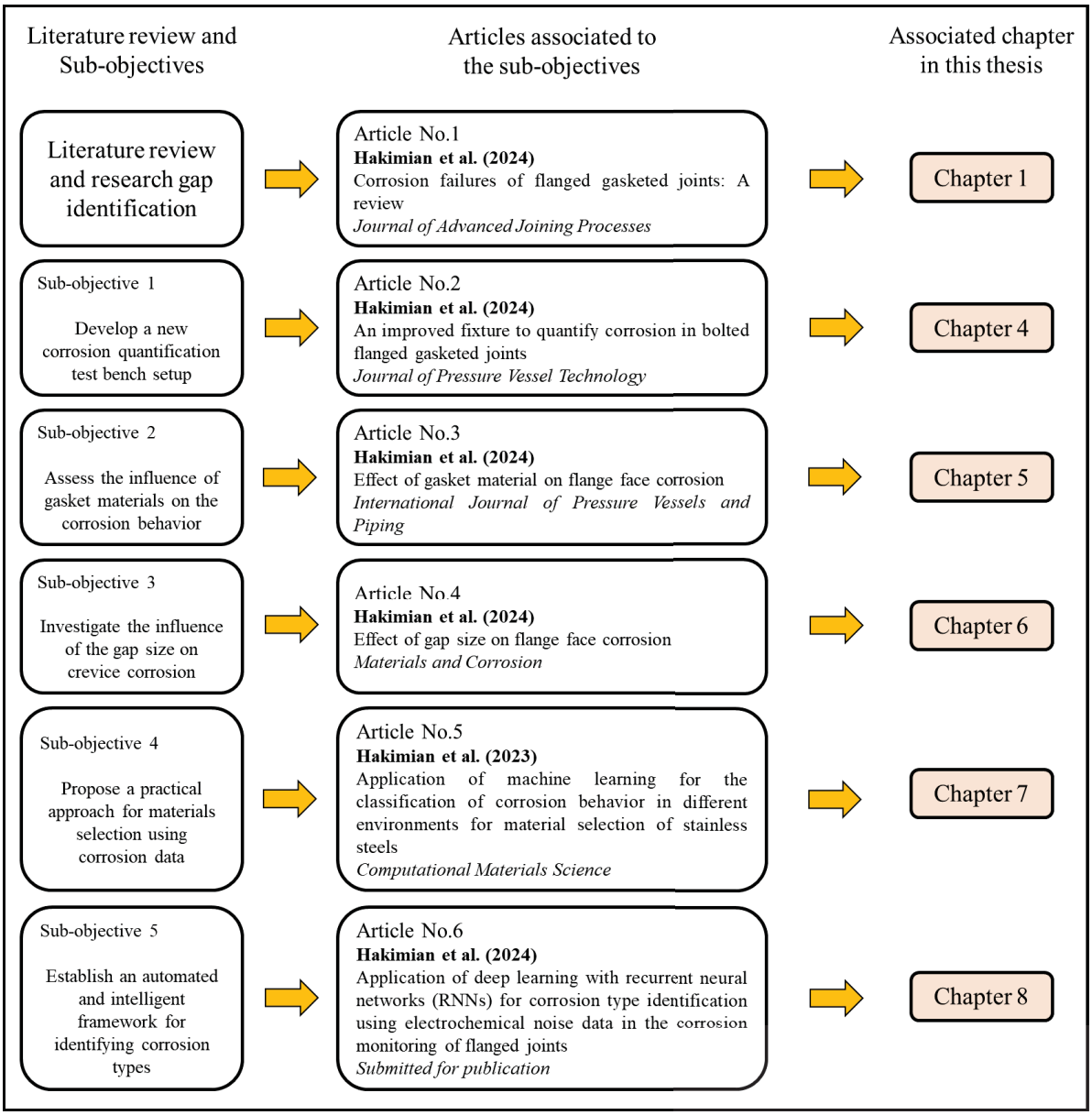

Figure 3.2 Sub-objectives, journal articles, and associated chapters

CHAPTER 4

AN IMPROVED FIXTURE TO QUANTIFY CORROSION IN BOLTED FLANGED GASKETED JOINTS

Soroosh Hakimian [a], Abdel-Hakim Bouzid [a], Lucas A. Hof [a]

[a] Department of Mechanical Engineering, École de technologie supérieure, 1100 Notre-Dame Ouest, Montréal, QC H3C 1K3, Canada

Paper published in: *Journal of Pressure Vessels Technology*, Volume 146, February 2024, 11302.
https://doi.org/10.1115/1.4063975

Abstract

This study discusses the corrosion behavior of bolted flanged gasketed joint systems. A novel fixture is proposed to quantify the corrosion at the gasket–flange interface under service conditions. Due to the presence of crevices and potential differences between gaskets and flanges, corrosion widely occurs in such joints. Crevice corrosion and galvanic corrosion can create paths to leakage of the pressurized fluid and may cause catastrophic failure. Corrosion in bolted gasketed joints was investigated previously; however, the effects of the operating conditions were not reported. Operating conditions include fluid flow, pressure, pH, conductivity, temperature, and average gasket contact stress. This study starts by introducing a new experimental setup to examine the corrosion behavior of bolted flanged gasketed joints. The developed fixture consists of a pressurized bolted gasketed joint that enables real-time monitoring and recording of the corrosion parameters under the influence of service conditions. Second, potentiodynamic polarization testing is conducted to measure the corrosion rate and obtain data on the corrosion behavior of a pair of flange and gasket materials. These tests are performed using the novel setup that reproduces the behavior of industrial bolted flanged gasketed joint systems. It consists of a working electrode (flange material), a reference electrode (Ag/AgCl), and an auxiliary electrode (a stainless steel rod). Three types of graphite

gaskets compressed in the fixture are subject to electrochemical corrosion tests with a 0.6 M NaCl solution. The morphology of the specimen's corroded surfaces is examined via confocal laser microscopy.

4.1 Introduction

Bolted flanged joints are extensively utilized in the seawater desalination and hydrocarbon processing industries to connect pressure vessels and piping. This type of connection enables easy disassembly of piping components for maintenance and cleaning purposes. Nevertheless, it also presents a potential risk of leakage failure, particularly when exposed to aggressive media and environments, especially at high pressures and temperatures (Nechache & Bouzid, 2007). Flange face corrosion is among the most frequent causes of leakage failure as reported in the literature (Kölblinger et al., 2022; Larché et al., 2016; Martin, Natishan, et al., 2004; Mathiesen & Bang, 2011; Tavares et al., 2018; Tsuda et al., 2021). Flange face corrosion occurs due to fluid penetration through gaps created between gasket and flange faces. These gaps are created by material loss due to corrosion and aging and facilitated by the loosening of the joint due to pressure, external loads, creep-relaxation (Nechache & Bouzid, 2007), (A. Bouzid et al., 1995; Nechache & Bouzid, 2008) rotation of the flange (A. Bouzid et al., 1994; H. Bouzid et al., 2004) and design errors (Worden, 2014b).

However, detecting flange face corrosion is a challenging task, as it often remains undetected until leakage occurs. This can have severe consequences, including significant financial losses, environmental hazards, and causes risks to human health and safety. Replacing or repairing the affected components typically leads to unexpected downtime, extra expenses, and decreased efficiency of the overall system. The impact on the environment can also be a major concern (Bengtsson, 2015a). To prevent such detrimental effects, flange corrosion mechanisms and predictions should be studied in details.

According to the literature, crevice and galvanic corrosions are commonly observed in bolted flange joints. The contact surface between the gasket and the flange face is typically susceptible to corrosion when the average contact stress is low, or the gasket is not adequately tightened. Gaps or crevices between gaskets and flanges are, in general, potential places for crevice

corrosion to take place. Figure 4.1 shows potential places between gaskets and flanges for crevice corrosion to proliferate (red circles) in connections with (a) spiral wound gasket, and (b) sheet gasket. This type of corrosion occurs in the crevices, which are wide enough to allow corrosive fluid entry but sufficiently narrow to maintain near stagnant zones (Kruger & Begum, 2016). Metals with passive behavior (e.g., stainless steel) suffer more from crevice corrosion (Hu et al., 2011a). This type of corrosion is extremely hazardous because it develops in the enclosed area near the gasket and flange interface, which is neither accessible nor visible.

When two dissimilar metals are in contact with each other while immersed in a corrosive solution, the metal having higher potential acts as a cathode and the other metal acts as an anode. As a result, galvanic corrosion occurs, and the metal acting as an anode will be subject to corrosion. In bolted flange joints, galvanic corrosion occurs when the gasket material is more noble (i.e., has higher potential, hence is more cathodic) in comparison to the (more anodic) flange material in electrochemical series (Bengtsson, 2015a; Francis & Byrne, n.d.). The difference in potentials causes the flow of electrons between the gasket and flange (Worden, 2014a).

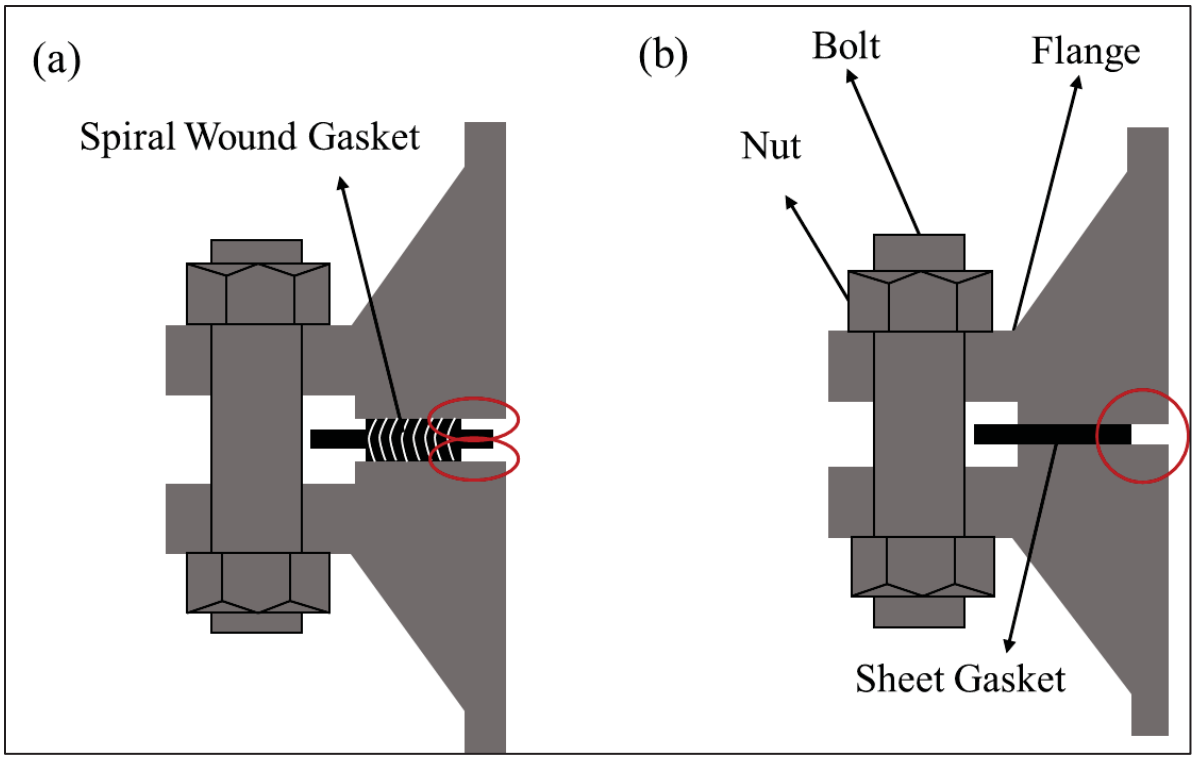

Figure 4.1 Schematic of the potential places for crevice corrosion which are indicated with red circles between gaskets and flanges in connections with (a) spiral wound gasket and (b) sheet gasket

Most of the corrosion cases reported in the literature are related to the application of stainless steel flanges in seawater. Although carbon steels have good mechanical properties, they have a high corrosion rate in seawater applications. Stainless steels form a passive chromium oxide (Cr_2O_3) layer on the surface, which is protective against general corrosion, also referred to as uniform corrosion, but in the presence of chloride ions in seawater it increases the susceptibility to localized corrosion, especially to crevice corrosion (Costa et al., 2023). Typically, the most problematic gasket material is graphite. Graphite gaskets are commonly used due to their wide range of chemical and temperature resistance capabilities, low cost, and good sealing performance. Graphite is conductive and noble (cathodic) in comparison to most metallic materials in electrochemical series (see Table 4.1); therefore, it causes galvanic corrosion on the flange surfaces and accelerates crevice corrosion.

Table 4.1 Measured corrosion potentials (E_{corr}) of alloys in flowing seawater

Alloy	**E_{corr} (Volts vs. saturated calomel reference electrode)**
Graphite	0.3 to 0.2
Hastelloy C-276	0.1 to -0.04
Alloy 825	0.04 to -0.02
Nickel 200	-0.1 to -0.2
Stainless steel 316, 317	0.0 to -0.15
Stainless steel 302, 304, 321, 347	-0.07 to -0.12
Nickel-chromium alloy 600	-0.38 to -0.47
Cast irons	-0.6 to -0.72
Mild steel	-0.6 to -0.72

In addition to the combined effect of flange and gasket materials, operational factors have a considerable influence on the corrosion state between these two parts. The operational factors include, fluid flow rate, temperature, pH, conductivity, fluid pressure, and average gasket contact stress. Therefore, the common potentiodynamic polarization test method proposed in ASTM G5 (ASTM International, 2014) lacks fundamental representativeness and requires adjustments to study and predict the corrosion behavior of bolted flange joints. Indeed, using this standard test method, the corrosion behavior of small samples is measured without the presence of a gasket. Moreover, with the solution being static, the effect of fluid flow inside of a bolted flange joint is ignored. Few researchers use novel methods to study the corrosion behavior of bolted flanged gasketed joints under conditions close to service. Although several attempts were made to build setups or assemblies with the intent to reproduce the service conditions close to the industrial applications, studies that include most of the above cited operational factors have yet to be published. Martin et al. (Martin, Lawrence, et al., 2004) investigated crevice corrosion of metallic plate and gasket combinations using potentiostatic tests. The used immersion crevice corrosion cell consists of a circular gasket specimen sandwiched between a square plate and an acrylic cell body hand-tightened with four nylon bolts and wingnuts. The experiments were carried out at 65^{o}C, and the whole assembly was immersed in a 20-litre chamber placed in a laboratory furnace to maintain the temperature

during tests. The gasket and metallic plate are in direct contact with the seawater solution, so that crevice corrosion at the contact surface between these two components can be quantified. Although the authors included the gasket in the setup, the corrosion experimental test was conducted under low average gasket contact stress in stagnant water with low to no pressure. Mathiesen et al. (Mathiesen & Bang, 2011) designed a new setup to investigate crevice corrosion at the gasket- flange interface. They used the potentiodynamic technique to measure corrosion in an NPS 2 stub end flange fitted with spiral wound (SW) graphite and fiber sheet gaskets. The potential at which crevice corrosion initiates in the UNS S31254 stainless steel flange was measured and the sample was slowly polarized in incremental steps (25 mV/6 hours) from the corrosion potential until the initiation of crevice corrosion. The tested flange with the graphite filled SW gasket showed the most noticeable and pronounced corrosion attacks.

Mameri et al. (Mameri et al., 1999, 2000) proposed a cell that provides situations similar to that encountered in the industry to quantify the corrosion of bolted flanged joints. Three-electrode linear polarization tests (current vs. potential) were conducted using a potentiostat to study the corrosion behavior. Unfortunately, parameters such as temperature, pH, flow velocity, and fluid pressure and average gasket contact stress could not be measured or controlled during the test. As well, the influential factors on the corrosion at the gaskets-to-flange interfaces were not studied in detail.

Therefore, the present study aims to address this research gap. This work presents the development of a fully instrumented test bench to address crevice corrosion of a pair of gasket and flange materials as near to real conditions as possible. The test bench is used to measure crevice and galvanic corrosion for a series of gasket and flange materials. The test results on graphite sheet gaskets used with 304L stainless steel flange material are presented.

4.2 Corrosion quantification test fixture

4.2.1 Setup design configuration

The developed Corrosion Quantification Test (COQT) setup is designed to measure, control, and record fluid characteristics such as temperature, pH, flow rate, pressure, and conductivity. For the system to be representative of the real conditions, the corrosive solution circulates through the inside of the gasket and plate fixture so that the circulating fluid wets them. According to ASTM G5, the three-electrode technique should be used to analyze the corrosion behavior using potentiodynamic polarization resistance measurements. Therefore, three electrodes, including a working electrode, a counter electrode, and a reference electrode are used in the setup. The applied stress on the gasket is measured since it is an important factor that influences corrosion at the interface between gaskets and flanges. Because only the corrosion between the gaskets and the flange faces is being studied here, these two components are isolated electrically from the other components of the setup. The setup is able to run at temperatures of up to 90 ^{o}C, as well as internal pressures up to 6 bar. The fixture can be tightened to produce an average gasket contact stress of 35 MPa.

4.2.2 Test fixture

The test fixture is the central part of the test setup. This is where the flange and gasket are located and wetted by the fluid, and where corrosion occurs. The COQT fixture is designed to mimic NPS 1 class 150 bolted flange joint as done with the successful ARLA device (Aged Relaxation Leakage Adhesion) (Marchand, Bazergui, et al., 1992a; Marchand, Derenne, et al., 1992a) used to measure the gasket relaxation load and leakage tightness after being aged with a sheet gasket material in an oven. Figure 4.2 shows the COQT test fixture that can assess and quantify corrosion on the specimen plate and gasket material pairs. This figure illustrates the different parts of the fixture. The central stud (1) allows the application of the compressive load on the gasket through the circular plates using a hydraulic tensioner. The compression plates (2) have slots to measure the variation of gasket thickness before and after the corrosion

tests. In addition, the compression plates have entrance and exit ports for the circulation of the corrosive solution. The specimen plates (3) of the test fixture are representative of the flanges of a bolted joint. They can easily be changed after each test to study different operating conditions and flange materials. The gasket material (4) is placed between two specimen plates. The rubber ring (5) provides electrical insulation between the specimen and the compression plates in order to accurately measure the corrosion of specimen plates. A plain washer (6) was used to increase the contact area between the compression plate and the Belleville washer. The Belleville washers (7) are useful to maintain the preload in the assembly and adjust the rigidity of the bolt joint if needed. It is to be noted that this parameter is important when relaxation is considered. The load ring (8) or spacer provides a robust contact interface for Belleville washers. The O-rings (10) provide the seal to the outside boundary. The plain washer (12) is used to increase the contact area between the compression plates and the nuts (9). The volume of the inside chamber is 20 mL. Gaskets with thicknesses ranging from 1/16” to 1/8” can be used in conjunction with the fixture for corrosion tests.

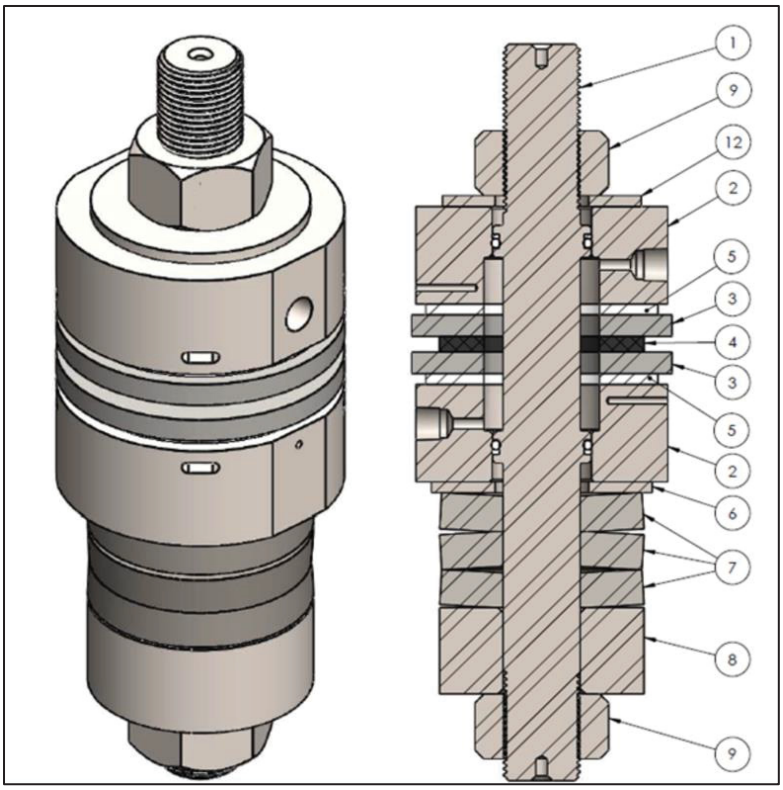

Figure 4.2 Test fixture and identification of each section. 1- Central stud; 2- Compression plate; 3- Specimen plate; 4- Gasket; 5- Rubber gasket; 6- Plain washer; 7- Belleville washer; 8- Load ring; 9- Nut; 10- O-Ring (between the central stud and the compression plates); 11- Back-up ring (between the central stud and the compression plates); 12- Plain washer

4.2.3 Test bench

The COQT fixture is part of the test rig shown in Figure 4.3. It is connected to a tubing circuit of the corrosive solution that has different equipment and instrumentation. The multiparameter meter (1) simultaneously measures the pH, conductivity, and temperature of the solution through the conductivity (2) and pH electrodes (3). The thermostatic water tank (4) is a container that heats the corrosive solution to the desired test temperature with precision of ±0.1ºC. The peristaltic pump (5) provides continuous solution flow from the beaker, which is placed in the thermostatic water tank, to the test fixture. The flowmeter (6) and pressure transducer (7) continuously monitor the flow and pressure of the solution. The three-electrode system is used to quantify the corrosion according to ASTM G5 requirements. Specimen plates are considered as working electrodes (8), the central stud is considered as a counter electrode

(9), and the Ag/AgCl as a reference electrode (10). In this test rig, the potentiostat (11) is the instrument that maintains the working electrode potential, and the measured potential is compared to the reference electrode. The salt bridge (12) is used as a conductive connection between the solution in the test fixture and the reference electrode to reduce the effect of distance between reference and working electrode. The thermocouple (13) measures the temperature of the test fixture. As indicated in Figure 4.3, the solution flows in and out from the bottom to the top of the fixture; hence, all the inner parts including the gasket and the metallic plate samples are soaked with the solution. The analogue signals from the sensors are transmitted to the printed circuit board (PCB-14) and converted to numerical values by the Data Acquisition Card (DAQ-15). The DAQ, potentiostat, and multiparameter meter are connected directly to the computer (16) through USB. A full Wheatstone strain gauge bridge (17) is installed on the central stud (transducer in mV) to measure the force of the central stud. This force measurement can subsequently be converted into the average gasket contact stress by simply dividing the force by the gasket area.

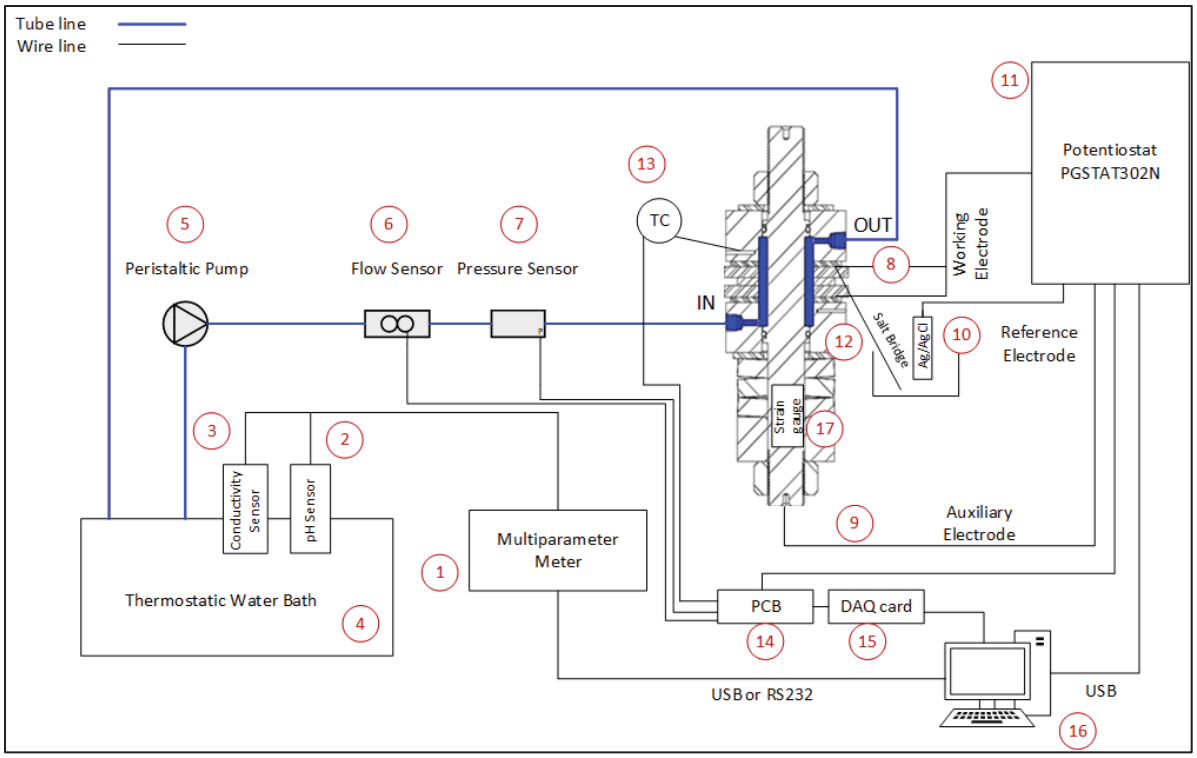

Figure 4.3 COQT bench: 1) pH and conductivity meter; 2) pH electrode; 3) Conductivity electrode; 4) Thermostatic water bath; 5) Peristaltic pump; 6) Flow sensor; 7) Pressure sensor; 8) Working electrode connection; 9) Auxiliary electrode connection; 10) Reference electrode; 11) Potentiostat; 12) Salt bridge; 13) Thermocouple; 14) PCB; 15) DAQ card; 16) Computer (PC); 17) Strain gauge

Figure 4.4 shows an image of the test bench during the electrochemical tests; the rectangular marker and the associated number specify the used equipment.

Table 4.2 provides a detailed overview of the equipment deployed for the COQT.

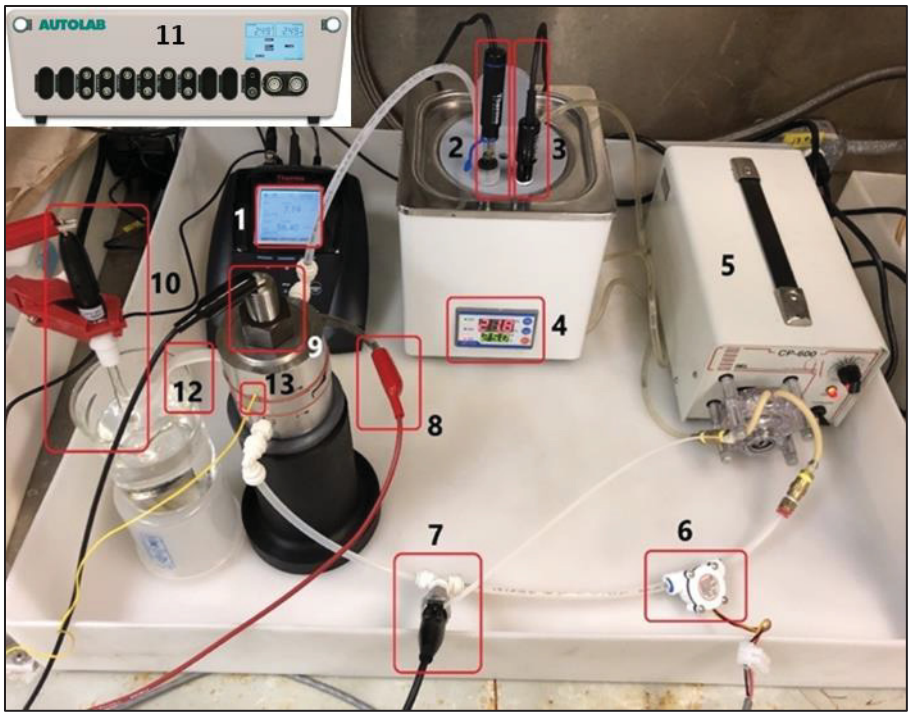

Figure 4.4 COQT bench: 1) pH and conductivity meter; 2) pH electrode; 3) Conductivity electrode; 4) Thermostatic water bath; 5) Peristaltic pump; 6) Flow sensor; 7) Pressure sensor; 8) Working electrode connection; 9) Auxiliary electrode connection; 10) Reference electrode; 11) Potentiostat; 12) Salt bridge; 13) Thermocouple

Table 4.2 Equipment used in the COQT bench

Equip. Nº	**Description**	**Function**
1	Multi-parameter meter	Measures pH, conductivity, and temperature of solution
2	pH meter electrode	Measures pH
3	Conductivity meter electrode	Measures conductivity
4	Thermostatic water bath	Controls temperature of the solution
5	Peristaltic pump	Circulates solution in system
6	Flow meter	Measures the flow rate
7	Pressure meter	Measures fluid pressure
8	Metallic ring	Connects working electrode wire to metallic plates

Equip. Nº	Description	Function
9	Stainless steel central stud	Auxiliary electrode
10	Ag/AgCl/KCl saturated reference electrode	Serves as reference for potential of working electrode measurement
11	Potentiostat	Applies potential/current to the specimen plate and measures the current/potential response
12	Salt bridge	Transfers current between reference and working electrode
13	Thermocouple	Measures fixture temperature
14	Printed circuit board (PCB)	Provides a platform for connecting and integrating the DAQ card into the system
15	Data acquisition card (DAQ)	Coverts physical signals into digital data that can be processed and analyzed by a computer
16	Personal computer (PC)	All data are displayed in the LabVIEW environment, which is programmed for this project, by connecting the DAQ card to the computer
17	Strain gauge	Measures the applied load on the central stud

4.3 Materials and methods

The objective of the COQT setup is to study corrosion of bolted flanged gasketed joints subjected to as near to real conditions as possible, including flexibility, average gasket contact stress, and fluid circulation. In addition, the potentiodynamic polarization method, as described in ASTM G5, is adopted to analyze the corrosion behavior.

4.3.1 Materials for corrosion tests

Several corrosion tests are carried out to verify the applicability of the setup. For these experiments, the following flange and gasket materials are selected. Stainless steel 304L plates are used as flange material, the chemical composition of which are given in Table 4.3. The characteristics of the three types of graphite gaskets used in the corrosion tests are given in Table 4.4.

Table 4.3 Chemical composition of the 304L stainless steel plates

Elements	**Weight percent (%)**	**Elements**	**Weight percent (%)**
Carbon	0.03	Nickel	8.1
Chromium	18.1	Nitrogen	0.024
Manganese	1.5	Phosphorus	0.03
Sulfur	0.01	Silicon	0.65

Table 4.4 Description of the graphite sheet gaskets

Properties	**Gasket No.**		
	1	**2**	**3**
Inside diameter (mm)	33.27	33.12	33.46
Outside diameter (mm)	58.45	58.71	58.67
Thickness (mm)	3.06	3.08	3.25
Ash content (%)	≤ 2.0	≤ 2.0	≤ 0.5
Density (g/cm^3)	1.1	-	1.05
Chloride content (ppm)	≤ 25	≤ 20	≤ 50
Fluoride content (ppm)	≤ 10	≤ 10	≤ 10
Sulfur content (ppm)	≤ 300	≤ 300	≤ 100
Total Halogen (ppm)	≤ 70	≤ 100	≤ 200

4.3.2 Analysis methods

Corrosion is an electrochemical reaction where electrons are reactants. Therefore, the rate of the reaction could be controlled by controlling the potential. In polarization tests, the anodic or cathodic reaction rates are controlled by withdrawing the electrons or adding the electrons to

the system (in other words, by controlling the potential using a potentiostat). The potential at which the cathodic and anodic reaction rates are equal is the corrosion potential (E_{corr}), and the related current density is the corrosion current density (i_{corr}). Tafel extrapolation is used to determine the corrosion current density. The Tafel equation shows the relation between the current density and potential according to Equation (4.1) (Baboian, n.d.).

$$E - E_{corr} = a \pm b\, log|i| \tag{4.1}$$

Here E is the applied potential in V, E_{corr} is the potential where corrosion occurs, E-E_{corr} is also called overpotential (η) in V, the sign "±" indicates in which domain operates the sample (+ anodic and – cathodic), a and b are the Tafel constant and slope, respectively, and i is the current density in A/cm^2. The current density is obtained by dividing the measured current to the geometric area of the working electrode exposed to the solution.

In situations where uniform corrosion occurs, Equation (4.2) below converts the corrosion current density to the mass loss rate using Faraday's law such that:

$$MR = K i_{corr}\, EW \tag{4.2}$$

Here MR is mass loss rate in g/m^2/d, K is 8.954×10^{-3} gcm^2/μA/m^2/d, i_{corr} is in μA/cm^2, and EW is the dimensionless equivalent weight. EW is the mass of metal oxidized by the passage of one Faraday (96500 C) of electric charge. The values of EW for typical stainless steel and carbon steel are given in ASTM G102 (ASTM International, 2015a).

Figure 4.5 demonstrates a typical polarization curve obtained by electrochemical polarization tests on stainless steels in an electrolyte. In region one (I), where the cathodic current is much larger than the anodic current, the reducing reaction takes place on the electrode. Cathodic and anodic currents are equal at the corrosion potential E_{corr}, in region two (II), and after that, the anodic current becomes larger than the cathodic current. In the passive region (III), a passive layer is formed on the stainless steel surface, so the surface is protected. A transpassive region occurs (IV) at higher potentials, where the passive layer dissolves, and localized corrosion occurs. A repassivation occurs in region five (V), which means the passive film is reformed,

and it decreases the diffusion rate from the surface and causes a steady state (Bengtsson, 2015a).

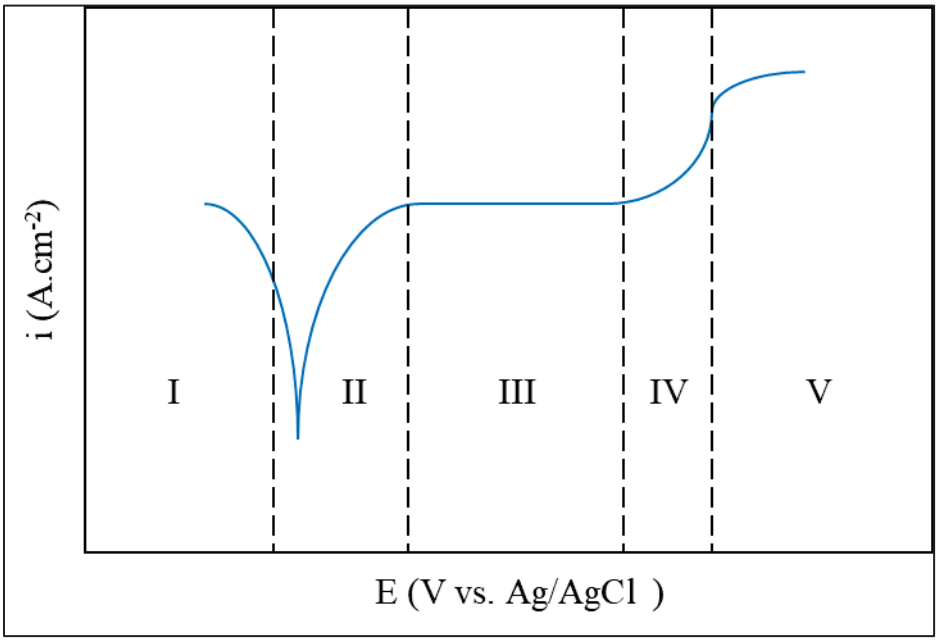

Figure 4.5 Schematic of the five regions in polarization test of stainless steel materials

The potentiodynamic polarization technique (according to ASTM G5), is performed to measure the corrosion mass loss rate and analyze the corrosion behavior of flange materials. The three-electrode setup consists of a working electrode, auxiliary electrode, and a reference electrode. In the developed fixture, the flange plate material is the working electrode, the 316L stainless steel bolt is the counter electrode, and a saturated Ag/AgCl is a reference electrode. Polarization tests are performed in a 0.6 M NaCl solution. Open circuit potential (OCP) takes one hour to reach the equilibrium state. Then the scan is initiated from 30 mV below the open circuit potential (OCP) and continues until 1500 mV above OCP. The scan rate is 0.001 V/s. An Autolab potentio/galvanostat PGSTAT302N-High Performance is used to produce the polarization curves for the discussed potential ranges. This equipment can set the current range between 10 nA and 1 A, and the potential range of ± 10 V. One polarization test is performed for each gasket. Nova version 2.1.6 software is used to calculate i_{corr} according to Eq. (1) for each polarization curve. After the polarization tests, the gasket material stuck to the plates was

removed, and the surfaces were cleaned with acetone and ethanol to better view the corroded zones.

To assess the corrosion behavior of the 304L stainless steel plate over longer time periods, another potentiodynamic anodic polarization test is performed with graphite gasket No.3. The OCP reading lasts 12 hours, with a start and stop potentials of 0 V and 0.28 V. As the scan rate is set to 1 μV/s, the test lasts for four days. The fluid flow rate is set at 0.4 L/min, and the average gasket contact stress of 13 MPa is applied for all corrosion tests. The surfaces of the corroded samples are examined using a Laser Confocal Microscope LEXT4100 to visualize the corrosion-induced damage, as well as to identify and measure the volume of crevices. A high precision balance (Secura Analytical Balance, resolution of 0.1mg) is used for measuring the mass of the metallic plates before and after corrosion tests to calculate the mass loss due to corrosion.

4.4 Results and discussion

4.4.1 Potentiodynamic polarization curves

Polarization tests are conducted to check the applicability of the novel setup for studying corrosion behavior between gaskets and flanges. At first, the mass loss rate of 304L stainless steel plates are calculated according to Eq. (2) and compared in combination of three types of gaskets. The current density and mass loss rate are shown in Table 4.5. Based on the results, the mass loss rate with gasket No. 3 is the fastest among the three. The polarization test continues to the higher potentials to study the behavior of the passive layer. Figure 4.6 indicates the polarization curve for gasket No.1. The current density increases without forming a passive layer until a potential of 1.4 V is reached. According to the polarization curve of the stainless steel and graphite gasket No.2 (Figure 4.7), a passive layer does not form on the surface of the plates, but at higher potential (1.4 V) the slope of the curve becomes lower, and a passive layer is about to form. The polarization curve for the stainless steel and graphite gasket No.3, has a completely different behavior in comparison to the two previous tests. Figure 4.8 shows that a passive layer forms at 0.5 V (shown by the red circle), and after that, the passive layer protects

the surface. The polarization curve of the longer test (Figure 4.9) shows that at -0.05 V passive layer forms on the surface of the stainless steel plates. The passive layer is damaged at 0.1 V, as the current is increased drastically at this potential (shown by the red circle), and localized corrosion occurs at this potential.

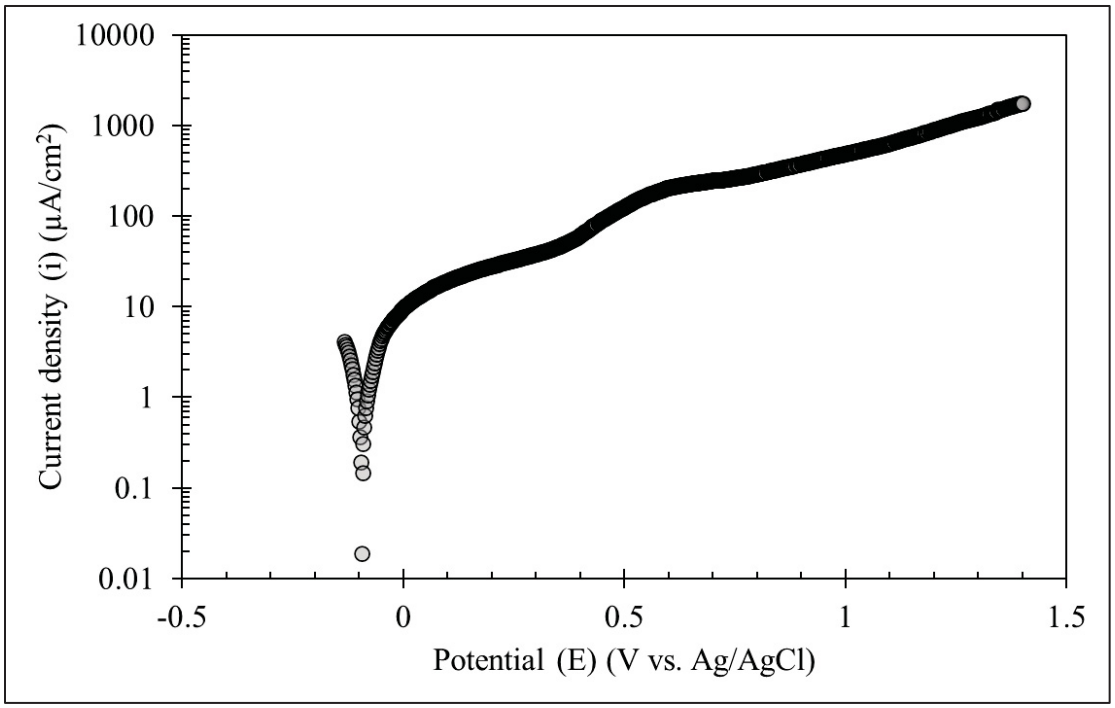

Figure 4.6 Polarization curve for the 304L stainless steel and graphite gasket No.1

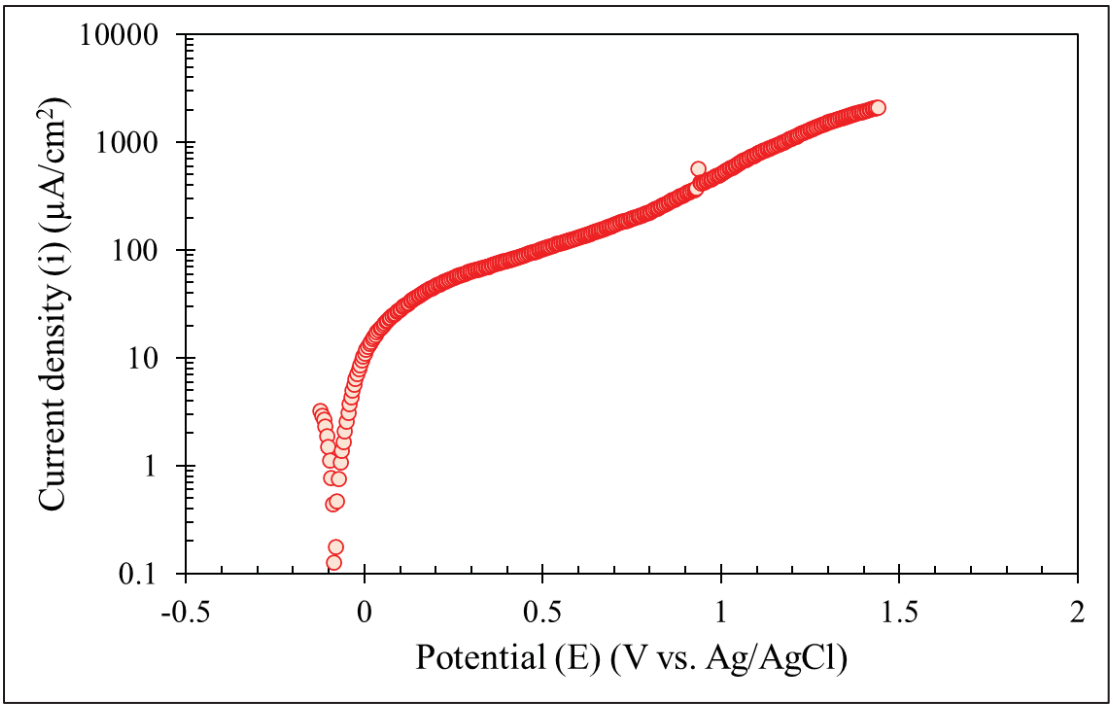

Figure 4.7 Polarization curve for the 304L stainless steel and graphite gasket No.2

Table 4.5 Current densities and mass loss rates calculated from the polarization curves

Gasket No.	**Current density (µA/cm²)**	**MR (g/m²/d)**
1	0.23	0.05
2	0.19	0.04
3	1.17	0.26

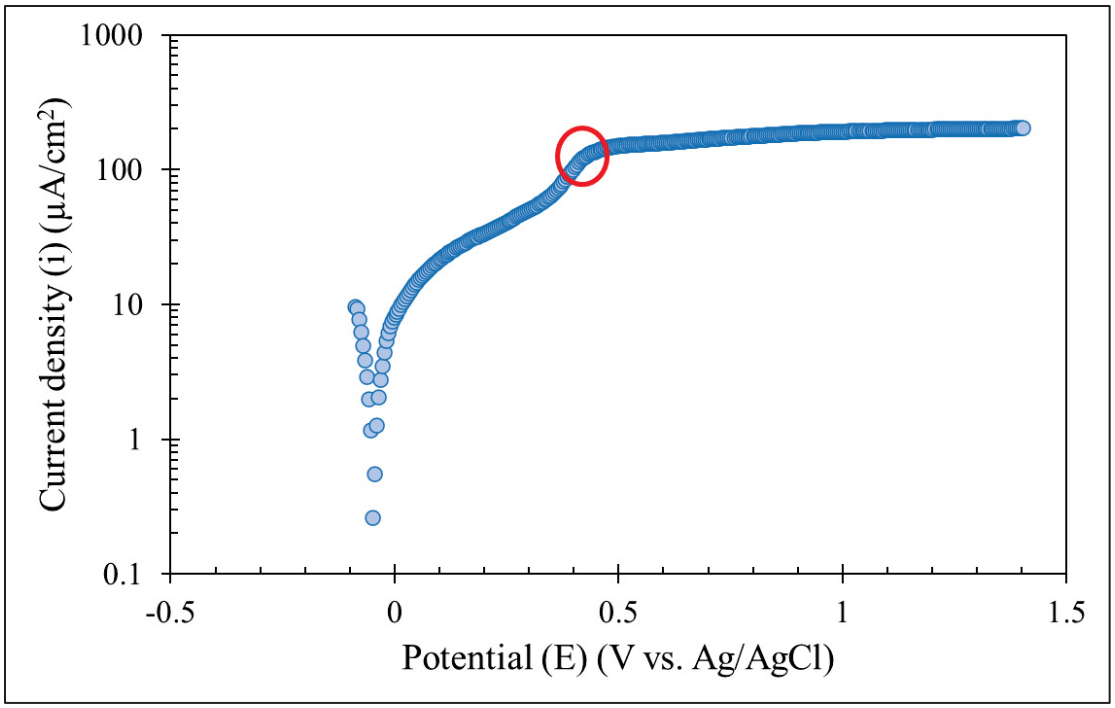

Figure 4.8 Polarization curve for the 304L stainless steel and graphite gasket No.3, with the red circle indicating the passivation potential

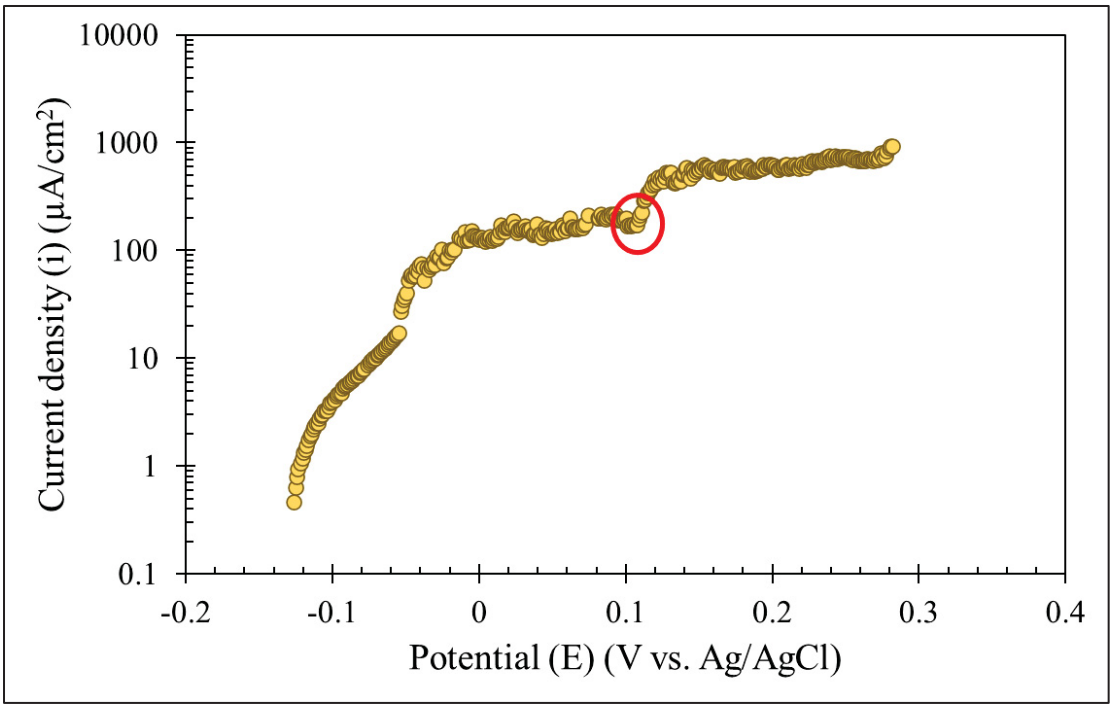

Figure 4.9 Long term polarization curve for the 304L stainless steel and graphite gasket No.3, with the red circle indicating the potential at which the passive layer breaks down

4.4.2 Surface characterization

Figure 4.10 (a) and (b) show the surface of the stainless steel upper and lower plates after the polarization test with graphite gasket No.1. The small black spots (one of them is marked with the red circle) on the surface seem to be these corroded zones. Nevertheless, to confirm these visual observations, microscopic characterization is used to estimate the metallic plate surface damage after the polarization tests. Figure 4.11 (a) and (b) show the surface of the 304L stainless steel plate after the polarization test with graphite gasket No.1. The small black spots are studied at two magnifications, 200X and 500X. At 200X magnification, the big black spots are visible, and their nature is confirmed with the magnification at 500X, and is associated to surface corrosion. As non-corroded surfaces surrounded the corroded surfaces, localized corrosion occurred on the 304L stainless steel plates.

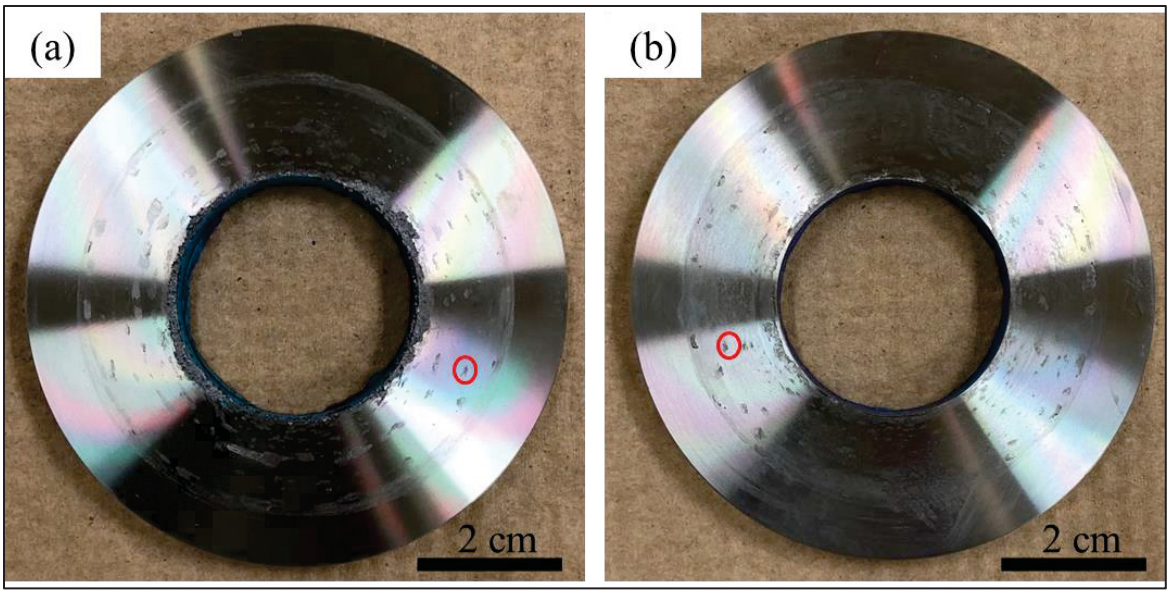

Figure 4.10 The (a) lower and (b) upper plates in the joint after polarization test with gasket No.1, with red circles indicating the small black corroded spots

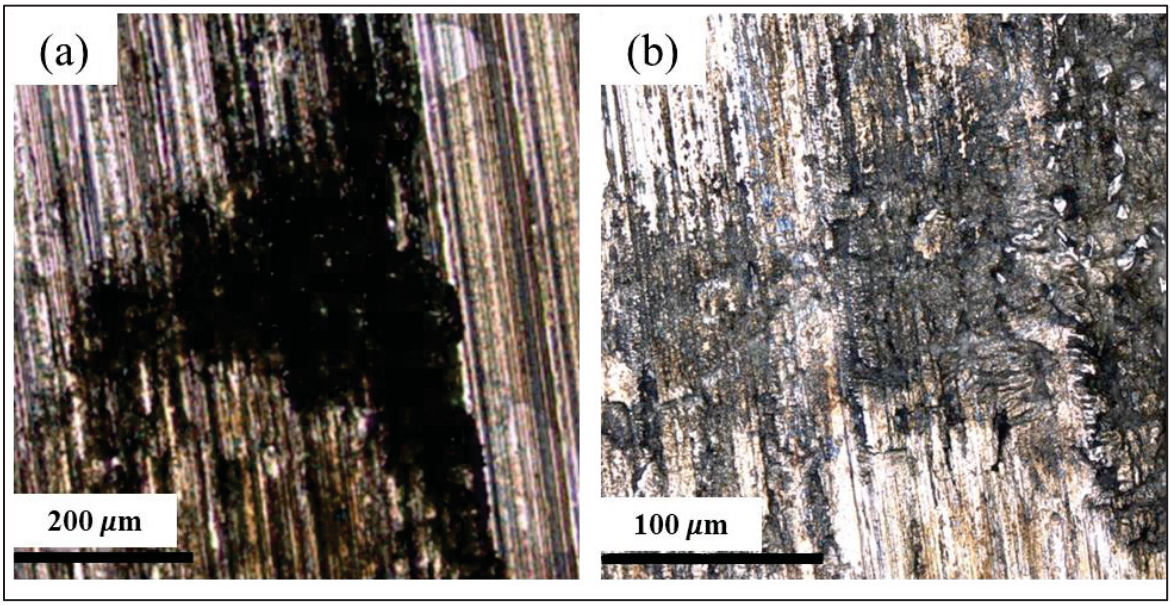

Figure 4.11 Confocal microscopy images of the 304L stainless steel plates after polarization tests with graphite gasket No.1. (a) 200X magnification; (b) 500X magnification

In Figure 4.12 (a) and (b), the surfaces of the 304L stainless steel plates after polarization tests with gasket item No.2 are indicated. The effect on the surfaces of these plates is similar to the previous test with gasket No.1, and it is in accordance with the MR results given in Table 4.5,

which shows that their mass loss rates are approximately equal. There are numerous small black spots (one of them is marked with the red circle) on the surfaces. The results of the confocal characterization at two magnifications (200X and 500X) are shown in Figure 4.13 (a) and (b) indicating that the black spots are localized corrosion. In Figure 4.13 (a), it is obvious that the brownish corrosion products (specified with an arrow and circle) are also formed in the vicinity of the corroded regions.

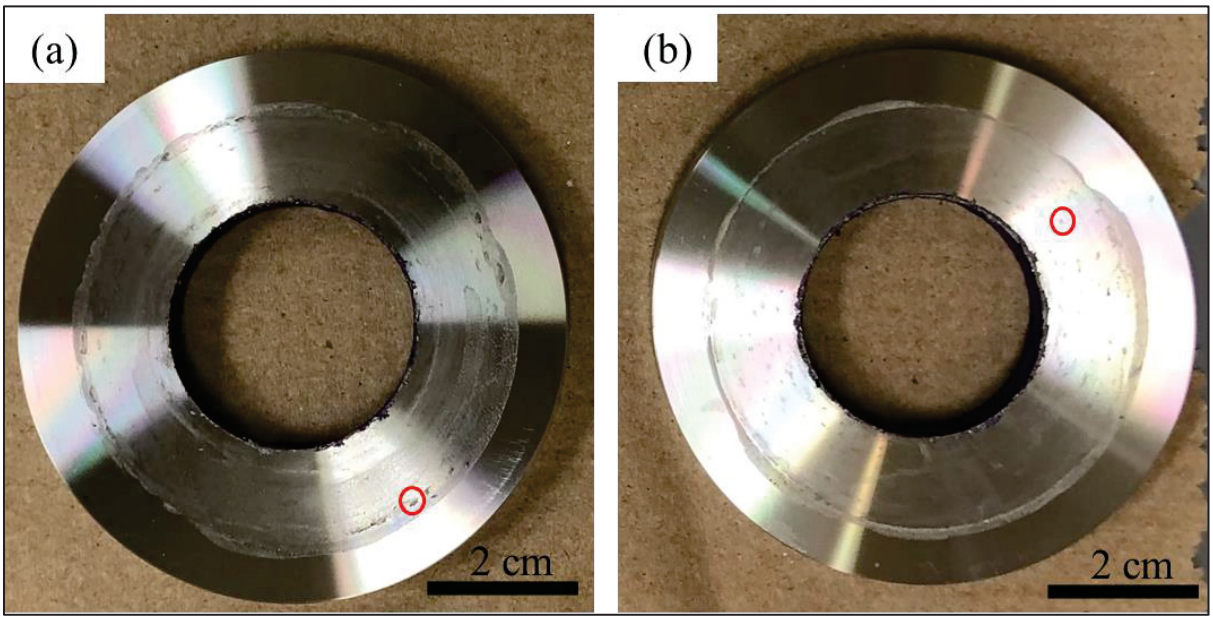

Figure 4.12 The (a) lower and (b) upper plates in the joint after polarization test with gasket No.2, with red circles indicating the small black corroded spots

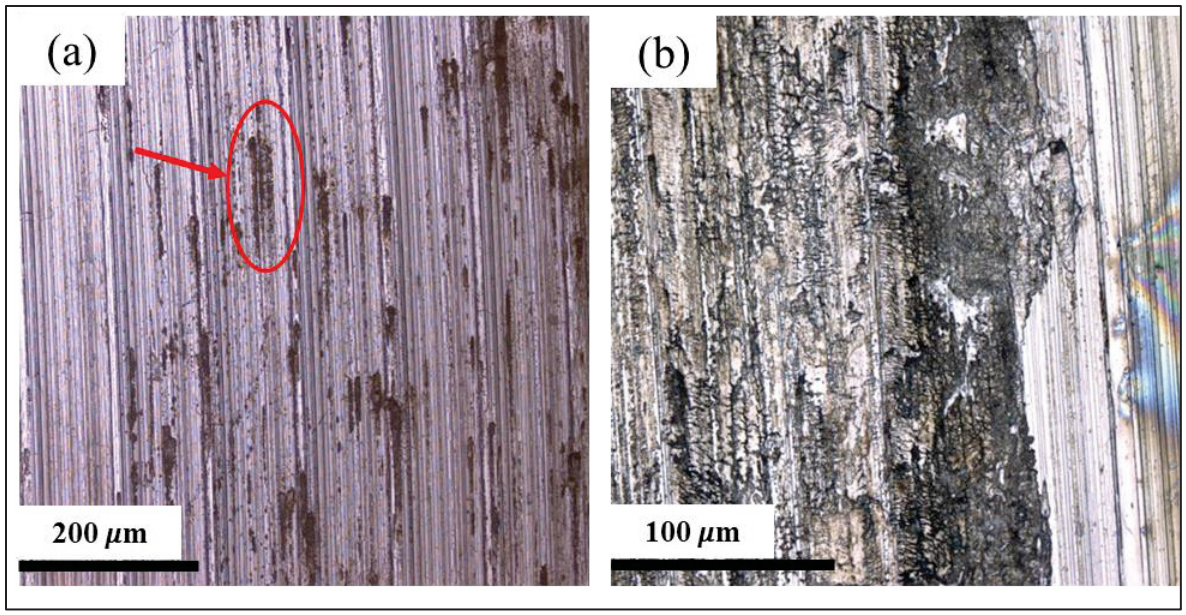

Figure 4.13 Confocal microscopy images of the 304L stainless steel plates after polarization tests with gasket No.2. (a) 200X magnification with the red circle indicating the small black corroded spot; (b) 500X magnification

As indicated in Table 4.5, the MR, after the polarization test with gasket No.3, is much higher than that with gasket No.1 and No.2. The image of the 304L stainless steel surfaces after the corrosion test with gasket No.3 also shows that the corroded area is bigger than previous tests (Figure 4.14 (a) and (b)), so the electrochemical results are in good agreement with the microscopic observations. As shown in Figure 4.15 (a) and (b), the black spots on the surfaces are corroded regions.

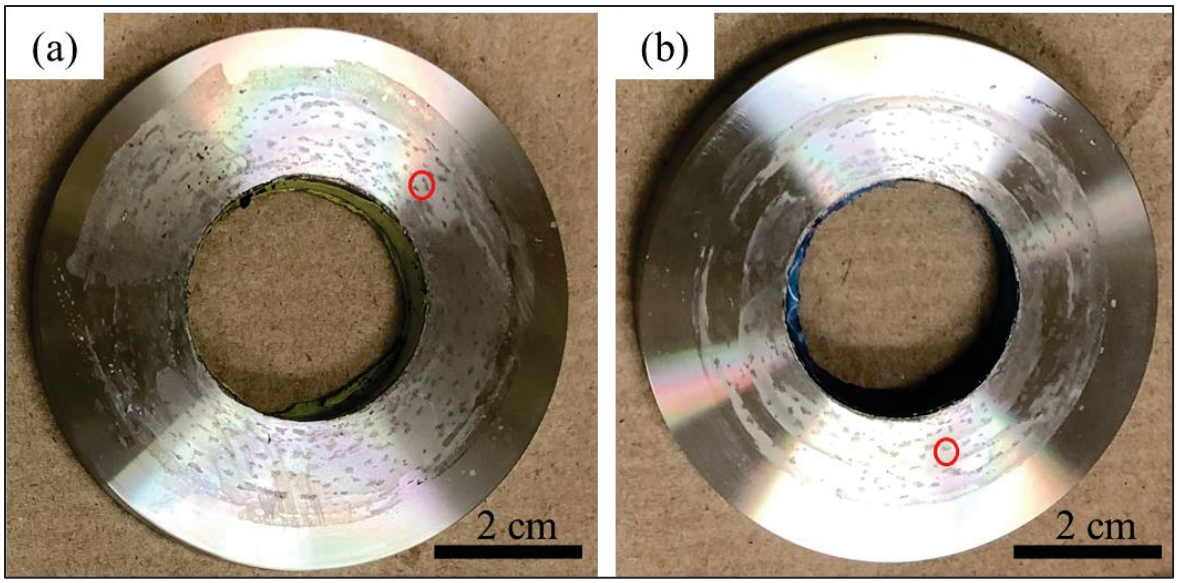

Figure 4.14 The (a) lower and (b) upper plates in the joint after polarization test with gasket No.3, with red circles indicating the small black corroded spots

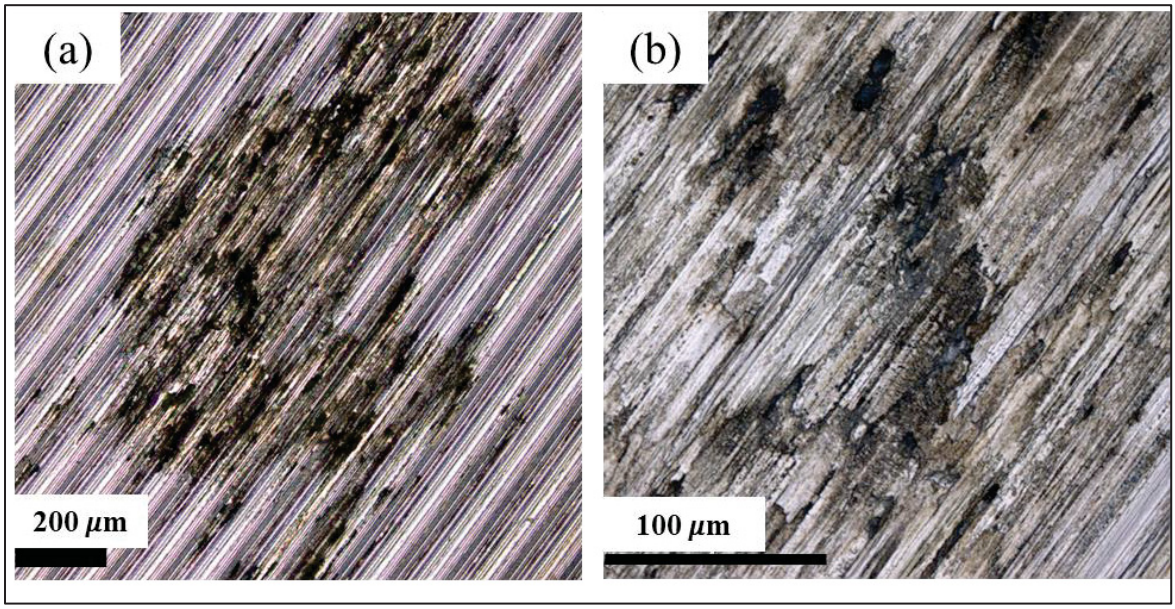

Figure 4.15 Confocal microscopy images of the 304L stainless steel plates after polarization tests with graphite gasket No.3. (a) 100X magnification; (b) 500X magnification

4.4.3 Long term polarization test

In the long-term polarization test, the surfaces of the plates show a darker band around the hole, and the edge of the hole seems completely corroded (Figure 4.16 (a) and (b)). The amount of weight loss confirms this observation after corrosion testing. The amount of weight loss for the upper plate is 0.4547 g and for the lower plate is 0.6171 g. Based on Figure 4.16 (a) and (b), it seems that a larger area on the surface of the plates is affected by the corrosion. Confocal images of two zones on the metallic plate after corrosion shed light on the details of the corroded surface. These two zones include the internal surface and the darker band's middle, as shown in Figure 4.16 (a).

Figure 4.17 (a) and (b) show zone 1 at 50X and 100X magnification. Figure 4.17 (a) presents a 50X magnification of the inner edge shown completely black, and under 100X magnification (Figure 4.17 (b)), the damage in the corroded area is more evident. In the second zone which is shown in Figure 4.18 (a) and (b) at the two magnifications, many black spots are visible close to the edge (Figure 4.18 (a)), and these spots (shown by red circles) are clearly the result of damage caused by corrosion (Figure 4.18 (b)).

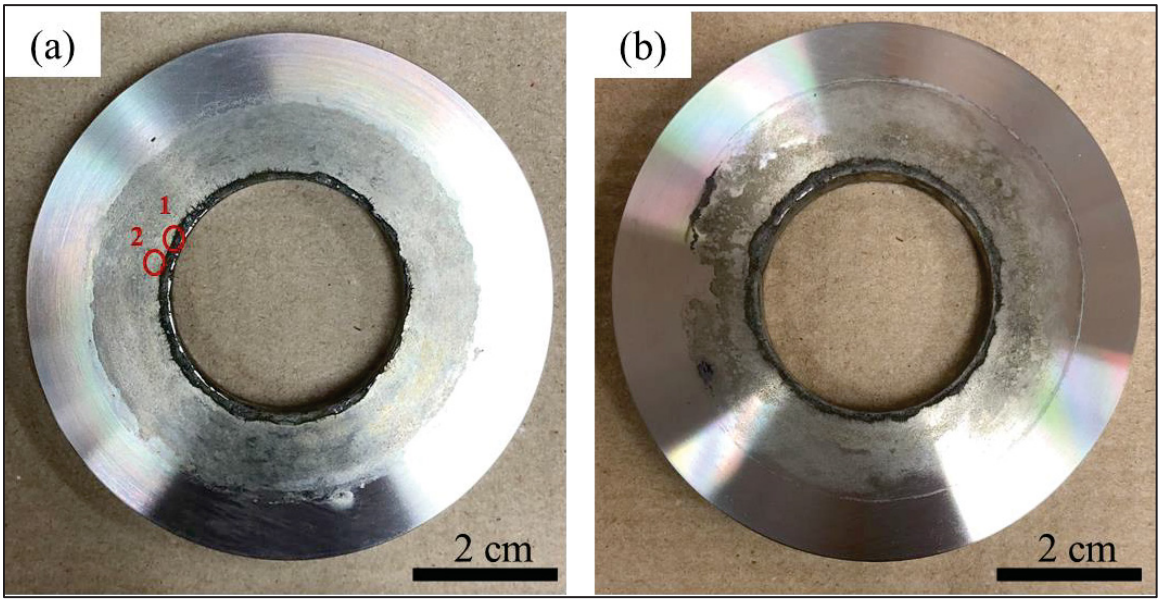

Figure 4.16 The (a) lower and (b) upper plates in the joint after long-term polarization test with gasket No.3, with two zones selected for microscopic characterizations by red circles No.1 and No.2

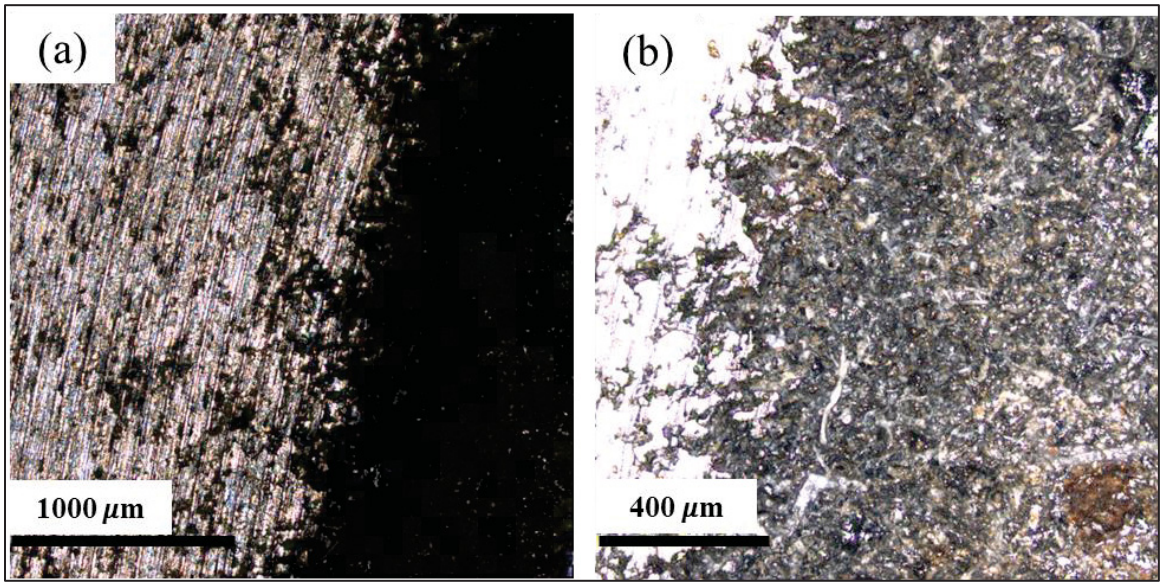

Figure 4.17 Confocal microscopy images of the 304L stainless steel plate after long term polarization test with graphite gasket No.3. (a) 50X magnification; (b) 100X magnification

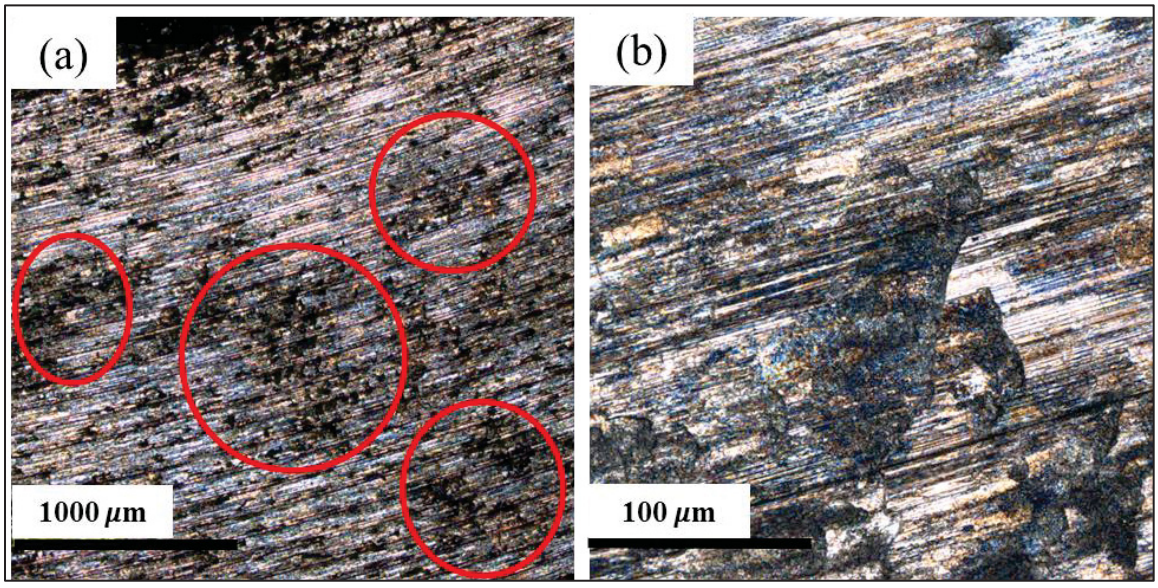

Figure 4.18 Confocal microscopy images of the 304L stainless steel plate after long term polarization test with graphite gasket No.3. (a) 50X magnification with red circles indicating the black corroded spots; (b) 500X magnification

4.5 Conclusion

In this study a COQT test bench is proposed to allow quantification corrosion at the interfaces between the flanges and the gasket in an ARLA like fixture exposed to saline solution. The test setup allows the monitoring and/or control of different service parameters, such as average gasket contact stress, fluid pressure and flow rate, temperature, pH, and conductivity. One of the main advantages of this system is the possibility of evaluating different combinations of flange materials and gasket types by simply changing two parts on the setup. Among its limitations, it is possible to list its inability to work at the higher pressures commonly found in the industry. Since there is a three-electrode cell in the setup, the corrosion behavior of the plates could be studied using the polarization curves. As demonstrated by the polarization test results, the rig proved to be workable and, therefore, could be used to quantify and study corrosion in bolted flanged joints. The comparison of the polarization results shows that gasket No.3, which has more halogen content than the other gasket materials, accelerates corrosion of 304L stainless steel surfaces. This study has demonstrated that the developed fixture is a suitable test bench for investigating the corrosion behavior of bolted joints. It can be utilized to assess the influence of the service conditions and other gasket materials than graphite on the corrosion behavior of flanges in bolted flanged joints.

Acknowledgment

This work was supported by the Natural Sciences and Engineering Research Council of Canada (NSERC) under the Discovery Grant (RGPIN-2019-05973 and RGPIN-2021-03780).

CHAPTER 5

EFFECT OF GASKET MATERIAL ON FLANGE FACE CORROSION

Soroosh Hakimian [a], Abdel-Hakim Bouzid [a], Lucas A. Hof [a]

[a] Mechanical Engineering Department, École de technologie supérieure, 1100, rue Notre-Dame Ouest, Montreal, Québec, H3C 1K3, Canada

Paper published in: *International Journal of Pressure Vessels and Piping*, Volume 209, June 2024, 105207.
https://doi.org/10.1016/j.ijpvp.2024.105207

Abstract

Bolted flanged joints play a crucial role in connecting pressure vessels and piping systems. The corrosion of the flange surface is one of the most common causes of leakage failure in bolted flanged joints. This research investigates the effect of three gasket materials on the corrosion behavior of 321 stainless steel flange material using a novel setup specially designed for corrosion quantification of such assemblies. The results show that graphite gaskets cause more corrosion to flange surfaces under the same working conditions compared to graphite gaskets with metal foil inserts and virgin polytetrafluoroethylene (PTFE) gaskets. The mechanism of flange face corrosion is that, for PTFE gaskets, corrosion propagation mainly occurs at the gasket inner diameter and propagates through the depth of the flange while, for graphite gaskets, corrosion occurs on the whole contact surface of the flange and the gasket.

5.1 Introduction

A bolted flanged joint (BFJ) is a type of a seal device that connects pressure vessels and piping components by means of flanges, gaskets, and bolts (Nechache & Bouzid, 2007). These types of joints are frequently used in industrial installations where there is a need to connect pipelines or pressure vessels that handle fluids under high pressure and temperature conditions, such as boilers, condensers, heat exchangers, reactors, steam generators, and piping systems (Abid et

al., 2018). Ease of assembly and disassembly for maintenance and repair services is the advantage of this type of connection compared to welded joints (Habib, 2010). However, it also has the potential to fail due to leaks, particularly when exposed to harsh and corrosive environments at high temperatures and pressures (X. Diao et al., 2020).

The frequent premature leakage failure of BFJ due to corrosion in different industrial applications necessitates the analysis of failure root causes and mechanisms (Hakimian et al., 2024b). The flange face corrosion usually occurs at the interface of the flange and gasket, where the corrosive solution can penetrate the gap between the two flange faces or between the flange and gasket (Long et al., 2022). These gaps are created by material loss due to corrosion and aging and facilitated by the loosening of the joint due to the creep-relaxation of the joint (A. Bouzid et al., 1995; Nechache & Bouzid, 2008), rotation on the flange (Bouzid A.; Chaaban A.; Bazergui A., 1994; A. H. Bouzid et al., 2004), and waviness and misalignment (Nurhadiyanto, 2014b; Worden, 2014a). Documented instances of premature corrosion failures mentioned that galvanic (Bengtsson, 2015b) and crevice corrosion (Kölblinger et al., 2022) are the most repeated types of corrosion in these joints. Galvanic corrosion accelerates the flange face corrosion in cases where metallic gaskets (Al-Abbadi et al., 2017), semi metallic gaskets (Hu et al., 2020), or graphite sheet gaskets (R. Francis; G. Byrne, 2007) are used in conjunction with flanges. Flange face corrosion compromises the necessary smoothness and evenness required for effective sealing. As a result, the joint may fail to maintain uniform pressure distribution on the gasket, resulting in leakage of pressurized fluid (Tavares et al., 2018).

Metallurgical factors (Tavares et al., 2018), environmental conditions (Kölblinger et al., 2022), gap or crevice geometry (Hakimian et al., 2024c), and the flange and gasket materials (Kain, 1998b; Troels Mathiesen; Henrik Bang, 2011) have an influence on the flange corrosion behavior. Tavares et al. (Tavares et al., 2018) reported that an inadequate chemical composition and microstructure of the flange material were the main reasons for an UNS S32750 flange corrosion failure. In another study, Kolblinger et al. (Kölblinger et al., 2022) demonstrated that the presence of bacteria in seawater caused microbiological-induced crevice corrosion (MIC) on an UNS S32760 superduplex steel flange face, although the microstructure and fabrication process were according to the ASTM A182 standard. The size of the gap, or crevice, is a

significant factor in the initiation and development of crevice corrosion (Costa et al., 2023). A recent study analyzed the effect of PTFE gasket size on the flange face corrosion in a 3.5 wt.% NaCl solution at 50 ºC, and the results showed that decreasing the gasket thickness have a significant effect on the initiation of crevice corrosion (Hakimian et al., 2024c).

Material selection is a crucial step in the design of engineering structures, as it determines the adequacy of the structure corrosion lifetime considering the environment to which it is exposed (Hakimian, Pourrahimi, et al., 2023). Therefore, the importance of studying the effect of flange and gasket materials on the flange face corrosion is acknowledged. Martin et al. (Farrel J. Martin; Paul M. Natishan; Steven H. Lawrence; Elizabeth A. Hogan; Keith E. Lucas; Elvin Dail Thomas, 2004) compared the crevice corrosion initiation and propagation of different Ni-Cr-Mo alloys in seawater at 65 ºC. This study deployed the pitting resistance equivalent number (PREN) method to find a correlation with the crevice corrosion penetration rate. It was reported that the higher the PREN, the lower the crevice penetration rate, at a constant polarized potential of 300 mV (Ag/AgCl) and 65 ºC of seawater. The effect of temperature, chlorination, and the flange material on crevice corrosion of high-grade stainless steels (SS) and Ni-based alloys was studied by Larche et al. (Nicolas Larché; Dominique Thierry; Pauline Boillot; Thierry Cassagne; Jéréme Blanc; Philippe Dézerville; Elisabeth Johansson; Jean Marc Lardon, 2016). Here, the crevice corrosion performance of several SS and nickel alloys was evaluated at 30 ºC and 50 ºC in chlorinated and natural seawater for a three-month exposure time. Among the tested materials in this study are UNS N06022 and UNS S31266 which were found to be resistant to crevice corrosion under all experimental conditions. Gaskets are the crevice formers in flanged gasketed joints that are used to prevent leakage in these joints. The material of the gasket is selected based on different factors, including the media inside the pipeline, temperature, pressure, bolting, and any cyclic or vibrational loading of the joint (Stephen Bond; Yi Li, 2020). As gaskets are in direct contact with flanges in BFJ, their material affects crevice corrosion initiation and propagation on the flange surface (Kain, 1998b). This research mainly focuses on studying corrosion mechanisms on the flange face by changing the gasket material.

Various electrochemical techniques have been utilized in the literature to measure flange face corrosion. These methods were employed to assess the susceptibility of flange and gasket

materials to crevice corrosion by comparing parameters such as the potential at which crevice corrosion initiates ($E_{crevice}$) (Troels Mathiesen; Henrik Bang, 2011), the critical crevice temperature (CCT) at which crevice corrosion occurs (Trond Rogne; John M. Drugli; Tone Solem; Hakon Salbu; Helge Sljellevik, 1998), and the time required for crevice corrosion to initiate (t_{init}) (Farrel J. Martin; Paul M. Natishan; Steven H. Lawrence; Elizabeth A. Hogan; Keith E. Lucas; Elvin Dail Thomas, 2004). However, studies on the corrosion behavior of flange materials are typically conducted under conditions that are not representative of actual operating conditions. For instance, these studies are often performed under conditions without fluid circulation, the presence of a gasket, or sufficient gasket contact stress, despite the critical role these factors play in the initiation and growth of crevice corrosion (Costa et al., 2023).
In this paper, the developed COrrosion Quantification Test (COQT) rig and fixture by the authors, detailed in reference (Hakimian et al., 2024a), are utilized to assess the impact of three types of gaskets: flexible graphite sheet, graphite sheet with foil inserts, and polytetrafluoroethylene (PTFE) sheet, on the corrosion behavior of ASTM A182 F321 flange material. This material is among the widely used SS flange materials (J. Wang et al., 2019). The mentioned fixture takes into account both electrochemical attributes and service conditions, allowing for the quantification of corrosion behavior using three-electrode electrochemical techniques, including cyclic potentiodynamic polarization (CPP) tests and potentiostatic polarization tests. Employed in the current study, CPP is the most widely used technique for assessing critical crevice corrosion potentials, while potentiostatic tests provide information about the initiation and propagation of crevice corrosion (Costa et al., 2023).

5.2 Corrosion quantification test rig and fixture

5.2.1 Test fixture

The COQT test fixture, which is capable of measuring and analyzing the corrosion of sample plate and gasket material pairings, is depicted in Figure 5.1. The fixtures' components are depicted in this image. It replicates the successful Aged Relaxation Leakage Adhesion (ARLA) device (Marchand, Bazergui, et al., 1992b; Marchand, Derenne, et al., 1992b), which measures

weight loss, load retention, gasket relaxation, and leakage tightness after aging a sheet gasket material in an oven. The COQT fixture is designed to mimic ASME B16.5 (ASME B16.5, 2021), NPS 1½ class 150 (gasket according to ASME B16.21 (ASME B16.21, 2022) dimensions) BFJ. Through the use of a hydraulic tensioner, the central stud allows the application of compressive stress on the gasket through the circular compression plates. The slots on the compression plates are designed to quantify the difference in gasket thickness before and after the corrosion tests. The corrosive solution can also circulate through the entry and exit ports on the compression plates. The test fixture is meant to simulate a BFJ. After every test, it is simple to exchange the corroded sample plates for new ones in order to examine the effects of different factors. To precisely measure the corrosion of the sample plates and prevent corrosion of the rest of the fixture, the electrical insulator creates electrical insulation between the sample plates and the compression plates. The Belleville washer and compression plate have more surface area in contact when a plain washer is utilized. The Belleville washers help to keep the assembly's preload constant and, if necessary, to modify the bolt joint's stiffness. It should be mentioned that this parameter matters when taking relaxation into account. The Belleville washers have a robust contact interface due to the load ring or spacer. The O-rings provide a seal to the outside and stop the stud from making electrical contact with the plates. The plain washer increases the contact area between the compression plates and the nuts. The inside chamber has a 20 mL capacity. The gaskets size is within an ID of 1.31 inches and an OD of 2.95 inches with thicknesses ranging from 1/16” to 1/8”.

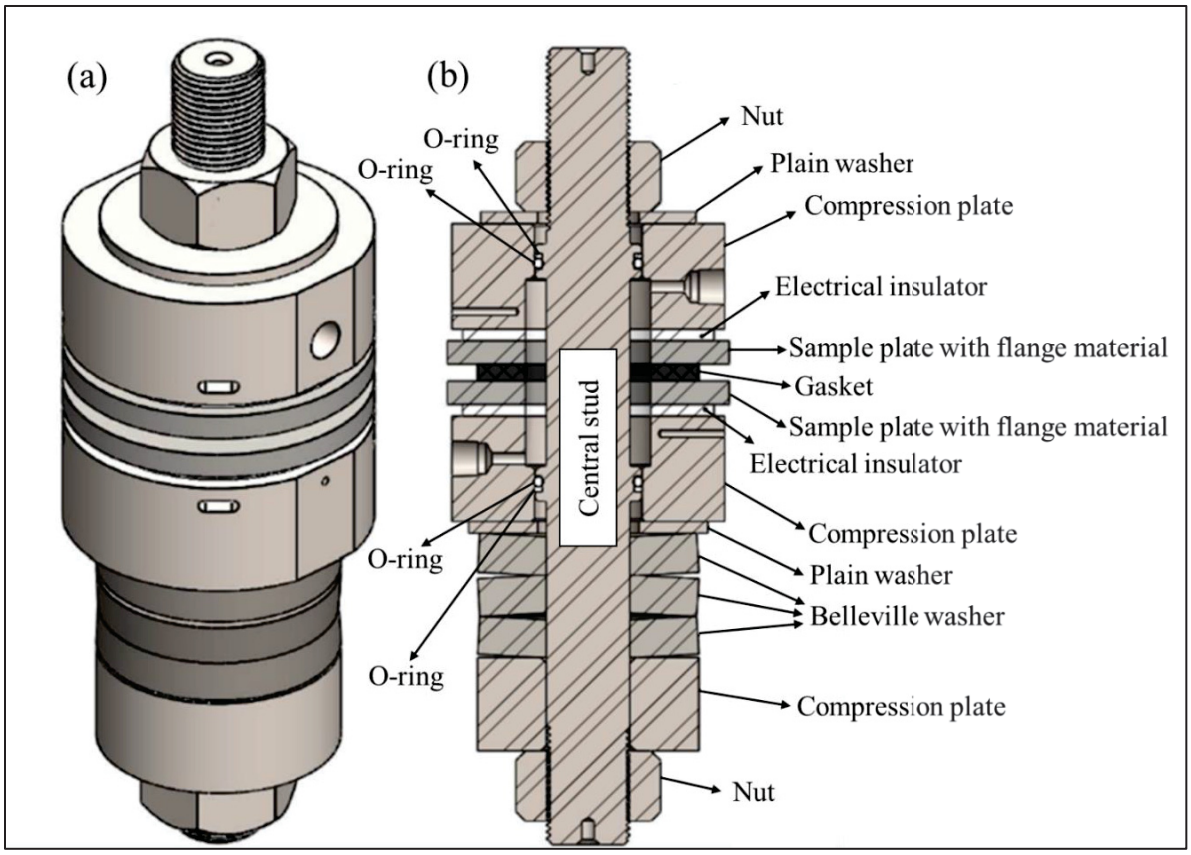

Figure 5.1 Test fixture (a) 3D view (b) cross section view and labelling of each item Adapted from Hakimian et al. (2024a)

5.2.2 Test rig

The COQT fixture is part of the test rig shown in Figure 4.3. It is connected to a tank containing a corrosive solution with a ¼ inch diameter circuit that has different equipment and instrumentation. The multiparameter meter (1) simultaneously measures the pH, conductivity, and temperature of the solution using a pH sensor (2) and a conductivity probe (3). The thermostatic water tank (4) is a container that heats the corrosive solution to the desired test temperature with precision of ±0.1 ºC. The peristaltic pump (5) provides continuous solution flow from the thermostatic water tank to the test fixture. The flow meter (6) and pressure transducer (7) continuously monitor the flow and pressure of the solution. The three-electrode system is used to quantify the corrosion according to ASTM G59 requirements (ASTM International, 2020d). Sample plates are considered as working electrodes (8), the central stud

is considered as a counter electrode (9), and the Ag/AgCl as a reference electrode (10). In this test rig, the potentiostat (11) is the instrument that maintains the working electrode potential, and the measured potential is compared to the reference electrode. To reduce the ohmic drop contribution between the reference and working electrodes, the salt bridge (12) is utilized as a conductive connection between the solution in the test fixture and the reference electrode. The test fixture's temperature is determined by the thermocouple (13). The circulating solution soaks all internal components of the fixture, including the gasket and the metallic sample plates, as shown in Figure 4.3, where it flows from the bottom to the top. The analogue signals from the sensors are transmitted to the printed circuit board (PCB-14) and converted to numerical values by the Data Acquisition Card (DAQ-15). The DAQ, potentiostat, and multiparameter meter are connected directly to the computer (16) through USB ports. A full Wheatstone strain gauge bridge is bounded to the central stud (transducer in mV) to measure the gasket load and converted to an average gasket contact stress (17).

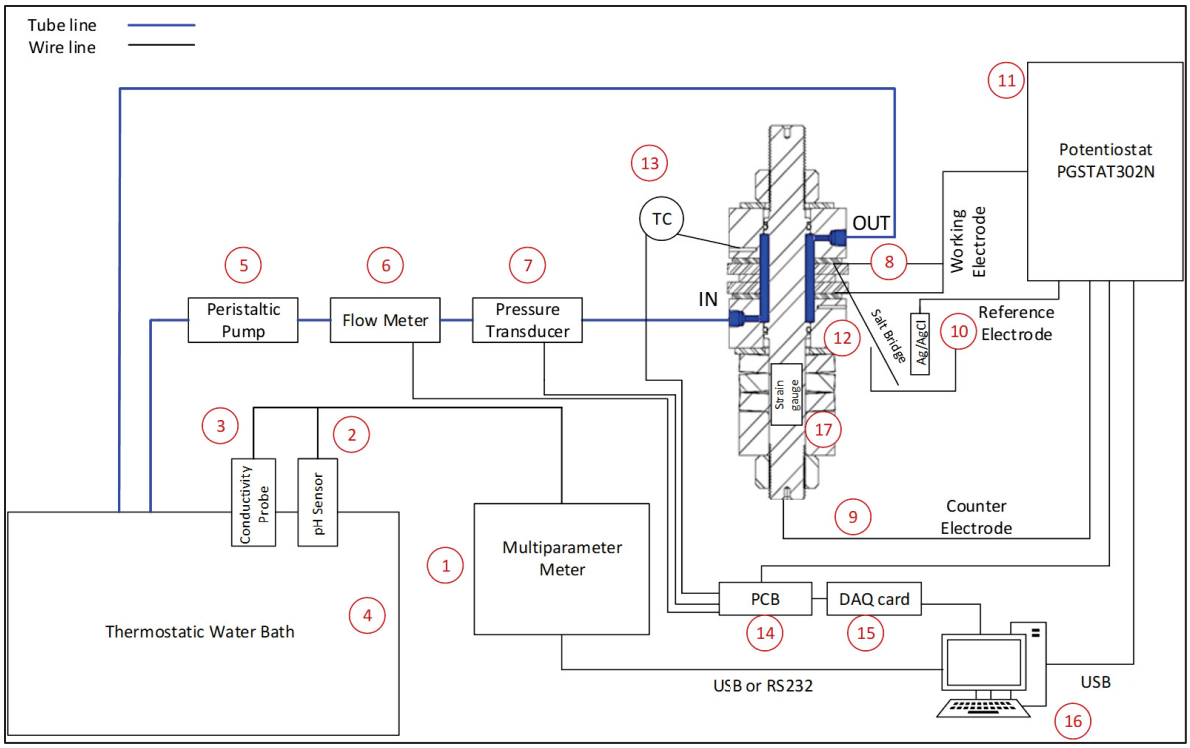

Figure 5.2 COQT bench: 1) pH and conductivity meter; 2) pH electrode; 3) conductivity electrode; 4) thermostatic water bath; 5) peristaltic pump; 6) flow sensor; 7) pressure sensor; 8) working electrode connection; 9) auxiliary electrode connection; 10) reference electrode; 11) potentiostat; 12) salt bridge; 13) thermocouple; 14) PCB; 15) DAQ card; 16) PC; 17) strain gauge
Adapted from Hakimian et al. (2024a)

5.3 Materials and methods

5.3.1 Materials

The sample plates, depicted in Figure 5.3 (a), have an outer diameter of 2.95 inches, an inner diameter of 1.31 inches, and a thickness of 0.25 inches. The roughness of the sample plates was measured using a Mitutoyo profilometer following the ISO 21920-2:2021 standard, as recommended by literature (Pourrahimi & Hof, 2024). A cut-off length of 0.8 mm and a short wavelength cut-off filter λs of 2.5 µm were used, resulting in an arithmetic mean of absolute height values Ra = 1.006 ± 0.05 µm. The material of the sample plate is 321 SS, which has a chemical composition according to ASTM A182 (ASTM International, 2020a) standard

specification for SS pipe flanges. The chemical composition is provided in Table 6.1. Between the sample plates, three types of gaskets including graphite sheet gasket (G-1), graphite gasket with metal foils (G-2), and virgin PTFE sheet gasket with dimensions of 1.92 inches inner diameter, 2.8 inches outer diameter, and 1/16-inch thickness are utilized (Figure 5.3 (b)). Table 2 provides G-1 and G-2 gaskets characteristics. The PTFE samples are made of barium sulfate filled PTFE gasketing material.

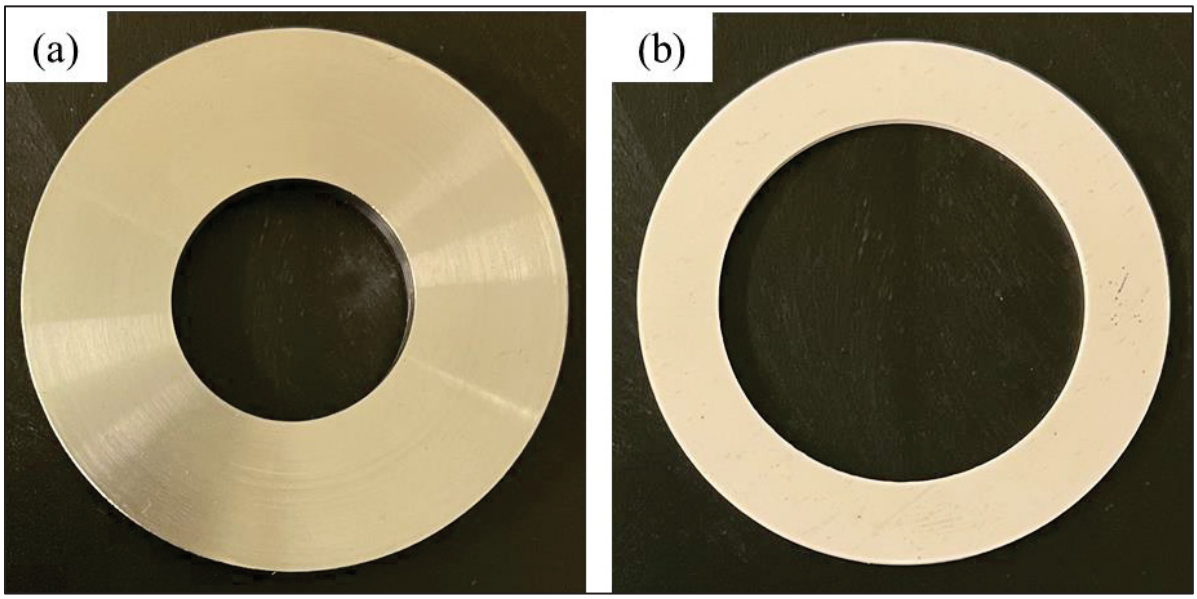

Figure 5.3 An overview of (a) the 321 SS sample plate; (b) the virgin PTFE gasket

Table 5.1 Chemical composition of 321 SS sample plate (wt.%)

C	N	Si	P	S	Cr	Mn	Ni	Mo	Cu	Ti
0.049	0.024	0.54	0.03	0.001	17.45	1.57	9	0.37	0.48	0.53

Table 5.2 Characteristics of G-1 and G-2 gaskets

Gasket	Ash content (%)	Density (g/cm^3)	Chloride content (ppm)	Fluorine content (ppm)	Sulfur content (ppm)	Total halogen (ppm)
G-1	≤ 2.0	1.1	≤ 50	≤ 10	≤ 750	≤ 310
G-2	≤ 2.0	1.1	≤ 25	≤ 10	< 300	≤ 70

5.3.2 Corrosion characterization

The current research uses electrochemical techniques and microscopic characterisation to explore the corrosion mechanism on the surfaces of the flanges in BFJs. These techniques will be discussed in the following sections.

5.3.2.1 Cyclic potentiodynamic polarization

The CPP test (according to ASTM G61 (ASTM International, 2018c)), is performed to measure the corrosion mass loss rate and quantify crevice corrosion behavior of flange materials. The three-electrode cell used for electrochemical measurements, including the sample flange plates (321 SS) as a working electrode (W.E.), a saturated Ag/AgCl as a reference electrode (R.E.), and 316L SS (central stud) as a counter electrode (C.E.). All potentials mentioned in this paper are measured with respect to the Ag/AgCl electrode, as the potential of this electrode does not change during the test. Before starting the polarization test, the fixture shown in Figure 5.1 is mounted on a stand equipped with a hydraulic tensioner to compress the gasket to an average low stress level of 15 MPa to account for the service loads such hydrostatic end effect and relaxation due to creep that tend to unload the gasket. The maximum stress that can be applied to the gasket with this fixture is 35 MPa. This low stress level ensures a tight seal, while facilitating solution penetration into the small gaps and leak paths, which is ideal for evaluating the impact of gasket material on crevice corrosion propagation. It should be noted that the fixture is designed to allow low pressure of the saline solution and in all cases, it remains below 0.1 MPa. Given this low-pressure level and the fact that hydrostatic area is confined between the central stud shank OD and gasket ID, the contribution of the hydrostatic end force to the overall gasket stress is negligible. A one litre glass cell of 3.5 wt.% NaCl solution (distilled water and analytical grade of NaCl) is placed in the thermostatic water bath and the temperature is set to 22 ± 1^{o}C, then the peristaltic pump circulates the solution in the fixture with a flow rate of 20 mL/min. The polarization test is initiated 24 hours after the solution has been in circulation inside the fixture, allowing sufficient time for the surfaces of the samples and the interface between the gaskets and sample plates to become wet. The scan begins from 0.03 V

below the Open Circuit Potential (OCP) and continues until the current reaches 5 mA, at which point it is reversed. The scan is discontinued when the potential reaches 0.03 V. For both forward and reverse scan, the scan rate is 0.167 mV/s. The exposed surface area of the 321 SS sample plates is 33.28 cm^2. Autolab potentio/galvanostat PGSTAT302N-High Performance is used to produce the polarization curves for the discussed potential ranges. Nova software version 2.1.6 is used to calculate i_{corr} according to Equation (5.1) for each polarization curve. Before polarization tests, the specimen plates are degreased with acetone followed by alcohol, and then air dried. To ensure result producibility, all polarization tests are conducted at least three times.

5.3.2.2 Electrochemical analysis method

Corrosion is an electrochemical reaction in which the electrons are reactants. Therefore, the rate of reactions is controlled by varying the potential. In polarization tests, the anodic or cathodic reaction rates are controlled by withdrawing or adding the electrons to the system, which is typically achieved by precisely controlling the potential using a potentiostat. The potential at which the cathodic and anodic reaction rates are equal is defined as the corrosion potential (E_{corr}), and the related current density is defined as the corrosion current density (i_{corr}). Tafel extrapolation is used to determine the corrosion current density. The Tafel equation shows the relation between the current density and potential according to Equation (5.1) (Baboian, 2005).

$$E - E_{corr} = a \pm b\ log|i| \tag{5.1}$$

Here E is the applied potential in V, E_{corr} is the potential where corrosion occurs, E-E_{corr} is the overpotential (η) in V, the sign "±" indicates in which domain the sample operates (+ if anodic and – if cathodic), a and b are the Tafel constant and slope, respectively, and i is the current density in A/cm^2. The current density is obtained by dividing the measured current to the geometric area of the working electrode exposed to the solution. Figure 5.4 depicts the schematic overview of the Tafel extrapolation technique used to determine i_{corr} and E_{corr}. The

intersection of the extrapolated Tafel anodic line (η>0) and the Tafel cathodic line (η<0) with E_{corr} determines i_{corr}, which provides the corrosion rate or mass loss rate. All the electrochemical parameters in Figure 5.4 are defined in the explanation of Equation (5.1).

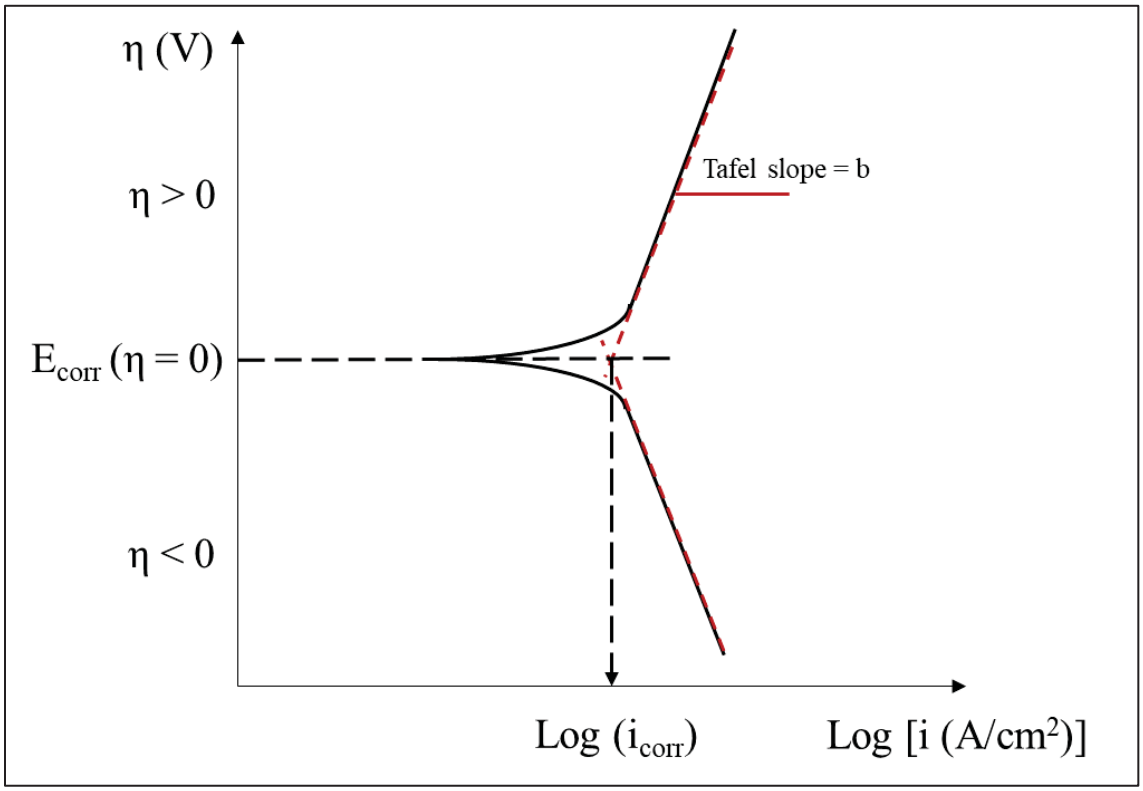

Figure 5.4 A schematic overview of the Tafel extrapolation represents the corrosion potential (E_{corr}), overpotential (η), Tafel slope (b), and corrosion current density (i_{corr})

In situations where general corrosion occurs, Equation (5.2) converts the i_{corr} to the mass loss rate using Faraday's law. This mass loss rate indicates the general corrosion rate in grams per square meter per day ($g/m^2/d$).

$$MR = Ki_{corr}\,EW \tag{5.2}$$

where MR is mass loss rate in $g/m^2/d$, K is 8.954×10^{-3} $gcm^2/\mu A/m^2/d$, i_{corr} is in $\mu A/cm^2$, and EW is the dimensionless equivalent weight. EW is the mass of metal oxidized by the passage

of one Faraday (96500 C) of electric charge. The value of *EW* for typical stainless steel and carbon steel is provided in ASTM G102 (ASTM International, 2015a).

5.3.2.3 Potentiostatic polarization

Since the potentiodynamic test discussed in the previous section was destructive, new samples are employed for the potentiostatic tests. Following a 24-hour period of 3.5 wt.% NaCl solution circulation in the fixture, potentiostatic tests are conducted at three time intervals: 6, 12, and 24 hours at 0.15 $V_{Ag/AgCl}$ for each gasket material.

5.3.3 Surface characterization

A Laser Confocal Microscope LEXT4100 is utilized to examine the surfaces of the corroded samples after the potentiostatic tests, enabling visualization of the damage caused by corrosion. This includes the examination and evaluation of crevice corrosion in terms of surface and depth. The corroded areas on the surface of the sample plates are measured using Fiji software, an open-source platform for image analysis (Schindelin et al., 2012). The entire corroded surface area (A_c) is calculated using Equation (5.3).

$$A_c = \sum_i^n A_{c,i} \tag{5.3}$$

Where $A_{c,i}$ represents the corroded area in region *i*, and *n* stands for the number of observed corroded areas on the sample plate surface. The morphology of the corroded area is analyzed using scanning electron microscopy (SEM). The Keyence VR-5200 digital microscope is used to examine the corroded surface of the sample plates, providing a zoomed-out view to illustrate the propagation mechanism of crevice corrosion.

To summarize the developed methodology, Figure 5.5 presents a flowchart including the different experimental steps followed in this study.

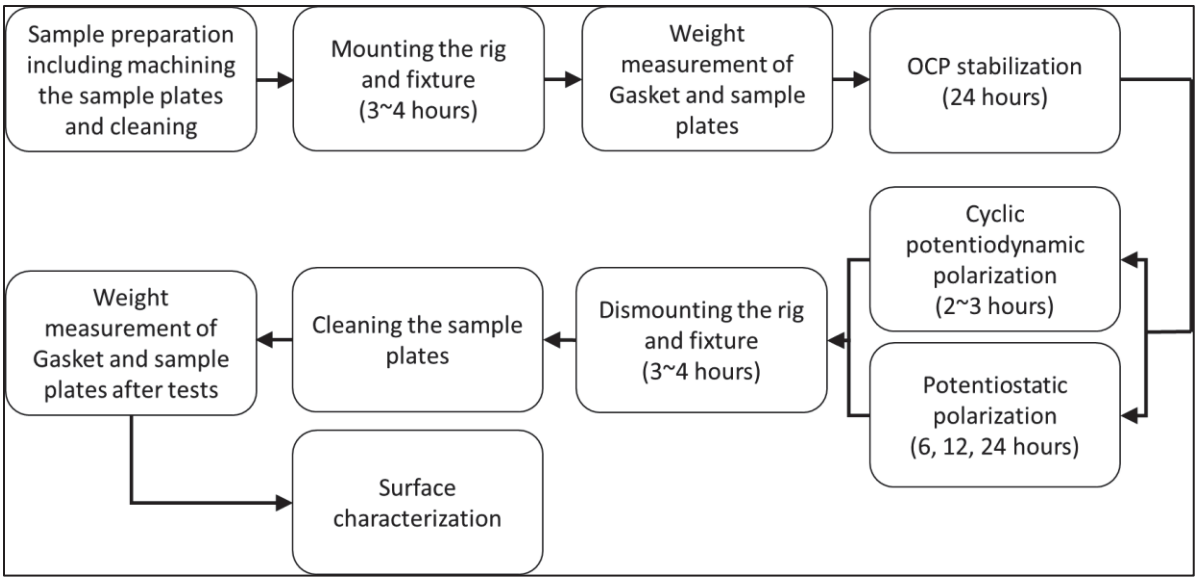

Figure 5.5 Flowchart indicating the experimental methodology

5.4 Results

5.4.1 Cyclic potentiodynamic polarization curves

Figure 5.6 (a-c) displays the results of CPP for the 321 SS sample plates assembled with virgin PTFE gasket, G-1 gasket, and G-2 gasket, while subjected to identical gasket contact stress, fluid flow rate, and temperature (as mentioned in section 5.3.2.1). These polarization curves measure the corrosion potential (E_{corr}) and breakdown potential (E_b) to evaluate the corrosion behavior of the samples. The corrosion potential represents the potential of the working electrode (sample plate) in relation to the reference electrode when no potential or current is applied to the working electrode. It serves as a thermodynamic parameter indicating the tendency of the working electrode to engage in corrosion reactions under specific conditions. In E_b, the current density experiences a significant and rapid increase. A higher positive breakdown potential obtained at a fixed scan rate in the polarization curve indicates a reduced susceptibility of the sample plate to the onset of localized corrosion (crevice or pitting corrosion) (B. Cai et al., 2010; Costa et al., 2023). To estimate the overall corrosion rate of the sample plates, the corrosion current density (i_{corr}) is calculated for each polarization curve using the Tafel equation (Equation (5.1)). The difference between $|E_{corr} - E_b|$ characterizes the

inclination towards localized corrosion, with higher values signifying a reduction in tendency (Vasilescu et al., 2009). Table 5.3 provides an overview of the primary electrochemical parameters obtained from the polarization curves in Figure 5.6. The E_{corr} value for the sample plate with the virgin PTFE gasket (-0.15 V) is found to be lower compared to the other specimens. The E_{corr} of the 321 SS sample plates with a G-1 gasket (0.07 V) was observed to be higher than that of the specimen with a G-2 gasket (-0.04 V). In terms of localize corrosion tendency, represented by the $|E_{corr} - E_b|$ difference, the 321 SS specimens with the virgin PTFE gasket exhibited a higher potential difference (0.44 V) compared to the specimens with the G-1 gasket (0.17 V) and G-2 gasket (0.34 V). This indicates that the joint with the virgin PTFE gasket has the lowest tendency for localize corrosion. The presence of graphite causes a galvanic effect, leading to higher MRs for the specimens with G-1 (0.13 $g/m^2/d$) and G-2 (0.06 $g/m^2/d$) compared to the specimen with the PTFE gasket (0.03 $g/m^2/d$). According to the potentiodynamic polarization results, the galvanic effect between the graphite gaskets and 321 specimen plates leads to a higher corrosion rate compared to the specimens coupled with a PTFE gasket. With regard to the galvanic effect, graphite, having a higher potential than the 321 SS, acts as the cathode, while the 321 SS specimen serves as the anode, resulting in accelerated corrosion on the surface of the samples exposed to the solution (Mohammadreza Tavakkolizadeh et al., 2001; Qiu et al., 2020).

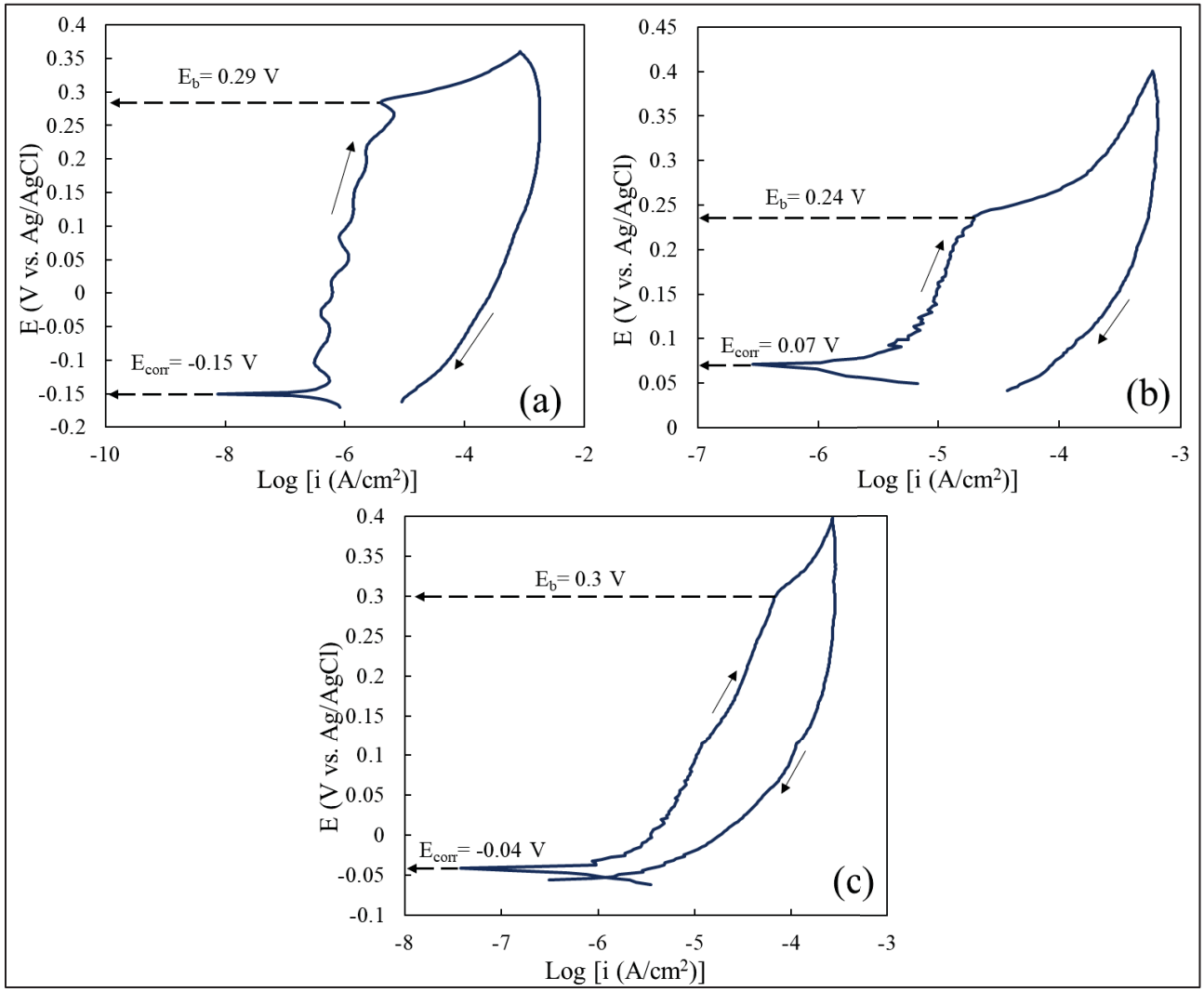

Figure 5.6 Potentiodynamic polarization curves of 321 SS sample plates coupled with (a) PTFE gasket; (b) G-1 gasket; and (c) G-2 gasket at 15 MPa gasket contact stress in 3.5% NaCl solution

Table 5.3 Main electrochemical parameters obtained from the polarization curves

Sample	E_{corr} (V)	E_b (V)	$\lvert E_{corr} - E_b \rvert$ (V)	i_{corr} (µA/cm²)	MR (g/m²/d)
321 SS and PTFE	-0.15	0.29	0.44	0.15	0.03
321 SS and G-1	0.07	0.24	0.17	0.59	0.13
321 SS and G-2	-0.04	0.3	0.34	0.28	0.06

As mentioned above, E_b is the potential at which the passive layer breaks down. This occurs due to pitting corrosion and/or crevice corrosion. Figure 5.7 shows that the breakdown of the passive layer occurs at the sample plate-gasket interface. Therefore, in this case, the breakdown of the passive layer is attributed to crevice corrosion on the surface of the plates. The configuration of the gasket and sample plates are defined in Figure 5.7 (a). Different areas on the sample plate surface are highlighted, including the area under the gasket and the area exposed to the solution. The crevice corroded 321 SS sample plate, after being coupled to PTFE gasket is shown in Figure 5.7 (b). The image shows the corroded sites by circles, and the crevice corrosion is observed in the boundary of the area exposed to the solution and the area under the gasket. The corroded sample plates of Figure 5.7 (c) and (d) are associated to the G-1 and G-2 gaskets, respectively. The corroded sites in the boundary of the exposed area and the area under the gasket are shown with circles. Additionally, corroded sites under the gasket area, are observed with graphite gaskets but not with virgin PTFE gaskets.

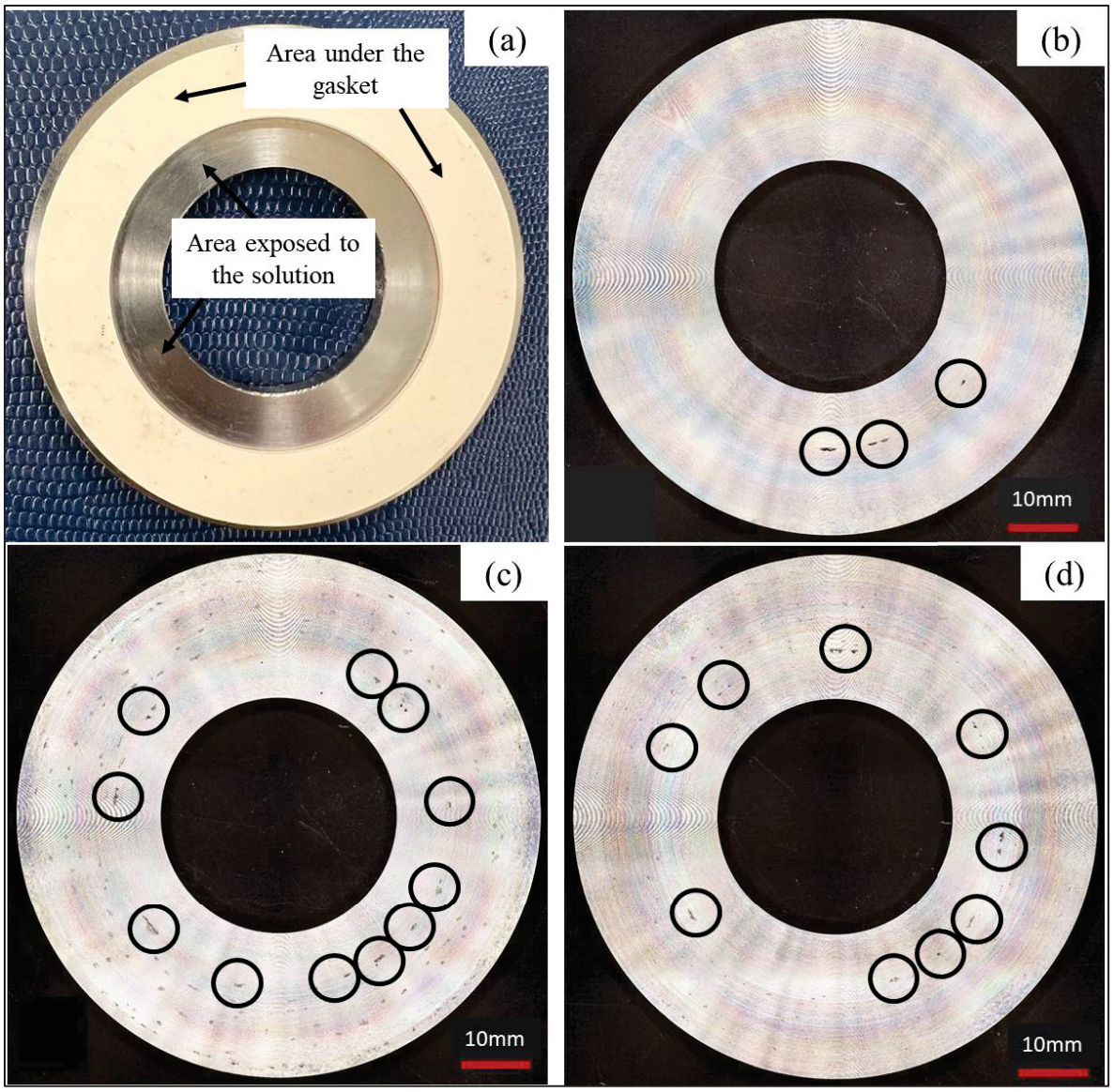

Figure 5.7 321 SS sample plates before and after corrosion tests; (a) Configuration of the gasket and 321 SS sample plate; (b) Crevice corroded area on the 321 SS sample plate with virgin PTFE gasket; (c) Crevice corroded area on the 321 SS sample plate with G-1 gasket; (d) Crevice corroded area on the 321 SS sample plate with G-2 gasket

5.4.2 Potentiostatic polarization test and surface analysis

The potential at which potentiostatic polarization is conducted is adjusted such that it falls within the passivation region, as indicated by the polarization curves in Figure 5.6. Figure 5.8 (a) depicts potentiostatic polarization curves of 321 SS plates in a 3.5% NaCl solution using

the three gasket materials over a 24-hour period. The crevice corrosion is divided to three stages based on the polarization curve features: 1) incubation, 2) initiation, and 3) propagation. These stages are marked in Figure 5.8 (b). The results indicate that the initiation time for the sample plate with the G-1 gasket is 1.2 hours, while for the sample plate with the G-2 gasket, it is 2.8 hours. In the case of the sample plate with the PTFE gasket, crevice corrosion did not initiate. To investigate the crevice corrosion propagation in the sample plate with PTFE gasket, the potentiostatic test is performed at a higher potential of 0.3 V. As depicted in Figure 5.9, the initiation time for the sample with the PTFE gasket is 4 hours. This indicates that even at higher potentials, it takes more time for crevice corrosion to initiate compared to G-1 and G-2. The potentiostatic tests indicate that the sample coupled with the G-1 gasket is more susceptible to crevice corrosion initiation, which is in accordance with the potentiodynamic polarization test results.

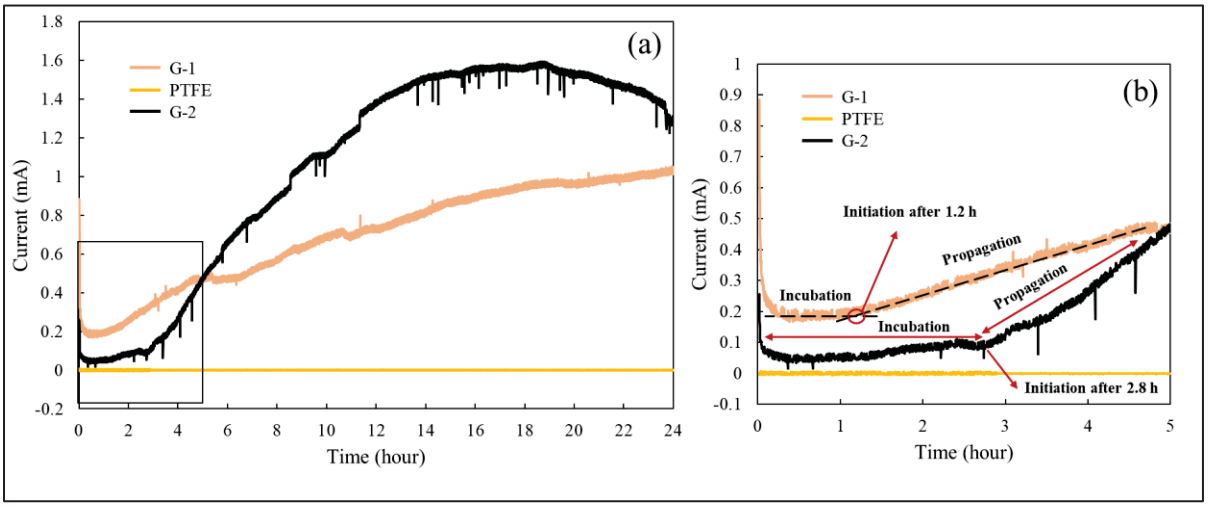

Figure 5.8 Time-dependent of polarization current behavior of 321 SS sample plates under 0.15 V in 3.5 wt.% NaCl solution with various gasket materials. a) the time-dependent polarization for 24 h; b) magnification of the initial 5 hours of the polarization curve revealing distinct stages of crevice corrosion

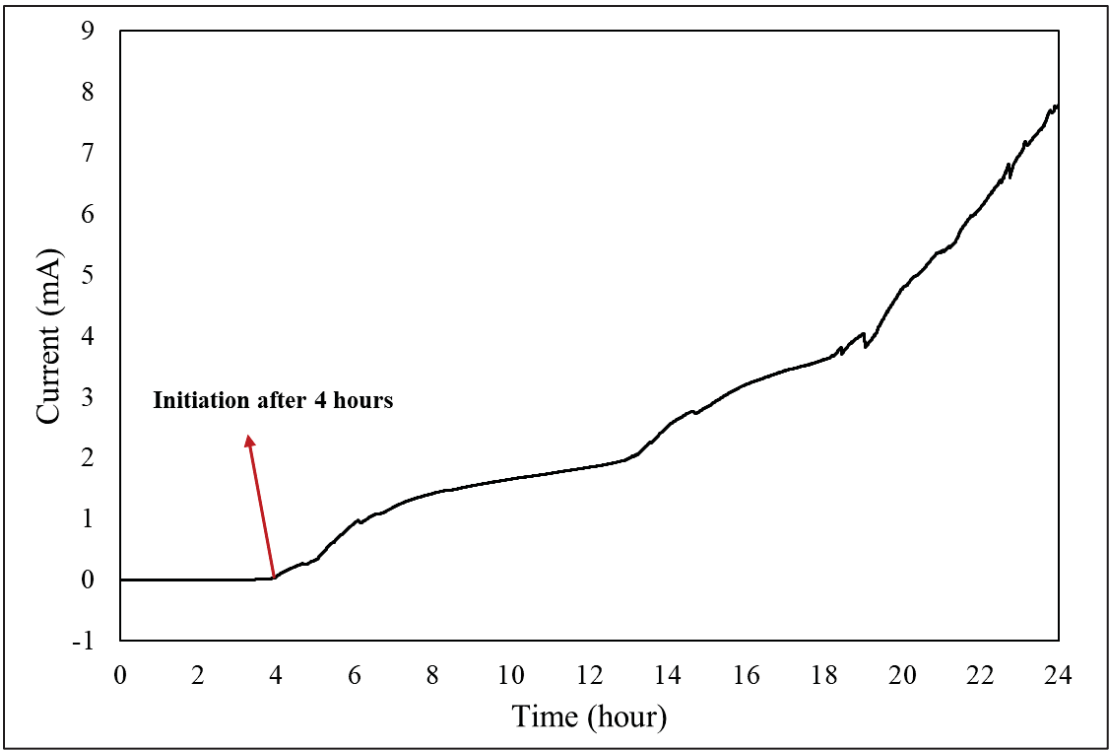

Figure 5.9 Time-dependent of polarization current behavior of 321 SS sample plates under 0.3 V in 3.5 wt.% NaCl solution with virgin PTFE gasket

To investigate the corrosion morphology on the surface of the corroded sample plates, surface analysis was conducted after 24 hours of potentiostatic tests, as depicted in Figure 5.10. As indicated in Figure 5.10 (a) and (b), corrosion took place not only along the boundary of the area exposed to the solution but also beneath the G-1 gasket. In fact, corrosion extended beyond the gasket immediate boundary. For the corroded sample plate used with the G-2 gasket, Figure 5.10 (c) and (d) reveal that corrosion was mainly concentrated along the boundary of the exposed area, forming a distinct ring. In contrast, the corroded area on the sample plate coupled with the PTFE gasket appeared to be deeper than the others. Corrosion occurred along the boundary of the exposed area and under the gasket, but it did not encircle the entire boundary. Instead, deep corrosion spots were observed, as illustrated in Figure 5.10 (e) and (f).

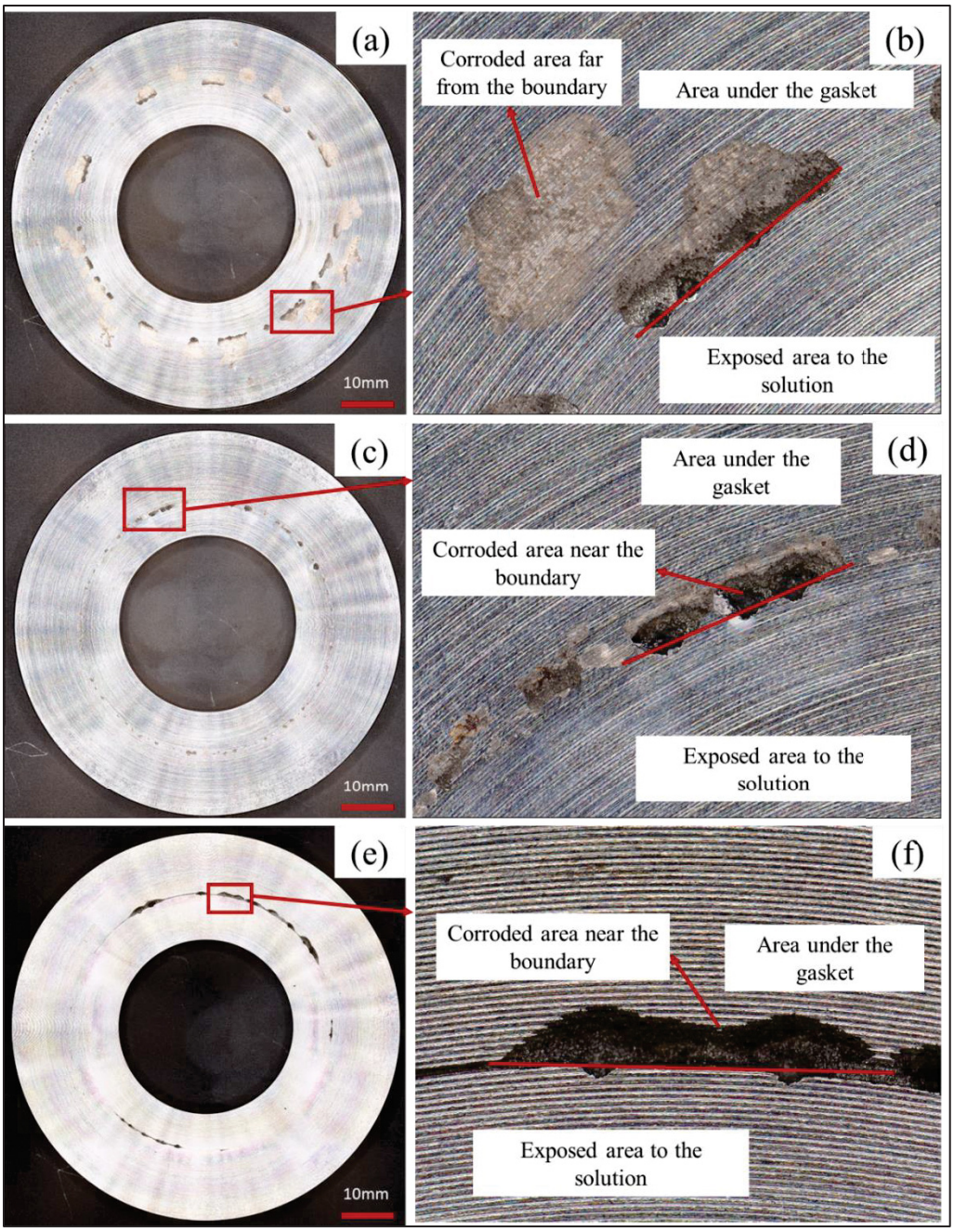

Figure 5.10 Morphology of the crevice corrosion after potentiostatic test of 321 SS sample plates with different gasket material. a) Crevice corrosion on the sample plate with G-1 gasket at 0.15 V; b) magnified image of the corroded sample plate used with G-1 gasket with specified area; c) crevice corrosion on the sample plate with G-2 gasket at 0.15 V; d) magnified image of the corroded sample plate used with G-2 gasket with specified area; e) crevice corrosion on the sample plate with PTFE gasket at 0.3 V; f) magnified image of the corroded sample plate used with PTFE gasket with specified area

For further examination, the corroded sites are examined after 6 hours of potentiostatic test using the confocal microscope, and the deepest corroded sites are magnified. Figure 5.11 (a) indicates the 3D surface morphology of a single crevice corrosion occurred on the sample plate coupled with G-1 gasket. The graphical representation of the corrosion damage depth profile along the cross-section line (indicated in Figure 5.11 (a)) of the single crevice site is shown in Figure 5.11 (b). The region that is covered by the gasket during the corrosion tests is schematically shown in this figure. The corrosion profile has a maximum depth of the 28 μm in the severely attacked region. The same approach is done for the 321 SS sample plates with PTFE and G-2 gaskets. Figure 5.11 (c) shows the magnified corroded site of the sample plate, and the depth of the severely corroded area is measured in Figure 5.11 (d) which is 108 μm. Figure 5.11 (e) indicates the magnified 3D morphology of the crevice corrosion on the sample plate with G-2 gasket. The depth of the deepest corroded site is measured as 72 μm in Figure 5.11 (d).

On the corroded surfaces, there are three distinct regions that can be observed, stretching from the boundary between the exposed area and the area under the gasket to the interior of the crevice. These regions are referred to as the passive region, severely attacked region, and lightly attacked region. The passive region represents the least affected area, encompassing the entirety of the exposed area on the plates. The severely attacked region begins at the edge of the area under the gasket, also known as the passive-to-active boundary. The lightly attacked region experiences less corrosion compared to the severely attacked region, primarily due to restricted diffusion of the solution into this area.

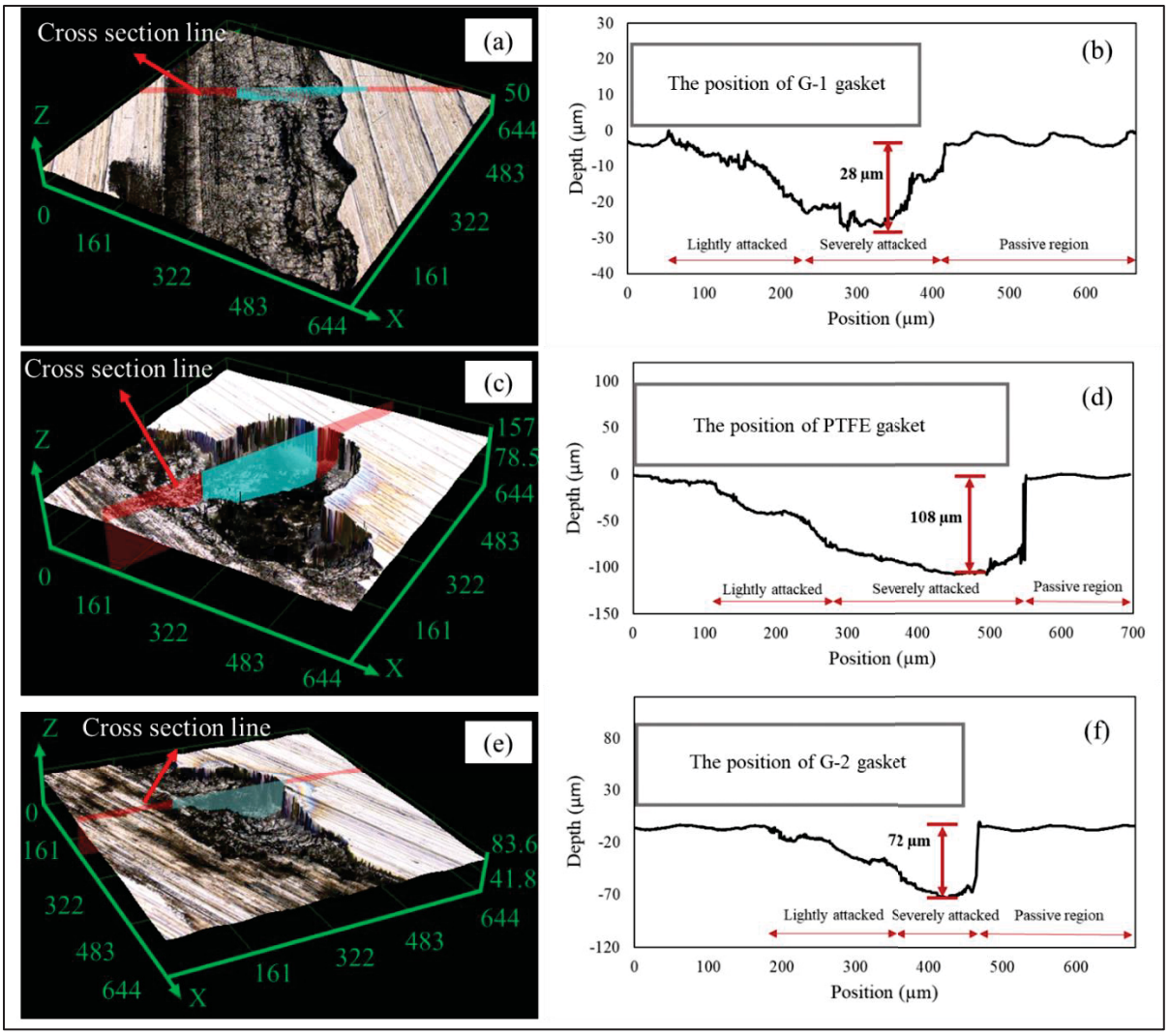

Figure 5.11 Magnified crevice corroded site on the 321 SS samples used in joint with gaskets; (a) 3D surface morphology on a single crevice corrosion site for the 321 SS samples used with G-1 gasket; (b) graphical representation of a single crevice corrosion profile for the 321 SS samples used with G-1 gasket; (c) 3D surface morphology of a single crevice corrosion site for the 321 SS sample used with virgin PTFE gasket; (d) graphical representation of a single crevice corrosion profile for the 321 SS sample used with virgin PTFE gasket; (e) 3D surface morphology of a single crevice corrosion site for the 321 SS sample used with G-2 gasket; (f) graphical representation of a single crevice corrosion profile for the 321 SS sample used with G-2 gasket

To investigate the corrosion growth mechanism at the interface of the gasket and sample plate, the corroded regions on the sample plate surfaces at three-time intervals are examined: 6, 12, and 24 hours after initiating potentiostatic tests. The corroded area on the surface and the deepest corroded spot on the sample plates are quantified, with the results presented in Figure

5.12 (a) displays the deepest corroded regions on the surface of the 321 SS sample plates coupled with three different gaskets. Over time, the depth of the deepest corroded region increased for the sample plates with all three gaskets. Notably, the deepest corroded region was most pronounced for the sample plate coupled with the PTFE gasket, surpassing the others. In terms of the depth of the deepest corroded region, the ranking across the three-time intervals is as follows: PTFE > G-2 > G-1.

Figure 5.12 (b) illustrates that the corroded area on the sample plate surfaces expanded over time for all three gaskets. The corroded area on the G-1 gasket is significantly larger than that on the others, while the corroded areas on the sample plates used with G-2 and PTFE gaskets exhibited similar growth trends. The order of corroded area size is as follows: G-1 > G-2 > PTFE.

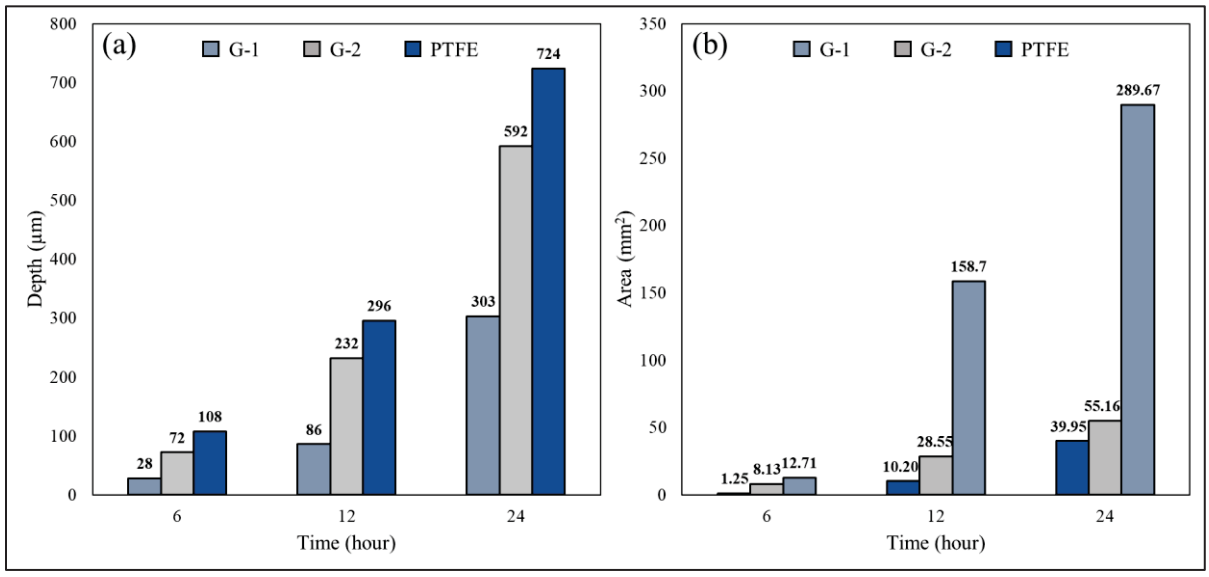

Figure 5.12 Results of measurement of the (a) penetration depth and (b) corroded area of the 321 SS sample plates over time following potentiostatic tests with various gasket materials

5.4.3 Gasket weight increase

After conducting potentiostatic polarization tests, the weights of the gaskets are compared to their initial values before testing, and the increased values are recorded in

Table 5.4. The weight of the gaskets increased due to the absorption of the test solution by the gasket materials. Among the gaskets, the G-1 gasket exhibited the highest absorption with a weight increase of 419 mg, followed by the G-2 gasket with a weight increment of 105 mg, and the PTFE gasket with a weight increase of 1.3 mg. Additionally, the thickness of the gaskets after applying a compression load are measured and reported in

Table 5.4. As mentioned in section 5.3.1, all gasket types in this study initially have a thickness of 1/16 in (1.58 mm). However, when subjected to the same compressive load, the G-1 gasket compressed more than the others, resulting in a compressed thickness of 1.04 mm. The G-2 and PTFE gaskets have compressed thicknesses of 1.14 mm and 1.47 mm, respectively. The thickness of the gasket in the joint has an inverse relationship with the susceptibility of the 321 SS sample plates to crevice corrosion. As the joint thickness decreases, the diffusion of the solution to the gap between the two plates is restricted. This restricted diffusion leads to the acidification of the stagnant solution in the gap, intensifying crevice corrosion (Luo et al., 2022; Shojaei et al., 2019).

Table 5.4 Gasket characteristic after 24 hours potentiostatic tests

Type of gasket	Weight increase (mg)	Thickness after applying compressive load (mm)
G-1	419	1.04
G-2	105	1.14
PTFE	1.3	1.47

5.4.4 Corrosion morphology

The initiation of crevice corrosion on the surface of the 321 SS sample plates occurs at a distance near the gasket, as shown in Figure 5.13 (a). The corroded area near the gasket serves as a pathway for the corrosive solution to diffuse into the region between the plate and the gasket, leading to the propagation of crevice corrosion within the crevice itself (area under the gasket), as depicted in Figure 5.13 (b) and (c). In the lightly corroded area (Figure 5.13 (d)), elongated pits and micro-cracks are observed, ranging in length from 5-40 μm. Furthermore, micro-pits are found surrounding the propagation front (Figure 5.13 (e)), indicating a potential

role of pits coarsening process in controlling the crevice propagation. Additionally, micro-cracks are observed within the micro-pits, possibly attributed to applied stress causing the widening of the pits. The pits that are observed in other reference are without cracks in compared to the pits observed in this study (Hornus et al., 2021; Malki et al., 2021; Park & Lee, 2004).

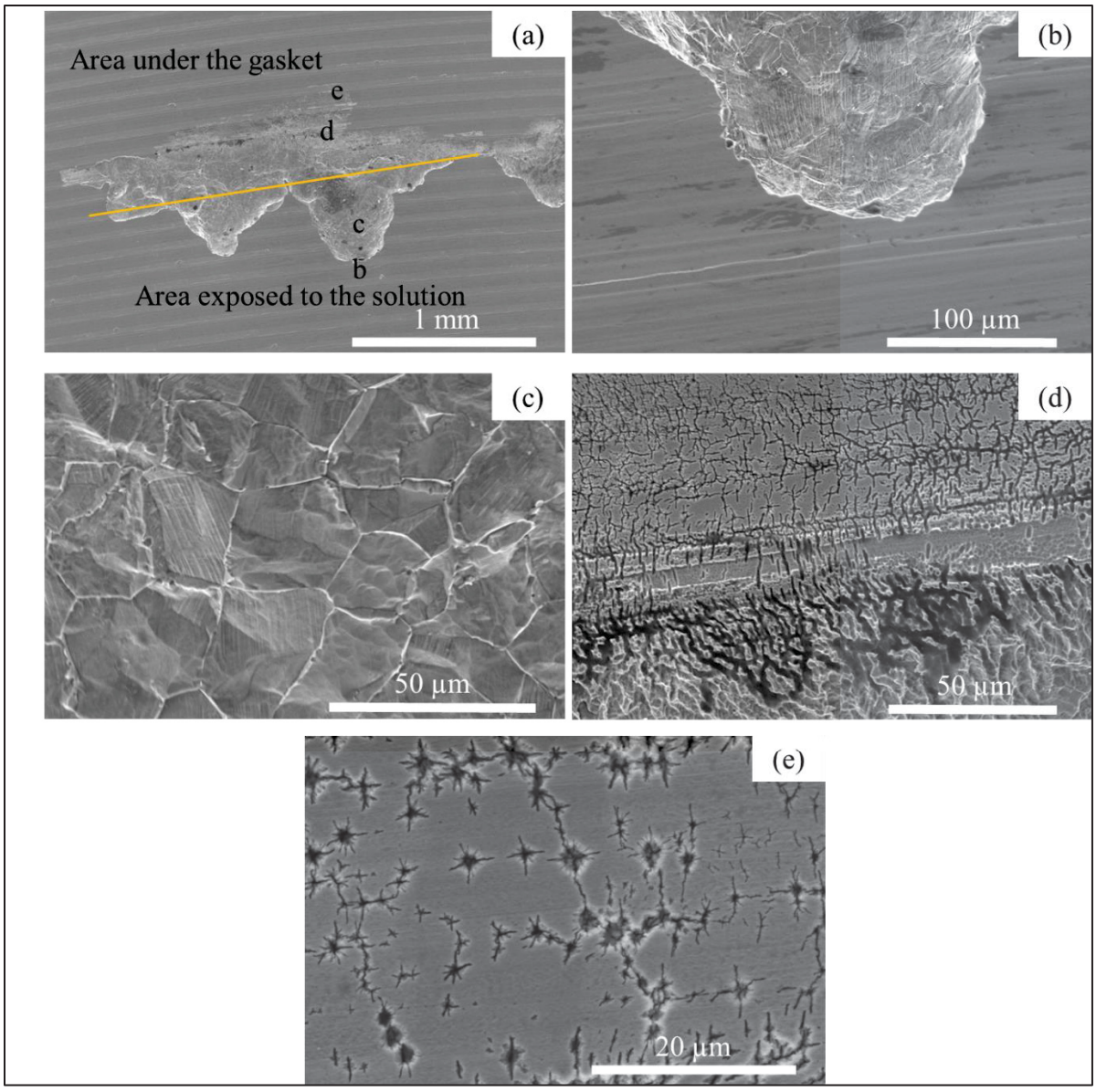

Figure 5.13 SEM micrographs of different regions of the 321 SS sample plate coupled with G-1 gasket crevice corrosion; (a) the crevice corroded site; (b) boundary of the passive region and severely corroded region; (c) severely corroded region; (d) lightly corroded region; (e) pits near the lightly corroded region

5.5 Discussion

5.5.1 Crevice corrosion initiation

Based on the results obtained from electrochemical tests, surface analysis, and measurements of gasket geometry and weight, the primary factor influencing the corrosion behavior of the 321 SS sample plates is the type of gasket material and its geometry. According to the findings from the CPP tests in section 5.4.1, it is evident that the 321 SS sample plates used with the G-1 gasket exhibit a higher susceptibility to crevice corrosion compared to the other types. Similarly, the potentiostatic tests conducted in section 5.4.2 indicate that the crevice corrosion initiation time for samples used with the G-1 gasket is shorter than for the other two gaskets. Furthermore, the initiation time for samples used with the G-2 gasket was shorter than for those used with the PTFE gasket. The variation in gasket thickness after applying the same amount of load appears to be the key contributing factor to differences in crevice corrosion susceptibility. As highlighted in

Table 5.4, the G-1 gasket exhibits the lowest thickness after applying the same amount of load among all the gaskets. The lower thickness of the G-1 gasket, results in the formation of a stagnant solution near the gasket inside diameter. The same rationale explains the higher susceptibility of the G-2 gasket compared to the PTFE gasket. The thickness of the gasket determines the gap between the two flanges which is the dominant factor in the initiation mechanism of the crevice corrosion (Luo et al., 2022). Conversely, the thickness of the G-2 and PTFE gaskets is greater, leading to a delayed initiation of crevice corrosion in the samples with the G-2 gasket and no initiation in the samples with the PTFE gasket when a voltage of 0.15 V is applied.

The initiation of crevice corrosion can be explained by the potential drop (IR drop) theory (Kennell et al., 2008), i.e., the decrease in potential that occurs within a crevice or gap as a result of the resistance encountered by an electric current passing through the solution in the crevice, which states that when the surface of the SS is in the passive form, the IR drop causes the crevice area to transition into the active region, initiating crevice corrosion. According to

the IR drop theory, the ohmic potential drop is dependent on parameters such as current, solution conductivity, and crevice geometry. The value of this ohmic drop can be calculated using Equation (5.4) (Abdulsalam, 2007; Lillard & Scully, 1994):

$$IR = \frac{x_{pass}\ I}{\sigma\ w\ t} \tag{5.4}$$

Here, *IR* represents the potential drop in mV, x_{pass} is the distance between the crevice mouth and the active-passive boundary inside the crevice in cm, I is the current in mA, σ is the conductivity in $\Omega^{-1}\cdot cm^{-1}$, w is the crevice width in cm, and t is the crevice gap thickness in cm. According to Eq. 4, the crevice gap thickness, which in this study is equal to the thickness of the gasket after applying the defined load, influences the IR drop and has an inverse relation. When the crevice gap thickness is high, as in the case of a PTFE gasket, the IR drop remains in the passive region, preventing the initiation of crevice corrosion.

5.5.2 Crevice corrosion propagation

As indicated in Table 5.4, G-1 absorbed a greater amount of solution compared to G-2 and PTFE gaskets. The surface analysis of the corroded samples at three different time intervals, as presented in Figure 5.10 and Figure 5.12, reveals distinct patterns of corrosion propagation based on the gasket type. In the sample plate used with the G-1 gasket, corrosion primarily occurred along the contact surface between the gasket and flange interfaces. This phenomenon can be attributed to the radial penetration of solution from inside to the outside of the G-1 gasket, as evidenced by the observed increase in weight. Conversely, for the G-2 gasket, which has a metal insert, water penetration was reduced, leading to corrosion primarily advancing in the depth of the sample. In the case of the PTFE gasket, characterized by its hydrophobic nature (Dhanumalayan & Joshi, 2018), water penetration was negligible, resulting in corrosion predominantly progressing within the depth of the sample plate. Figure 5.11 illustrates that the corrosion site near the gasket boundary acts as a pathway for the solution to diffuse into the crevice created at the interface of the gasket and specimen plate.

5.5.3 Mechanism of the corrosion

The mechanism of crevice corrosion in BFJs can be described as follows:

1) Crevice corrosion is significantly influenced by the occluded geometry of the crevice, restricting the mass transport of species into and out of the occluded region. In BFJs, the crevice is formed near the gasket inside diameter due to stagnation of the solution at the gap between the two flanges. Figure 5.14 (a) and (c) present a schematic representation of the occluded solution in the gap in a BFJ with a gasket. According to the critical crevice solution theory (Costa et al., 2023; Kennell et al., 2008), the solution becomes acidified due to the depletion of oxygen (O_2) in the gap.

2) The reaction of metallic ions with chloride ions (Cl^-) occurs, followed by the subsequent hydrolysis of metal chloride in water. This hydrolysis produces hydrochloric acid (HCl), reducing the pH in the gap to 2 (Nishimoto et al., 2016b). The acidified solution then corrodes the 321 SS plate near the gasket, as shown in Figure 5.14 (b) and (d). Subsequently, the acidified solution diffuses to the area between the gasket and the 321 SS specimen plate, leading to leakage over longer exposure times. For the 321 SS flange used with the G-1 gasket, the solution radially penetrates and causes a larger area of corrosion on the surface of the flange.

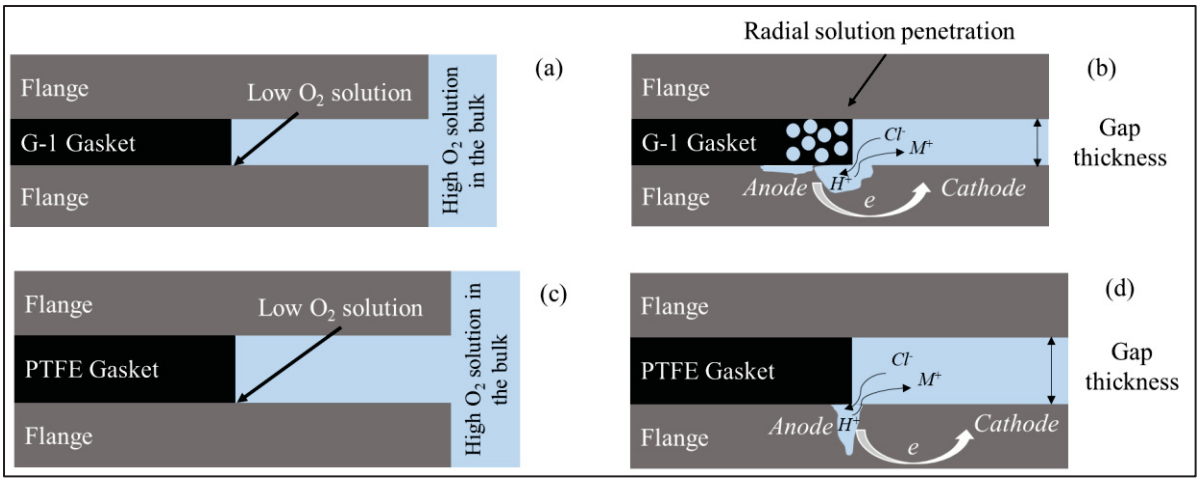

Figure 5.14 Schematic overview of the mechanism of crevice corrosion in BFJs: a) a flanged joint with a G-1 gasket at the initial time of exposure; b) a flanged joint with a G-1 gasket after crevice corrosion initiation; c) a flanged joint with a PTFE gasket at the initial time of exposure; d) a flanged joint with a PTFE gasket after crevice corrosion initiation

5.6 Conclusion

The comparison of polarization results, surface analysis, as well as gasket geometry and weight characterization revealed that:

- Two factors significantly influence corrosion at the interface of the flange and gasket: the size of the gap between the two flange surfaces and solution penetration into the gasket. These factors contribute to increased susceptibility to corrosion in joints used with graphite gasket materials compared to the PTFE gasket materials.
- Additionally, among the two graphite gaskets, the graphite sheet gasket (G-1) exhibits greater susceptibility to crevice corrosion than the graphite gasket with a metal insert (G-2) due to the formation of tighter gaps and a larger amount of solution absorption in the gasket structure.
- A larger corrosion area on the surface of the flange between the gasket and flange for the flange samples is obtained with the G-1 gasket causing corrosion propagation through the surface that eventually leads to early leakage comparatively with other gaskets.

- The corrosion propagation for the PTFE gasket was mainly through the depth of the flange near the gasket inside diameter; and therefore, would take more time for leakage to occur.

Acknowledgments

This work was supported by the Natural Sciences and Engineering Research Council of Canada (NSERC) under the Discovery Grant (RGPIN-2019-05973 and RGPIN-2021-03780).

CHAPTER 6

EFFECT OF GAP SIZE ON FLANGE FACE CORROSION

Soroosh Hakimian [a], Abdel-Hakim Bouzid [a], Lucas A. Hof [a]

[a] Mechanical Engineering Department, École de technologie supérieure, 1100, rue Notre-Dame Ouest, Montreal, Québec, H3C 1K3, Canada

Paper published in: *Materials and Corrosion*, April 2024.
https://doi.org/10.1002/maco.202414367

Abstract

Bolted flanged joints play a critical role in offshore wind turbine tower structures, serving as integral components that connect various sections of the tower. This research study employs electrochemical techniques to investigate the effect of gap dimensions, which determine the crevice gap thickness and crevice depth, on corrosion behavior of 321 stainless steel flange sample plates in a 3.5 wt% NaCl solution at 50°C. Gaskets are used in this study to create gaps between two flange surfaces. A novel fixture is utilized to simulate the applied stress on the gasket, fluid flow within the fixture, and the geometric aspects of the gasket and flange. The findings reveal that increasing the gap thickness from 1.58 to 6.35 mm results in a rise in the general corrosion rate of the flange surface from 0.09 to 1.03 mm y^{-1}, and crevice corrosion initiation time increases from 0.23 to 3.12 h. Furthermore, reducing the crevice depth (d) from 7.49 to 0 mm leads to a decrease in the general corrosion rate from 0.09 mm y^{-1} to 0.04 µm y^{-1}, and cases with d = 3.81 and d = 0 mm show no observable crevice corrosion after potentiostatic tests.

6.1 Introduction

Bolted flanged joints are a type of connection in which two flanges are tightened together with bolts, and may include a gasket compressed between them to provide sealing (Nelson et al., 2023). These joints are commonly used in various industrial applications, such as offshore

wind turbines (OWT), pressure vessels, and pipeline systems and other industries for the purpose of connecting sections (S. Z. Li et al., 2023; Nechache & Bouzid, 2007). OWTs are generally composed of three primary components: the tower, transition piece (TP), and foundation. The main application of bolted flanged joints in OWTs is for connecting the different tower segments (Weijtjens et al., 2020). These joints are vulnerable to fatigue corrosion in marine environments due to the combination of strong wind-wave loads, and high corrosivity. It is well established that, a direct correlation between corrosion and fatigue failure exists, as corrosion accelerates the initiation and propagation of fatigue cracks (Lachowicz & Lachowicz, 2021). The corrosion of bolts in bolted flanged joints has been the subject of a lot of studies in offshore wind turbine towers (Zhang et al., 2024). However, the initiation and propagation of corrosion at the interface of flanges remain a research gap in the field of corrosion of bolted flanged joints. Gaskets are widely used in bolted flanged connections to provide a tight seal by filling the leak paths and compensating for the unevenness and roughness on the flange surfaces (Mehmanparast et al., 2020). According to reported failure cases in the literature, crevice corrosion initiates on the flange faces due to the presence of occluded areas at the interface of the flange and gaskets (Hakimian et al., 2024b). Identifying corrosion at the flange interface prior to failure is a challenging task. Neglecting this detection may lead to potentially costly consequences (Bond et al., 2018). Gaps and crevices between flanges, arising from raised faces or the presence of the gasket, joint loosening due to creep-relaxation (A. Bouzid et al., 1995; Nechache & Bouzid, 2007, 2008), rotation on the flange (Bouzid A.; Chaaban A.; Bazergui A., 1994; A. H. Bouzid et al., 2004), and waviness and misalignment (Worden, 2014a), represent potential sites for crevice corrosion.

Crevice corrosion is a common failure mode observed in corrosion resistant alloys (CRAs) and is considered more hazardous than pitting corrosion as it occurs in occluded regions, that are generally inaccessible and invisible. Critical factors influencing crevice corrosion include environmental factors, such as pH, temperature, and chloride concentration, the chemical composition and microstructure of the metal, and crevice geometry. While most studies on crevice corrosion focus on the impact of pH, temperature, chloride concentration, and alloying compositions, only a few papers consider the effect of crevice geometry on crevice corrosion (Costa et al., 2023; Hu et al., 2011a). Additionally, the studied sizes of crevice geometries do

not align with the actual sizes present in real-world engineering structures. Crevice geometry encompasses factors such as crevice gap thickness, depth, and the surface electrode ratio of inside to outside of the crevice, that significantly influence reactions within the crevice, including the concentration of oxygen, H^+, and Cl^- (Luo et al., 2022; Shojaei et al., 2019).
Hence, this paper aims to utilize a fixture developed by the authors (Hakimian et al., 2024a) for investigating the impact of the gasket geometry on crevice corrosion in bolted flanged joints. The fixture simulates real crevice geometry conditions by applying a range of compression loads similar to those in actual bolted joints in wind turbine and pipeline applications. It also allows the use of gaskets in accordance with ASME B16.5. Flange and gasket sizes and materials are selected based on the most commonly used in bolted flanged joints applications. In addition, the fixture is a sealed container to facilitate the study of corrosion in the presence of fluid flow in a closed loop to mimic an operation of a bolted flanged joint in a piping system. Electrochemical techniques, including cyclic potentiodynamic polarization (CPP), electrochemical impedance spectroscopy (EIS), and potentiostatic tests, are employed to examine the influence of flange and gasket geometry on the initiation and propagation of crevice corrosion.

6.2 Materials and method

6.2.1 Test fixture

The test fixture is the central part of the experimental setup and is representative of a bolted flange joint. Indeed, this is where the flange platens and gasket are located and wetted by the fluid to allow for corrosion to take place. The Corrosion Quantification Test (COQT) fixture is designed to mimic an ASME B16.5, NPS 2 class 150 gasket according to ASME B16.21 dimensions bolted flanged joint as done with the successful Aged Relaxation Leakage Adhesion (ARLA) device (Marchand, Bazergui, et al., 1992b; Marchand, Derenne, et al., 1992b) used to measure weight loss, load retention, gasket relaxation and leakage tightness after aging a sheet gasket material in an oven. Figure 6.1 shows the COQT test fixture that can assess and quantify corrosion of the flange and gasket material pairs. This figure shows the

different parts of the fixture. The central stud allows the application of the compressive load on the gasket through the circular compression plates using a hydraulic tensioner. The compression plates have slots to measure the variation of gasket thickness before and after the corrosion tests by a caliper. In addition, the compression plates have entrance and exit ports for the circulation of the electrolyte. The used flange plates can easily be changed to new ones after each test in order to study the influence of the different experimental parameters and service conditions. The electrical insulator provides electrical insulation between the sample plates and the compression plates in order to accurately measure corrosion of the sample plates and avoid corrosion of the rest of the fixture. A plain washer is used to increase the contact area between the compression plate and the Belleville washer. The Belleville washers are useful to maintain the preload in the assembly and adjust the stiffness of the bolt joint if needed, which is an important parameter when considering relaxation. The load ring or spacer provides a robust contact interface for the Belleville washers. The O-rings prevent electrical contact of the stud with the plates and provide a seal to the outside boundary. The plain washer is used to increase the contact area between the compression plates and the nuts. The volume of the inside chamber is 20 mL. The gaskets sizes are within an internal diameter (ID) of 1.31 inches and an outer diameter (OD) of 2.95 inches with thicknesses ranging from 1/16” to 1/4”. A full Wheatstone strain gauge bridge is installed on the central stud (transducer in mV) to measure the force of the central stud. This force measurement can subsequently be converted into the average gasket contact stress by simply dividing the force by the gasket area.

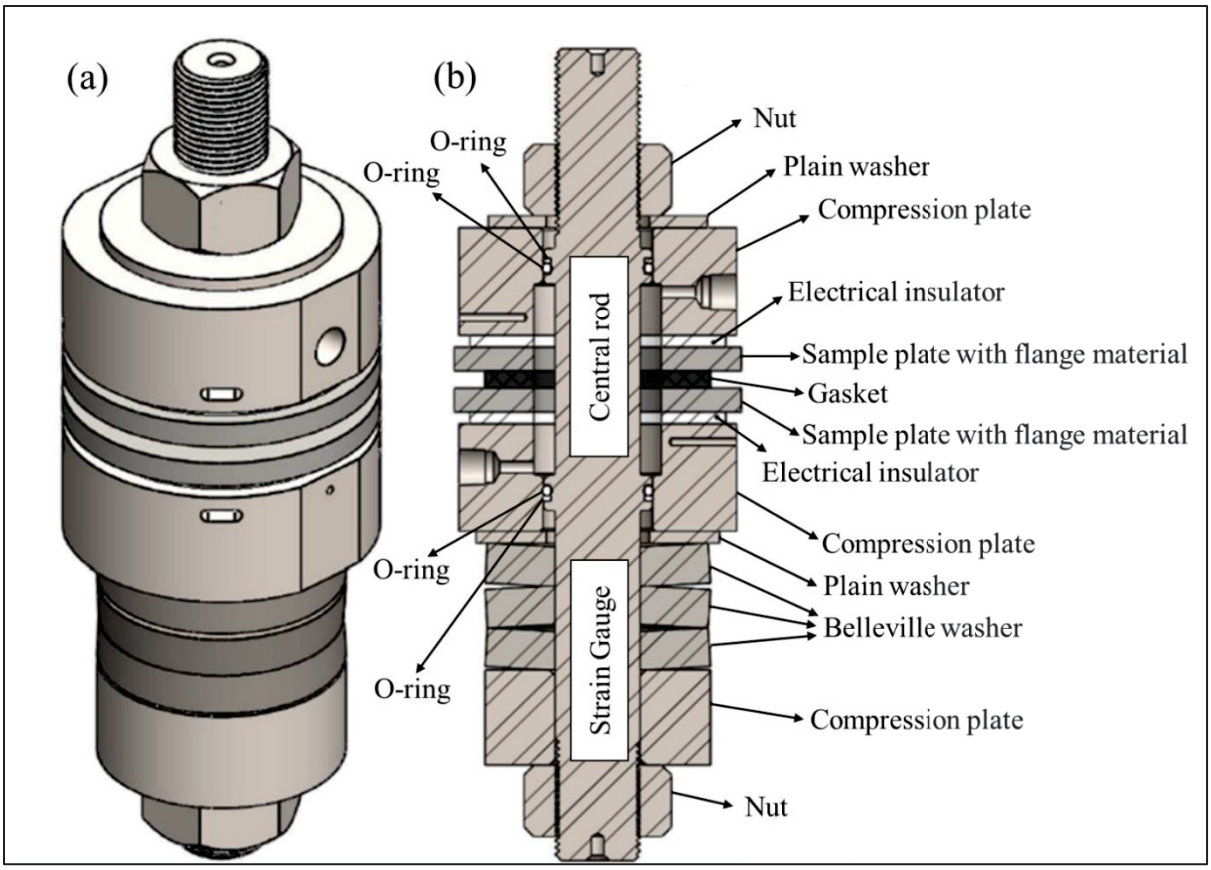

Figure 6.1 Test fixture (a) 3D view (b) cross section view and labelling of each item Hakimian et al. (2024a)

6.2.2 Test rig

The COQT fixture is part of the test rig shown in Figure 6.2. It is connected to a tubing circuit of the electrolyte that has different equipment and instrumentation. The multiparameter meter (ThermoFisher STARA2150 series) simultaneously measures the pH, conductivity, and temperature of the electrolyte through the conductivity electrode and pH electrode. The water-jacketed glass cell is a type of apparatus used to control and maintain the temperature (± 0.1 ^{o}C) of the test solution. The glass cell is surrounded by a jacket filled with water. This water jacket acts as a temperature buffer and helps maintain a stable temperature within the cell. The peristaltic pump (BRL Life Technologies CP-600) provides continuous solution flow from the water-jacketed glass cell to the test fixture. The flow sensor and pressure transducer continuously monitor the flow and pressure of the solution. The three-electrode cell used for

electrochemical measurements, include the sample flange plates (321 SS) as a working electrode (W.E.), a saturated Ag/AgCl as a reference electrode (R.E.), and the 316L SS central stud as a counter electrode (C.E.). All measured potentials are done with respect to the Ag/AgCl electrode. An Autolab potentio/galvanostat, PGSTAT302N-High Performance, is used to produce the polarization curves for the discussed potential ranges. Nova software version 2.1.7 is used for analyzing electrochemical data. A salt bridge is used as a connection between the solution in the test fixture and the reference electrode to minimize the ohmic drop contribution between the reference and working electrodes. As indicated in Figure 6.2, the solution flows in and out from the bottom to the top of the fixture; hence, all the inner parts including the gasket and the metallic sample plates are soaked with the solution.

The analogue signals from the sensors are transmitted to the printed circuit board (PCB) and converted to numerical values by a National Instruments Data Acquisition Card (DAQ). The DAQ, potentiostat, and multiparameter meter are connected directly to the computer through a USB connection. The heated circulating bath system circulates water within the jacket of the glass cell and controls the temperature through a heating or cooling system.

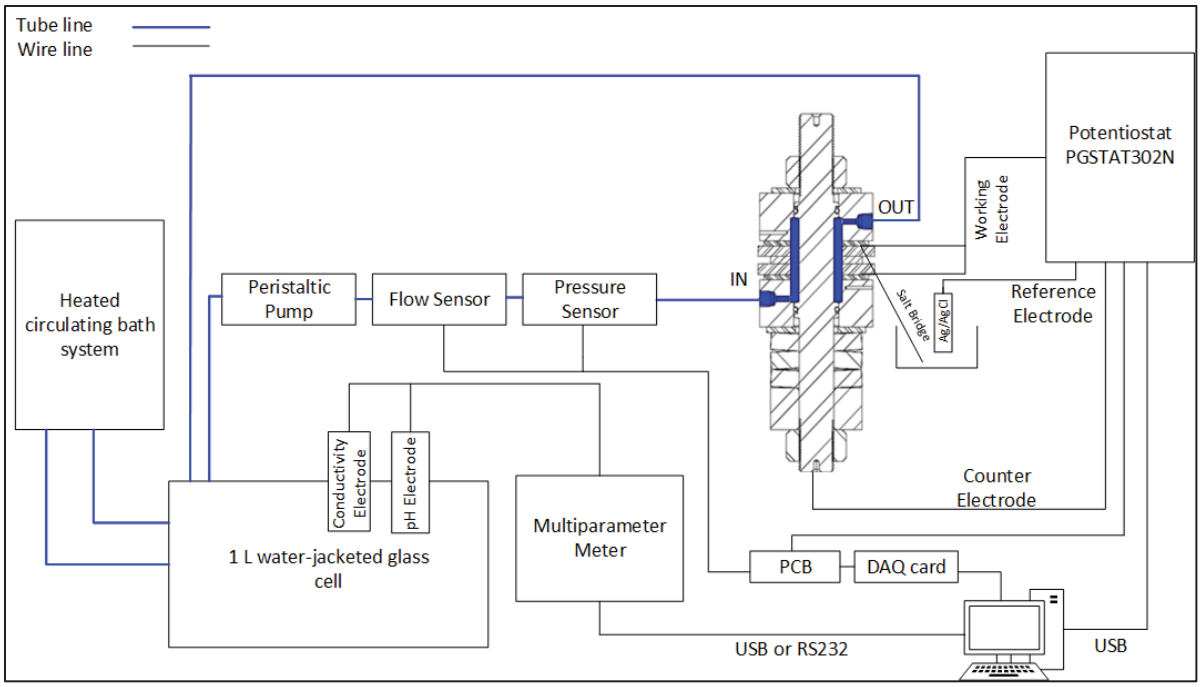

Figure 6.2 Schematic of the test rig including: pH and conductivity meter; pH electrode; conductivity electrode; thermostatic water bath; peristaltic pump; flow sensor; pressure sensor; working electrode connection; counter electrode connection; reference electrode; salt bridge; PCB; DAQ card; PC
Adapted from Hakimian et al. (2024a)

6.2.3 Materials

The sample plates have an outer diameter (OD) of 2.95 inches (74.93 mm), an inner diameter (ID) of 1.31 inches (33.27 mm), and a thickness of 0.25 inches (6.35 mm) (as shown in Figure 6.3 (a)). The material of the sample plate is 321 stainless steel (SS), with a chemical composition according to the ASTM A182 standard specification for SS flanges. The chemical composition is provided in Table 6.1. Virgin polytetrafluoroethylene (PTFE) gaskets of various sizes are used between the sample plates, following to the specifications of ASME B16.21 for nonmetallic flat gaskets used in flanges. This approach is aimed at investigating the influence of gasket sizes (thickness and ID) on the corrosion behavior of flange faces by creating different crevice gap thickness and crevice depth. The exposed area to the solution on the flange sample plate is determined by the gasket ID used between two sample plates, illustrated in Figure 6.3 (b).

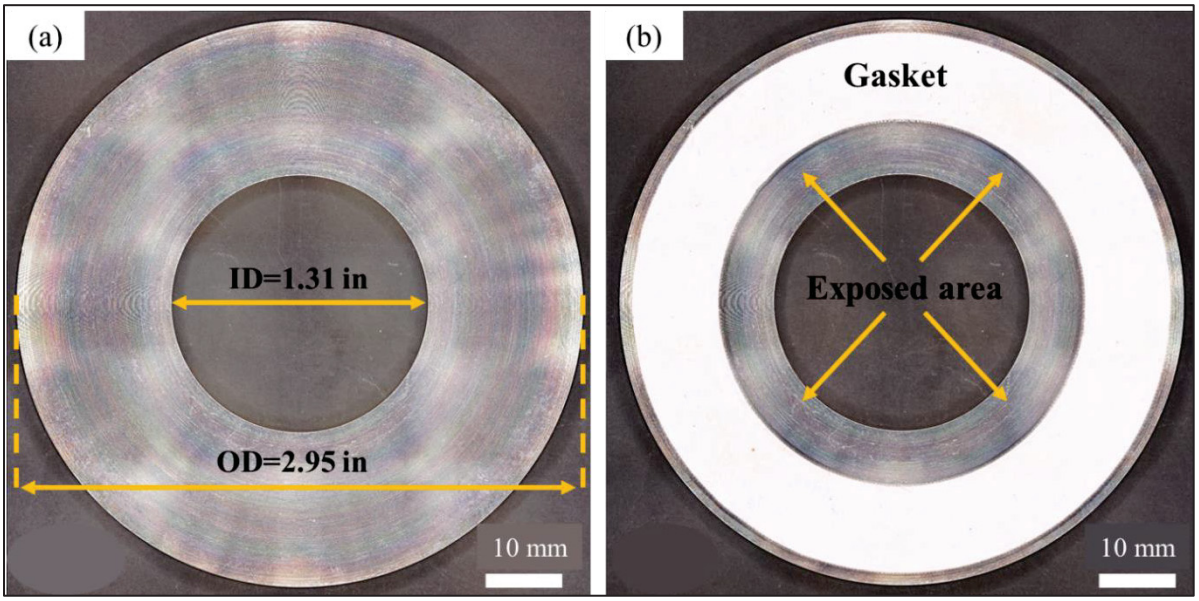

Figure 6.3 The sample plate used in the joint; (a) inner and outer diameter of the sample plate; (b) the exposed surface area to the solution for the gasket with the ID of 48.26 mm

Table 6.1 Chemical composition of 321 SS sample plate (wt.%)

C	N	Si	P	S	Cr	Mn	Ni	Mo	Cu	Ti
0.049	0.024	0.54	0.03	0.001	17.45	1.57	9	0.37	0.48	0.53

Equation (6.1) presents the relation for calculating the exposed surface area on the flange face. In this equation, ID_g represents the gasket ID in cm, and ID_f denotes the flange ID in cm.

$$Exposed\ surface\ area\ on\ the\ flange\ face = (ID_g^2 - ID_f^2) \times \frac{\pi}{4} \qquad (6.1)$$

This study employs gasket thicknesses as typically utilized in bolted flange joints: 1/16 inches (1.58 mm), 1/8 inches (3.17 mm), and 1/4 inches (6.35 mm). The gasket IDs are chosen based on the gasket groups specified in the ASME B16.21 standard. Two types of gaskets are considered: the first type, known as a full-face gasket that, covers the entire flange face. In the second type, the gasket ID equals the outer diameter of the pipe, implying that the exposed area on the flange face is equivalent to the pipe thickness. Pipe schedule describes the wall thickness of a pipe, with common schedule number being 40. According to ASME B36, the

thickness for pipes with schedules 40 and nominal pipe size of 2 and 8 is 0.15 inches (3.81 mm) and 0.3 inches (7.49 mm), respectively. Consequently, three distinct values for the gasket ID are selected: 1.31 inches (33.27 mm), 1.61 inches (40.89 mm), and 1.91 inches (48.26 mm). When considering gasket sizes in this study, two variables are defined: gasket thickness or crevice gap thickness, denoted by g, representing the gap between two flange sample plates; and the distance d between the flange ID and the gasket ID (crevice depth), obtained from Equation (6.2). Here, ID_g and ID_f represent the gasket ID and the flange ID in mm, respectively.

$$d = (ID_g - ID_f) \div 2 \tag{6.2}$$

The configuration of the flange and gasket is depicted in Figure 6.4. Figure 6.4 (a) presents the cross-section of an actual bolted flanged joint with a full-face gasket that entirely covers the flange face, and it identifies all the components of a bolted flanged joint. Figure 6.4 (b) and (c) illustrate bolted flanged joints with gaskets having IDs larger than the flange ID, with the variables d and g represented by yellow arrows. Figure 6.4 (d), (e), and (f) demonstrate how the configuration of the flange sample plate and gasket in the experiments of this study replicates the actual flange and gasket configuration in real world bolted flanged gasketed joints.

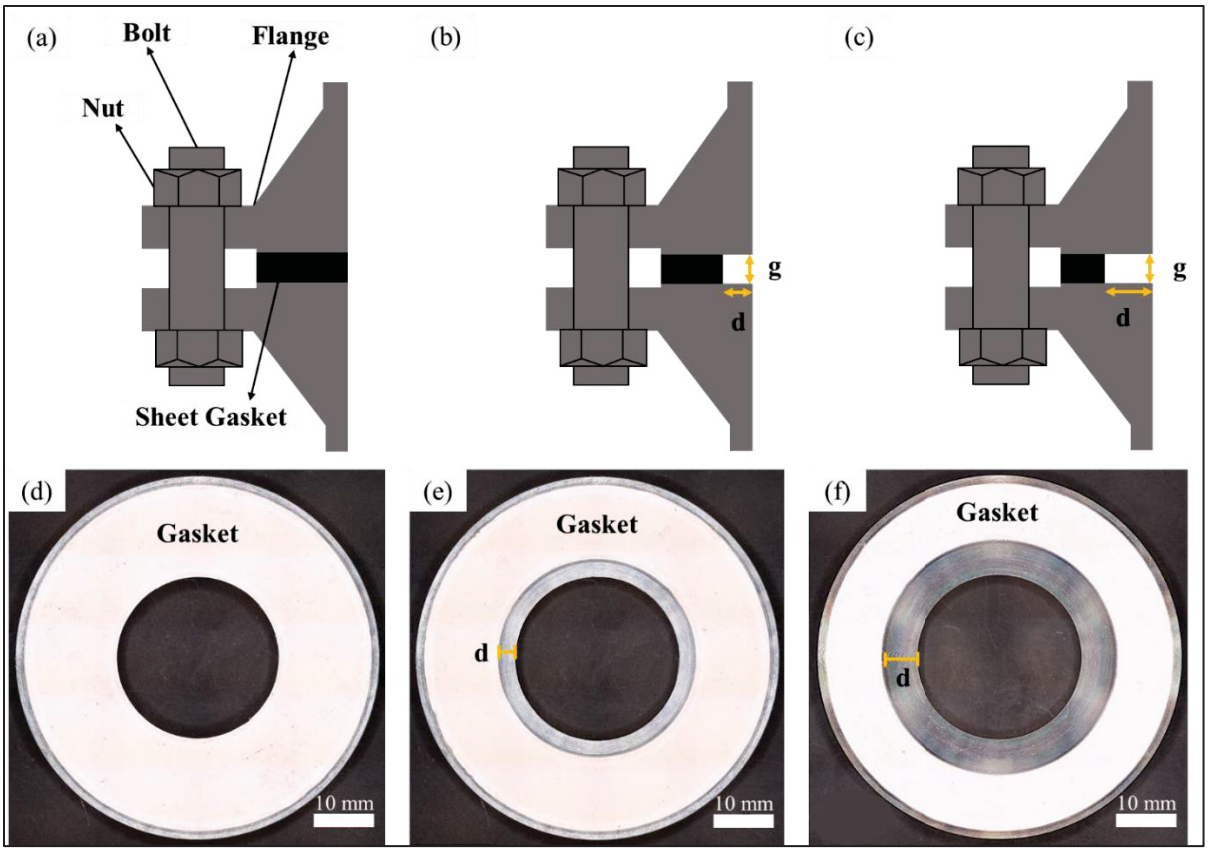

Figure 6.4 Configuration of the flange and gasket in a real bolted flanged gasketed joint: (a) schematic cross-section illustrating the bolted flanged joint with a full-face gasket, including component identification; (b) schematic cross-section of the bolted flanged joint with a gasket featuring an ID of 36.05 mm, with yellow arrows indicating variables *d* and g; (c) schematic cross-section of the bolted flanged joint with a gasket having an ID of 48.26 mm, with yellow arrows indicating variables *d* and g; (d) image depicting the sample plate and gasket with an ID of 33.27 mm; (e) image showing the sample plate and gasket with an ID of 36.05 mm; (f) image illustrating the sample plate and gasket with an ID of 48.26 mm

Concluding this section, Table 6.2 summarizes the dimensions of the gaskets utilized in this study, along with key variables, where *d* is crevice depth calculated using Equation (6.2), and *g* represents the crevice gap thickness measured with a caliper. Each configuration of gasket and flange sample plate is assigned a Gasket No. as an identifier, and this number will be used throughout the rest of the paper, as indicated in Table 6.2. For Gasket No. 5, both the exposed surface area on the flange face and the *d* value are zero, as the ID of the gasket matches the ID of the flange sample plate, in accordance with Equations (6.1) and (6.2).

Table 6.2 The dimensions of the gasket used in the joint for experiments

Gasket No.	Gap thickness/ *g* (mm)	ID (mm)	OD (mm)	Weight (g)	Depth/ *d* (mm)	Exposed surface area on the flange (cm^2)
1	1.58	48.26	71.12	9.25	7.49	9.73
2	3.17	48.26	71.12	19.28	7.49	9.73
3	6.35	48.26	71.12	38.95	7.49	9.73
4	1.58	40.89	71.12	11.37	3.81	4.38
5	1.58	33.27	71.12	13.51	0	-

6.2.4 Corrosion characterization

To understand the corrosion mechanism occurring on the surfaces of the flanges in bolted flanged joints, the current study employs electrochemical techniques and microscopic characterization methods. These techniques will be discussed in the following sections.

6.2.4.1 Electrochemical measurements

Before starting the electrochemical measurements, the fixture shown in Figure 6.1 is mounted on a stand equipped with a hydraulic tensioner to compress the gasket to an average initial stress of 15 MPa. The water jacketed glass cell is filled with a 3.5 wt.% NaCl solution (distilled water and analytical grade of NaCl) and the solution is heated to 50ºC. The peristaltic pump circulates the solution in the fixture with a flow rate of 90 mL/min. The sample plates are degreased by ethanol in ultrasonic for 20 minutes, and then air dried before electrochemical tests.

The EIS test is initiated 6 hours after the solution has been in circulation inside the fixture, allowing sufficient time for the surfaces of the samples and the interface between the gasket and sample plates to become wet and for the open circuit potential (OCP) to stabilize. This EIS

test is performed at the OCP over a frequency range of 10000 Hz to 0.01 Hz with a sinusoidal alternating amplitude of 50 mV.

The CPP is the most common technique for measuring critical crevice corrosion potentials. This method is outlined in ASTM G61 (ASTM International, 2018d), and it identifies the potential at which crevice corrosion initiates (E_{crev} or E_b), the repassivation potential (E_{rep}), and the corrosion potential (E_{corr}). The scan begins from -0.05 V vs. OCP and continues until the current reaches 5 mA, at which point it is reversed. The scan is discontinued when the potential reaches -0.05 V or the backward scan current density intersects the forward scan current density. For both forward and reverse scans, the scan rate equals 0.0167 mV/s. The exposed surface area of the 321 SS sample plates varies according to Table 6.2. In order to calculate the current density, the current values obtained from the polarization tests are divided by the corroded area obtained from microscopic characterization, as explained in section 6.2.4.2. To calculate the general corrosion rate (*CR*) of the 321 SS sample plates with different Gasket No., the obtained corrosion current densities (i_{corr}) from the CPP curves are used in Equation (6.3). This equation converts the corrosion current density to the corrosion rate (ASTM International, 2015b).

$$CR = K\frac{i_{corr}}{\rho}EW \tag{6.3}$$

Where CR represents the corrosion rate in mm/y, i_{corr} signifies the corrosion current density in μA/cm², ρ represents the density in g/cm³, and K is a constant equal to 3.27×10^{-3} mm. g/μA/cm/year. EW is the dimensionless equivalent weight and denotes the mass of metal oxidized by the passage of one Faraday (96,500 C) of electric charge. The values of EW and ρ for 321 SS are provided in ASTM G102 and ASTM G1 (ASTM International, 2015b, 2017c), and they are defined as 25.13 and 7.94 g/cm³, respectively.

Crevice corrosion initiation and propagation are assessed in a 3.5 wt.% NaCl solution at 50°C through potentiostatic polarization using the same rig and fixture as the one for cyclic potentiodynamic polarization. The hold potential is determined prior to the transpassive dissolution of 321 SS or the potential leading to active metal dissolution. This potential is chosen based on the CPP curves, and the selected potential is 0.15 V.

6.2.4.2 Surface characterization

The corroded area of each flange sample plate is measured after CPP and potentiostatic polarization. The images of the corroded area are obtained using a Keyence VHX-7000 digital microscope. Then the area of the corroded surface is measured by ImageJ software (Schindelin et al., 2012). The entire corroded surface area (A_c) is calculated using Equation (6.4).

$$A_c = \sum_i^n A_{c,i} \tag{6.4}$$

Where $A_{c,i}$ represents the corroded area in region i, and n stands for the number of observed corroded areas on the sample plate surface. The morphology of the corroded surface on the flange face is examined by scanning electron microscopy (SEM).

6.3 Results

The results section is divided into four parts: (1) CPP curves, (2) crevice corrosion initiation and propagation, (3) general corrosion resistance, and (4) corrosion morphology. All of these results are obtained under the same testing conditions, including temperature, fluid flow rate, and average gasket contact stress, as mentioned in section 6.2.4.1.

6.3.1 CPP curves

The polarization curves, depicted in Figure 6.5, illustrate the corrosion potential (E_{corr}) and breakdown potential (E_b) used for assessing the corrosion behavior of the sample plates. The corrosion potential represents the potential of the working electrode (sample plate) against the reference electrode when no potential or current is applied to the working electrode. This parameter serves as a thermodynamic indicator, reflecting the tendency of the working electrode to undergo corrosion reactions under specific conditions. The E_b is characterized by a significant and rapid increase in current density. A higher positive E_b, achieved at a constant

scan rate in the polarization curve, suggests a reduced susceptibility of the sample plate to the initiation of localized corrosion, such as crevice or pitting corrosion (B. Cai et al., 2010; Costa et al., 2023).

The potential difference $|E_{corr} - E_b|$ signifies the inclination towards localized corrosion, with higher values indicating a diminished tendency (Vasilescu et al., 2009). Due to the simultaneous passivation in the anodic branch of the polarization curves, the anodic Tafel region is not well-defined. Therefore, to determine the general corrosion rate of the flange sample plates, the i_{corr} is calculated by intersecting the extrapolation of the cathodic branch at E_{corr} (Salleh et al., 2015). Table 6.3 provides an overview of the key electrochemical parameters derived from the polarization curves in Figure 6.5. The polarization curves presented in Figure 6.5 (a), (b), (c), (d), and (e) all demonstrate positive hysteresis in the CPP curve, where the reverse scan current density surpasses that of the forward scan. This positive hysteresis serves as an indicator of the initiation of localized corrosion (Liu et al., 2024). Notably, in Figure 6.5 (c), the backward scan intersects with the forward scan, indicating repassivation at that specific potential, also known as E_{rep} (Esmailzadeh et al., 2018). The more positive the E_{rep}, the less likely localized corrosion occurs (ASTM International, 2018d). It is essential to highlight that E_{rep} has a potential higher than E_{corr} for the sample plate used with Gasket No. 3, signifying that at E_{corr}, localized corrosion does not occur. Localized corrosion occurs if the corrosion potential of a metal in a given environment exceeds the E_{rep} (He et al., 2007). The E_{corr} values are -0.01, 0.05, -0.15, -0.05, and -0.06 V for the tests with Gasket No. of 1, 2, 3, 4, and 5, respectively. The E_b values are 0.17, 0.18, -0.03, 0.13, and 0.17 V for test with Gasket No. of 1, 2, 3, 4, and 5, respectively. Among the $|E_{corr} - E_b|$ values, the highest value is observed for the tests with Gasket No. 5, which was found to be 0.23 V. The remaining values are ranked in the following order: Gasket No. 1 and 4, both of which are 0.18 V; Gasket No. 2, which is 0.13 V; and Gasket No.3, which is 0.12 V. The corrosion rates for tests with Gasket No. 1, Gasket No. 2, and Gasket No. 3 are 0.09 mm. y^{-1}, 0.4 mm. y^{-1}, and 1.03 mm. y^{-1}, respectively. These results suggest that as the gap thickness increases, the corrosion rate also increases. Conversely, for the test with Gasket No. 4, the corrosion rate is 0.03 mm. y^{-1}, and for the test with Gasket No. 5, it is 4.17e-04 mm. y^{-1}, indicating a decrease in corrosion rate with a reduction in the *d* (crevice depth) value.

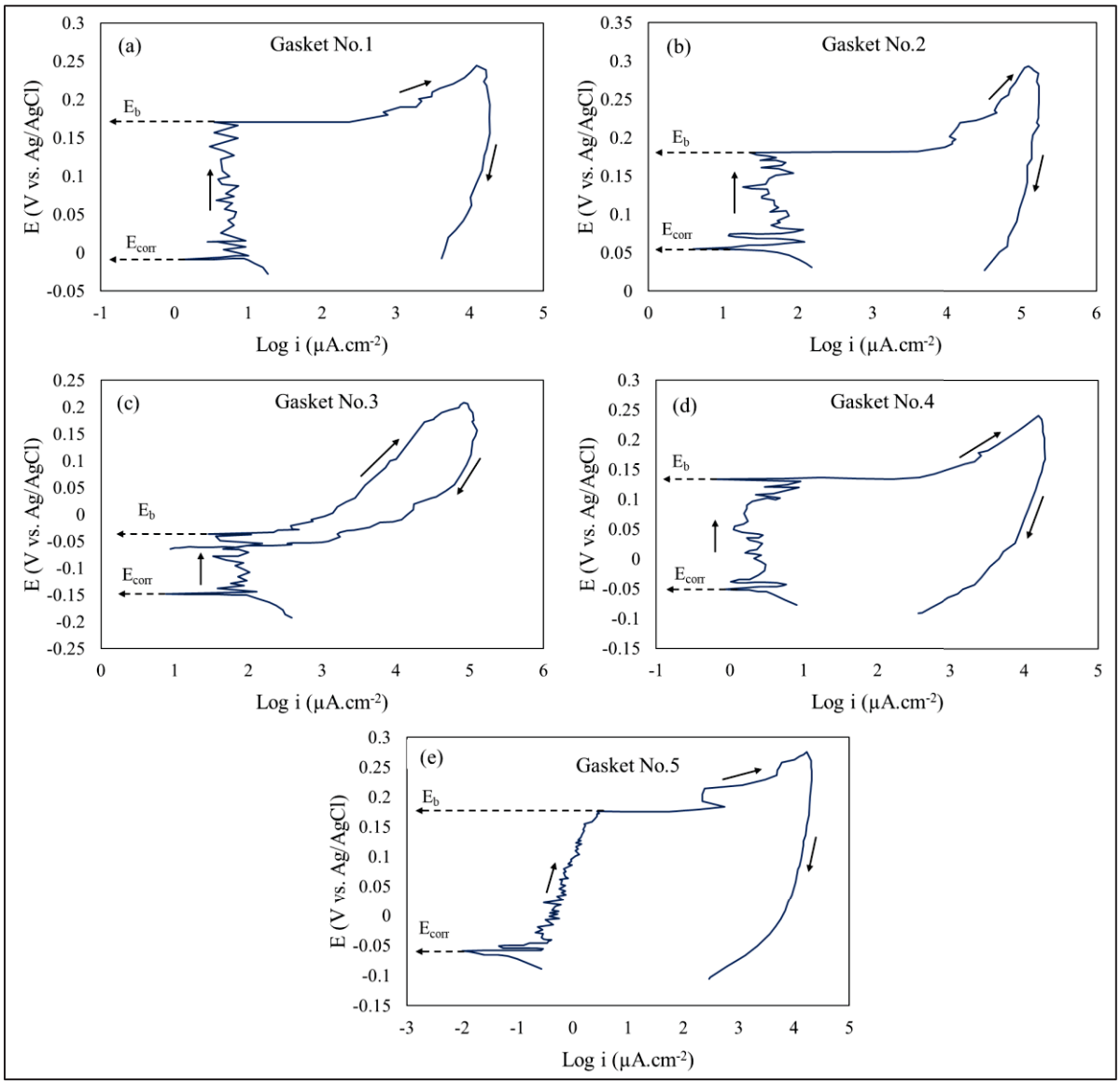

Figure 6.5 Cyclic potentiodynamic polarization curves of 321 SS sample plates in 3.5 wt.% NaCl in 50°C for tests with different gasket sizes; (a) Gasket No. 1; (b) Gasket No. 2; (c) Gasket No. 3; (d) Gasket No. 4; (c) Gasket No. 5

Table 6.3 Electrochemical parameters obtained from the CPP curves

Gasket No.	**E_{corr} (V)**	**E_b (V)**	**$\lvert E_{corr} - E_b \rvert$ (V)**	**i_{corr} ($\mu A.cm^{-2}$)**	**Corrosion rate ($mm.y^{-1}$)**
1	-0.01	0.17	0.18	9.33	0.09

Gasket No.	E_{corr} (V)	E_b (V)	$\lvert E_{corr} - E_b \rvert$ (V)	i_{corr} ($\mu A.cm^{-2}$)	Corrosion rate ($mm.y^{-1}$)
2	0.05	0.18	0.13	38.71	0.4
3	-0.15	-0.03	0.12	99.6	1.03
4	-0.05	0.13	0.18	2.75	0.03
5	-0.06	0.17	0.23	0.04	4.17e-04

According to the polarization curves, at E_b, rapid and continuous increase of current is observed which is related to the localized corrosion. To study localized corrosion on the flange sample plates with different gasket sizes, the top view and microscopic images of the corroded samples are shown in Figure 6.6. As shown in Figure 6.6 (a) both crevice corrosion and pitting corrosion are occurred on the sample plate used with the Gasket No. 1. The magnified image of (a) is shown in Figure 6.6 (f), which shows that crevice corrosion significantly occurred in the interface of the gasket with the sample plate or the boundary between the area under the gasket and the area exposed to the solution. However, pitting corrosion occurred in the area exposed to the solution. For the sample plate with Gasket No. 2 (Figure 6.6 (b)), both crevice and pitting corrosion are observed on the flange sample plate; however, the magnified image (Figure 6.6 (g)) shows that the crevice corrosion area seems smaller than the crevice corrosion area on the sample plate used with Gasket No. 1. Figure 6.6 (c) indicates that only pitting corrosion occurred on the flange sample plate, and crevice corrosion is not observed in the interface of the flange and gasket. As shown in Figure 6.6 (h), stable pits are formed in the area exposed to the solution. On the flange sample plate with Gasket No. 4 (Figure 6.6 (d)), both pitting and crevice corrosion are observed on the corroded surface. The magnified image Figure 6.6 (i) shows that crevice corrosion occurred in the boundary of the area under the gasket and the exposed area to the solution. Figure 6.6 (e) reveals that for the sample plate used with Gasket No. 5, only crevice corrosion occurred on the flange surface, and the magnified image (Figure 6.6 (j)) verifies that crevice corrosion started on the flange surface from the interface of the flange and gasket both of which have the same ID.

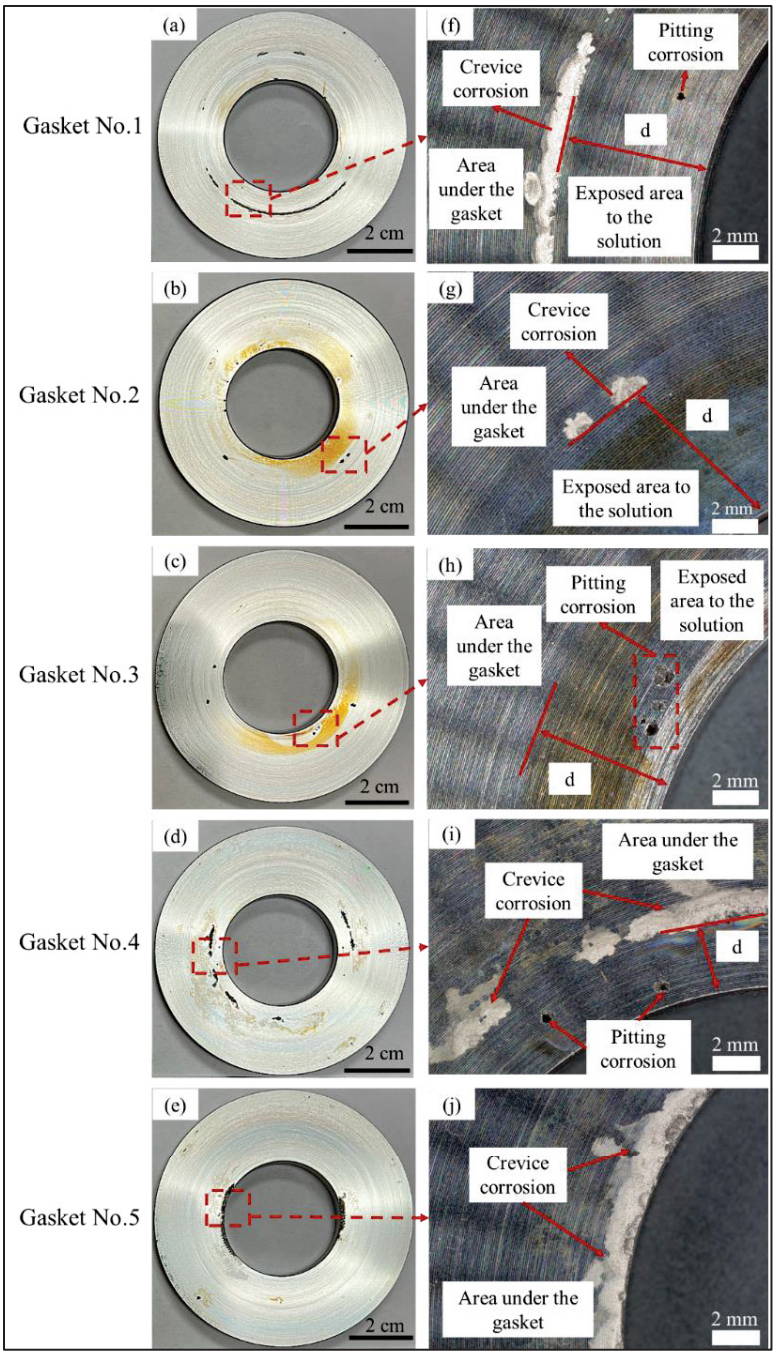

Figure 6.6 Corroded flange sample plates after CPP test: (a) Top view of the sample plate with Gasket No. 1; (b) top view of the sample plate with Gasket No. 2; (c) top view of the sample plate with Gasket No. 3; (d) top view of the sample plate with Gasket No. 4; (e) top view of the sample plate with Gasket No. 5; (f) Microscopic image of the corroded area for the sample plate Gasket No. 1; microscopic image of the corroded area for the sample plate with Gasket No. 2; microscopic image of the corroded area for the sample plate with Gasket No. 3; microscopic image of the corroded area for the sample plate Gasket No. 4; microscopic image of the corroded area for the sample plate with Gasket No. 5

To assess crevice and pitting corrosion on the flange sample plates, measurements of crevice corrosion area, maximum crevice depth, number of pits, maximum pit depth, and average pit depth are conducted using a Keyence digital microscope at 500X magnification, as reported in Table 6.4. The results indicate that increasing the gap thickness from 1.58 mm to 6.35 mm leads to a decrease in crevice corrosion area from 0.4 cm² to 0 cm². Furthermore, the average pit depth increases from 462.7 μm to 661.3 μm as the gap thickness increases. As *d* (crevice depth) decreases, both crevice corrosion area and average pit depth decrease. Conversely, the average pit depth decreases from 462.7 at d = 7.49 to 429.5 at d = 3.81 and becomes 0 at d = 0.

Table 6.4 Characteristics of crevice and pitting corrosion obtained through examination of the corroded surfaces

Gasket No.	Depth/ *d* (mm)	Gap thickness/g (mm)	Crevice corrosion area (cm^2)	Maximum Crevice depth	Number of pits	Maximum pit depth (μm)	Average pit depth (μm)
1	7.49	1.58	0.4	218.1	4	703.7	462.7
2	7.49	3.17	0.04	478.2	6	704.4	528.6
3	7.49	6.35	0	0	7	903.8	661.3
4	3.81	1.58	0.34	311.4	7	657.5	429.5
5	0	1.58	0.28	661.6	0	0	0

The information obtained from the CPP tests is presented in the graphs depicted in Figure 6.7. These graphs illustrate the variations of the passive potential range (Figure 6.7a), crevice corrosion area (Figure 6.7b), and average pit depth (Figure 6.7c) in relation to the gap volume. The gap volume is calculated using Equation (6.5), with the Gap volume in cm^3, Exposed surface area on the flange in cm^2, and the gap thickness in cm, as per the dimensions provided in Table 6.2.

$$Gap\ volume = Exposed\ surface\ area\ on\ the\ flange \times gap \qquad (6.5)$$

Figure 7 (a) reveals that the passive potential range ($|E_{corr} - E_b|$) decreases with an increase in gap volume. This decrease suggests a breakdown in the passive layer at lower potentials. As all the CPP tests in the forward scan continue until reaching a 5 mA current, samples with a lower passive range exhibit higher average pit depths (Figure 7 (c)). In the case of Gasket No. 5, which has the highest passive range, the resulting current after breakdown is only derived from the crevice corroded area (Figure 7 (b)). Conversely, in Gasket No. 3, the resulting current only originates from the pitting corrosion formed on the flange surface.

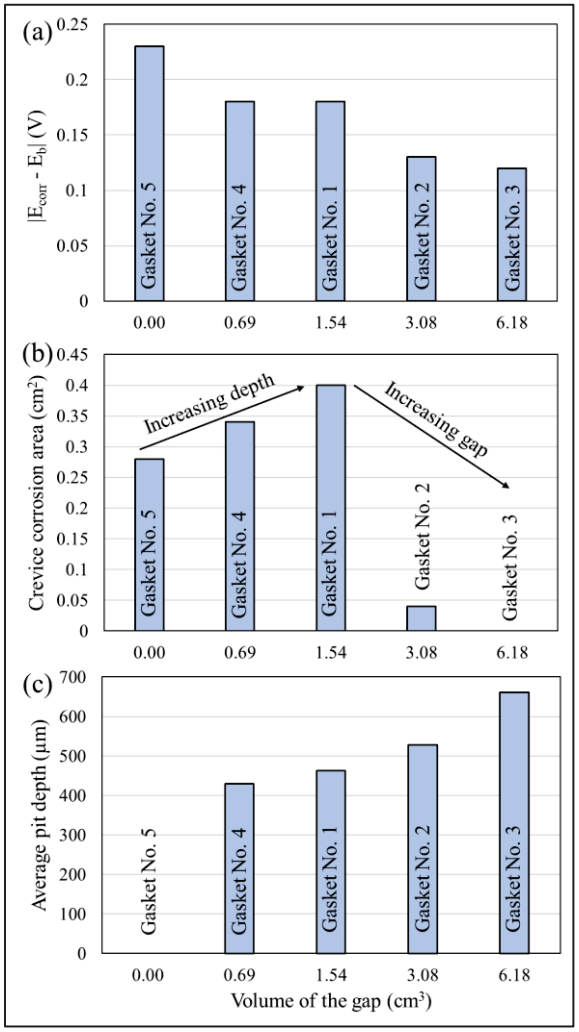

Figure 6.7 Variations in (a) potential range of passive region, (b) crevice corrosion area, and (c) average pit depth vs. volume of the gap

6.3.2 Crevice corrosion initiation and propagation

The potential for potentiostatic polarization is adjusted to fall within the passivation region, as indicated by the polarization curves in Figure 6.5. Figure 6.8 (a) illustrates potentiostatic polarization curves of 321 SS plates in a 3.5% NaCl solution using different gasket sizes over a 12-hour period. The information obtained from the potentiostatic curves is presented in Table 6.5. The crevice corrosion process is divided into two stages based on the polarization curve features, including incubation and propagation. The incubation time represents the duration required for the development of an acidic solution within the crevice. Subsequently, due to a sharp decrease in pH and an increase in Cl^- concentration, crevice corrosion propagates spontaneously (Nishimoto et al., 2016a). Table 6.5 represents data related to both initiation and propagation of crevice corrosion by reporting the initiation time (t_{ini}) and the maximum propagation current density (i_{max}). According to the obtained experimental results, the incubation time for crevice corrosion in the joint increases with an increase of the gap thickness (at a fixed value of d). The incubation time for the gasket with a thickness of 1.58 mm is 0.23 h, subsequently, it increases to 2.37 h with a gap thickness of 3.17 mm, and reaching a maximum of 3.12 h when using a gasket with a thickness of 6.35 mm in the joint. Crevice corrosion propagates with the maximum current density of 116.24 $mA.cm^{-2}$ in 12 hours when the gap thickness size is 1.58 mm. The maximum current density decreases to 77.15 and 18.03 $mA.cm^{-2}$ with an increase of the gap thickness to 3.17 mm and 6.35 mm, respectively. By decreasing *d* from 7.49 mm to 3.81 and 0 mm (at a fixed value of g), there is no significant increase in the current density observed in the potentiostatic curves. The maximum current density for $d = 3.81$ reaches 0.06 $mA.cm^{-2}$, and for $d = 0$, it is 1 $\mu A.cm^{-2}$. These results indicate that increasing the gap thickness leads to damage to the passive layer due to the erosive effect of the flowing solution from inside the fixture. This makes it less aggressive for crevice corrosion to occur. Conversely, reducing the crevice depth, as the gasket shields the flange surface from Cl^- ions and the erosive effect of the flowing solution, reveals a wider potential range for passivation.

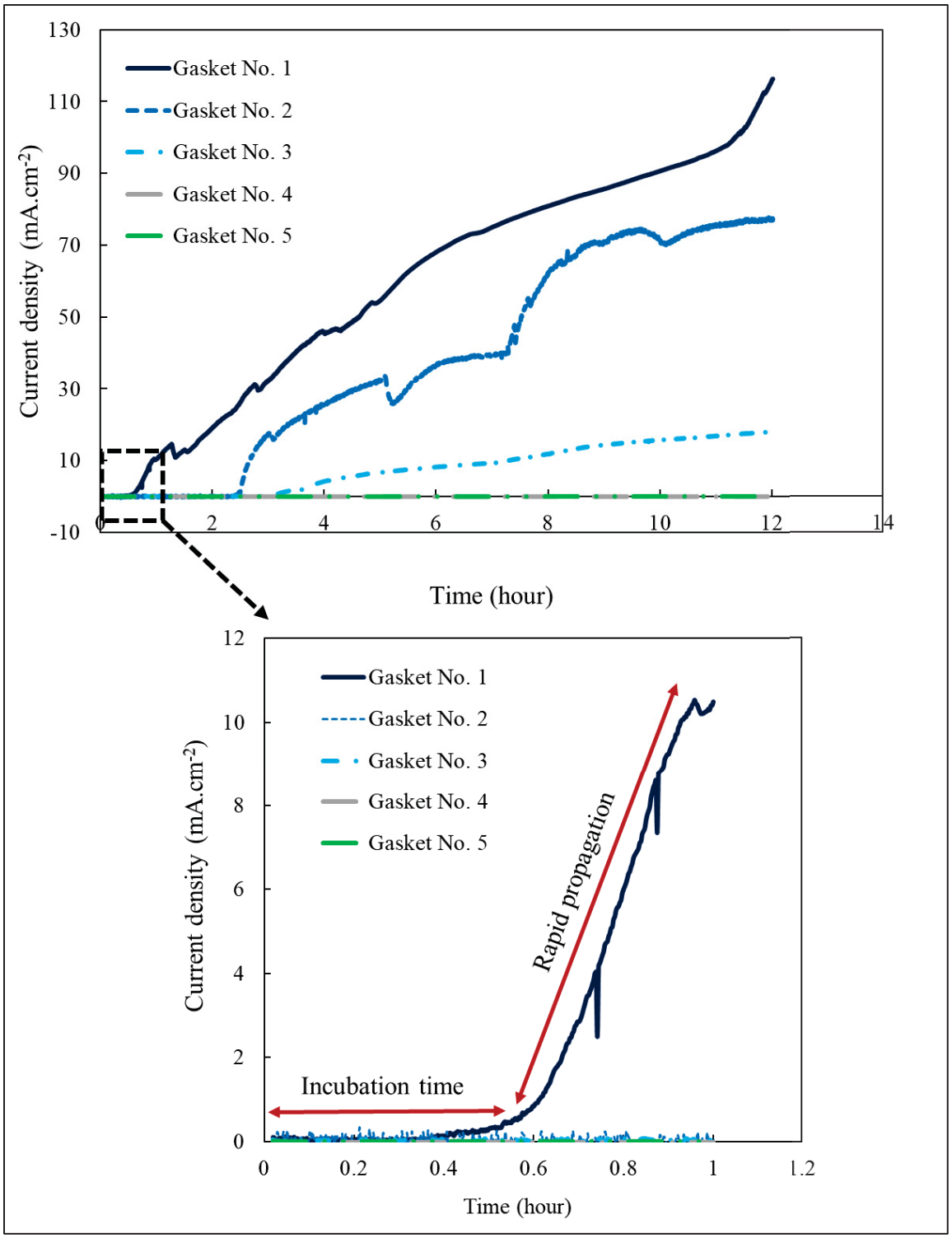

Figure 6.8 Current density vs. time curves for different gasket sizes in 3.5 wt.% NaCl solution in 50°C for 12 hours. The onset, depicted by the dotted line rectangle, magnifies the curve over 1hour of the potentiostatic test

Table 6.5 Crevice corrosion initiation time and the maximum current density obtained from the potentiostatic polarization test

Gasket No.	Gap thickness/ *g* (mm)	Depth/ *d* (mm)	t_{ini} (h)	i_{max} (mA.cm^{-2})
1	1.58	7.49	0.23	116.24
2	3.17	7.49	2.37	77.15
3	6.35	7.49	3.12	18.03
4	1.58	3.81	-	0.06
5	1.58	0	-	0.001

6.3.3 General corrosion resistance

To study the effect of gasket size on the general corrosion resistance of the 321 SS flange sample plates, EIS measurements are performed on the sample plates used with different gap thicknesses. In EIS analysis, only tests with the same exposed surface area are considered (Gasket No. 1, 2, 3). Figure 6.9 (a)-(c) show the EIS Nyquist and Bode plots for different gap thicknesses. It can be observed in the Nyquist plots (Figure 6.9 (a)) that all spectra exhibit an incomplete capacitive semi-circle, which implies a similar corrosion mechanism for various gap thicknesses. Two time constants are observed in the bode plots (Figure 6.9 (b)). Therefore, a two-time-constant electrical equivalent circuit (EEC) inside of Figure 6.9 (a) is used in the modeling procedure. In the EEC, R_s denotes the resistance of the solution (electrolyte), with the higher-frequency section of the spectrum linked to the behavior of the electrochemical double-layer capacitance (CPE_1) and charge-transfer resistance (R_1). Moving charged species through the passive oxide layer is a slow process, and the low-frequency responses are attributed to these slow processes, characterized by CPE_2 and R_2. Instead of using only a pure capacitance (C) in the fitting procedure, a frequency-dependent constant phase element, CPE (Ω^{-1} S^n cm^{-2}) with exponent n, is employed to achieve a more accurate alignment between theoretical and experimental data. Due to the surface inhomogeneity of the sample, a CPE is considered instead of C (Habibzadeh et al., 2014). EEC parameter values obtained by fitting of the experimental data in Figure 6.9, are presented in Table 6.6. Other than the defined

parameters, this table includes the total resistance values that are obtained from Equation (6.6). The R_{total} represents the corrosion resistance in kΩ.cm^2.

$$R_{total} = R_1 + R_2 \tag{6.6}$$

According to Table 6.6, the total corrosion resistance is 10725 kΩ.cm^2 when the gap thickness is 1.58 mm, and then it decreases to 482 kΩ.cm^2 by increasing the gap thickness to 3.17 mm, and it has the minimum value with a gap thickness of 6.35 mm, which demonstrates 293 kΩ.cm^2. The EIS analysis indicates that increasing the gap thickness between two flanges results in an decrease in R_{total}. Furthermore, it is observed that the value R_2 has a higher contribution compared to R_1. This observation suggests that the mass transfer of species (such as metal ions or oxygen-containing species) through the passive layer is slower as the gap thickness decreases.

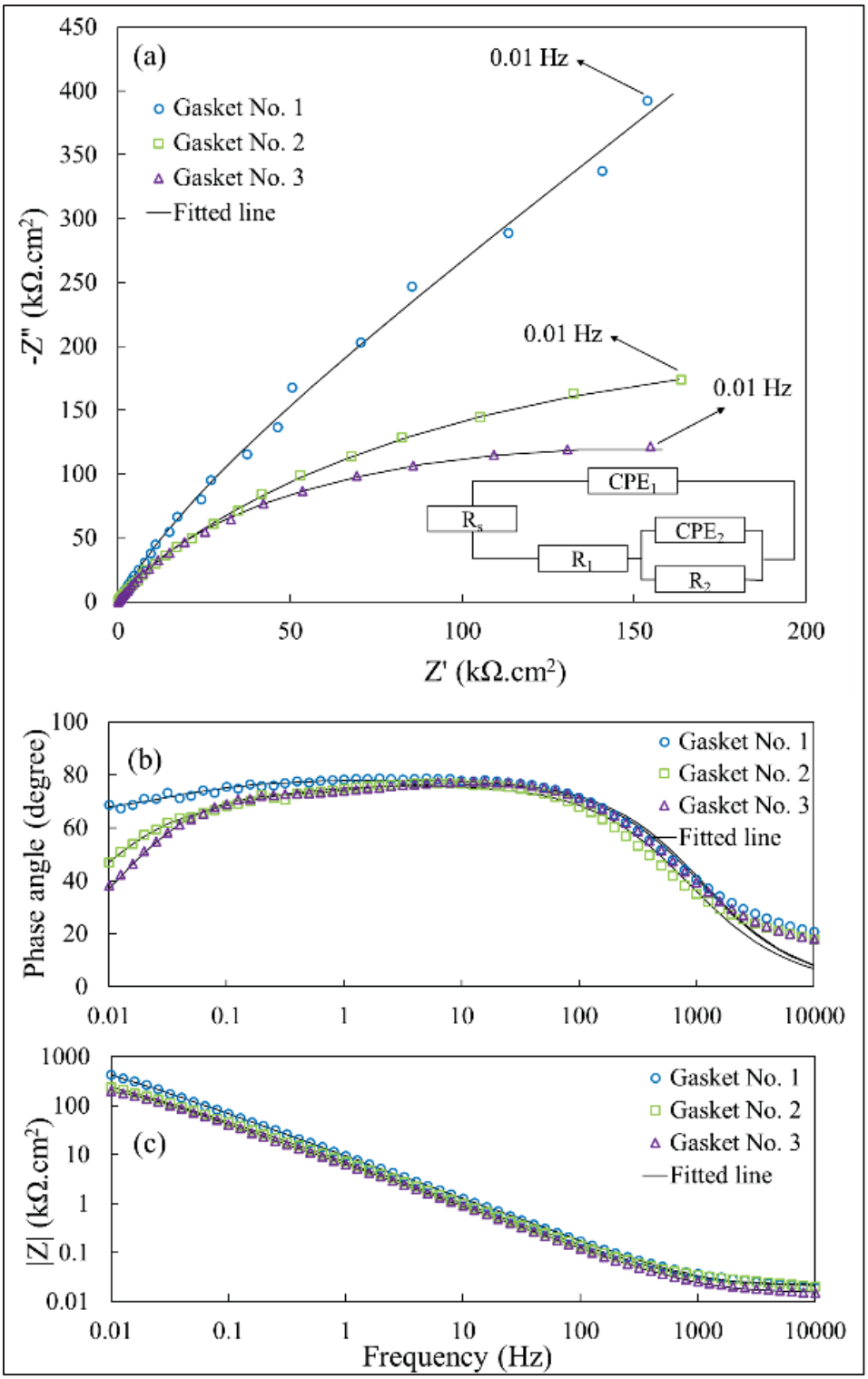

Figure 6.9 (a) Nyquist, (b) bode phase, and (c) bode modulus representation of electrochemical impedance response of the 321 SS flange sample plates exposed to the 3.5 wt.% NaCl at 50°C under different gap thicknesses

Table 6.6 Electrochemical parameters estimated by fitting the EEC to the EIS data of 321 SS under various gap thicknesses

Gasket No.	Gap thickness/ *g* (mm)	R_s (Ω)	R_1 (kΩ.cm^2)	CPE_1 (μΩ^{-1}.s^n.cm^{-2})	n_1	R_2 (kΩ.cm^2)	CPE_2 (μΩ^{-1}.s^n.cm^{-2})	n_2	R_{total} (kΩ.cm^2)
1	1.58	2.11	995	21.3	0.87	9730	6.81	0.72	10725
2	3.17	2.21	224.48	29.28	0.85	257.62	15.77	0.84	482
3	6.35	1.55	85.38	31.31	0.86	207.61	6.98	0.95	293

6.3.4 Corrosion morphology

Figure 6.10 presents the crevice corrosion morphologies of a 321 SS flange sample plate after a potentiostatic polarization test for 12 hours with Gasket No. 1. The corroded area is located at the interface of the flange and gasket, and the maximum corroded depth is located near the gasket area as shown in the color map of Figure 6.10 (a). According to the critical crevice solution (CCS) theory, the acidification of the crevice is due to the oxygen concentration cell, and Cl^- ions that enter the crevice, and as well through the hydrolysis reactions that make the crevice acidic and breaks down the passive layer. As there is a compressive stress applied on the gasket with 15 MPa, it is difficult for the solution to penetrate through the gasket and flange sample plate interface. Therefore, in the initial steps, corrosion develops through the vertical direction and then it penetrates under the gasket area. As the solution in the crevice is locally acidic, the grain boundaries are observed in the corroded area, which is due to the preferential corrosion of grain boundaries in an acidic solution (Figure 6.10 (c)). The morphology of the corrosion on the edges of the corroded area is different in the region exposed to the solution (Figure 6.10 (b)) and in the region under the gasket (Figure 6.10 (d)). Figure 6.10 (b) shows that on the side exposed to the solution, there is a sharp edge between the severely corroded area and passive area, while no crack was observed. However, Figure 6.10 (d) reveals that the corroded area under the gasket is full of cracks and these cracks are presented with greater detail in Figure 6.10 (e). As the flange-gasket interface is under stress, possibly these cracks are attributed to the effect of the local vertical surface stress (Fischer & Zitter, 1960) on the

corroded area and coarsening the pits or cracks and lead to the propagation of corrosion in this area. The profile of the corroded area in Figure 6.10 (f) shows that the corroded depth is the highest in the severely corroded area, and it decreases as corrosion propagates in the area under the gasket. Comparing the corroded region in the lightly corroded area with other literature that studied crevice corrosion reveals that in those studies, cracks were not observed, as the stress levels were not as high as in this study. Pits without cracks are observed near the crevice-corroded area (Hornus et al., 2021; Malki et al., 2021).

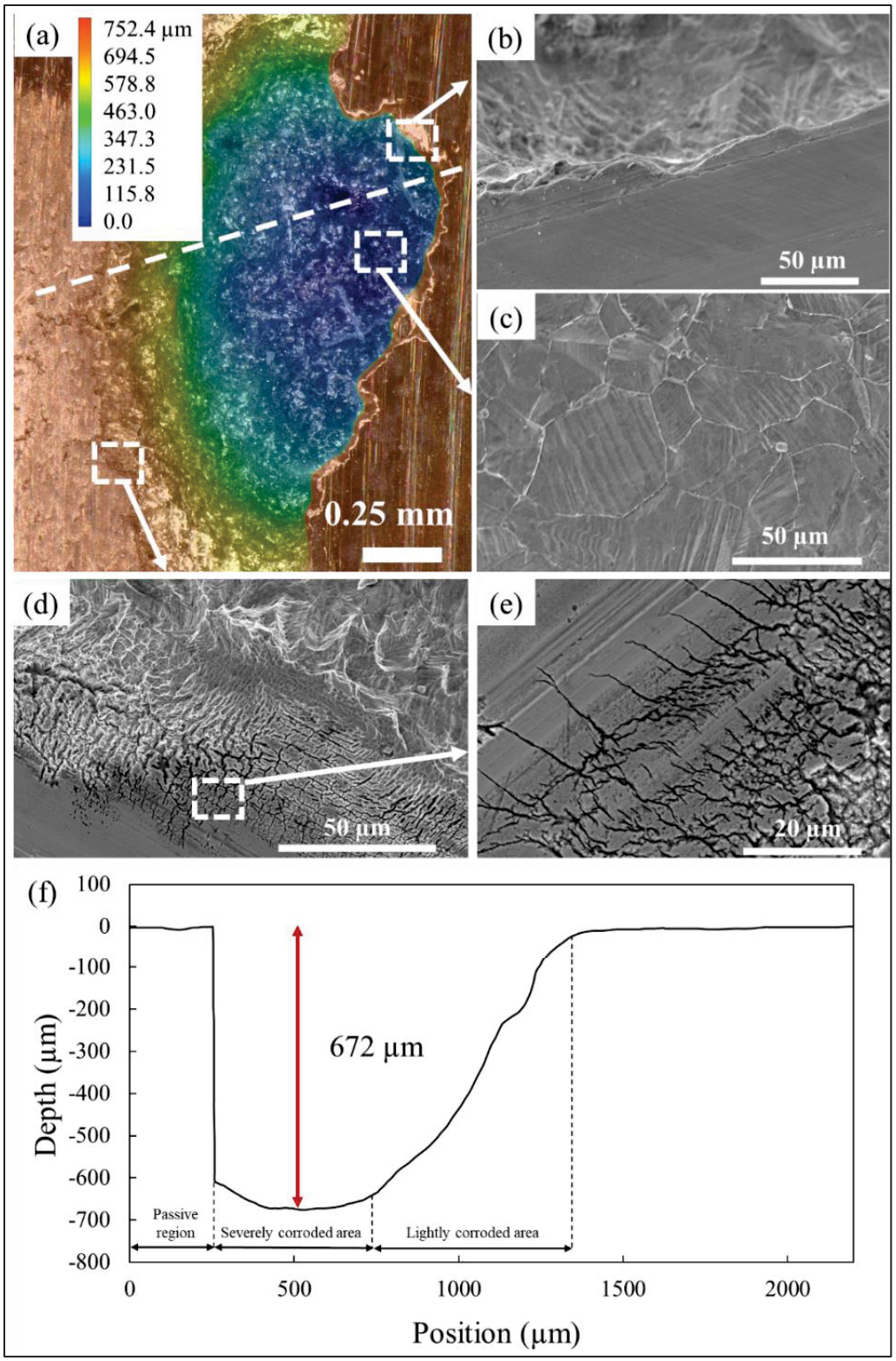

Figure 6.10 Crevice corrosion morphology of the 321 SS flange sample plate tested with Gasket No. 1 after 12 h of potentiostatic polarization test in 3.5 wt.% NaCl solution and 50°C

6.4 Discussion

6.4.1 Effect of gap thickness on the flange face corrosion

Crevice corrosion on the SSs in a neutral chloride solution occurs due to the formation of an oxygen concentration cell between the crevice or occluded area and the bulk solution (Figure 6.11 (a)). Because of the low oxygen concentration in the crevice, Cl^- ions react with metal ion (M^+) to maintain the electric balance (Figure 6.11 (b)) (Hu et al., 2011b). Then, hydrolysis will take place, lowering the pH inside the crevice and causing acidification. Consequently, the passive layer in the crevice area transforms into the active area. This transformation causes the potential of the SS sample to drop in the active region due to the *IR* drop, where *I* refers to the current and *R* refers to the resistance (Pickering, 1989) . Based on the electrochemical results, it can be concluded that the thickness of the crevice gap (shown in Figure 6.11 (b)) between the flange faces, influenced by the presence of the gasket or flange raised faces, affects the resistance of the flange sample plates to both general and localized corrosion (pitting and crevice).

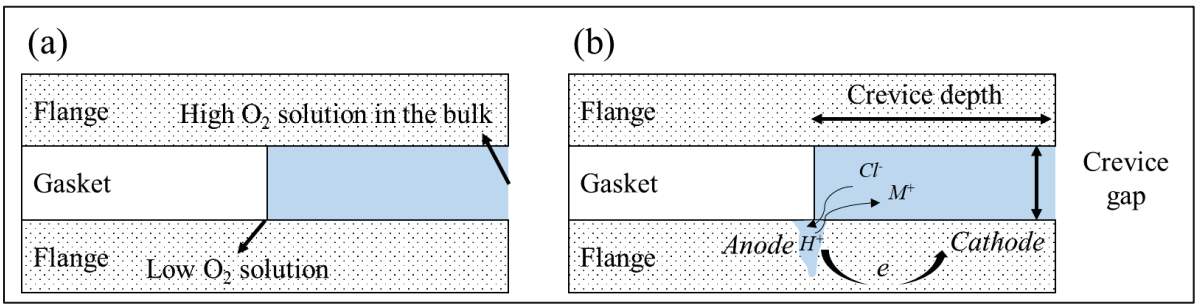

Figure 6.11 Schematic representation of (a) the formation of oxygen concentration cell in the crevice and (b) acidification of the crevice due to hydrolysis

On the corroded sample plates, a larger crevice-corroded area is observed with a decreasing gap thickness, and deeper pits are observed with an increasing gap thickness. For the sample plate used with Gasket No .3 in CPP, crevice corrosion is not observed as the gap thickness is wide enough to allow more local fluid circulation. In this case, with the gap thickness at its

maximum value, the flowing solution has caused damage to the passive layer. Even at higher potentials, more pits have formed in the area exposed to the solution and have deepened. The earlier initiation of crevice corrosion at the same applied potential on the flange sample plate with Gasket No. 1, along with a higher development current density, confirms that Gasket No. 1 creates the most susceptible conditions for the initiation and propagation of crevice corrosion. As the gap thickness increases, it allows more space for the circulating solution in the fixture to enter the gap, and there is an increase in the volume of the solution within the gap (as shown in Figure 6.12). This prevents the depletion of oxygen concentration in the crevice (interface of flange and gasket), consequently leading to observed delays in the initiation of crevice corrosion in potentiostatic tests. Additionally, no crevice corrosion is observed in the flange sample plate used with Gasket No. 3 in CPP tests.

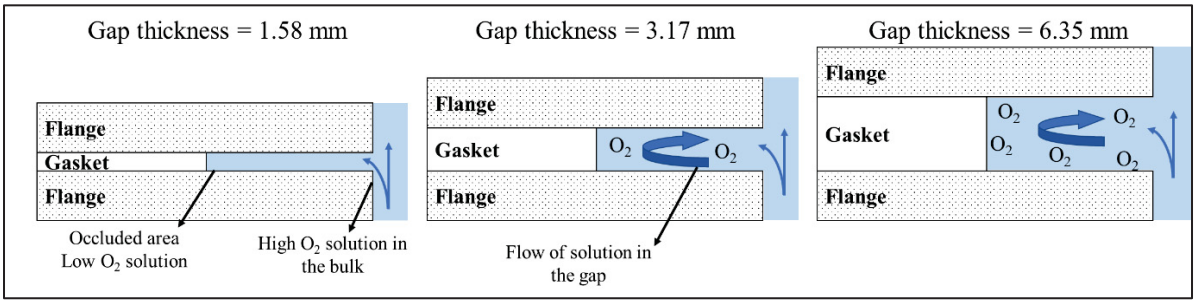

Figure 6.12 Schematic representation of the effect of gap thickness on the flow of solution in the gap between two flanges and the volume of the solution

The erosion effect of the flowing solution inside the fixture, with the presence of Cl^- ions, damages the passive layer formed on the flange sample plate. This damage results in lower resistance observed in the EIS results and an increase in the average pit depth as the gap thickness increases.

The initiation of crevice corrosion can be explained by the potential drop (*IR* drop) theory (Kennell et al., 2008), i.e., the decrease in potential that occurs within a crevice or gap as a result of the resistance encountered by an electric current passing through the solution in the crevice. This theory states that when the surface of the stainless steel is in the passive form, the *IR* drop (derived from Equation (6.7)) causes the crevice area to transition into the active region, initiating crevice corrosion (Abdulsalam, 2007; Lillard & Scully, 1994).

$$IR = \frac{x_{pass}\ I}{\sigma\ w\ t} \tag{6.7}$$

Where *IR* denotes the potential drop measured in mV, x_{pass} stands for the distance from the crevice mouth to the active-passive boundary within the crevice, measured in cm. The variables include *I* for current in mA, σ for conductivity in $ohms^{-1}.cm^{-1}$, *w* for crevice width in cm, and *t* for crevice gap thickness in cm. According to Equation (6.7), the crevice gap, influences the *IR* drop and has an inverse relation.

While larger gaps between the flange and gasket may cause more damage to the passive layer and increase the general corrosion rate, the threat of crevice corrosion poses a greater danger to the integrity of an engineering structure. As a localized form of corrosion, it propagates in the confined area between the gasket and flange, rapidly degrading the flange material in a hidden manner. Therefore, it is recommended to use a thicker gasket in bolted flanged joints.

6.4.2 Effect of crevice depth (d) on the flange face corrosion

The variation in crevice depth, denoted as *d*, affects the transfer of species between the bulk and crevice solution. When the crevice depth reaches its maximum value of 7.49 mm, the exchange of species between the bulk and crevice solution becomes more challenging. This suggests that, during the crevice corrosion process, oxygen is consumed more rapidly by the cathodic reaction in deeper crevices. Consequently, the acidification process is accelerated, leading to a shorter incubation time for crevice corrosion at a crevice depth of 7.49 mm. For *d* values of 3.81 and 0, as the flowing solution passes, it avoids the formation of stagnant solution in the interface of the flange and gasket, preventing acidification and breakdown of the passive layer.

Equation (6.7) also illustrates the influence of crevice depth on crevice corrosion. As mentioned in section 6.4.1, x_{pass} is the distance between the crevice mouth and the active-passive boundary inside the crevice, and in this study, we can substitute the x_{pass} value with *d* (crevice depth as shown in Figure 6.11(b)). Thus, it can be concluded that for *d* = 3.81 and 0 mm, the *IR* drop remains in the passive region, preventing the initiation of crevice corrosion.

However, in the CPP tests, due to the formation of pits at high potentials on the exposed area (d = 3.81 mm), the IR drop increases significantly as the current I increases with the formation of pits on the flange face. Therefore, crevice corrosion also occurred in the interface of the flange and gasket. Full-face gaskets protect the flange surface from pitting and general corrosion; therefore, it is recommended to use these types of gaskets in bolted flanged joints.

6.5 Conclusion

In the present study, the effect of gap size (thickness and depth) on the 321 SS flange surface corrosion was studied using electrochemical techniques and surface analysis methods. All electrochemical tests were performed with a fixture that simulates the real-world conditions in bolted flanged joints including the applied stress on the gasket, fluid flow inside the fixture, and the crevice geometry between the gasket and flange. Both general and localized corrosion of the flange sample plates are investigated in this study. It is found that gaps between the flange plates in bolted flanged joints will cause localized corrosion on the flange surfaces. In this study, gaskets are used to create the gaps, as they are commonly used in various applications such as wind turbines and pipe flanges. The findings of this study are as follows:

- The passive potential range $|E_{corr} - E_b|$ decreases as the volume of the gap increases, and both crevice corrosion and pitting corrosion cause the breakdown of the passive layer in CPP tests. The gap size influences the contribution of crevice corrosion and pitting corrosion on the flange surface.
- Both EIS and CPP tests reveal that the overall corrosion resistance of the flange surface is influenced by variations in the gap size. With an increase in gap thickness, the corrosion rate of the flange surface rises. Additionally, reducing the d value (or crevice depth) leads to a decrease in the general corrosion rate of the flange surfaces.
- Corrosion pits develop on the area exposed to the solution, and the average pit depth increases with the widening of the gap thickness. In contrast, the average pit depth decreases as the value of d decreases and the surface is covered with the gasket.
- Crevice corrosion initiates at the flange gasket interface and propagates to the area under the gasket. The initiation time of crevice corrosion increases with an increase in

gap thickness. No crevice corrosion is observed on sample plates with the same ID as the gasket.

Acknowledgments

This work was supported by the Natural Sciences and Engineering Research Council of Canada (NSERC) under the Discovery Grant (RGPIN-2019-05973 and RGPIN-2021-03780).

CHAPTER 7

APPLICATION OF MACHINE LEARNING FOR THE CLASSIFICATION OF CORROSION BEHAVIOR IN DIFFERENT ENVIRONMENTS FOR MATERIAL SELECTION OF STAINLESS STEELS

Soroosh Hakimian [a], Shamim Pourrahimi [a], Abdel-Hakim Bouzid [a], Lucas A. Hof [a]

[a] Mechanical Engineering Department, École de technologie supérieure, 1100, rue Notre-Dame Ouest, Montreal, Québec, H3C 1K3, Canada

Paper published in: *Computational Materials Science*, Volume 228, September 2023, 112352.
https://doi.org/10.1016/j.commatsci.2023.112352

Abstract

Corrosion behavior prediction of materials in any given environmental condition is important to minimize timeconsuming experimental work to avoid failures and catastrophes in industry. Supervised machine learning (ML) techniques are recently explored to predict corrosion behavior. However, there is still a lack of research that proposes a model capable of predicting the corrosion behavior of a wide range of stainless steel grades in varying environments, including acids, bases, and salts. Moreover, conventional experimental approaches are often insufficient in identifying the most influential factors in the corrosion process due to its multivariate and non-linear nature. This study presents the development and evaluation of multiple ML models in predicting the corrosion behavior of different types of stainless steel in varying environments. The prediction performance of four ML algorithms, decision tree (DT), support vector machine (SVM), random forest (RF), and bagging classifier, were compared. Initially, the algorithms were fitted to a dataset based on the type of electrolyte (Dataset No. 1) and then modeled on a modified dataset (Dataset No. 2) in which the types of electrolytes were replaced with their critical ions contributing to corrosion reactions. The Bagging classifier achieved the highest prediction accuracy of 94.4% for Dataset No. 1, while the DT model was the most suitable for Dataset No. 2 with a testing accuracy of 93.95%. The application-driven

approach of confusion matrix analysis to select the model's capacity to correctly identify severe and poor corrosion behavior confirmed that Bagging and DT classifiers are the most suitable ML algorithms for predicting corrosion behavior in Dataset No. 1 and No. 2, respectively. Furthermore, the feature importance analysis identified hydrogen and sulfide concentrations in corrosive environments, as well as the sum of the number of alloying elements, as the most influential factors, contributing up to 77.8% to the corrosion behavior. As a result, users of stainless steels can leverage this model to predict the corrosion behavior of specific materials in specific environments, facilitating informed material selection for various applications, without the need of lengthy and costly experiments.

7.1 Introduction

In the past few decades, stainless steels (SS) have gained considerable attention in a wide range of industries including nuclear power plants, chemical plants (Alvino et al., 2014), biomedical implants (Talha et al., 2013), civil engineering (Gedge, 2008), heat exchangers, and food industries (Zaffora et al., 2021). This high industrial demand of SSs is due to their desirable characteristics such as superior manufacturability, mechanical properties, physical properties, and corrosion resistivity (Cheng et al., 2021; Karimi et al., 2012; Lo et al., 2009). The alloying elements in SS are providing the steel its "stainless" attribute and make it resistant in corrosive environments. The presence of chromium (Cr) is the key element to create an adhering, self-healing protective passive layer on the steel surface. Other alloying elements such as Ni, Mo, N, and Mn are also typically added to SS composition to control its microstructure, passive layer thickness and stability, and give it specific characteristics like pitting corrosion resistance (J. Sun et al., 2022). A wide range of SS grades are available with varying chemical compositions (Cashell & Baddoo, 2014; McGuire, 2001; Nilsson, 2013) tailored for different applications. The specific application using SS products must be carefully considered for selecting its suitable grade in terms of corrosion resistivity.

In fact, material selection is one of the critical steps in designing a structure for industrial applications. In addition to the material's physical and chemical properties, the choice of material is also affected by the environmental conditions of the operating or manufacturing

process (Aslam et al., 2022). These environmental conditions may cause material degradation due to corrosion. It has been shown that, globally, degradation by corrosion represents a cost of 3% to 4% of each nation's gross domestic product (GDP), and 35% of corrosion related costs could be avoided with the application of knowledge and appropriate technology (Koch, 2017). Corrosion processes are highly influenced by chemical composition and multiple environmental or operating factors, such as temperature, pH, humidity, stray currents, oxygen concentration, impurity level, and chloride content (Kritzer et al., 1999; Lavigne et al., 2014; Wasim et al., 2018). As such, these factors should be considered when selecting a SS grade for a specific application. Different electrochemical and immersion techniques have been described in the literature for evaluating the corrosion behavior of SSs (ASTM International, 2014, 2015a, 2017b, 2018c, 2020d, 2020e); however, in most cases, these techniques are destructive, lengthy, require dedicated equipment, and results analysis experience. Hence, predicting corrosion behavior of a widely used material, such as SS, in common environments without conducting experimental tests is helpful in efficiently selecting materials for industrial applications by reducing testing time and costs.

Recently, machine learning (ML) methods have been extensively used in materials research thanks to their powerful data mining capabilities (Yan et al., 2020). Rather than using predetermined equations, it learns from sample data and experience. In corrosion research, ML algorithms such as random forest, support vector regression, and artificial neural networks have been used to study corrosion behavior (Y. Diao et al., 2021; Jiménez-Come et al., 2019; Lv et al., 2020; Pei et al., 2020). ML methods were used in corrosion research for several purposes, such as the prediction of corrosion rates (Y. Diao et al., 2021; Kamrunnahar & Urquidi-Macdonald, 2010; Lv et al., 2020; Pei et al., 2020; Wen et al., 2009; Yan et al., 2020), the prediction of pitting corrosion behavior (Jiménez-Come et al., 2019), and the modeling of maximum pit dimensions (Cavanaugh et al., 2010b). Also, ML methods were used to study the corrosion behavior by considering the underlying physical laws that map alloy composition and environmental factors to the corrosion behavior. Data visualization, simulation, correlation analysis, and multivariate fitting are among the applications of ML demonstrated in these studies. Compared with conventional regression analysis methods (Y. Cai et al., 2019; Chico et al., 2017), ML techniques can process a variety of features, perform powerful regressions,

and are able to robustly generalize datasets of any size (Pruksawan et al., 2019). Hence, ML facilitates profound research on corrosion behavior and its prediction. In addition, in the field of corrosion science, various factors (e.g. environmental conditions, alloying elements) have been identified as contributing to corrosion behavior (Chawla, 1959; Wasim et al., 2018). However, the relative importance of these factors on corrosion performance remains a subject of debate. With the advent of ML, it is now possible to use data-driven approaches to determine the relative importance of each factor in predicting material behavior (J. Schmidt et al., 2019). Therefore, this contribution presents the development of an ML model that enables users to predict the corrosion behavior of specific stainless steel materials in specific environments. This model allows for informed material selection for various applications without the need for expensive and time-consuming experiments. The present study is based on a dataset which includes information on the chemical composition of 34 different grades of SS, and the type, concentration and temperature of different corrosive environments. By mapping these features to corrosion behavior labels, that are defined based on corrosion rates, this work applies multiple ML techniques and it compares their accuracy. Moreover, the impact of feature creation on model accuracy was assessed. Specifically, a new dataset was generated in the feature creation step by replacing the type of electrolyte with the critical ions that contribute predominantly to the corrosion reaction. This study also seeks to use ML techniques to investigate the relative importance of features in chemical composition and type of corrosive environment on the corrosion behavior of SS alloys. The results of such analysis can provide valuable insight for decision-making in the selection of materials for specific corrosive environments.

7.2 Methodology

A schematic overview of the developed procedure to evaluate the corrosion state of SSs in different corrosive environments is presented in Figure 7.1. The first step involves preprocessing the data prior to its use in the ML modeling phase. Two distinct datasets (Dataset No. 1 and Dataset No. 2) are considered as inputs for the ML models. Dataset No. 1 consists of features such as the type of electrolyte and its concentration, while Dataset No. 2 is a

transformed representation of the first dataset, where the electrolyte and its concentration are converted into the concentration of critical ions in corrosion phenomena. This conversion process, referred to as feature creation, is described in detail in Section 7.2.4. Four ML algorithms, including decision tree (DT), random forest (RF), support vector machine (SVM), and Bagging are considered as classification methods in this study. DT is a predictive model that uses a tree-like structure to classify or regress data based on a series of decisions. It works by recursively splitting the data into subsets, based on the most important features, until a decision can be made (Safavian & Landgrebe, 1991). RF is an extension of the DT algorithm that uses multiple decision trees and combines their results to improve accuracy and reduce overfitting. SVM is a classification algorithm that separates data points by finding the best hyperplane that maximizes the margin between different classes. It can handle both linear and non-linear datasets, by transforming the data into a higher dimensional space (Belgiu & Drăgu, 2016). SVM can be used for binary and multi-class classification tasks. Bagging is a technique that combines multiple models to improve the overall accuracy and stability of the predictions (Noble, 2006). It works by creating several bootstrap samples of the training data and training each model on a different subset. Bagging can be used with any type of model, but is particularly effective with high-variance algorithms like DTs. The predictions of the individual models are combined using averaging or voting to make a final prediction (Quinlan, n.d.). After model fitting, the model's performances are evaluated by calculation of training and testing accuracies. The confusion matrix is also established to assess the models based on their sensitivity, specificity, accuracy, and risk (Beguería, 2006). Hyperparameter tuning is performed to optimize the model hyperparameters and subsequently improve the model performance (A. Y. T. Wang et al., 2020). After model evaluation, the best ML algorithm for classifying corrosion behavior of SS in different environmental conditions is introduced. For Dataset No. 2, based on ion concentration, the same procedure is repeated to evaluate the feature creation approach. Also, the features are sorted based on their importance and their influence on corrosion behavior.

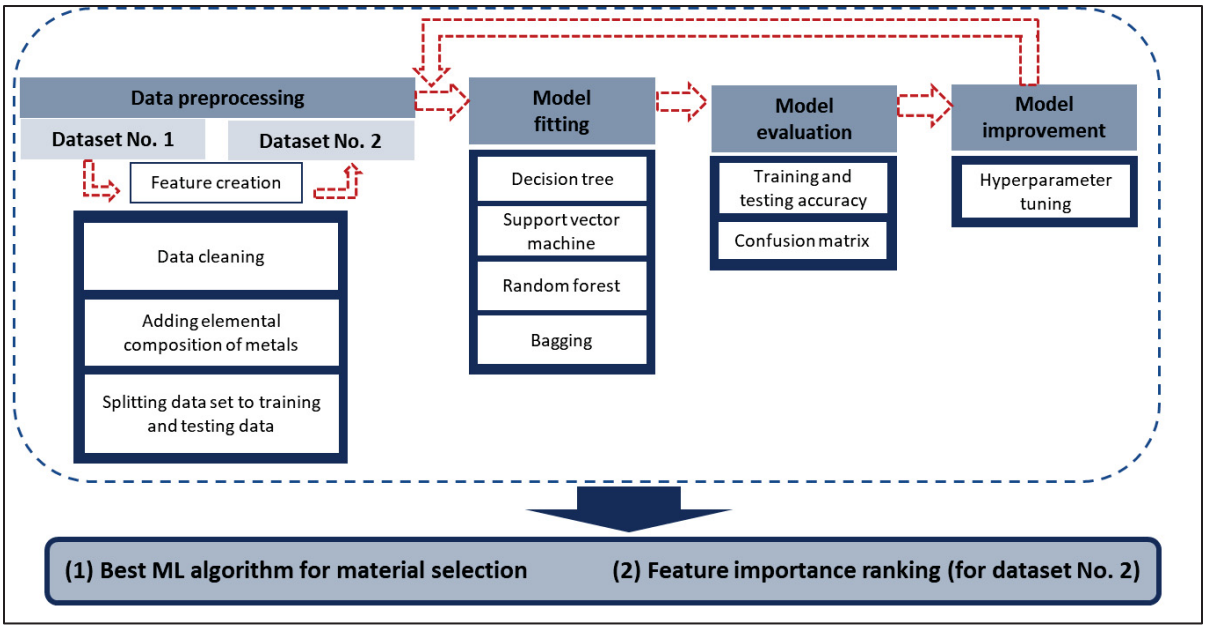

Figure 7.1 Schematic overview of the developed and applied (iterative) processes to classify and predict the corrosion behavior

The sub sections 7.2.1, 7.2.2, 7.2.3, and 7.2.4 outline the details of the used database, the developed preprocessing methods, fitted models, feature importance ranking, and feature creation methods used in the developed ML classification techniques.

7.2.1 Corrosion data preprocessing

Data preprocessing in ML modeling involves several steps to clean, transform, and prepare the data to allow its use for training and testing of the ML model. Initially, a uniformity check was performed on the database. The used Dataset No. 1 was extracted from a document reporting the chemical resistance of SSs, provided by the German National library of Science and Technology (Thyssen Edelstahlwerke AG, 1992). This database was designed to assist customers in selecting the appropriate SS grade for their specific applications. The availability of such a database from one of the largest steel manufacturers (*Thyssen Edelstahlwerke AG*) confirms the value of developing a predictive model for industrial applications. This dataset includes more than 4000 rows of data after data preprocessing. The features of this Dataset No. 1 are defined as the chemical composition of SS alloys, type of corrosive environment as well

as its concentration, and temperature. The different corrosion behaviors in this dataset were qualified and labelled as *Resistant*, *Good*, *Poor*, and *Severe*. The definition of each label is identified as follows:

- *Resistant*: Material is resistant to the applied corrosive condition (i.e., mass loss rate < 0.1 g/h.m^2; corresponding to a corrosion rate < 0.11 mm decrease in thickness per year).
- *Good*: Material shows a minor attack by the corrosive environment (i.e., 0.1 - 1.0 g/h.m^2 corresponding to a 0.11 - 1.10 mm decrease in thickness per year).
- *Poor*: Material is barely resistant to a corrosive environment, and it is practically not usable (1.0 - 10.0 g/h.m^2 corresponding to 1.1 - 11.0 mm decrease in thickness per year).
- *Severe*: Not resistant to corrosion (i.e., either > 10.0 g/h.m^2 corresponding to > 11.0 mm decrease in thickness per year by uniform corrosion degradation).

In this study, the database includes information on the corrosion behavior of SSs in different environments, such as molten salts, gases, and solutions. The type of SS, type of environment, concentration, temperature, and corrosion behavior are included in each row of the database. To prepare the data for the ML model, the corrosion behavior of SSs in typical solutions was extracted from the database and preprocessed. In some cases, the electrolyte temperature was referred to as "boiling temperature" in the reference, which was converted into a numerical value based on the literature and replaced with the corresponding value in the database for use in the developed model.

The chemical composition of each SS material (304, 304L, 409, …) was extracted from the literature (ASTM International, 2017a, 2020b). This study defined 16 features, including 13 features for the material's chemical composition (i.e., the weight percentage of 13 elements in the SS alloy as shown in Table 7.1) and other features describing the environmental conditions (e.g., type of electrolyte, electrolyte temperature and concentration, as presented in Table 7.2). As well, Table 7.2 includes the electrolyte concentration and temperature features for a wide range of values, and the corrosion behavior is included as an output feature in Table 7.2.

Table 7.1 Chemical composition of SSs used in the ML models based on literature ASTM International (2017a) ASTM International (2020b)

S.S.	%C	%Mn	%Si	%P	%S	%Cr	%Mo	%Ni	%N	%Ti	%Nb	%Al	%Fe
403	0.15	1	0.5	0.04	0.03	11.5	0	0.6	0	0	0	0	86.18
405	0.08	1	1	0.04	0.03	11.5	0	0.6	0	0	0	0.1	85.65
S41050	0.04	1	1	0.045	0.03	10.5	0	0.6	0.1	0	0	0	86.685
416	0.15	1.25	1	0.06	0.35	12	0	0	0	0	0	0	85.19
410	0.15	1	1	0.04	0.03	11.5	0	0.75	0	0	0	0	85.53
420	0.15	1	1	0.04	0.03	12	0.5	0.75	0	0	0	0	84.53
430F	0.12	1.3	1	0.06	0.35	16	0	0	0	0	0	0	81.17
440C	1.2	1	1	0.04	0.03	16	0.75	0	0	0	0	0	79.98
S41500	0.05	1	0.6	0.03	0.03	11.5	0.5	3.5	0	0	0	0	82.79
409	0.03	1	1	0.04	0.02	11.5	0	0.5	0.03	0.36	0.17	0	85.35
430	0.12	1	1	0.04	0.03	16	0	0.75	0	0	0	0	81.06
431	0.2	1	1	0.04	0.03	15	0	1.25	0	0	0	0	81.48
303	0.15	2	1	0.2	0.35	17	0	8	0	0	0	0	71.3
441	0.03	1	1	0.04	0.03	17.5	0	1	0.03	0.1	0.3	0	78.97
434	0.12	1	1	0.04	0.03	16	0.75	0	0	0	0	0	81.06
630	0.07	1	1	0.04	0.03	15	0	3	0	0	0.15	0	79.71
631	0.09	1	1	0.04	0.03	16	0	6.5	0	0	0	0.75	74.59
304	0.08	2	0.75	0.045	0.03	18	0	8	0.1	0	0	0	70.995
305	0.12	2	0.75	0.045	0.03	17	0	10.5	0	0	0	0	69.555
304L	0.03	2	0.75	0.045	0.03	18	0	8	0.1	0	0	0	71.045
301	0.15	2	1	0.045	0.03	16	0	6	0.1	0	0	0	74.675
304LN	0.03	2	0.75	0.045	0.03	18	0	8	0.1	0	0	0	71.045
304N	0.08	2	0.75	0.045	0.03	18	0	8	0.1	0	0	0	70.995

S.S.	%C	%Mn	%Si	%P	%S	%Cr	%Mo	%Ni	%N	%Ti	%Nb	%Al	%Fe
321	0.08	2	0.75	0.045	0.03	17	0	9	0.1	0.9	0	0	70.095
347	0.08	2	0.75	0.045	0.03	17	0	9	0	0	0.8	0	70.295
316	0.08	2	0.75	0.045	0.03	16	2	10	0.1	0	0	0	68.995
316L	0.03	2	0.75	0.045	0.03	16	2	10	0.1	0	0	0	69.045
316LN	0.03	2	0.75	0.045	0.03	16	2	10	0.1	0	0	0	69.045
317L	0.03	2	0.75	0.045	0.03	18	3	11	0.1	0	0	0	65.045
317LN	0.03	2	0.75	0.045	0.03	18	3	11	0.1	0	0	0	65.045
329	0.08	1	0.75	0.04	0.03	23	1	2	0	0	0	0	72.1
S31803	0.03	2	1	0.03	0.02	21	2.5	4.5	0.08	0	0	0	68.84
316Ti	0.08	2	0.75	0.045	0.03	16	2	10	0.1	0.9	0	0	68.095
316Cb	0.08	2	0.75	0.045	0.03	16	2	10	0.1	0	0.8	0	68.195

Table 7.2 List of features used in the developed models for corrosion classification (Dataset No. 1)

Feature	Unit	Descriptions/Amount
Material	wt.%	Carbon (C) Manganese (Mn) Silicon (Si) Phosphorus (P) Sulfur (S) Chromium (Cr) Molybdenum (Mo) Nickel (Ni) Nitrogen (N) Titanium (Ti) Niobium (Nb) Aluminum (Al)

Feature	Unit	Descriptions/Amount
		Iron (Fe) am
Type of electrolyte	-	Formic acid, Ammonium chloride, Acetic acid, Potassium hydroxide, Lactic acid, Oxalic acid, Phosphoric acid, Sulfuric acid, Nitric acid, Hydrochloric acid, Citric acid, Potassium bisulfate, Potassium nitrate, and Magnesium chloride
Concentrations	wt.%	0.5, 1, 2, 2.5, 5, 7, 7.5, 10, 15, 20, 25, 30, 37, 40, 45, 50, 60, 66, 70, 75, 80, 98, 99, 100
Temperature	^{o}C	20, 50, 70, 80, 86, 90, 100, 100.5, 100.6, 100.8, 101, 102, 105, 106, 107, 110, 113, 115, 119, 120, 121, 122, 125, 132, 134, 138, 140, 150, 157, 158, 168, 205, 335
Corrosion behavior	Qualitative	Severe Poor Good Resistant

7.2.2 ML approach

This work presents a Python-based implementation of the selected four ML algorithms (DT, RF, SVM, and Bagging classifier) using the scikit-learn library (Pedregosa FABIANPEDREGOSA et al., 2011) and it evaluates and compares their predictive performance on corrosion behavior. Here, 80% of the data is used as a training dataset and 20% as a testing dataset for each of these ML methods. The used database contains four classes of corrosion behavior: Resistant (1311 labels), Good (722 labels), Poor (753 labels), and Severe (1233 labels). The symbolic labels (Severe, Poor, Good, and Resistant) are quantified automatically using the *label_encoder* function. The accuracy of the test and training sets for

each model was calculated using the *sklearn.metrics.accuracy_score* function. A confusion matrix was plotted for each model to analyze misclassified labels. The training set was defined using two variables, *X_train* and *y_train*, and a DT classifier was trained on these variables with *random_state=0*. The maximum depth of the DT was set to the default value of *None*, which expands the nodes until all leaves are pure (i.e., contain only one class). Hyperparameter tuning resulted in a set of parameters with *max_depth=None* and *criterion=entropy*.

For the SVM model, at first, the *svm.svc* function was fitted on the training data with the default hyperparameters (*C = 1* and *gamma = scale*) and *kernel = rbf*. Then hyperparameter tuning was carried out to improve the model accuracy. The hyperparameter tuning is applied during training by inspecting the regularization parameter *C* and the Kernel coefficient *gamma* with a reciprocal random distribution. The resulting hyperparameters were *C = 1.38* and *gamma = 0.019*. Following the use of the SVM algorithm, the RF algorithm was applied as well for comparison. Therefore, the RF Classifier with *random_state = 0* was fitted to the training data. Also, a hyperparameter tuning between 1 to 50 was applied to find the best number of trees in the forest (*n_estimators*) for this algorithm. A number of *n_estimators = 42* was recognized as the appropriate number of estimators for RF classification. It is worth mentioning that a further increase of the parameter *n_estimators* has no positive influence on the accuracy. As the last deployed classification model, the Bagging ensemble method was applied using the scikit-learn library. This method involves creating multiple DT models on bootstrapped samples of the training dataset and combining the results through a voting mechanism. The Bagging classifier implementation in scikit-learn is based on the RF algorithm, which involves additional randomization during the tree-building process.

7.2.3 Feature importance

Feature importance in ML refers to the relative importance of each feature in determining the target output. In other words, it measures the contribution of each feature to the prediction performance of a model. It can also provide insight into the underlying patterns and relationships in the data and help to better understand the factors that are driving the decision-making process. The present study calculates the feature importance to determine the most

influent factors on the corrosion behavior of SSs. The feature importance is calculated for the model that has the highest accuracy, using the *feature_importance_* attribute. This attribute is calculated after the tree has been trained on a dataset and is based on the frequency that a particular feature is used to split the data and to which extend such a split improves the classification accuracy. The importance values are then normalized to rank the features in order of importance.

7.2.4 Feature creation

As mentioned in Table 7.2, there are three categories of electrolytes including acids, salts, and bases with varying concentrations that are typical for common SS applications. To enhance the generalizability of the model, the concentration of the electrolytes is converted into the concentration of four key ions active in corrosion phenomena: $[Cl^-]$, $[H^+]$, $[OH^-]$, and $[S^{2-}]$. These ions have been extensively studied and are known to play a critical role in the corrosion behavior of SSs (Abd El Meguid et al., 2000; Dastgerdi et al., 2019a; D. G. Li et al., 2014). For simplicity and consistency, the concentration of these ions is only considered at 20°C, as the concentration would vary and be difficult to calculate at higher temperatures. Hence, a new database (Dataset No. 2) is created based on the concentrations of $[Cl^-]$, $[H^+]$, $[OH^-]$, and $[S^{2-}]$ ions at 20°C, and the additional data, which includes higher temperature measurements, are removed. This operation resulted in a dataset size including 1544 samples. As shown in Figure 7.1, the procedure that is applied to Dataset No. 1 will be applied to Dataset No. 2 as well. The features considered in this dataset are presented in Table 7.3.

Table 7.3 List of features used in models after feature creation (Dataset No. 2)

Feature	Unit	Descriptions/Amount
Material	wt.%	Carbon (C) Manganese (Mn) Silicon (Si) Phosphorus (P) Sulfur (S)

Feature	Unit	Descriptions/Amount
		Chromium (Cr) Molybdenum (Mo) Nickel (Ni) Nitrogen (N) Titanium (Ti) Niobium (Nb) Aluminum (Al) Iron (Fe) am
Type of ion	-	$[Cl^-]$, $[H^+]$, $[OH^-]$, and $[S^{2-}]$
Concentrations	mol/dm^3	0, 0.052, 0.1646, 0.1866, 0.1918, 0.222, 0.367, 0.3732, 0.397, 0.4665, 0.52, 0.793, 0.933, 0.984, 1.11, 1.3, 1.3995, 1.6772, 1.7485, 1.866, 1.918, 2.396, 2.47, 2.6, 2.6504, 2.799, 2.95, 3.56, 3.732, 4.94, 5.99, 7.463, 8.633, 8.743, 8.8652, 8.881, 8.91, 11.195, 11.51, 11.98, 13.252, 13.42, 14.927, 15.34, 15.8136, 18.285, 19.18, 21.204, 23.7204, 26.504,
Temperature	^oC	20
Corrosion behavior	Qualitative	Severe Poor Good Resistant

7.3 Results and discussion

The results of the ML modeling using the DT, SVM, RF, and Bagging classifier algorithms for Dataset No. 1 are presented in Section 7.3.1, along with the introduction of the best model for this dataset. The results for Dataset No. 2 are presented in Section 7.3.2, where Subsection

7.3.2.1 discusses the feature importance for identifying the most influential factors contributing to the corrosion behavior of SS material.

7.3.1 Evaluation of ML algorithms for Dataset No. 1

In this section, the performance of the different developed models is evaluated and compared by the testing accuracy. To improve understanding of the models' performance, the confusion matrices are also created to visually demonstrate the errors made in the predictions in order to identify the model with the highest accuracy and to evaluate its performance.

7.3.1.1 ML model comparison based on accuracy

In Figure 7.2, the testing accuracies of the four ML models - DT, SVM, RF, and Bagging classifier - are presented before and after hyperparameter tuning. The results show that SVM had the highest improvement in accuracy, with an increase of 19% after tuning. DT and RF had minimal improvement of less than 1%. Among the four models, the Bagging classifier achieved the highest testing accuracy of 94.4% for this specific dataset. Therefore, it can be concluded that the Bagging classifier is the most effective model for predicting the corrosion behavior of SS grades in common environments and service conditions. While accuracy is an important metric for evaluating the performance of a classification model, it should not be the only factor considered in the selection of the best model. A high accuracy may not necessarily reflect a well-performing model, as it is possible to have a high accuracy with incorrect predictions in specific classes. In order to get a more complete understanding of the performance of each model, a confusion matrix analysis was performed. Section 7.3.1.2 presents the confusion matrix analysis, and it is discussed how it can provide valuable insights on the performance of the developed models beyond accuracy.

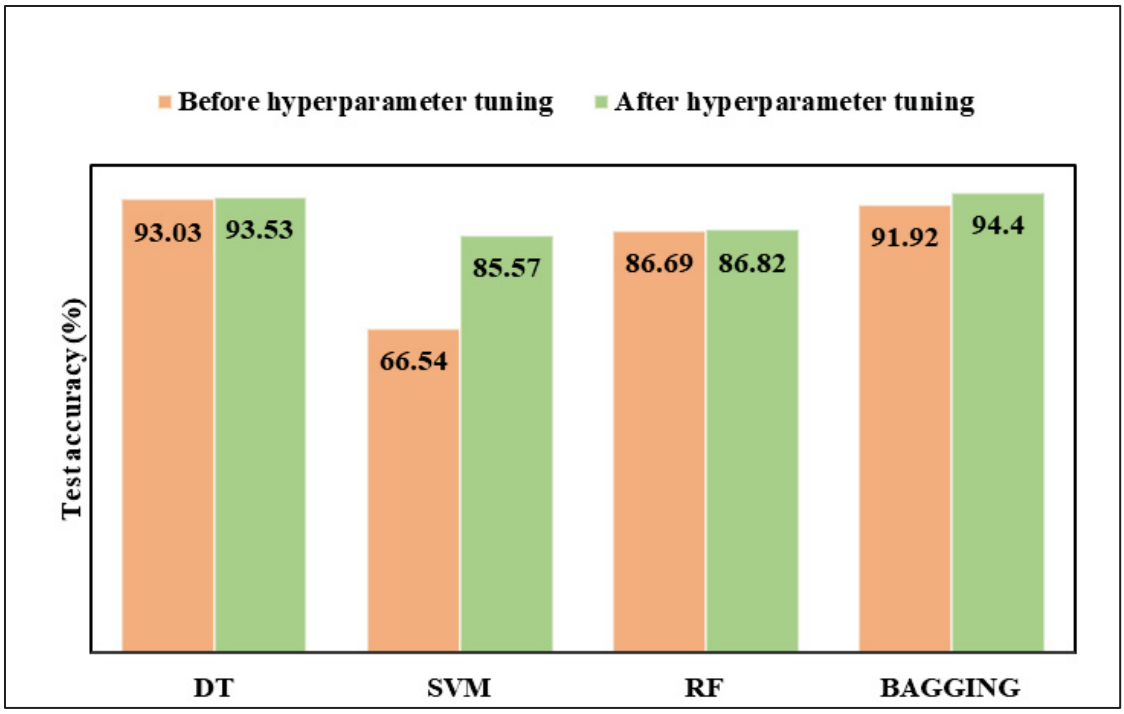

Figure 7.2 Testing accuracies of different ML models before and after hyperparameter tuning for Dataset No. 1

7.3.1.2 ML model comparison based on confusion matrix analysis

An analysis of the confusion matrix provides a more informative evaluation of the model's performance, allowing for a detailed assessment of false predictions. In the context of the developed corrosion classification model, we are interested in prioritizing the accurate detection of severe and poor corrosion behavior. This is because the cost of failing to detect "Severe" and "Poor" corrosion labels can be much higher than the cost of flagging a SS with "Good" behavior as having "Severe" corrosion behavior. In such cases, our model selection would be based on not only accuracy but also application-driven asymmetric costs. Therefore, it is important to carefully consider the application context and the costs of different types of errors when evaluating and optimizing the model's performance.

Figure 7.3 shows the 4x4 confusion matrices of DT, SVM, RF, and Bagging models fitted on the data obtained in section 7.3.1.1. Each row of the matrix represents the instances in an actual class, while each column represents the instances in a predicted class. The diagonal elements

of the matrix represent the number of correct predictions for each class, while the off-diagonal elements represent the number of instances that were incorrectly classified.

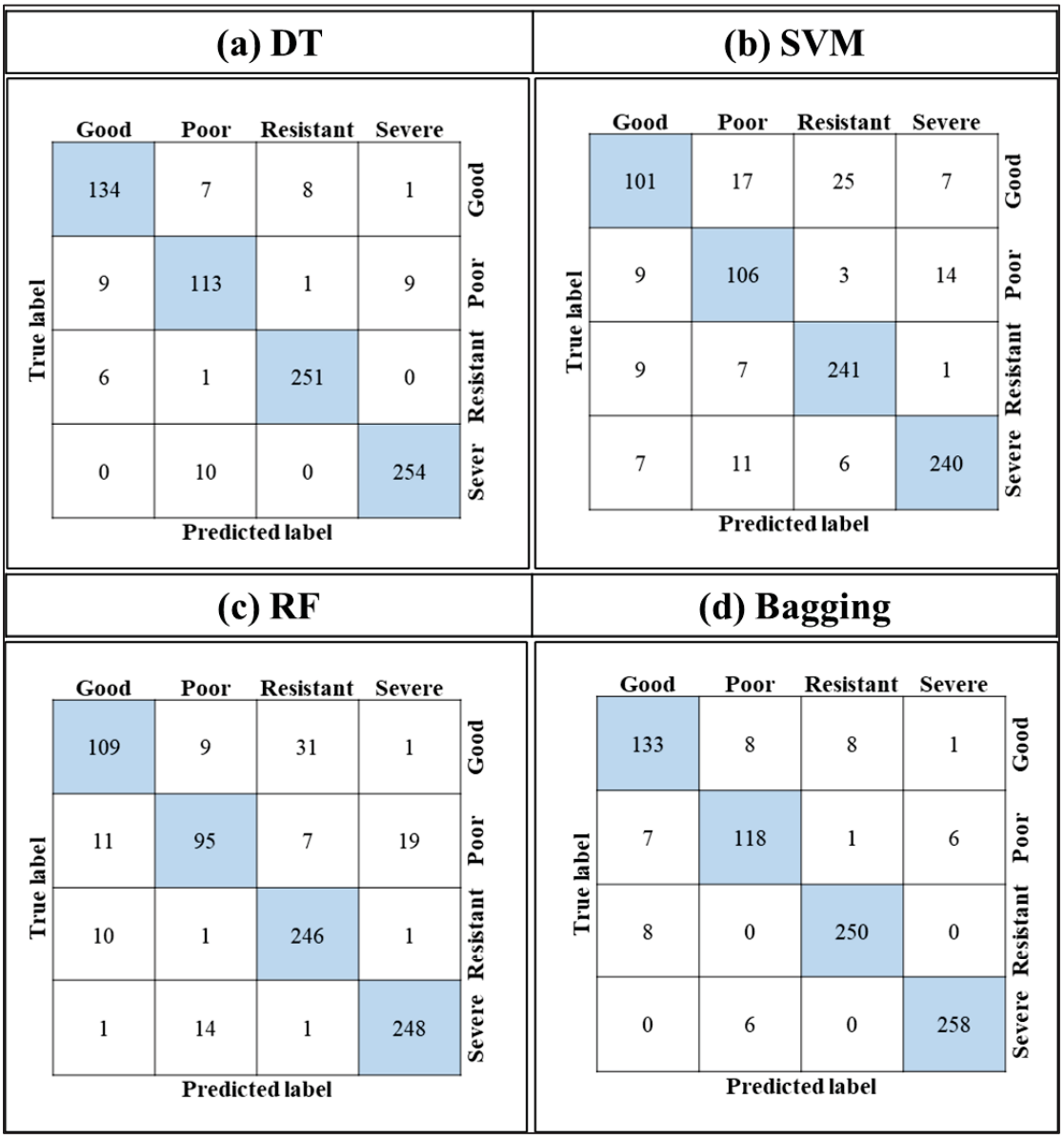

Figure 7.3 Confusion matrices of (a) DT, (b) SVM, (c) RF, and (d) Bagging classifier models for Dataset No. 1

In a next step, calculating the precision is useful for evaluating the performance of a classifier. The precision for each row is the proportion of correct predictions (blue squares) to the total

predicted instances in that row as shown in Equation (7.1). These values can be obtained from the confusion matrix (Figure 7.3).

$$Precision = \frac{number\ of\ correct\ predictions}{number\ of correct\ predicions + number\ of false\ predictions} \quad (7.1)$$

Using Equation (7.1), the precision values for all four classes, which are presented in Table 7.4, were calculated. The results indicate that DT achieved the highest prediction precision for the "Good" and "Resistant" classes, with values of 89.3% and 97.3%, respectively. On the other hand, Bagging exhibited the highest precision for the "Severe" and "Poor" classes, with values of 97.7% and 89.3%, respectively. As discussed before, in this case correct predictions of “Severe” and “Poor” classes are more valuable than those of “Good” and “Resistant”. Further analysis of the confusion matrices revealed that the Bagging model had a higher precision for the "Severe" class, with 258 out of 264 testing data correctly classified and 6 mislabeled as "Poor". In comparison, both the SVM and RF models made false predictions for the "Good" and "Resistant" classes when predicting the "Severe" class, which could lead to serious consequences in the industry if the wrong material is chosen. This indicates that the Bagging classifier may provide safer (i.e., “Severe” or “Poor” classes are not predicted as “Resistant” or “Good” classes) and more accurate predictions for the "Severe" class compared to the other models.

Table 7.4 Precision of DT, SVM, RF, and Bagging models for each class of corrosion behavior

Models	Severe	Poor	Good	Resistant
DT	96.2 %	85.6 %	89.3 %	97.3 %
SVM	90.9 %	80.3 %	67.3 %	93.4 %
RF	93.9 %	72.0 %	72.7 %	95.3 %
Bagging	97.7%	89.3%	88.7%	96.9%

Based on the discussion in sections 7.3.1.1 and 7.3.1.2, it can be claimed that the Bagging classifier is the best ML model for predicting the corrosion behavior of SS material in different

environmental conditions. This selection is based on both data-driven and application-driven approaches, which consider numerical accuracy and safe prediction, respectively.

7.3.2 Evaluation of ML algorithms for Dataset No. 2

This section presents the results of corrosion behavior modeling using Dataset No. 2, and similar to section 7.3.1, the best model is identified based on accuracy, confusion matrix analysis, and prediction precision. Additionally, the importance of input features that contribute to the corrosion behavior of SS material is discussed in detail.

7.3.2.1 ML model comparison based on accuracy

In this study, Dataset No. 2 was created using the method explained in section 7.2.4, and the four models that were previously applied to the first dataset were used to test the accuracy of the models on the new dataset. Figure 7.4 illustrates the obtained accuracies before and after hyperparameter tuning. Hyperparameter tuning resulted in the SVM model exhibiting the greatest improvement in accuracy (from 53.07% to 75.4%), whereas the accuracy of the RF model remained unchanged at 73.79%, which may suggest that the default hyperparameters were already optimal for this dataset. The DT and Bagging models had minor improvements of approximately 3% after hyperparameter tuning. On this dataset, the DT model achieved the highest accuracy (93.53%) among the models used, whereas the Bagging model had the highest accuracy in Dataset No. 1. A comparison between Figure 7.2 and Figure 7.4 shows that both the DT and Bagging models perform well on these two datasets. In contrast, the accuracy of the SVM and RF models experienced a significant decrease in Dataset No. 2, indicating that these models may not be the optimal choice for this classification problem. The consistent performance of the DT and Bagging models on both datasets makes them promising options for this classification problem.

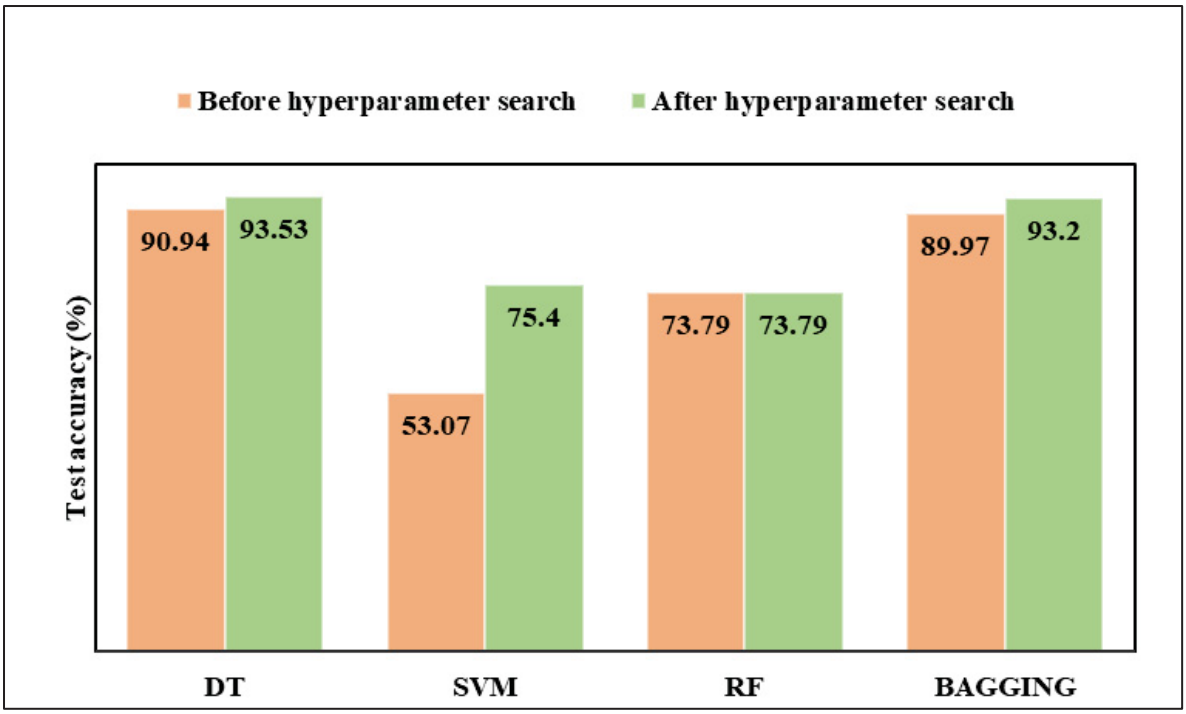

Figure 7.4 Testing accuracies after applying different models on the Dataset No. 2

7.3.2.2 ML model comparison based on confusion matrix analysis

Similar to section 7.3.1.2, an assessment of the confusion matrix was performed to measure the effectiveness of the corrosion classification model on the second dataset (Dataset No. 2, see Table 7.3). As in the first dataset, we consider the accurate detection of severe corrosion behavior to be of primary importance in this context, due to the high costs associated with failing to detect such behavior. Therefore, a similar approach to balance both numerical accuracy and application-driven costs in the evaluation and optimization of the model's performance is adopted. The confusion matrices for the four ML models are shown in Figure 7.5. The prediction precision for each class is calculated according to Eq.1 and the results are presented in Table 7.5. The results indicate that both DT and Bagging have the highest precision of 95.3% for the "Severe" class, meaning they have made an equal number of incorrect predictions. However, when comparing the two models, the confusion matrix reveals that DT made two incorrect "Poor" predictions for the "Severe" class, while the Bagging classifier made one "Poor" and one "Good" incorrect prediction for this class. Therefore, DT

is considered a better algorithm because it does not make "Good" or "Resistant" predictions for this class, and it has the highest prediction precision for the "Poor" and "Good" classes. Although the DT model does not give the highest prediction precision for the "Resistant" class, it is still selected as the best-performing model for Dataset No. 2 because the priority is on accurately detecting severe and poor corrosion behavior based on the application-driven approach for model selection.

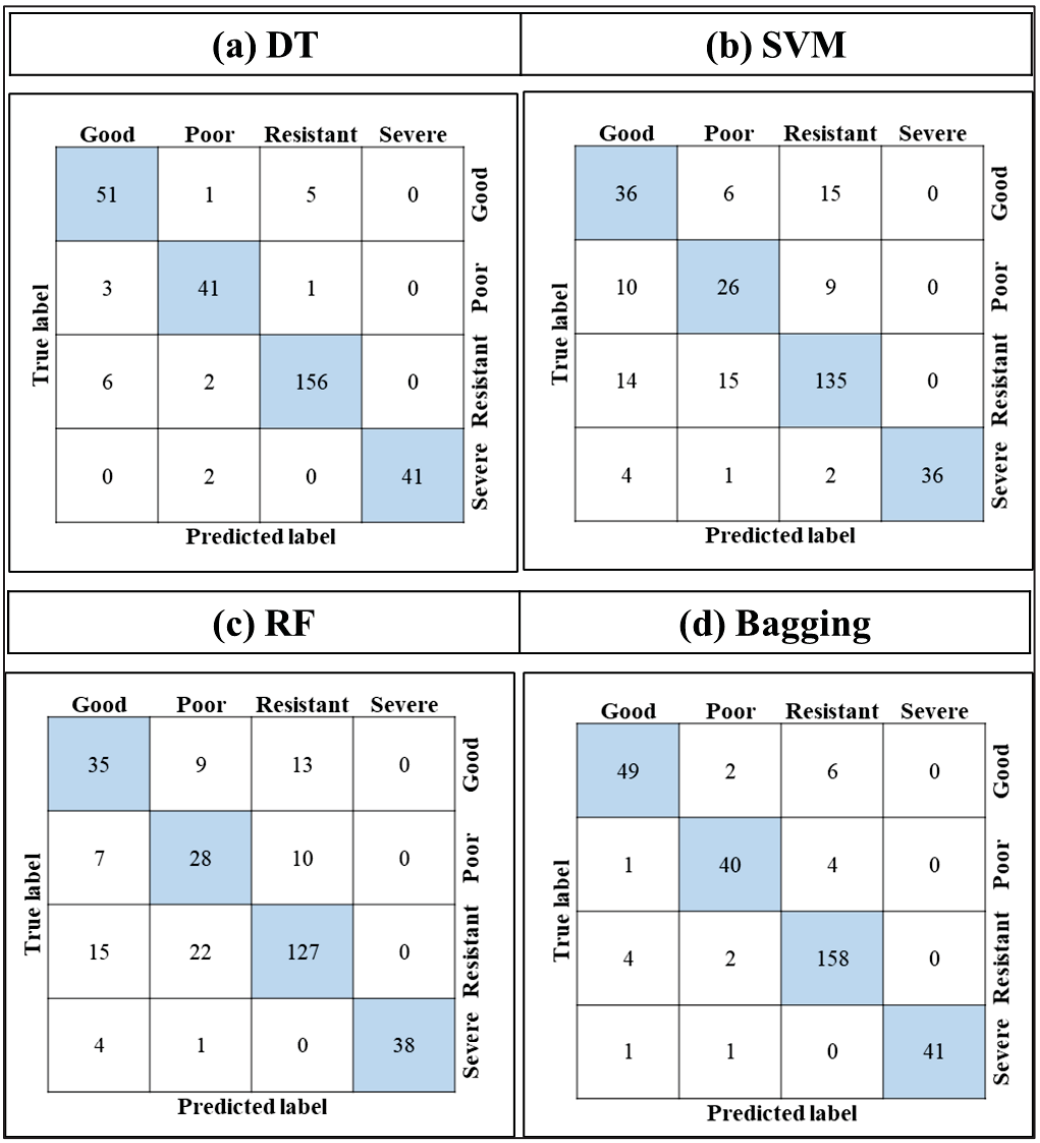

Figure 7.5 Confusion matrix of (a) DT, (b) SVM, (c) RF, and (d) Bagging classifier models for Dataset No. 2

Table 7.5 Precision of DT, SVM, RF, and Bagging models for each class of corrosion behavior

Models	Severe	Poor	Good	Resistant
DT	95.3 %	91.1 %	89.5 %	95.1 %
SVM	83.7 %	57.8 %	63.1 %	82.3 %
RF	88.4 %	62.2 %	61.4 %	77.4 %
Bagging	95.3%	88.9%	86.0%	96.3%

Regarding the good performance of Bagging classifier and DT models for datasets No. 1 & 2, respectively, it is worth mentioning that both datasets comprise the weight percentages (wt.%) of 13 elements, representing the SSs' chemical compositions. All materials in these datasets belong to the same category of steel known as "stainless steel". To be more specific, although different grades of SSs are considered in these datasets, a certain amount or range of some elements is required for the steel to be included within SS category. Consequently, the values of the chemical compositions are closely situated and frequently overlap. SVMs excel in cases where the data exhibits clear separation, allowing for distinct class margins. However, if the datasets lack linear separability or contain overlapping classes, SVMs may struggle to determine an optimal decision boundary, resulting in reduced accuracy (Santos et al., 2022). Consequently, even after hyperparameter tuning, the SVM classifier exhibits the lowest accuracy compared to the other models applied to both datasets. While RF is an ensemble method that builds upon the DT algorithm, there are instances where RF may not perform as effectively as individual DTs or Bagging classifiers. RF, DT, and Bagging classifiers are all ML algorithms belonging to the ensemble method family and are based on DTs. However, they differ in their fundamental principles and the approach through which they generate final predictions. In the RF model, instead of utilizing all features for each split in the DTs, a random subset of features is considered at each split. In these two datasets, the RF model may randomly select features that possess identical values but exhibit different corrosion behaviors, thereby leading to misclassifying the corrosion behavior, and lower accuracy compared to the DTs and Bagging classifier (Bernard et al., 2009). To conclude, one drawback of the RF model in this study dataset is the utilization of feature randomization. However, both the Bagging classifier and DT models do not involve feature subset selection or randomization in their training

process. This absence of randomization can be considered as a strength that contributes to the good performance of the DT and Bagging classifier models for this dataset (Quinlan, n.d.).

7.3.2.3 Feature importance

In DTs, feature importance refers to the relative importance of each feature in making a prediction. It is a metric that calculates the contribution of each feature to the accuracy of the DT model. A high feature importance score indicates that a particular feature is more informative and has a greater impact on the DT's ability to make accurate predictions (Zhou et al., 2021).

Feature importance values were computed only for Dataset No. 2, as applying this analysis to Dataset No. 1 would not produce meaningful insights, as that dataset is classified based on the type of corrosive environment. For example, feature importance values for Dataset No. 1 would show that the importance of Hydrochloric acid is higher than Potassium bisulfate in the classification of SS corrosion behavior, which is trivial information for an end-user. However, in Dataset No. 2, the importance of ions and chemical compositions in the classification of SS corrosion behavior is directly related to the chemical reactions of the involved materials. Therefore, calculating the feature importance for Dataset No. 2 provides insights into the chemical factors that influence SS corrosion behavior, which can be used to optimize corrosion-resistant material design and selection.

Figure 7.6 shows the ranking of feature importance for Dataset No. 2 in the DT model. This ranking provides insights into the factors that have the most significant impact on the classification of SS corrosion behavior, allowing for better-informed decisions in the design of materials and the selection of appropriate corrosive environments. The three most important features, according to this ranking, are hydrogen ion concentration (0.38), sulfide ion concentration (0.20), and the weight percentage of iron in the chemical composition of the SS (0.19). These features are ranked respectively as number one to three in terms of importance, with hydrogen ion concentration having the highest importance and iron weight percentage having the third highest. The other input features appear to have lower relative importance values, ranging from 0.049 for Mo to 0 for some features like S and Mn. This suggests that

these features are less important in determining the classification of SS corrosion behavior in the dataset. Although the weight percentages of Cr and Ni are known to significantly influence the corrosion behavior of SSs, it is worth noting that this dataset only includes SSs as the materials of interest. Since all SSs contain Cr and Ni, the weight percentages of these elements cannot serve as a decisive factor in the classification of materials in this specific context. As a result, the relative importance of these factors is not particularly high in this study. Similarly, the environmental temperature has a clear influence on the corrosion behavior of SSs. However, in Dataset No. 2, since the temperature of all data samples was fixed at 20 ºC, it did not have any relative importance in predicting the corrosion behavior in this context.

To discuss the importance of the top three features from both material and environmental perspectives, it is worth noting that hydrogen ion concentration can significantly affect the corrosion behavior of SS. As the concentration of hydrogen ions increases, the pH of the solution decreases, resulting in a more acidic environment. This increased acidity can accelerate the rate of corrosion by reacting with the surface of the steel, removing the protective oxide layer and exposing the metal to further corrosion (Dastgerdi et al., 2019a; Z. Wang et al., 2018). Sulfide ion concentration is another important factor that affects SS corrosion. When sulfide ions come into contact with SS, they can react with the iron to form iron sulfide, which can lead to pitting corrosion. The rate of corrosion increases with an increase in the concentration of sulfide ions. At high concentrations, sulfur can also cause cracking of the SS, which can significantly compromise its structural integrity. Moreover, the presence of sulfide in the environment can lead to the formation of sulfuric acid, which further accelerates the corrosion of SS (Betova et al., 2010; Z. Wang et al., 2018; Zhang et al., 2021). Iron is a major element in SS alloys and its weight percentage is representative of the alloying level in steels. An increase in the weight percentage of iron may lead to a decrease in the material's resistance to corrosion. In general, SS is highly resistant to corrosion due to the formation of a passive oxide layer on its surface. This layer is composed mainly of chromium oxide and is responsible for protecting the underlying metal from corrosive attack. However, an increase in the weight percentage of iron can lead to the formation of other oxides, such as iron oxide, that can compromise the integrity of the passive layer and reduce the overall corrosion resistance of the material (B. Sun et al., 2020; J. Sun et al., 2022).

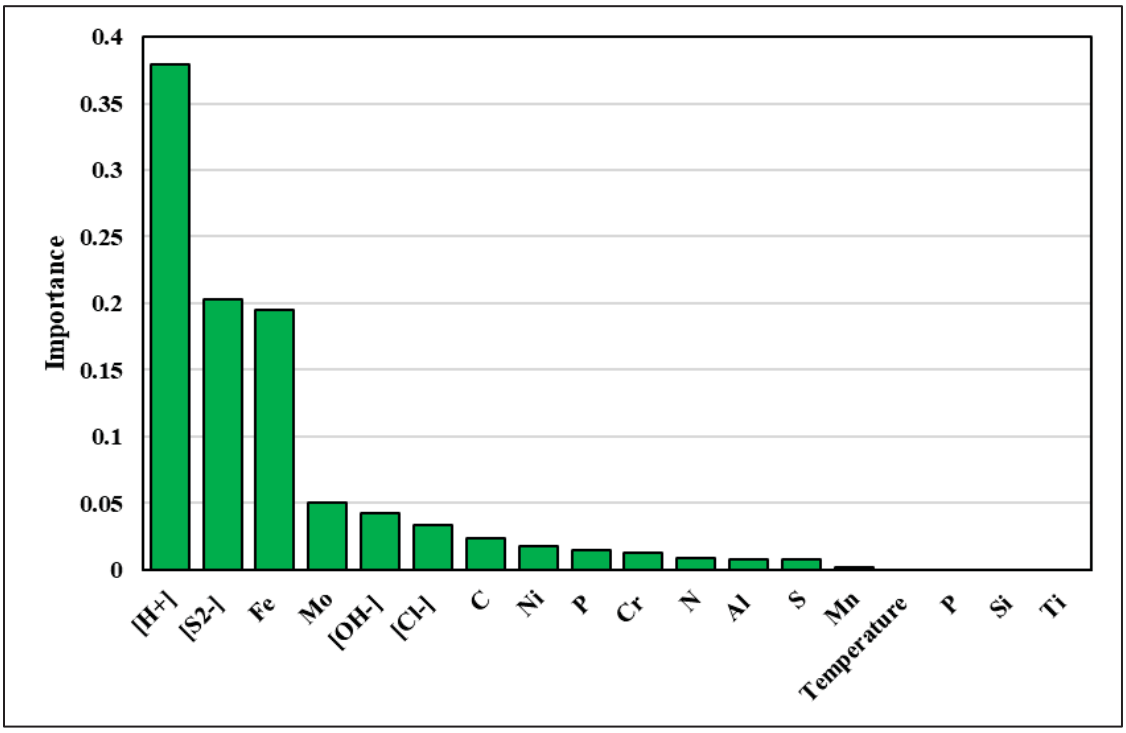

Figure 7.6 The importance sequence of input features in Dataset No. 2

Due to the higher accuracy achieved by the DT model when applied to Dataset No. 2, it was specifically trained using only three inputs: hydrogen, sulfide, and iron concentrations. Consequently, the testing accuracy of this model decreased from 93.53% (when all 18 features were considered) to 89.64% (with only the three most important features included). Figure 7.7 illustrates the confusion matrix of the DT model following feature reduction. In comparison to Figure 7.5 (a), it can be observed that within the "Severe" class, one instance was misclassified as "Good." Similarly, within the "Poor" class, one instance was misclassified as "Good," and two instances were misclassified as "Resistant." According to the reported accuracies in Table 7.6, the precision of the DT model after feature reduction exhibited a significant decrease in the "Poor" and "Good" classes compared to the "Severe" and "Resistant" classes. This indicates that feature reduction has a greater impact on the "Poor" and "Good" classes. The DT model applied to Dataset No. 2 after feature reduction demonstrated both high accuracy and high precision across different classes, thus confirming the importance of the selected features. Therefore, in situations where information about other feature values is unavailable, the

corrosion behavior of the SS can still be predicted by solely considering hydrogen ion, sulfide ion, and iron concentrations.

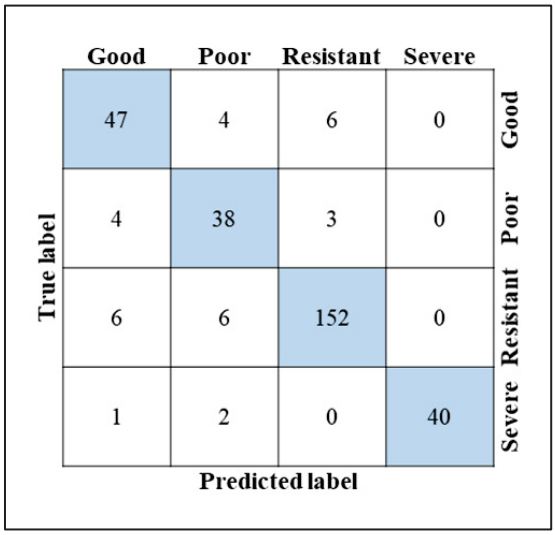

Figure 7.7 Confusion matrix of DT model for Dataset No. 2 after feature reduction

Table 7.6 Precision of DT model for each class of corrosion behavior

Models	Severe	Poor	Good	Resistant
DT	93.02 %	84.44 %	82.45 %	92.68 %

As a result, the feature importance ranking can guide the adjustment of environmental conditions for the service application of specific SS materials, by highlighting the significance of pH and sulfide ion on corrosion behavior. Additionally, by utilizing the elemental ranking, it can be observed that high alloy SS with low iron content has the best corrosion resistivity. Further insights from the ranking of other elements can support the selection of the most suitable alloy for a specific application.

7.3.3 Material selection practical approach

As mentioned in the introduction, the primary aim of this study is to present an informative model that can assist in the selection of SS materials for various environments. Figure 7.8 illustrates a practical flowchart for the systematic process of choosing the appropriate SS grade

based on its corrosion resistance. Depending on the available information regarding the material (e.g., chemical composition) and the environment (such as solution type, concentration, and temperature), three models have been developed to predict the corrosion behavior of the SS. The selection of these models (Bagging, DT, DT + feature reduction) is based on two comprehensive analyses, considering both their accuracy and their suitability for practical applications.

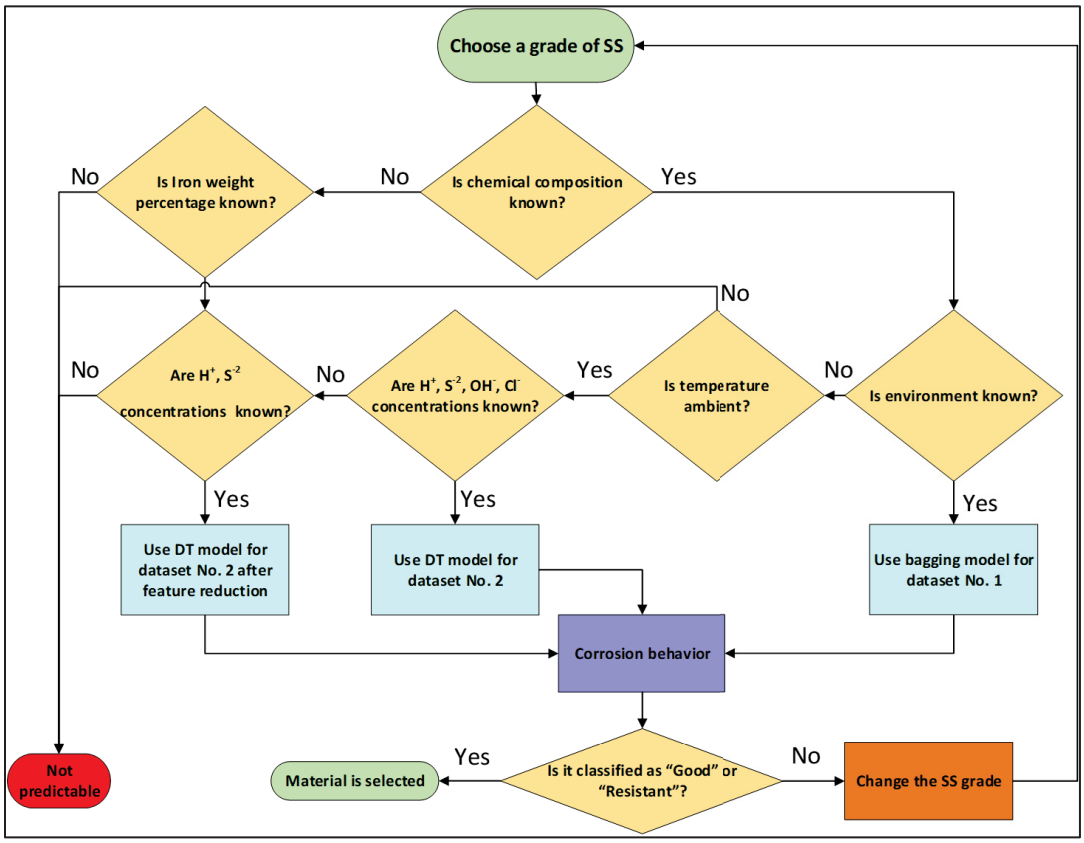

Figure 7.8 Flowchart illustrating the selection process for SS material using the developed models

7.4 Conclusion

In this paper, ML models, including Decision Tree, Support Vector Machine, Random Forest, and Bagging classifier, were evaluated for their performance in predicting the corrosion behavior of SS in different environments and service conditions which were considered as two

different types of inputs (Dataset No. 1 and Dataset No. 2). According to the obtained results and analysis it was revealed that:

- Bagging classifier achieved the highest testing accuracy of 94.4% for Dataset No. 1, making it the most effective model for predicting the corrosion behavior of SS grades.
- Confusion matrix analysis was used to evaluate the models' performance beyond accuracy with application-driven approach for model selection. Again, Bagging model exhibited the highest precision for the "Severe" and "Poor" corrosion behavior classes, which are more critical to detect accurately than the "Good" and "Resistant" classes.
- For Dataset No. 2, the DT model achieved the highest accuracy (93.53%) among the deployed classification models, and it also was selected as the most suitable model based on the confusion matrices analysis.
- By conducting a feature importance analysis on Dataset No. 2, the most influential factors contributing to the corrosion behavior of SS in different environments were identified, providing valuable insights for material selection and design. The analysis revealed that hydrogen and sulfide concentrations in corrosive environments, as well as the amount of alloying elements (which are complementary to the amount of iron in SS), are three features that can influence corrosion behavior up to 77.8%.

The developed model can predict the corrosion behavior of different grades of SSs in 14 different corrosive environments (Dataset No. 1) without requiring any experimental testing. In order to increase the generalizability of the model and to enable its application to a wider range of environments beyond those considered in this study, a second model was developed that considers only the concentration of four corrosion critical ions (Dataset No. 2). These developed models have the potential to prevent failures due to corrosion by providing important information about SS behavior in specific environments. The ability to predict corrosion behavior without the need for experimental testing, can help save time and resources while improving the reliability of corrosion-related decisions. Future work could include expanding the dataset to include more environmental conditions and different types of steels rather than only SSs.

Acknowledgments

This work was supported by the Natural Sciences and Engineering Research Council of Canada (NSERC) under the Discovery Grant (RGPIN-2019-05973 and RGPIN-2021-03780).

CHAPTER 8

CORROSION TYPE IDENTIFICATION IN FLANGED JOINTS USING A NOVEL RECURRENT NEURAL NETWORK TECHNIQUE APPLIED TO ELECTROCHEMICAL NOISE MEASUREMENTS

Soroosh Hakimian [a], Abdel-Hakim Bouzid [a], Lucas A. Hof [a]

[a] Mechanical Engineering Department, École de technologie supérieure, 1100, rue Notre-Dame Ouest, Montreal, Québec, H3C 1K3, Canada

Paper submitted for publication, November 2024.

Abstract

Bolted flanged joints are critical to connect piping and process equipment. These engineering structures are subjected to general and localized corrosion leading to leakage. Localized corrosion within these joints propagates rapidly from the inside, making leaks due to corrosion both unpredictable and sudden, and limiting the effectiveness of commonly used periodic monitoring techniques. Electrochemical noise (EN) measurements are effective in detecting localized corrosion. However, processing raw EN data requires expertise and is time-consuming. In the present study, recurrent neural networks (RNNs) are applied to process electrochemical noise (EN) signals generated by spontaneous electrochemical reactions on flange surfaces to differentiate corrosion types occurring on these surfaces. The primary contribution of this work is the fully automated differentiation of corrosion types without the need to preprocess the measured input current and potential data as RNN model inputs. Experimentally obtained EN data serve as the database for this work, where three approaches—supervised, hybrid, and unsupervised techniques—are tested and compared on classification performance. Among the supervised models, the long short-term memory (LSTM) model demonstrates the highest classification accuracy, achieving 93.62% accuracy in identifying corrosion types. A hybrid approach using a random forest (RF) model combined with LSTM autoencoder-extracted features achieved an accuracy of 97.85%. The developed

unsupervised approach, utilizing the LSTM autoencoder with principal component analysis for dimensionality reduction and k-means clustering, provides a promising solution for real-time corrosion monitoring to detect corrosion types. Identifying the types of flange face corrosion enables effective decision-making for material protection strategies to prevent potential engineering failures.

Keywords: Recurrent neural networks; Electrochemical noise measurement; Machine learning; Deep learning; Localized corrosion; Corrosion classification

8.1 Introduction

Bolted flanged joints are extensively used to connect pipelines, pressure vessels, and different structural components in seawater desalination equipment, hydrocarbon processing, nuclear industries, and wind turbine industries. This type of connection allows disassembly of pipelines for maintenance or cleaning, but poses a risk of leakage failure especially when exposed to aggressive media and environments while operating at high pressures and temperatures (Nechache & Bouzid, 2007). Flange face corrosion is one of the most repeatable cause of leakage failure according to the literature (Kölblinger et al., 2022). Corrosion on flange faces arises when fluids penetrate gaps and leak paths formed at the gasket and flange interface. These gaps result from material degradation due to corrosion and aging and are further widened by joint loosening due to creep-relaxation effects (A. Bouzid et al., 1995; Nechache & Bouzid, 2007, 2008), rotation of the flange (A. Bouzid et al., 1994; H. Bouzid et al., 2004), and flange face irregularities (Worden, 2014a). Localized corrosion, such as pitting and crevice corrosion, at the interface of the flange and gasket is a major cause of leakage failure in flanged gasketed joints (Farfan-Cabrera et al., 2021; Hakimian et al., 2024b, 2024c; Kain, 1998a; Kölblinger et al., 2022). Crevice corrosion is not easily detectable or visible at the flange-gasket interface, and due to its localized nature, it exhibits a higher corrosion rate compared to general corrosion by several orders of magnitude (Nyby et al., 2021). Corrosion of the flange surface becomes detectable only when a leak already occurs, necessitating pipeline shutdowns and resulting in

the loss of revenue and costly resources. Therefore, detection and monitoring of the early stages of localized corrosion are critical to prevent extensive damage on such systems.

Electrochemical noise measurement (ENM) is a method that gains increasing attention in the field of electrochemical monitoring methods (Kearns et al., 1996; Nazarnezhad-Bajestani et al., 2019). The spontaneous fluctuations in potential and current are stemming from the corrosion processes on the metal surface that can be measured by ENM (A. M. Homborg, Tinga, et al., 2014). This method is suitable for *in situ* corrosion monitoring without applying an external potential, and it can also be used to detect the type of corrosion (Al-Mazeedi & Cottis, 2004; Ma et al., 2019a). Characterization of localized corrosion through current and potential signal monitoring is the most interesting application of ENM (Hladky & Dawson, 1981). This technique is also a valuable tool in assessing the performance of protective coatings and corrosion inhibitors (A. M. Homborg, Van Westing, et al., 2014; Jamali et al., 2024). Indeed, ENM shows great potential as a non-destructive monitoring tool; however, distinguishing between localized and general corrosion remains challenging because EN data is dependent on factors such as the electrode system type, electrode surface area, and the measurement technique used (Xia et al., 2020). In the literature, data analysis methods are typically categorized according to their operational domain, including time (Ramírez-Platas et al., 2021), frequency, and time-frequency domain (A. M. Homborg et al., 2013). Obtaining appropriate feature variables and analytical approaches from the measured EN data to distinguish between different forms of corrosion during the monitoring is the main difficulty of this method (Abdulmutaali et al., 2024).

Recently, machine learning (ML) and deep learning (DL) techniques have been increasingly utilized in the field of corrosion to analyze EN data for prediction or classification. Homborg et al. (A. Homborg et al., 2024) investigated the application of convolutional neural networks (CNN) for DL-based classification of images of the electrochemical noise time-frequency transient information from two types of pitting corrosion data. In this approach, two methods including continuous wavelet transform (CWT) spectra and modulus maxima (MM) are used to train the CNN. Their results show that training the CNN with the CWT and MM combination has a higher classification accuracy compared to using each method separately. In another study, Hou et al. (Hou et al., 2017) extracted twelve features from the EN signals using a

recurrent quantification analysis and they then classified the corrosion behavior to general, passive, and pitting corrosion using random forests (RF) and linear discriminant analysis (LDA). Nazarnezhad et al. (Nazarnezhad-Bajestani et al., n.d.) used EN analysis parameters obtained from time domain, frequency domain, and time-frequency domain analysis methods as inputs in an artificial neural network (ANN) model and using galvanostatic electrochemical impedance spectroscopy as target values to determine the pitting stage in stainless steel 321. Furthermore, Alves et al. (Alves et al., 2019) extracted features from EN data using wavelet transform and recurrence quantification analysis to train several ML techniques including the ANN type multilayer perceptron (MLP), probabilistic neural network (PNN), support vector machine (SVM), k-nearest neighbor (kNN), and decision tree (DT). Finally, Jian et al. (Jian et al., 2013) deployed a feature vector of 10 elements obtained from the EN datasets as an input for training ANN and SVM models to distinguish the type of corrosion. Table 8.1 summarizes all ML and DL techniques that are used to analyze EN data for corrosion type classification.

Table 8.1 Summary of the ML and DL techniques used in analyzing EN data for corrosion type classification

Input features	**Types of corrosion**	**ML or DL methods**	**Number of features**	**Reference**
Images of the CWT spectrum and MM including transient locations	Pitting	CNN	Unsupervised feature extraction	(A. Homborg et al., 2024)
Recurrence quantification variables	General Pitting Passivation	LDA RF	12	(Hou et al., 2017)
Recurrence quantification variables	General Pitting Passivation	MLP	4	(Hou et al., 2016)
Time domain, frequency domain, time-frequency domain parameters	Pitting	ANN	26	(Nazarnezhad-Bajestani et al., n.d.)

Input features	Types of corrosion	ML or DL methods	Number of features	Reference
R_n, q, f_n, energy of 7-level wavelet crystal	General Pitting Passivation	ANN SVM	10	(Jian et al., 2013)
Wavelet transform and recurrence quantification parameters	Crevice Passivation Pitting Watermark	MLP PNN kNN DT SVM	35	(Alves et al., 2019)

It can be concluded from the reviewed literature that ML and DL approaches used so far are promising, but require substantial amounts of labeled data to achieve accurate classification. This presents a major barrier for practical use in industrial applications, because collecting extensive labeled datasets in real-world corrosion environments is challenging. Additionally, these techniques are often limited by their dependence on feature vectors based on static signal characteristics, like noise resistance or frequency content, which may not adapt well to dynamic conditions in corrosion processes.

Therefore, the main objective of this study is to investigate the potential of utilizing recurrent neural networks (RNN) for classifying EN data and to compare its accuracy with traditional ML techniques such as RF. RNNs are well-suited for time-series or sequential data as they can detect hidden patterns or recurring trends in nonlinear and dynamic datasets (Durstewitz et al., 2023). One of the key strengths of RNNs is their ability to retain information from previous hidden states, enabling the prediction of future outcomes (Mienye et al., 2024). This characteristic has made them widely adopted in fields like natural language processing and speech recognition (Graves et al., 2013; Yin et al., 2017). Due to their recurrent structure, RNNs have the potential to be more flexible in handling variability within EN data compared to static classifiers.

This paper introduces three novel approaches using RNN models to classify corrosion types based on two input features; current and potential signals from EN data. In these developed

approaches, firstly, labeled data obtained through controlled laboratory experiments, are used to train RNN models. Then, using these labeled data, a hybrid approach is used to improve the model's performance. Finally, an unsupervised approach is proposed that is trained using unlabeled data, as mostly occurs in real-time corrosion monitoring.

To evaluate the classification performance of these models, different techniques including confusion matrix and other classification metrics, e.g., F1-score, precision, and recall are calculated. Indeed, the effectiveness of the different RNN-based methods for EN data analysis are validated by experimental corrosion data using an in-house developed bolted joint test rig (Hakimian et al., 2024a), highlighting their potential for real-time corrosion monitoring.

8.2 Methodology

The overview of the methodology used in this study is shown in Figure 8.1. In order to study the applicability of RNN models to process EN data, in a first step, experimental tests are performed to collect data for model training. Then, collected data are preprocessed and prepared by removing outliers, labeling the dataset, and encoding categorical data, to feed the models. Subsequently, different learning models, as shown in Figure 8.1, are trained and their performances are evaluated and compared with each other, using confusion matrices and other typical DL and ML performance metrics (section 8.2.5). Three approaches are considered, namely supervised learning, hybrid learning, and unsupervised learning. The supervised and hybrid learning models need labeled data to train and predict labels, but the unsupervised learning models are used in cases where data are not labeled, which is typically the case in uncontrolled, real-world environments. Hyperparameter tuning is conducted for each model to identify the parameter values that yield the highest accuracy. Confusion matrices are also used in the evaluation step to visualize the predicted corrosion types versus true corrosion types. All ML models are built using Python in Jupyter notebook. The details of each step in Figure 8.1 is discussed in the following sub-sections (8.2.1 to 8.2.5).

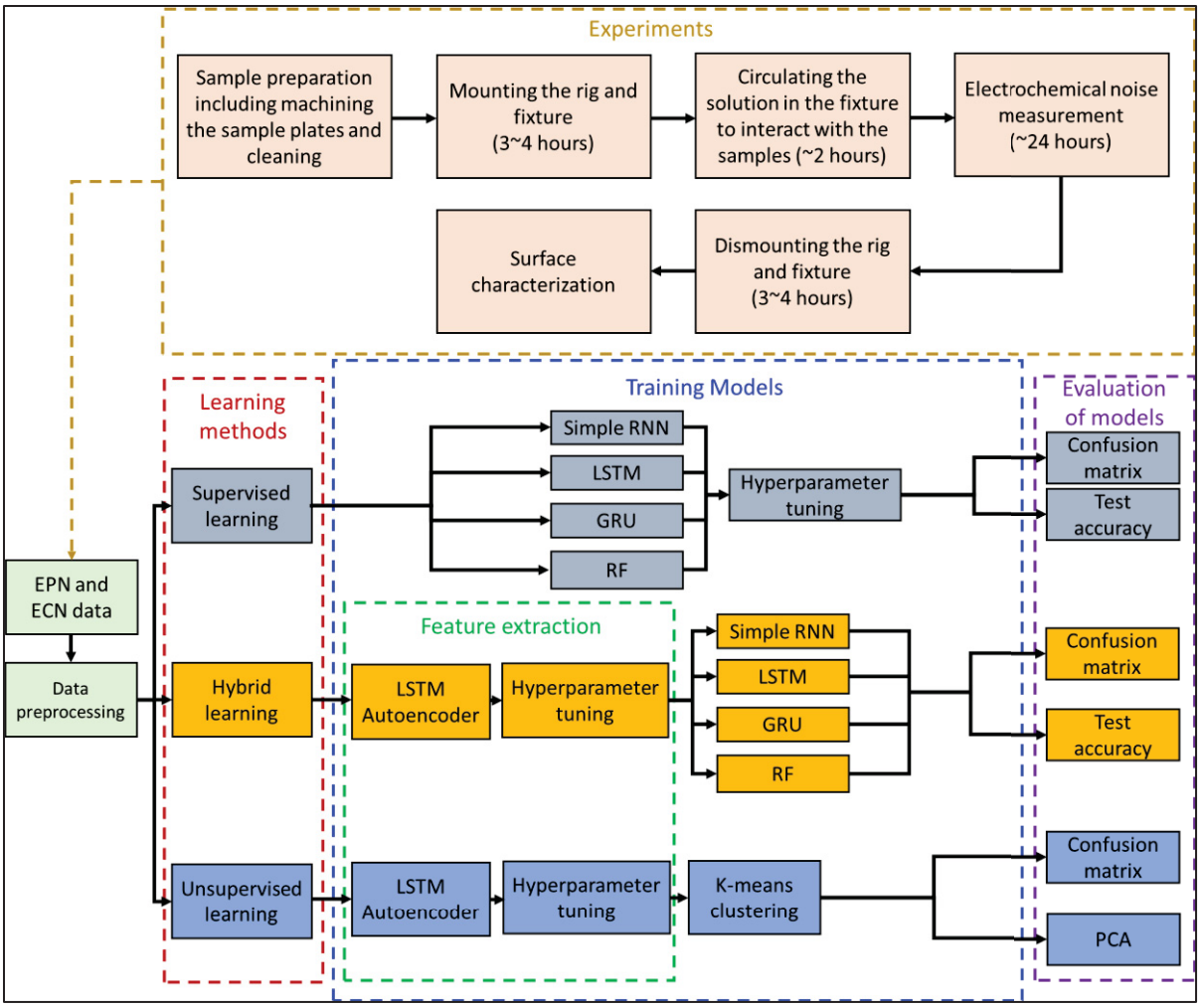

Figure 8.1 Schematic overview of the methodology used for the classification of the type of corrosion

8.2.1 Experiments

In this section, the details of the experiments, including materials, electrochemical tests, and corroded flange surface analysis, are comprehensively discussed in the following subsections (8.2.1.1 to 8.2.1.3).

8.2.1.1 Materials

The materials of the sample plates are ASTM A105 carbon steel, and ASTM A182 F321 stainless steel (SS) which are widely used in the manufacturing of flanges. The chemical compositions of the flange materials are provided in Table 8.2. The flange sample plates have an outside diameter OD of 2.95 in. (74.93 mm), an inside diameter ID of 1.31 in. (33.27 mm), and a thickness of 0.25 in. (6.35 mm) (as shown in Figure 8.2 (a)). Virgin polytetrafluoroethylene (PTFE) gaskets are used between the sample plates, following the specifications of ASME B16.21(ASME B16.21, 2022) for non-metallic flat gaskets used in flanges. The thickness of the gasket is 3.17 mm with the ID and OD of 48.26 and 71.12 mm, respectively (as shown in Figure 8.2 (a)). The surface area of the flange that is exposed to the solution is equal to 9.73 cm^2 for each sample plate. The roughness of the sample plates is measured using a Mitutoyo Surftest SJ-410 mechanical profilometer following the ISO 21920-2:2021 standard, as commonly used in the literature (Pourrahimi & Hof, 2024). A cut-off length of 0.8 mm and a short wavelength cut-off filter λ_s of 2.5 μm are used, resulting in an arithmetic mean of absolute height values Ra= 1.006 ± 0.05 μm after three measurements on three different samples

Table 8.2 Chemical composition of flange sample plates (wt. %)

Elements	**C**	**N**	**Si**	**P**	**S**	**Cr**	**Mn**	**Ni**	**Mo**	**Cu**
321 SS	0.049	0.024	0.54	0.03	0.001	17.45	1.57	9	0.37	0.48
A 105	0.19	0.01	0.22	0.01	0.02	0.17	1.09	0.09	0.03	0.24

8.2.1.2 Electrochemical tests

In order to perform electrochemical tests in conditions close to real-world flanged gasketed joints, the gasket is sandwiched between two flange sample plates as shown in Figure 8.2 (a), and then placed in the fixture (Figure 8.2 (b)) of an in-house developed test rig. Since flanged gasketed joints are secured using hydraulic tensioners that apply high initial compressive stress (Murali Krishna et al., 2007), the fixture illustrated in Figure 8.2 (b) is positioned on a stand

with a hydraulic tensioner to compress the gasket to an initial average stress level of 15 MPa. This contact stress is calculated based on the measurement of the central bolt force using a full Wheatstone bridge with strain gauges attached to the central stud before testing.

The fixture is composed of nuts for fastening the joints after applying the compressive load, plain washers to increase the contact area, compression plates that have entrance and exit ports for the solution, electrical insulators to avoid electrical short circuits between the flange sample plates, which are also used as working electrodes (W.E.1 and W.E.2), compression plates and Belleville washers to maintain the preload during the electrochemical tests. The O-rings are placed between the central stud and the compression plates to seal the solution chamber and avoid electrical short circuits between the central stud and the compression plates. The details of the drawings are shown in ANNEX I.

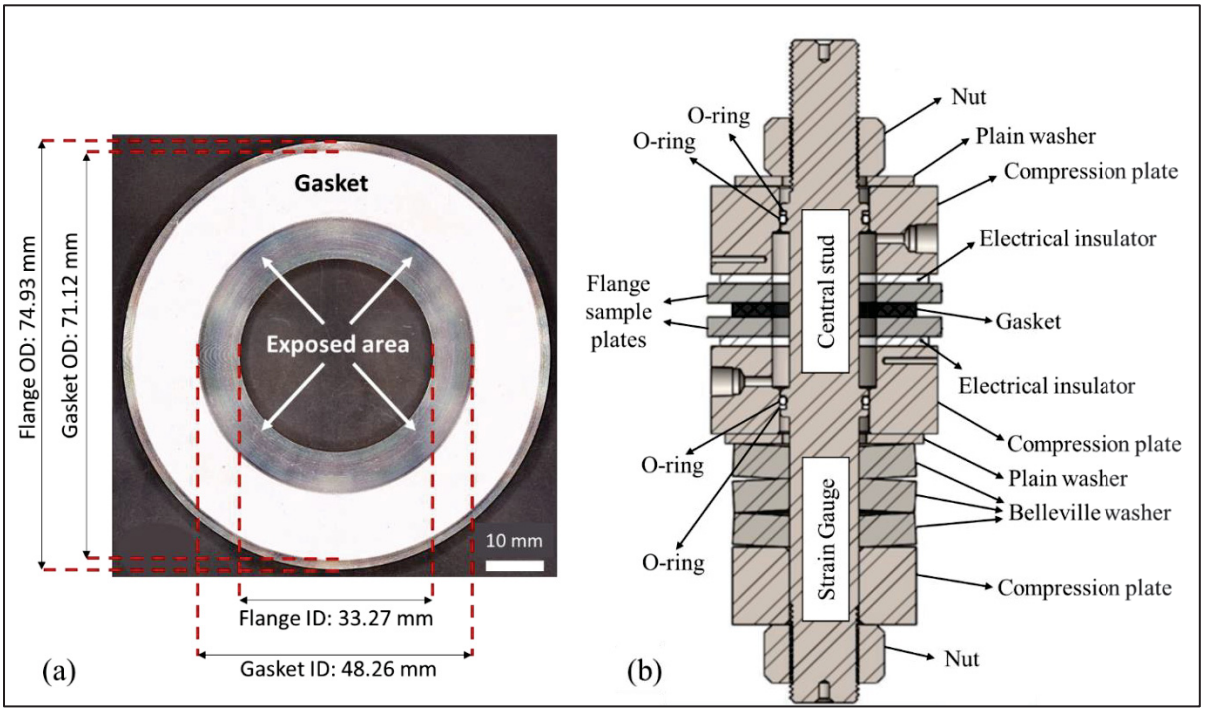

Figure 8.2 The schematic illustration of the (a) flange sample plate including the sizes and the exposed area to the solution; and (b) the test fixture including the labels of each item in the fixture

After mounting the fixture, the tubes and electric wires are connected as shown in Figure 8.3. The electrolytic solution passes through a water-jacketed glass cell used to control and

maintain the temperature to ± 1 ^{o}C. The water jacket surrounds the solution inside the glass cell and acts as a temperature buffer. The heated circulating bath system (Polystat Cole-Parmer CR500WU) controls and maintains the temperature of the water in the jacket side of the glass cell by a heating and cooling system. The electrolyte solution in the glass cell flows into the tubes (identified by the dark blue lines in Figure 8.3) through the peristaltic pump (BRL Life Technologies CP-600). The solution flow rate is adjusted by the peristatic pump and measured by the flow sensor (Digiten FL-402B). The conductivity, pH, and temperature of the solution are measured by the conductivity and pH electrodes connected to a benchtop multiparameter meter (Thermo Fisher STARA2150 series). For the EN tests, a Metrohm Autolab PGSTAT302N High-Performance potentiostat/galvanostat, including a dedicated ECN module (Metrohm ECN.S X19-6), is employed to capture both current and potential data. A Pine Research single-junction, saturated Ag/AgCl reference electrode, equipped with a porous ceramic tip and filled with a 3 M KCl solution, serves as the reference electrode (R.E.), and all potentials are measured relative to this Ag/AgCl electrode. To minimize the effect of the ohmic drop between the reference and working electrodes, a salt bridge is used to connect the test solution in the fixture to the reference electrode. Sensor-generated analog signals are transmitted to a custom-designed printed circuit board (PCB) and digitized by a National Instruments data acquisition (DAQ) card (ANNEX II). The DAQ, potentiostat, and multiparameter meter interface directly with the computer via USB, managed through a LabVIEW program (ANNEX III).

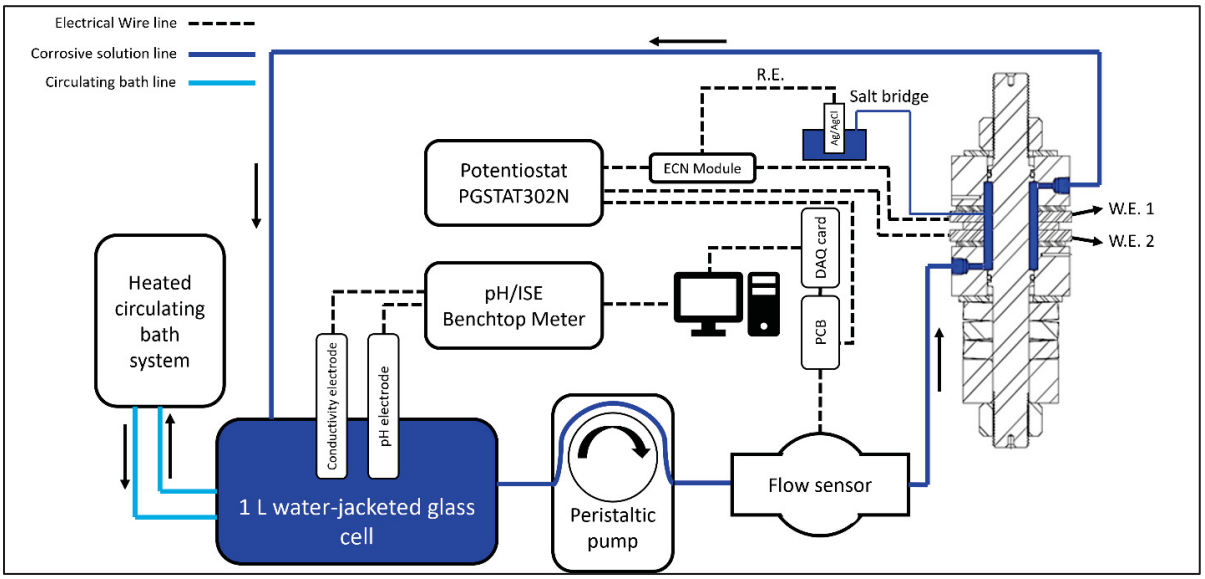

Figure 8.3 The schematic of the test rig including all the sensors and equipment for measurements and monitoring

The EN data are collected from four different experimental conditions (C1-C4). Hence, four test solutions are prepared using the analytical grades which are 0.1 M sodium chloride (NaCl) (C1), 0.5 M sodium hydrogen carbonate ($NaHCO_3$) (C2), 0.45 M sodium hydrogen carbonate + 0.1 M sodium chloride (0.45 M $NaHCO_3$ + 0.1 M NaCl) (C3), and 0.6 M sodium chloride (NaCl) (C4). These solutions are used to induce general corrosion, passivation, pitting, and crevice corrosion, respectively. To induce pitting corrosion, the sample plates are passivated in the 0.5 M $NaHCO_3$ solution for 1 hour before placing in the fixture for testing. The EN measurements are performed by connecting the upper flange sample plate as W.E. 1 and the lower one as W.E. 2 (as shown in Figure 8.2 (b)) in the test rig, which are nominally identical samples and parallel to each other.

The current between the two electrodes is measured using the Zero Resistance Ammeter (ZRA) mode of the Autolab potentiostat, and the potential of the W.E.s is measured relative to the R.E. using the high-resolution Metrohm ECN module. The EN data is collected with a frequency of 2 Hz. Table 8.3 indicates the experimental conditions to build the dataset for training and testing the classification ability of RNN models.

The sample plates are degreased in an ultrasonic bath with ethanol for 20 minutes, followed by air drying before subjected to EN testing. The EN tests start two hours after letting the electrolyte solution circulate within the fixture, ensuring sufficient time for the surfaces of the sample plates and the interface with the gasket to soak. The EN test for each condition is repeated three times to ensure reproducibility of the corrosion type occurring on the flange faces.

Table 8.3 Experimental conditions to make a dataset to test the classification ability of the RNN model

Condition	Rows of data	Material	Solution	Temperature (^oC)	Type of corrosion	Time (h)
C1	154817	Carbon steel A105	0.1 M NaCl	22	General corrosion	21
C2	172712	Carbon steel A105	0.5 M $NaHCO_3$	22	Passive	24
C3	144493	Carbon steel A105	0.5 M $NaHCO_3$ + 0.1 M NaCl	22	Pitting corrosion	20
C4	53742	321 SS	0.6 M NaCl	50	Passive	7.5
C4	101130	321 SS	0.6 M NaCl	50	Crevice corrosion	14

8.2.1.3 Surface analysis

Following each experiment, the flange sample plates are first rinsed with distilled water, then further cleaned with ethanol. The samples are subsequently air-dried at room temperature. The corroded surfaces are observed using a digital microscope (Keyence VHX-7000) with a VHX E20 lens with the tilt angle of 0 degree to characterize and determine the type of corrosion that took place on them.

8.2.2 Data preprocessing

The potential and current signals obtained from the EN tests are labeled during the data preprocessing stage, as illustrated in Figure 8.1. These labels correspond to the type of corrosion observed in the signals and microscopic images: “General,” “Passive,” “Pitting,” and “Crevice.” The categorical labels are then converted into numerical values using the LabelEncoder from the sklearn.preprocessing (*Scikit-Learn: Machine Learning in Python — Scikit-Learn 1.0.1 Documentation*, n.d.) module, allowing the models to process the data.

8.2.3 Deep learning and machine learning models

This section introduces both the DL and ML models used in this research, and provides a detailed discussion of the evaluation and hyperparameter tuning techniques applied.

8.2.3.1 Recurrent Neural Network (RNN)

RNNs are a type of neural network architecture featuring recurrent connections, primarily used to identify patterns within sequential data. This data can include handwriting, genetic sequences, speech, or numerical time series, commonly generated in industrial settings (e.g., by sensors) (R. M. Schmidt, 2019). RNNs contain high-dimensional hidden states characterized by non-linear dynamics. This hidden state structure acts as memory for the network, with each hidden layer state at a given moment influenced by its preceding state (Salehinejad et al., 2017). This allows the network to maintain and update contextual information as it processes a sequence of data. The hidden state update is represented as Equation (8.1), where h_t is the current hidden state, $h_{(t-1)}$ is the previous hidden state, x_t is the current input, W_h and W_x are weight matrices, b is a bias term, and f is an activation function (Jun et al., 2020). The output y_t of the RNN network is obtained by Equation (8.2) at each time step t. The size of the hidden state is a hyperparameter that can be tuned. Larger hidden states can potentially capture more information but also require more computational resources.

$$h_t = f(W_h \times h_{t-1} + W_x \times x_t + b_h) \quad (8.1)$$

$$y_t = W_y \times h_t + b_y \quad (8.2)$$

Figure 8.4 depicts the architecture and operation of a RNN across multiple time steps. The inputs at different time steps (x_{t-1}, x_t, x_{t+1}, …, x_{t+n}) are represented by the blue circles on the left. Each input is processed through several hidden layers (h_1, h_2, h_3) at each time step t. The hidden layers are shown by the gray circles. The states at time t (h_t) depend on the current input and the hidden state from the previous time step, showing how information is passed through time. The weights from input to hidden layers are represented as w_x, w_1, and w_2. The hidden-to-hidden weights are shown as $w_{h,1}$, $w_{h,2}$, and $w_{h,3}$, indicating how the hidden state from one time step influences the next. The output weights are shown as w_y. The network produces outputs at each time step (y_{t-1}, y_t, y_{t+1}, …, y_{t+n}), represented by the yellow circles on the right. RNNs are a class of DL models, made of artificial neurons with one or more feedback loops. They can be trained on labeled sequential data, where the network learns to predict an output sequence given an input sequence (Salehinejad et al., 2017).

One of the limitations with the RNN is the vanishing gradient issue, which affects the effectiveness of this method (Pascanu et al., 2012). To overcome this problem long short-term memory (LSTM) (Y. Yu et al., 2019) and gated recurrent units (GRUs) (Dey & Salemt, 2017) which are popular RNN architectures and also used to compare their classification accuracies. In this study, TensorFlow libraries (Abadi et al., n.d.) are used to train RNN models.

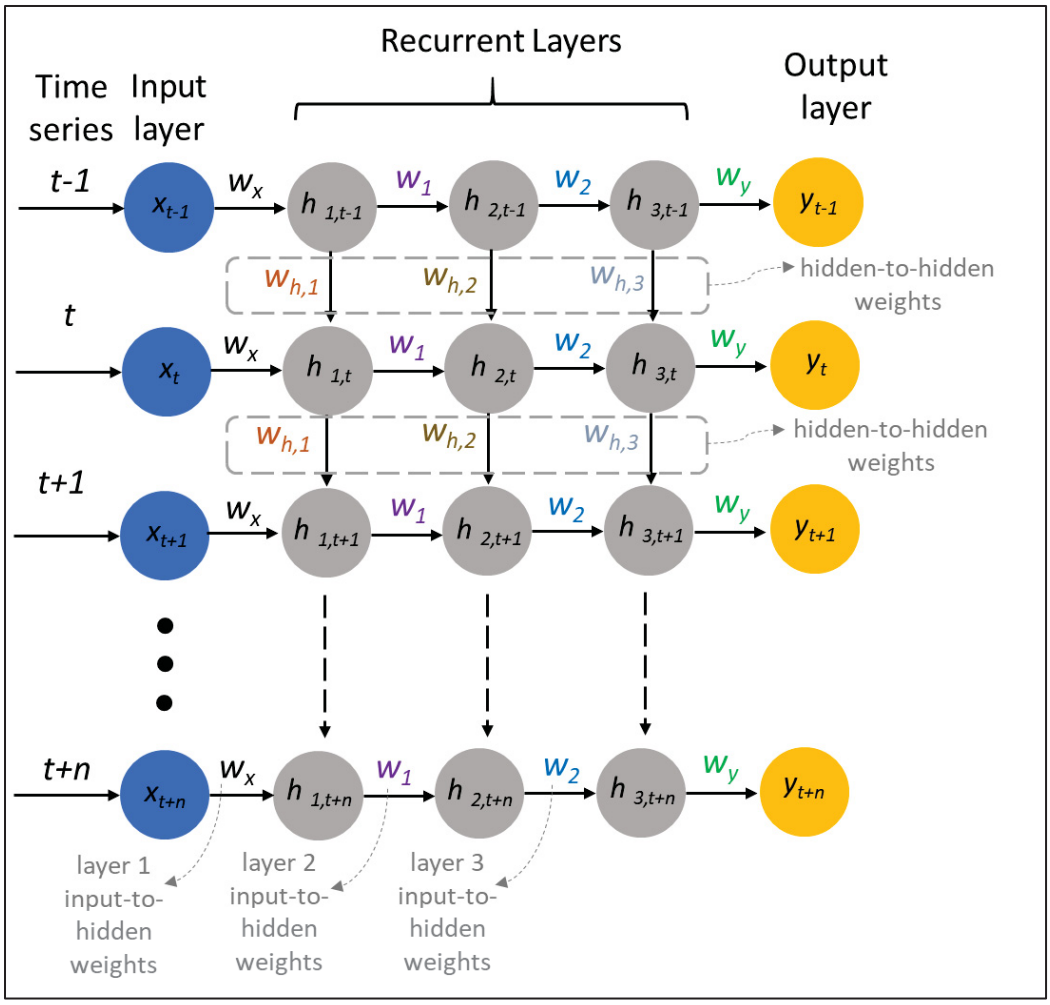

Figure 8.4 Schematic of the detailed RNN workflow indicating how each hidden state (highlighted in gray) depends on the previous hidden state, capturing the temporal dependencies in the data

8.2.3.2 Long Short-Term Memory (LSTM)

To address the vanishing gradient issue in Simple RNN models, LSTM networks update hidden states with extra learning parameters, including the forget gate f_t, input gate i_t, output gate o_t, and cell state c_t. These values can be calculated using the following equations (Sak et al., 2014):

$$f_t = \sigma\left(W_{if}x_t + b_{if} + W_{hf}h_{t-1} + b_{hf}\right) \tag{8.3}$$

$$i_t = \sigma\left(W_{ii}x_t + b_{ii} + W_{hi}h_{t-1} + b_{hi}\right) \quad (8.4)$$

$$g_t = tanh\left(W_{ig}x_t + b_{ig} + W_{hg}h_{t-1} + b_{hg}\right) \quad (8.5)$$

$$o_t = \sigma\left(W_{io}x_t + b_{io} + W_{ho}h_{t-1} + b_{ho}\right) \quad (8.6)$$

$$c_t = f_t \odot c_{t-1} + i_t \odot g_t \quad (8.7)$$

$$h_t = o_t \odot tanh(c_t) \quad (8.8)$$

Where h_t represents the hidden state at time t, c_t denotes the cell state at time t, and x_t is the input at time t. Similarly, h_{t-1} refers to the hidden state at the previous time step $t-1$ or the initial hidden state at time 0. The symbols i_t, f_t, g_t, and o_t correspond to the input, forget, cell, and output gates, respectively. Here, σ is the sigmoid activation function, and Θ represents the element-wise Hadamard product (Sak et al., 2014).

8.2.3.3 Gated Recurrent Unit (GRU)

The GRU model also addresses the vanishing gradient problem, offering performance similar to LSTM by utilizing a gated structure. However, GRU requires fewer variables and applies a multi-layer gated recurrent unit RNN to process an input sequence. For each item in the input sequence, each layer performs the following function (*GRU — PyTorch 2.5 Documentation*, n.d.):

$$r_t = \sigma\left(W_{ir}x_t + b_{ir} + W_{hr}h_{t-1} + b_{hr}\right) \quad (8.9)$$

$$z_t = \sigma\left(W_{iz}x_t + b_{iz} + W_{hz}h_{t-1} + b_{hz}\right) \quad (8.10)$$

$$n_t = tanh\left(W_{in}x_t + b_{in} + r_t \odot \left(W_{hn}h_{t-1} + b_{hn}\right)\right) \quad (8.11)$$

$$h_t = (1 - z_t) \odot n_t + z_t \odot h_{(t-1)} \quad (8.12)$$

Where the terms r_t, z_t, and n_t correspond to the reset, update, and new gates, respectively.

8.2.3.4 Long Short-Term Memory (LSTM) autoencoder

Autoencoders are unsupervised representation learning techniques that define non-linear encoder and decoder functions to compress and reconstruct data (Nguyen et al., 2021). LSTM networks can be used in autoencoders to capture temporal dependencies or early anomaly detection in sequential data. LSTM autoencoder extracts the features from the database by reducing the dimensions in the encoding layers. This model is trained by reducing the difference between the original input and the reconstructed data in the decoding layers.

8.2.3.5 Random forest (RF)

RF method is an ensemble learning approach that combines predictions from several decision trees by aggregating their outputs (Speiser et al., 2019). This technique generally shows strong performance in generalizing to unseen data. In this paper, this method is used to compare its performance as a classical ML model with RNN models, as it has a wide application in classification tasks.

8.2.3.6 K-means clustering

K-means clustering is an unsupervised technique that classifies the data based on their similarities (Shi et al., 2010). This technique associates each input with a label from 1 to k, and it introduces centroids (μ_1, …, μ_k), then adjusts both the centroids and the cluster assignments until each input is close to its assigned centroid (Likas et al., 2003). In this study, the outputs of the LSTM autoencoders are fed to the k-means clustering model to cluster the data.

8.2.4 Hyperparameter tuning

Hyperparameter tuning refers to the process of optimizing the performance of a ML model by selecting the best values for hyperparameters. Unlike parameters that the model learns during training, hyperparameters are set prior to training and determine the overall behavior of the

model (T. Yu & Zhu, 2020). In the present study, two techniques are used for hyperparameter tuning which are Bayesian hyperparameter optimization and grid search.

The grid search technique searches through a predefined grid of hyperparameter combinations (Liashchynskyi & Liashchynskyi, 2019). Each combination is tested by training the model and evaluating its performance, using cross validation. Grid search is deployed for tuning the depth and number of estimators in the RF model.

Bayesian optimization builds a probabilistic model of the objective function, such as validation accuracy, and uses that model to decide where to evaluate the next set of hyperparameters (Victoria & Maragatham, 2021). Such Bayesian based approach aims to find the optimal hyperparameters with fewer evaluations compared to grid search, making it faster and more computationally feasible (Wu et al., 2019). This method is useful when tuning DL models or models with many hyperparameters, such as the number of layers and units in RNN. Bayesian optimization reduces the number of trials by focusing the search on promising regions of the hyperparameter space based on previous evaluations, making it suitable for scenarios where model training is computationally expensive.

8.2.5 Evaluation of the learning models

To evaluate model performance, k-fold cross-validation with three folds is employed using the KFold method from sklearn.model_selection. This process is done to ensure that overfitting is not occurred to a single training set (Wong & Yeh, 2020). To evaluate the classification performance of the models, the confusion matrix, accuracy score, F1-score, precision, and recall are typically calculated for each model (Powers & Ailab, 2020). All these metrics are therefore adopted in the present study and are computed using the test data that the models have not seen during training.

The accuracy represents the proportion of correctly predicted labels out of the total number of predictions and is calculated using Equation (8.13) (Chicco & Jurman, 2020).

$$Accuracy = \frac{TP + TN}{TP + TN + FP + FN} \tag{8.13}$$

Where TP denotes the true positives, i.e., correctly predicted positive instances, TN represents the true negatives, i.e., correctly predicted negative instances, FP denotes the false positives, i.e., incorrectly predicted positive instances, and FN presents the false negatives, i.e., incorrectly predicted negative instances.

Precision is the proportion of the TP predictions out of all positive predictions made by the model as shown in Equation (8.14) (Chicco & Jurman, 2020). As such, a high precision indicates that the model makes only few false positive errors.

$$Precision = \frac{TP}{TP + FP} \tag{8.14}$$

Recall measures the proportion of actual positives that are correctly identified as calculated in Equation (8.15) (Chicco & Jurman, 2020), and high recall means the model captures most of the positive instances, but it might also include more false positives.

$$Recall = \frac{TP}{TP + FN} \tag{8.15}$$

The F1-score is the harmonic mean of precision and recall and is calculated using Equation (8.16) (Chicco & Jurman, 2020). It balances the two metrics and is particularly useful when dealing with unbalanced classes. A high F1-score indicates that the model has both good precision and recall, making it an effective overall measure of model performance.

$$F1 - Score = 2 \times \frac{Precision \times Recall}{Precision + Recall} \tag{8.16}$$

A confusion matrix is a table used to evaluate the performance of a classification model on a test dataset with known true values. It has two dimensions: one indexed by the actual class and the other by the predicted class provided by the classifier (Deng et al., 2016). It provides the counts of TPs, FPs, TNs, and FNs.

8.3 Results and discussion

8.3.1 Surface morphology and the corresponding noise signals

The current (blue lines) and potential (black lines) noise signals obtained from the EN tests are presented in Figure 8.5 (a–d). Figure 8.5 (a) displays the transient signals associated with pitting corrosion on the flange sample plate. In pitting corrosion, the distinct current transients signify the initiation and progression of localized pits (A. M. Homborg et al., 2018). In the passive state (Figure 8.5 (b)), potential and current fluctuate steadily between -0.1 and 0.1 μA, except for the initial 10 ks, where fluctuations range from -0.3 to 0.3 μA. For crevice corrosion (Figure 8.5 (c)), noticeable transients in both current and potential signals indicate the initiation and propagation of crevice corrosion (Hu et al., 2010). These transients are typically observed as rapid increases or decreases in the signals, depending on which W.E. is undergoing corrosion. In the case of general corrosion (Figure 8.5 (d)), the current fluctuations range between -3 and 2 μA, exceeding those of the passive state. The current and potential signals for pitting corrosion, general corrosion, and the passive state are detrended; however, the signals for crevice corrosion are not detrended to preserve the detection of transient events in the current and potential signals.

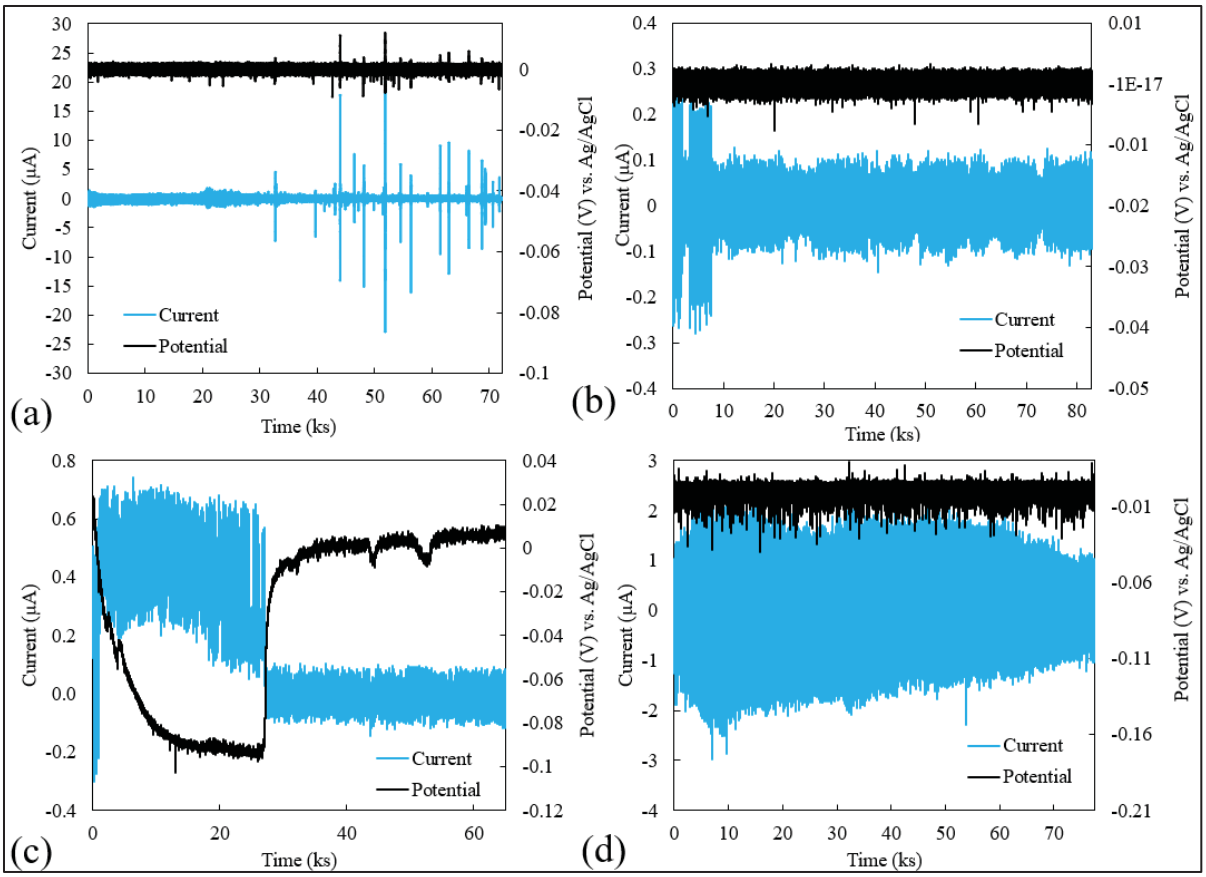

Figure 8.5 Electrochemical current and potential noise signals corresponding to the different types of corrosion occurred on the flange surface. (a) Pitting corrosion; (b) passive state; (c) crevice corrosion; (d) general corrosion

Microscopic analysis of the flange sample plate surfaces after EN tests confirmed the presence of four distinct corrosion types on the flange sample plates. Figure 8.6 (a) illustrates pitting corrosion, observed on plates that are passivated before exposure to the 0.5 M $NaHCO_3$ + 0.1 M NaCl solution. Figure 8.6 (b) shows a passivated flange sample with no visible signs of corrosion. In Figure 8.6 (c), crevice corrosion morphology is evident at the interface between the gasket and flange, consistent with literature reports that crevice corrosion typically occurs in this area of flanged gasketed joints (Hakimian et al., 2024d). As shown in Figure 8.6 (c), the boundary line between the area under the gasket and the area freely exposed to the solution, where crevice corrosion initiates and propagates. Figure 8.6 (d) shows that general corrosion occurs uniformly across the flange sample plate surface.

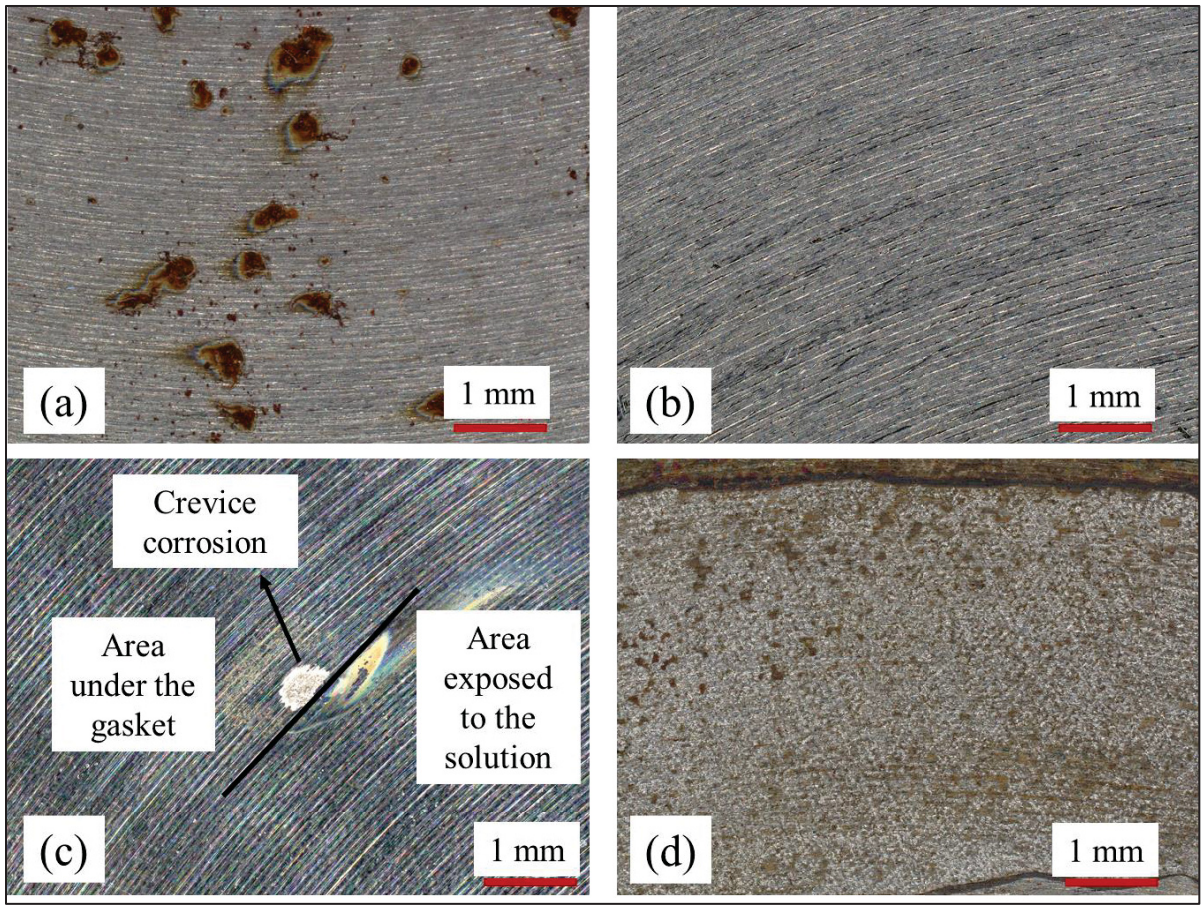

Figure 8.6 Microscopic images of the corroded areas on the flange sample plates, illustrating various types of corrosion after EN tests: (a) Pitting corrosion; (b) passive state; (c) crevice corrosion; (d) general corrosion

8.3.2 Supervised learning techniques

Hyperparameter tuning for the RNN models focuses on optimizing three key parameters: the number of layers (num_layers), the number of neurons per layer (units), and the sequence length (seq_length). The sequence length in RNN models is determined based on the dependency length present in the data, with the optimal sequence length being the one that best captures the patterns within the signals. Figure 8.7 provides an example of a raw current signal and demonstrates how it is divided into sequences (X_1 to X_t) used by the RNN models.

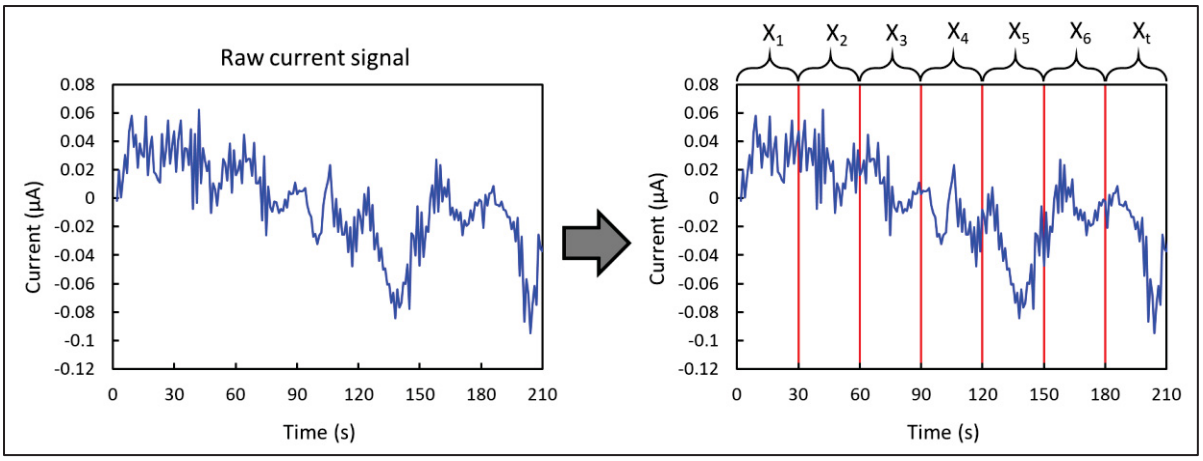

Figure 8.7 Example of the transformation of the raw current signal to the sequences of data that are used directly in the RNN models including LSTM, Simple RNN, and GRU

To optimize the model configurations, Keras Tuner with Bayesian Optimization is employed. The optimal values obtain after tuning are then used to evaluate the models on the test dataset, with the results summarized in Table 8.4. For the RF model, the hyperparameter tuning targeted parameters including the number of trees in the forest (n_estimators), maximum tree depth (max_depth), minimum samples required for a split (min_samples_split), minimum samples required at a leaf node (min_samples_leaf), and whether to use bootstrapping (bootstrap). This tuning is performed using the GridSearchCV method from the sklearn.model_selection library, which automates the search for the optimal hyperparameters by exploring the specified parameter grid, using cross-validation to assess different combinations. Table 8.4 presents the search space and optimized hyperparameter values for each model, highlighting the effectiveness of the tuning approach in improving model performance.

Table 8.4 Hyperparameters, search spaces explored, optimised values, and best test accuracy for each model used for training

Model	**Hyperparameters**	**Search space**	**Optimised value**
LSTM	Sequence length (seq_length)	10 to 100 in steps of 10	30

Model	Hyperparameters	Search space	Optimised value
Simple RNN	number of hidden layers (num_layers)	1 to 3	2
	number of units (units)	32 to 128	32, 64
	sequence length (seq_length)	10 to 100 in steps of 10	80
	number of hidden layers (num_layers)	1 to 3	2
	number of units (units)	32 to 128	96, 64
GRU	sequence length (seq_length)	10 to 100 in steps of 10	30
	number of hidden layers (num_layers)	1 to 3	2
	number of units (units)	32 to 128	128, 64
RF	n_estimators	10, 50, 100	50
	max_depth	None, 10, 20, 30	10
	min_samples_split	2, 5, 10	2
	min_samples_leaf	1, 2, 4	1
	bootstrap	True, False	False

Figure 8.8 shows the confusion matrices for all the trained models, and it indicates the performance of the models in classification and identification of the types of corrosion. The vertical axis in these images shows the True label of the test data and the horizontal axis shows the Predicted labels by the models. The diagonal of the confusion matrix shows the correctly detected types of corrosion. As shown in this figure, crevice corrosion is the most challenging type of corrosion to be detected. There is misidentification between crevice corrosion and

passive state by all models but this misclassification is significantly observed with the RF model.

The LSTM model shows high accuracy for most corrosion types, with perfect classification for "General" and "Pitting" corrosion (1,529 and 1,466 correct predictions, respectively). There is, however, some misclassification of "Crevice" and "Passive" categories. Specifically, 232 instances that belong to the "Crevice" category are misclassified as "Passive," while 167 "Passive" samples are identified as "Crevice." These misclassifications suggest that the LSTM model struggles to differentiate between these two types of corrosion, potentially due to similarities in the EN signals during testing.

The Simple RNN model demonstrates lower performance compared to the LSTM model, particularly with the "Crevice" category, where 552 instances are misclassified as "Passive." This model identifies a high number of FNs of crevice corrosion. Despite these issues, the Simple RNN model still performs well for general and pitting corrosion, with perfect classification for both categories.

The GRU model performance is relatively similar to LSTM, with slightly higher misclassifications of "Crevice" and "Passive" categories. For example, 374 "Passive" instances are classified as "Crevice," indicating some overlap in how these two categories are interpreted by the model. The GRU model effectively identifies general and pitting corrosion without any misclassifications, except one instance of misclassification of pitting corrosion, suggesting its strength in handling distinct corrosion signals.

The RF model shows lower performance across all categories, with very high misclassification rates, especially for "Crevice" and "Passive" categories. For instance, nearly all "Crevice" instances (25,688) are misclassified as "Passive". This indicates that the RF model struggles to capture the temporal dependencies in the data, which are crucial for distinguishing between different corrosion types. The inability of RF to handle sequential patterns as effectively as RNN-based models could be the primary reason for its poor performance. Overall, the RNN-

based models (LSTM, Simple RNN, and GRU) outperform the RF model in classifying corrosion types.

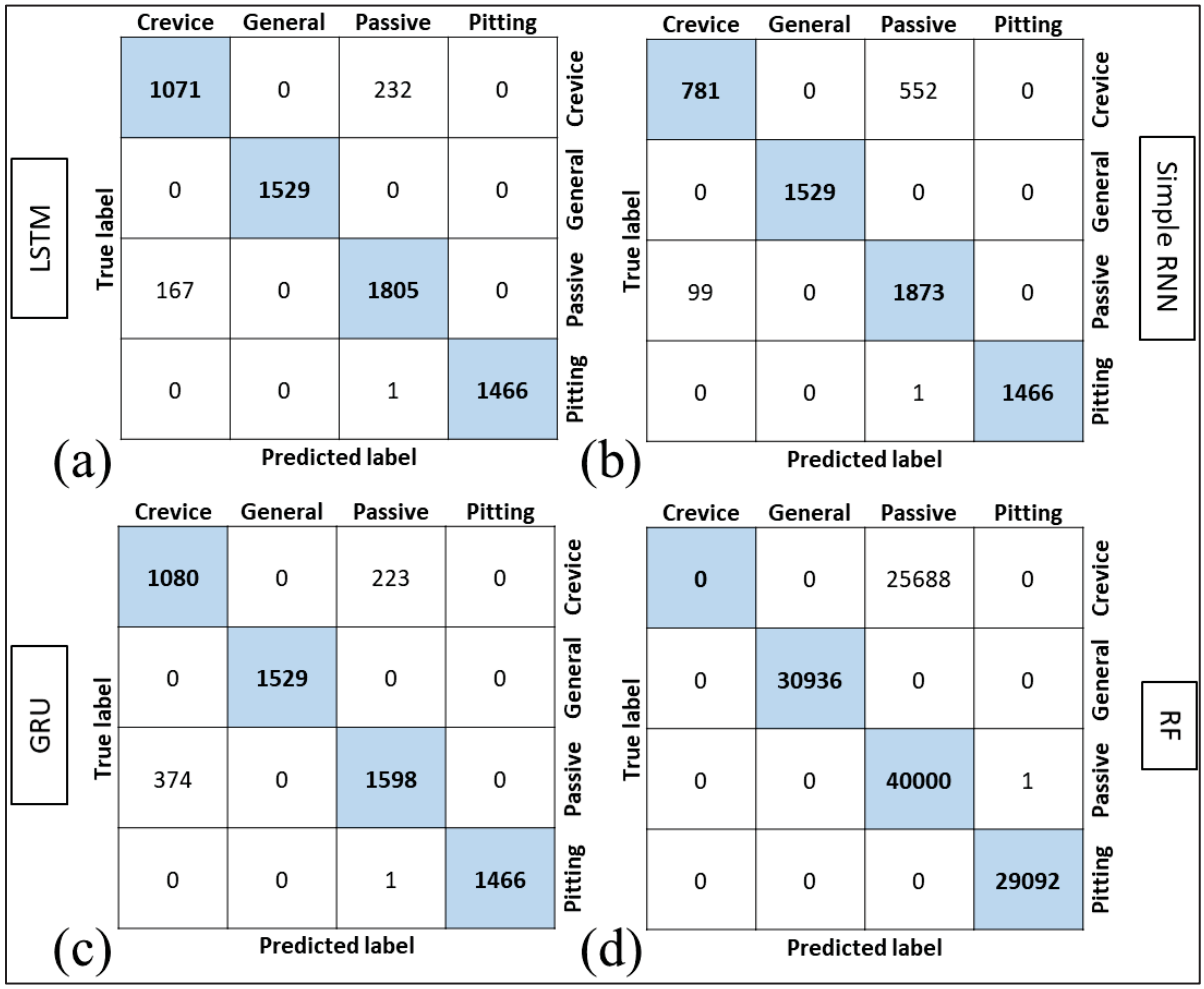

Figure 8.8 Confusion matrices for the classification performance of models trained with optimized hyperparameters: (a) LSTM; (b) Simple RNN; (c) GRU; (d) RF

Table 8.5 indicates an evaluation of the DL models and RF for classifying corrosion types using EN data. The performance metrics include precision, recall, F1-score, and best test accuracy for crevice corrosion, general corrosion, passive state, and pitting corrosion.

The LSTM model exhibits strong performance across all corrosion types, with an overall best test accuracy of 93.62%. The LSTM's performance is notable for general and pitting corrosion, achieving perfect precision, recall, and F1-scores (1.00), indicating that the model correctly identifies these corrosion types with no FPs or FNs. For the passive state, the model maintains

high precision (0.89) and recall (0.92), resulting in a F1-score of 0.90. However, crevice corrosion shows lower metrics, with a precision of 0.87, recall of 0.82, and an F1-score of 0.84, reflecting some misclassification issues.

The Simple RNN model achieved a lower overall accuracy (90.08%) compared to LSTM. While it also performed perfectly on general and pitting corrosion (precision, recall, and F1-score of 1.00), the performance drops significantly for crevice corrosion, with an F1-score of 0.72. The precision-recall difference for crevice corrosion (0.89 precision vs. 0.60 recall) suggests that while the model can correctly identify some crevice cases, it struggles to detect all instances, leading to a higher rate of FNs. The performance on passive state (F1-score of 0.86) indicates that the simple RNN is effective in identifying this type of corrosion, although it lags behind the LSTM's accuracy.

The GRU model shows performance with an overall accuracy of 90.46%. The results for general and pitting corrosion remain perfect (1.00 for all metrics), similar to the other models. However, for crevice corrosion, the GRU achieves an F1-score of 0.78, which is better than the Simple RNN but still lower than the LSTM performance. This suggests that the GRU ability to retain temporal dependencies helps to some extent, but the model may still struggle with distinguishing features of crevice corrosion. For the passive state, the GRU model shows slightly lower precision (0.88) compared to the LSTM, resulting in an F1-score of 0.84. This indicates that the GRU model, may not generalize as well as the LSTM for some corrosion types.

The RF classifier has the lowest overall test accuracy at 79.52%. While it performs perfectly on general and pitting corrosion, the metrics for crevice corrosion are poor, with precision, recall, and F1-scores all at 0.00. This indicates that the model fails to identify any instances of crevice corrosion, which could be due to the complexity of electrochemical noise data that requires capturing sequential dependencies, which cannot be achieved by the RF algorithm. For the passive state, the RF model achieves a recall of 1.00 but has a lower precision (0.61), leading to an F1-score of 0.76. This suggests that while the model is able to detect all instances

of passive state, it also misclassifies other corrosion types as passive, resulting in a high number of FPs.

The LSTM model outperforms the others, achieving the highest overall accuracy and consistently high F1-scores across all corrosion types. All models struggle with accurately identifying crevice corrosion. This indicates that crevice corrosion may have features that overlap with other corrosion types, making classification difficult for non-sequential models like RF, or even simpler sequential models, such as Simple RNN. All models achieve perfect scores for general and pitting corrosion, suggesting that the distinguishing features for these corrosion categories are well-represented in the dataset. Although all models perform relatively well, there is still room for improvement in handling crevice corrosion and the passive state. Indeed, the results indicate that recurrent models are well-suited for analyzing EN data to classify different types of corrosion. The sequential nature of these models allows them to capture temporal dependencies in the data that traditional algorithms, such as RF cannot identify.

Table 8.5 Classification report showing precision, recall, and F1-score for different corrosion types using supervised learning models.

Model	**Type of corrosion**	**Precision**	**Recall**	**F1-score**	**Best test accuracy (%)**
LSTM	Crevice	0.87	0.82	0.84	93.62
	General	1.00	1.00	1.00	
	Passive	0.89	0.92	0.90	
	Pitting	1.00	1.00	1.00	
Simple RNN	Crevice	0.89	0.60	0.72	90.08
	General	1.00	1.00	1.00	
	Passive	0.78	0.95	0.86	
	Pitting	1.00	1.00	1.00	
GRU	Crevice	0.74	0.83	0.78	90.46
	General	1.00	1.00	1.00	

Model	Type of corrosion	Precision	Recall	F1-score	Best test accuracy (%)
RF	Passive	0.88	0.81	0.84	79.52
	Pitting	1.00	1.00	1.00	
	Crevice	0.00	0.00	0.00	
	General	1.00	1.00	1.00	
	Passive	0.61	1.00	0.76	
	Pitting	1.00	1.00	1.00	

As shown in Table 8.5, the LSTM model achieves the highest test accuracy among all the evaluated models. This performance is reached when using a sequence length of 30 and a two-layer LSTM architecture, as depicted in Figure 8.9. The architecture includes 32 units in the first LSTM layer and 64 units in the second layer. The model input is a matrix of dimensions $T \times l$ (X_1 to X_T), where l represents the length of the sequences and T denotes the number of sequences. Each input is first passed through a tanh activation function, which facilitates the non-linear transformation of the data before entering the LSTM layers. In this architecture, the final Dense layer, combined with a softmax activation function, is responsible for classifying the input into the target categories. This softmax layer outputs a probability distribution over the possible classes, and then the predicted label is the one that has the highest probability.

Compared with previous studies, which focus on extensive feature engineering to enhance classification, the present study demonstrates that RNN models, particularly LSTM, can perform well using only two input features: current and potential noise. While RF models in the literature have often required numerous input features to classify corrosion types, they typically showed lower performance and struggled with differentiating between passivation and pitting corrosion (Hou et al., 2016). This limitation in previous RF models may come from the lack of hyperparameter tuning, which is addressed in this study, contributing to the improved performance of the RF model.

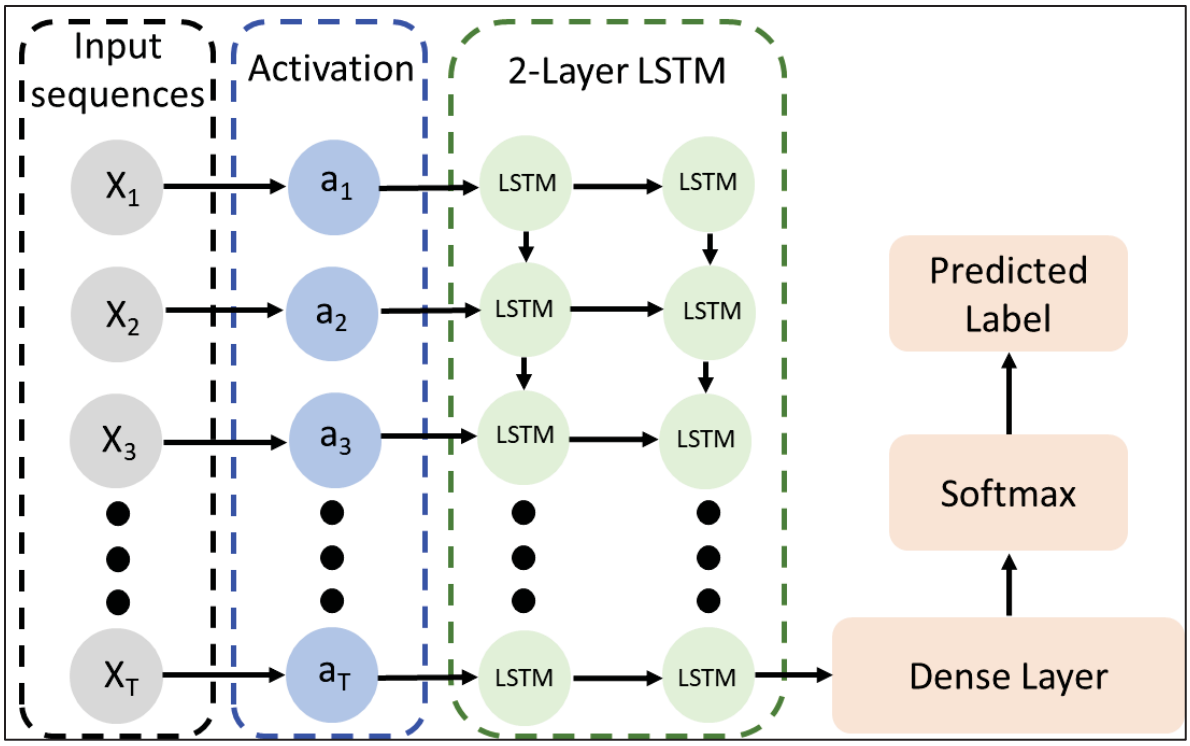

Figure 8.9 Structure of the tuned LSTM model with 2 layers and tanh as activation function

As discussed in this section (8.3.2), the RNN models perform well in differentiating various types of corrosion using EN data, surpassing the performance of the RF model. A key accomplishment of the developed supervised learning approach employed in this study is the use of only two input features, current and potential, in the RNN models. As highlighted in the introduction, it is common in the literature to engineer a large number of features derived from current and potential signals to classify different types of corrosion. However, the results of the present study indicate that only two features, current and potential, are sufficient for capturing the sequential dependencies and recurring patterns in EN data using RNN models. This leads to a significant reduction in computational costs, which is particularly important for real-world corrosion monitoring applications, where large datasets are typically generated.

Although the RF model shows lower performance compared to the RNN models, it detects all instances of general and pitting corrosion. This represents a notable improvement over previously reported results in the literature for identifying these corrosion types. The enhanced performance of the RF model in distinguishing general and pitting corrosion can be attributed

to the hyperparameter tuning applied in this study, an aspect not extensively explored in prior research.

8.3.3 Hybrid learning

As discussed in the literature review section, previous studies have employed various feature extraction techniques to generate predictors for ML models. In the previous section (8.3.2), it is demonstrated that RNN models can effectively classify different types of corrosion using labeled datasets and only two input features: the obtained current and potential signals by ENM. In this section (8.3.3), a hybrid approach combining supervised and unsupervised learning techniques is applied to train the RNN and RF models. The aim of this hybrid approach is to improve the classification performance of the models by automating the feature selection process through the use of an LSTM autoencoder. Hyperparameter tuning is employed to optimize the parameters of the LSTM autoencoder, and the resulting values are presented in Table 8.6.

Table 8.6 Hyperparameters, search spaces, and optimized values for the LSTM autoencoder model

Model	Hyperparameters	Search space	Optimized value
LSTM autoencoder	Sequence length (seq_length)	10 to 100	20
	number of hidden layers (num_layers)	1 to 3	2
	number of units (units)	32 to 128	50, 50

The extracted features from the LSTM autoencoder are directly used in the supervised models discussed in the previous section. The LSTM autoencoder is an unsupervised DL technique which extracts the most important features from data without labeling the data. The confusion matrices obtained after training the models are shown in Figure 8.10. The LSTM model exhibits robust performance across various corrosion types. For example, the model correctly classifies 1,058 crevice corrosion instances, with a relatively small number of

misclassifications (245 samples) categorized as "Passive." Both general and pitting corrosion types are perfectly classified, which indicates that the LSTM model effectively handles these categories. In comparison, the Simple RNN model shows a slightly lower accuracy. While 1,028 crevice corrosion instances are classified correctly, 275 crevice corrosion instances are misclassified as passive state, highlighting the model challenge in distinguishing between these two types of corrosion. This suggests that the LSTM model, with its memory retention capabilities, performs better than Simple RNN for temporal data patterns. However, similar to the LSTM model, the Simple RNN correctly classifies all general and pitting corrosion instances. The GRU model demonstrates robust performance, with 1,071 correct classifications for crevice corrosion and fewer FPs (232) compared to the LSTM model. However, the GRU model has more FPs for passive state than the LSTM model. For general corrosion, all 1,529 instances are classified correctly, and similarly, all 1,466 pitting corrosion instances are accurately identified. This shows that while the GRU efficiently handles sequential data, the LSTM architecture slightly outperforms it in distinguishing between corrosion forms. The RF model displays a significant improvement in detecting crevice corrosion, with 1,214 correct classifications - higher than the other models - and only 89 FPs, which is lower compared to other models. Moreover, the RF model excels in detecting and differentiating the passive state from crevice corrosion, with 1,926 correct classifications and only 46 misclassifications. Similar to the other models, RF correctly classifies all general and pitting corrosion instances. The performance improvement, particularly in the RF model, is attributed to the automatic feature extraction capability of the LSTM autoencoder, which selects the most critical features for training the subsequent supervised model.

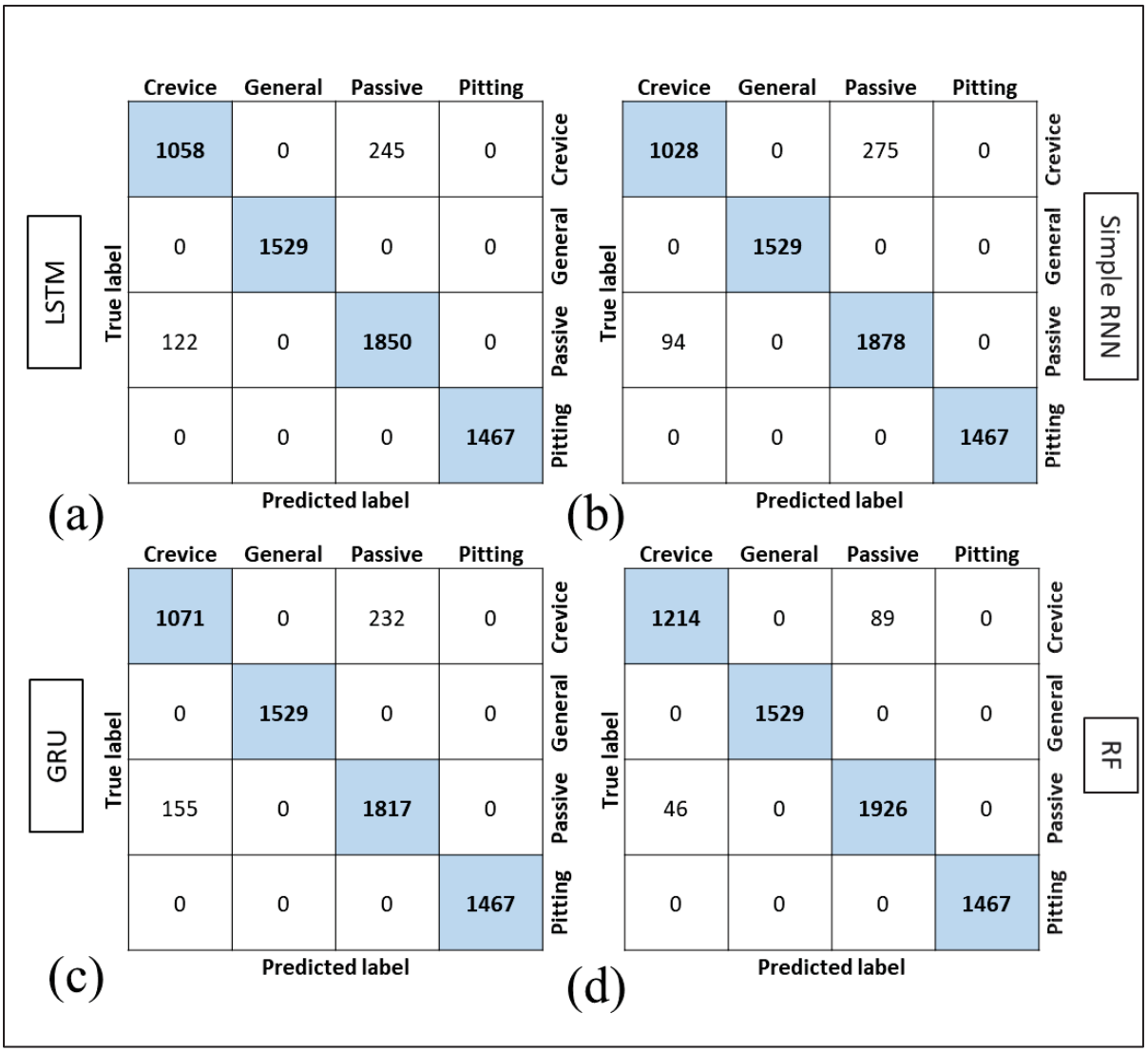

Figure 8.10 Confusion matrices obtained after training the hybrid model including the LSTM autoencoder and then supervised learning models (a) LSTM; (b) Simple RNN; (c) GRU; (d) RF

Table 8.7 compares the performance of the four models - LSTM, Simple RNN, GRU, and RF - in identifying different types of corrosion, as indicated by precision, recall, F1-score, and test accuracy.

LSTM shows solid performance for crevice corrosion detection with an F1-score of 0.85, though it slightly underperforms in recall (0.81), indicating that the model occasionally misses some crevice corrosion instances. The LSTM model achieves a perfect score (Precision, Recall, and F1-score of 1.00) for both general and pitting corrosion. This suggests that the

LSTM captures the characteristics of these corrosion types. This model achieves an F1-score of 0.91 for the passive state, reflecting a well-balanced performance. Its recall is higher than precision (0.94 vs. 0.88), showing that while it correctly identifies most passive state cases, a few FPs are included. With a best test accuracy of 94.15%, the LSTM model is highly reliable overall, particularly for identifying corrosion types like pitting and general corrosion.

The Simple RNN achieves similar results as the LSTM for crevice corrosion, with an F1-score of 0.85 and slightly higher precision (0.92), which indicates better identification of crevice corrosion instances compared to LSTM. Like the LSTM, Simple RNN achieves perfect scores (1.00) in both general and pitting corrosion, demonstrating the model ability to handle clear and distinct patterns in these types of corrosion. The model achieves an F1-score of 0.91 for passive state, similar to LSTM, but it has slightly better recall (0.95 vs. 0.87 precision). This suggests that the model excels at capturing true passive state cases, though it might include some misclassifications. The Simple RNN achieves an overall test accuracy of 94.12%, which is roughly equal to the test accuracy of LSTM model. Its performance on crevice corrosion is notable, as it demonstrates higher precision than LSTM.

The GRU model has an F1-score of 0.85 for crevice corrosion, with balanced precision (0.87) and recall (0.82). This is slightly below the performance of both LSTM and Simple RNN but remains a good result overall. Like the other RNN-based models, the GRU achieves perfect scores (1.00) for general and pitting corrosion, suggesting that it can handle clearly distinguishable corrosion patterns well. With an F1-score of 0.90, GRU performs slightly below the LSTM for passive state but still exhibits a strong balance between precision (0.89) and recall (0.92). With a best test accuracy of 93.83%, the GRU model performs slightly below the LSTM and Simple RNN models but remains a competitive option. Its performance on all corrosion types is strong, though it appears to face similar challenges in differentiating crevice corrosion and passive state.

The RF model excels in detecting crevice corrosion, achieving an F1-score of 0.95 with a high recall (0.93) and precision (0.96). This indicates a superior ability to correctly identify and classify crevice corrosion compared to the RNN models. Like the RNN models, RF achieves perfect scores (1.00) for general and pitting corrosion, meaning it effectively handles these corrosion types. RF demonstrates outstanding performance for passive state detection, with an

F1-score of 0.97. Its recall (0.98) is higher than precision (0.96), meaning that while it detects almost all instances of passive state, it may occasionally misclassify other types as passive. With a best test accuracy of 97.85%, the RF model outperforms the RNN-based models in terms of overall accuracy. This indicates that RF is particularly robust when trained on features extracted by the LSTM autoencoder and can differentiate between corrosion types more effectively than the sequential models.

Table 8.7 Classification report showing precision, recall, and F1-score for different corrosion types using unsupervised LSTM autoencoder and supervised learning models

Model	Type of corrosion	Precision	Recall	F1-score	Best test accuracy (%)
LSTM	Crevice	0.9	0.81	0.85	94.15
	General	1.00	1.00	1.00	
	Passive	0.88	0.94	0.91	
	Pitting	1.00	1.00	1.00	
Simple RNN	Crevice	0.92	0.79	0.85	94.12
	General	1.00	1.00	1.00	
	Passive	0.87	0.95	0.91	
	Pitting	1.00	1.00	1.00	
GRU	Crevice	0.87	0.82	0.85	93.83
	General	1.00	1.00	1.00	
	Passive	0.89	0.92	0.90	
	Pitting	1.00	1.00	1.00	
RF	Crevice	0.96	0.93	0.95	97.85
	General	1.00	1.00	1.00	
	Passive	0.96	0.98	0.97	
	Pitting	1.00	1.00	1.00	

The structure of the hybrid model is illustrated in Figure 8.11. The input data is first passed through the LSTM autoencoder, where critical features are automatically extracted from the

raw electrochemical current and potential signals during the encoding phase. These extracted features form a matrix of dimensions T × N (f_1 to f_T), where T represents the number of sequences and N denotes the number of extracted features. In the subsequent decoding step, the LSTM autoencoder attempts to reconstruct the input data from the extracted features, and the reconstructed data is compared with the original input to assess the autoencoder's performance in capturing essential features. The LSTM autoencoder architecture consists of two LSTM layers with tanh activation for encoding and one LSTM layer for decoding. The latent representations generated by the LSTM autoencoder are then fed into DL and ML models for classification of different corrosion types. For simplicity, Figure 8.11 only illustrates the LSTM model, though other DL models are used as well. The first step of the hybrid model is unsupervised, as the LSTM autoencoder evaluates the extracted features by reconstructing the input data without the need for labeled data. The second step is a supervised learning process, in which labeled datasets are used to classify the corrosion types through DL and ML models.

The hybrid learning approach, underscores the LSTM autoencoder ability to capture complex patterns and dependencies of EN data, which enhances the classification accuracy of both RNN-based models and, particularly, the RF model. The RF model, traditionally less effective in handling sequential data, benefits from the autoencoder learned features, which retain key temporal dependencies. Consequently, the LSTM autoencoder proves to be a powerful tool in reducing the need for extensive feature engineering, allowing the models to focus on essential patterns within current and potential noise as input features, thereby improving classification accuracy and efficiency in corrosion monitoring applications.

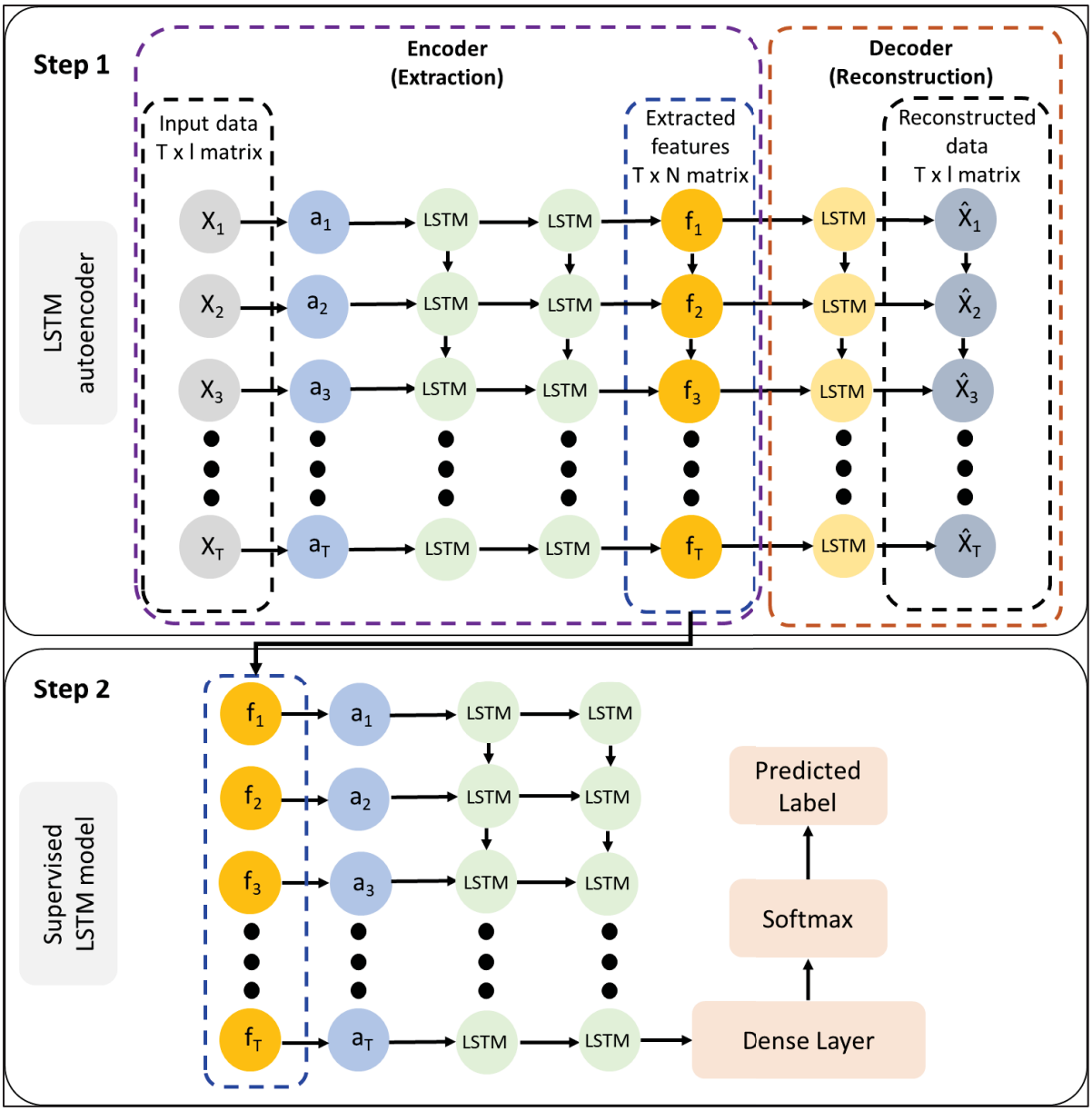

Figure 8.11 Architecture of the hybrid approach, incorporating feature extraction using a two-layer LSTM autoencoder (unsupervised technique) with 50 units per layer, followed by classification using a two-layer LSTM model (supervised technique) with 32 and 64 units

8.3.4 Unsupervised learning

Since real-world corrosion monitoring scenarios often involve obtaining unlabeled data from EN tests, an unsupervised learning technique to differentiate between various types of corrosion on flange surfaces using unlabeled data is finally proposed. This approach consists

of two main steps. In the first step, critical features are automatically extracted using an LSTM autoencoder, and in the second step, these features are used as inputs for clustering via the k-means algorithm. The hyperparameters utilized in the LSTM autoencoder are shown in Table 8.8 and are optimized within a defined search space. Two sequence lengths, 20 and 700, are tested with this approach to evaluate the model differentiation performance across different types of corrosion, as variations in sequence length affect the model classification capabilities for specific corrosion types.

Table 8.8 Hyperparameters, search spaces, and optimized values for the LSTM autoencoder model for unsupervised learning

Model	**Hyperparameters**	**Search space**	**Optimized value**
LSTM autoencoder	Sequence length (seq_length)	10 to 1500	20, 700
	number of hidden layers (num_layers)	1 to 3	2
	number of units (units)	32 to 128	50, 50

Figure 8.12 presents the confusion matrices for the hybrid learning technique at two different sequence lengths. In Figure 8.12 (a), which corresponds to a sequence length of 20, the model successfully distinguishes all instances of crevice corrosion, demonstrating complete accuracy in identifying this type of corrosion. Similarly, general corrosion cases are entirely classified correctly. However, the model misclassifies all instances of the passive state as crevice corrosion. For pitting corrosion, the model accurately identifies 919 instances, but 548 instances are erroneously categorized as the passive state. Thus, with a sequence length of 20, the hybrid model effectively differentiates crevice and general corrosion, though it struggles with the passive state and pitting corrosion. In contrast, when the sequence length is increased to 700, as shown in Figure 8.12 (b), the model exhibits an improved performance for all corrosion types except crevice corrosion. In this case, all instances of crevice corrosion are misclassified as the passive state. Despite this limitation, the model correctly classifies all cases of general corrosion and the passive state. For pitting corrosion, 27 cases are accurately identified, while 11 cases are misclassified as crevice corrosion. This comparison indicates

that, while a sequence length of 700 enhances the model ability to differentiate most corrosion types, it introduces challenges in correctly identifying crevice corrosion.

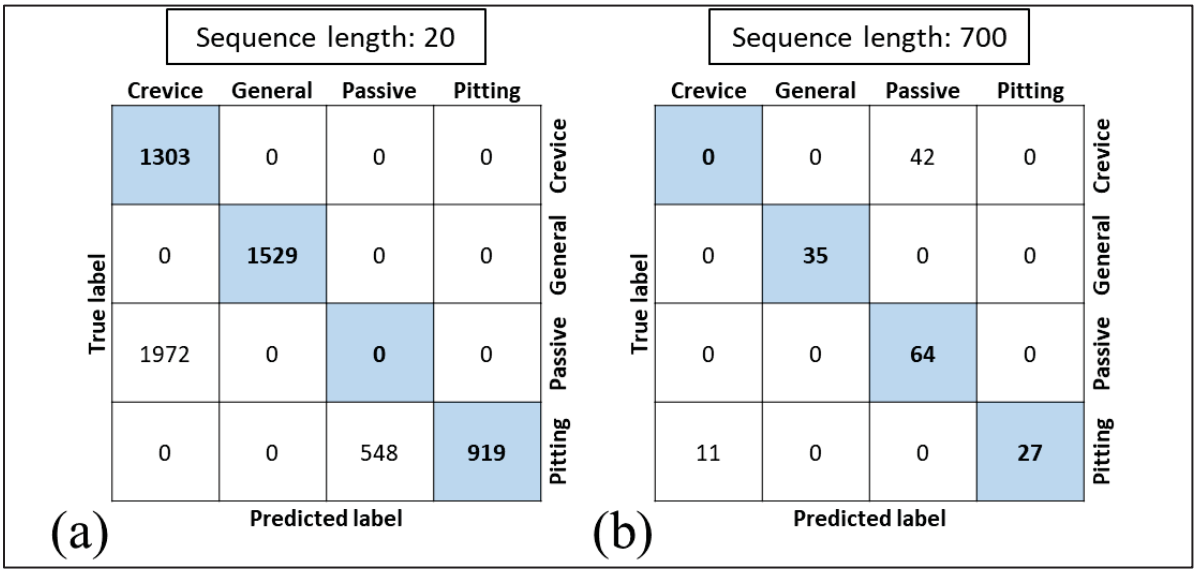

Figure 8.12 Confusion matrices obtained after training the LSTM autoencoder and then k-means algorithm in the (a) sequence length of 20; (b) sequence length of 700

The evaluation metrics for measuring model performance are presented in Table 8.9. For a sequence length of 20, the model achieves a precision of 0.40, a recall of 1.00, and an F1-score of 0.57 for detecting crevice corrosion. In contrast, for general corrosion, all three metrics—precision, recall, and F1-score—are 1.00, indicating perfect classification performance. The model performance for the passive state is notably poor, with all metrics recorded as 0.00. For pitting corrosion, the model achieves a precision of 1.00, a recall of 0.71, and an F1-score of 0.83. The overall test accuracy of the hybrid model for a sequence length of 20 is 59.82%. When using a sequence length of 700, the model performance changes notably. For crevice corrosion, all evaluation metrics are 0.00, indicating a complete misclassification. For general corrosion, all metrics remain at 1.00, showing consistent accuracy. For the passive state, the model achieves a precision of 0.60, a recall of 1.00, and an F1-score of 0.75. For pitting corrosion, the precision remains at 1.00, while recall is 0.71, and the F1-score is 0.83. The highest test accuracy observed for the model with a sequence length of 700 is 70.39%.

Table 8.9 Classification report showing precision, recall, and F1-score for different corrosion types using unsupervised LSTM autoencoder with clustering in different sequence lengths

Sequence length	Model	Type of corrosion	Precision	Recall	F1-score	Best test accuracy (%)
20	LSTM autoencoder with k-means	Crevice	0.40	1.00	0.57	59.82
		General	1.00	1.00	1.00	
		Passive	0.00	0.00	0.00	
		Pitting	1.00	0.63	0.77	
700	LSTM autoencoder with k-means	Crevice	0.00	0.00	0.00	70.39
		General	1.00	1.00	1.00	
		Passive	0.60	1.00	0.75	
		Pitting	1.00	0.71	0.83	

The PCA visualization of the encoded features illustrates the separation between different types of corrosion in the latent space. In Figure 8.13, each color in the scatter plot corresponds to a specific type of corrosion: crevice, general, passive state, and pitting. PCA is used here to project the high-dimensional latent features extracted by the LSTM autoencoder into two principal components, making it easier to visualize the distinction of corrosion types. As shown in Figure 8.13 (a), which is related to the sequence length of 20, the clusters for crevice corrosion (in blue) and general corrosion (in red) are distinctly isolated from the other types. This suggests that, on the one hand, the encoded features corresponding to these corrosion types are unique enough to be reliably distinguished. On the other hand, there appears to be a slight overlap between the clusters for pitting (in yellow) and passive states (in green). This overlap could indicate some similarities in the features between these two corrosion types.

In Figure 8.13 (b), which corresponds to a sequence length of 700, the general corrosion and passive states are clearly distinguished from the other corrosion types. This clear isolation indicates that the extracted features effectively capture the differences between these types and the rest. However, there is a slight overlap between the clusters representing pitting and crevice corrosion, suggesting that the extracted features from inputs with a sequence length of 700

learned the dependencies in the data more effectively for distinguishing general corrosion and passive states.

After transforming the extracted features into a lower-dimensional space using PCA, k-means clustering is used to group similar data points, where each cluster represents a specific corrosion type. Within each cluster, the distance of each point to its centroid is calculated. The centroid, identified by a black cross in Figure 8.13 represents the typical behavior for a given corrosion type. The 95% threshold or control limit is set based on the 95^{th} percentile of these distances (shown by a black dashed line in Figure 8.13 (a) and (b)), defining a boundary within which data is considered to be typical for the corrosion type associated with the cluster.

The unsupervised approach can be applied in real-time corrosion monitoring. For example, if the normal operating condition is general corrosion or passive state, the measured EN data will be located inside the control limits (dashed lines in Figure 13) of these types of corrosion. If the input data is located outside of the control limits of general corrosion or passive state, it can be concluded that crevice corrosion or pitting corrosion is initiated in the flanged joint.

Although confusion matrices and classification metrics show lower performance for the unsupervised approach than the supervised and hybrid approaches, after applying PCA the types of corrosion could be distinctly identified and then clustered using k-means, specifically in the sequence length of 700 and for general and passive corrosion. Unsupervised approach has higher applicability in real-time corrosion monitoring than the other proposed approaches in this study as the corrosion monitoring data are mostly unlabeled.

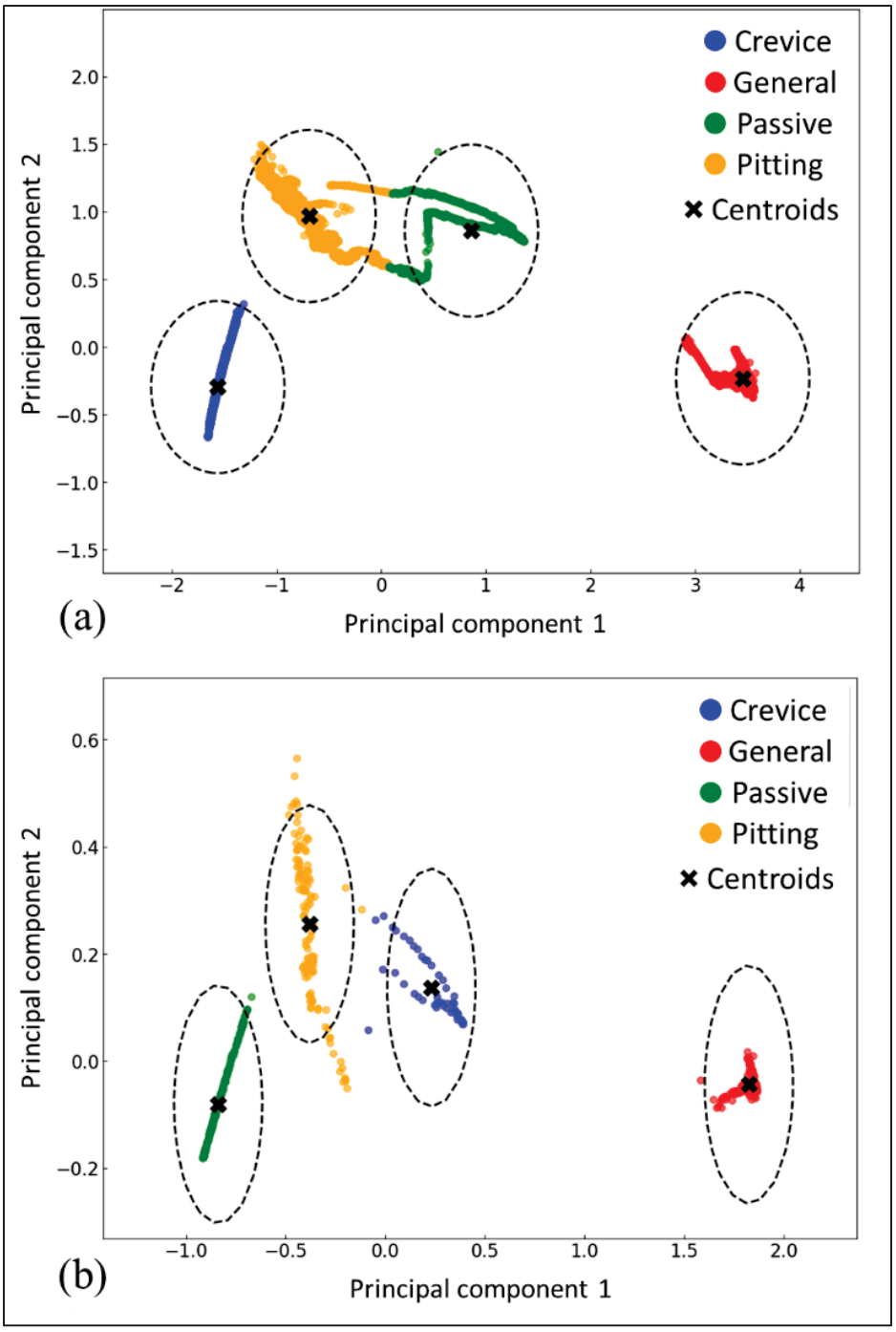

Figure 8.13 Visualization of the extracted features from the LSTM autoencoders using PCA method in two dimensions for the (a) sequence length of 20; (b) sequence length of 700

8.4 Conclusion

This study demonstrates the potential of RNN models including simple RNN, LSTM, GRU and particularly LSTM networks and autoencoders in distinguishing the types of corrosion by analyzing EN data obtained from flange sample plate surfaces under different experimental conditions. The findings and analyses reveal that:

- Among the supervised models, the LSTM achieved the highest test accuracy of 93.62%, effectively uncovering hidden patterns in the EN data, which enabled robust classification of corrosion types.
- To enhance the models' accuracies, a hybrid approach is implemented, resulting in improved performance across all models. The RF model achieved the highest test accuracy of 97.85% in distinguishing corrosion types, demonstrating the effectiveness of feature extraction through LSTM autoencoders for pattern recognition.
- The supervised and hybrid approaches, leveraging labeled data, successfully distinguish between general corrosion, pitting, crevice corrosion, and passive states. However, the performance of the unsupervised technique, which operates without labeled data—a more typical scenario in real-world corrosion monitoring—is less effective in comparison.
- In the unsupervised approach, PCA assists in clustering based on features extracted by the LSTM autoencoder, improving its ability to detect transitions between corrosion types. In real-time monitoring scenarios, this system can continuously classify incoming EN data and detect shifts from passive states to aggressive forms of corrosion, such as pitting or crevice corrosion, based on the cluster assignments.

This study is the first in the literature that proposes the use of RNN models for processing EN data in corrosion monitoring. It was demonstrated that using the developed RNN approach the identification of localized corrosion initiation (pitting or crevice) can be automated, without the need for disassembly of bolted joints in pipelines that causes shutdowns and significant losses.

In future research, the developed approaches can be improved by adding more corrosion types to the database and increasing the range and type of service conditions. Then, the presented

RNN-based model can be applied in corrosion monitoring to reassess the effectiveness of coatings and inhibitors, as data from ineffective coatings or inhibitors will be mapped to distinct clusters, enabling early detection of reduced performance. Using databases related to coatings and inhibitors, the model's ability for detecting and evaluating the effectiveness of these protective measures can be validated and enhanced, and as such create a novel powerful tool for enhanced corrosion management and predictive maintenance in industrial environments.

Acknowledgments

This work was supported by the Natural Sciences and Engineering Research Council of Canada (NSERC) under the Discovery Grant (RGPIN-2019-05973 and RGPIN-2021-03780).

CONCLUSION

In this thesis, the understanding of corrosion behavior in bolted flanged joints, with an emphasis on crevice and pitting corrosion that commonly occur in industrial applications has been advanced. The experimental and analytical work presented offers novel insights into how specific factors, such as gap size, gasket material, and joint configuration, influence corrosion initiation and progression. These findings contribute to the development of more robust designs and material selection criteria to enhance the longevity and reliability of critical engineering components in corrosive environments.

The review of failure mechanisms and contributing factors for corrosion in flanged joints provide an essential context for our study. Crevice, pitting, and galvanic corrosion are identified as primary drivers of degradation, with specific environmental factors, such as temperature, fluid flow, and chlorination, exacerbating these effects. This comprehensive review reinforces the need for corrosion-resistant designs and emphasizes the importance of selecting appropriate gasket materials to avoid premature failures and costly maintenance.

The study begins with the design of an innovative fixture that simulates real-world service conditions for bolted flanged joints. This fixture allows for corrosion assessment under different service conditions, addressing a significant gap in corrosion research of bolted flanged joints.

Investigation of the effect of gasket materials on the corrosion behavior reveals substantial differences in corrosion behavior based on the gasket material composition. The comparison of potentiostatic and potentiodynamic polarization results, surface analysis, and gasket geometry and weight characterization indicate that corrosion at the flange-gasket interface is influenced by two factors: the gap size between the flange surfaces and solution penetration into the gasket material. These factors increase corrosion susceptibility, particularly in joints with graphite gaskets compared to PTFE gaskets. Between the two graphite gaskets, the graphite sheet gasket (G-1) shows greater susceptibility to crevice corrosion than the metal-

inserted graphite gasket (G-2), due to tighter gap formation and higher solution absorption within the gasket structure. This increased susceptibility with the G-1 gasket leads to a larger corrosion-affected area between the flange and gasket surfaces, facilitating corrosion propagation and potentially causing earlier leakage than with other gaskets. For PTFE gaskets, corrosion propagation is more localized, occurring primarily in the flange depth near the gasket's inner diameter, resulting in a slower path to leakage.

This study also reveals that the size of the gaps in bolted flanged joints affect the corrosion behavior of the flanges. Increasing gap thickness from 1.58 mm to 6.35 mm raises the general corrosion rate of the flange surface from 0.09 mm. y^{-1} to 1.03 mm. y^{-1}, while the initiation time for crevice corrosion extends from 0.23 hours to 3.12 hours as the gap size increases. Both EIS and CPP electrochemical tests confirm that larger gap thickness correlates with increased corrosion rates, while reduced crevice depth (d) minimizes general corrosion. Corrosion pits develop on areas exposed to the solution, with pit depth increasing as gap thickness widens; in contrast, pit depth decreases with reduced d values when surfaces are covered by the gasket. The passive potential range $|E_{corr} - E_b|$ decreases as the volume of the gap increases, and both crevice corrosion and pitting corrosion cause the breakdown of the passive layer in CPP tests. The gap size influences the contribution of crevice corrosion and pitting corrosion on the flange surface.

To enhance corrosion monitoring and predictive maintenance strategies, machine learning models are used to classify corrosion behaviors in different environments. ML models, including DT, SVM, RF, and Bagging classifier, were evaluated for their performance in predicting the corrosion behavior of SS in different environments and service conditions. Bagging classifier achieved the highest testing accuracy of 94.4%, making it the most effective model for predicting the corrosion behavior of SS grades. By conducting a feature importance analysis on Dataset No. 2, the most influential factors contributing to the corrosion behavior of SS in different environments were identified, providing valuable insights for material selection and design. The analysis revealed that hydrogen and sulfide concentrations in corrosive environments, as well as the number of alloying elements (which are complementary

to the amount of iron in SS), are three features that can influence corrosion behavior up to 77.8%.

In real-time corrosion monitoring applications, the RNN-based system proposed in this work holds potential for continuous classification of EN data, enabling timely detection of shifts from passive to localized corrosion states, such as the transition to pitting or crevice corrosion. Among the supervised models, the LSTM models achieved the highest test accuracy of 93.62%, effectively uncovering hidden patterns in the EN data. The RF model achieved the highest test accuracy of 97.85% in distinguishing corrosion types, demonstrating the effectiveness of feature extraction through LSTM autoencoders for pattern recognition. In the unsupervised approach, PCA assists in clustering based on features extracted by the LSTM autoencoder, improving its ability to detect transitions between corrosion types.

In conclusion, this PhD research established a standard test method for evaluating the corrosion behavior of flanges under simulated real-world conditions of bolted flanged joints in industrial settings. Additionally, it provided insights through experiments to improve the design of bolted joints, reducing their susceptibility to corrosion. The developed deep learning models offer significant improvements in accuracy, automation, and adaptability in online corrosion monitoring, setting it apart from existing state-of-the-art techniques. The findings and methodologies have the potential to reduce maintenance costs, minimize downtime, and prevent resource losses and environmental contamination, ultimately enhancing the sustainability and efficiency of industrial operations.

RECOMMENDATIONS FOR FUTURE WORK

Based on the findings of this study, several recommendations for future work are proposed to enhance the understanding and further the field of corrosion in bolted joints:

- The results of this research have shown evidence of crack initiation and propagation alongside crevice corrosion. It is recommended that future studies focus more comprehensively on the effect of stress at the interface of the gasket and flange to determine whether these cracks are a direct result of stress or other contributing factors. Investigating the role of stress in crack development could provide critical insights into the combined mechanical and chemical interactions that exacerbate corrosion.

- To facilitate a deeper understanding of crevice corrosion propagation, it is recommended to build the fixture using a transparent material such as silicone-based or fluoropolymer gaskets. This modification would allow researchers to visually monitor the progression of crevice corrosion during real-time corrosion monitoring. Capturing images of the corrosion process as it clarifies would offer valuable data for analyzing the kinetics and morphology of corrosion propagation and support more accurate modeling.

- To achieve a more accurate calculation of corrosion current density through Tafel extrapolation, it is recommended to use a counter electrode made of a material more noble than stainless steel. This adjustment will allow for the application of higher cathodic potentials, enabling better identification and characterization of corrosion behavior.

- The presented work can serve as a basis for developing a new ASTM standard for corrosion testing of bolted flange connections, therefore it is recommended to present this work to the ASTM Task Group on Gaskets.

- Another area deserving further exploration is the effect of gases on crevice corrosion. It is recommended to conduct experiments that examine the influence of gases such as SO_2 and CO_2 on corrosion behavior. For such studies, it is essential to use tubes and connections that ensure safe handling and containment of these reactive gases. Understanding how gaseous environments impact corrosion could provide insights into real-world applications where exposure to industrial gases is common.

- Although challenging, it is recommended to attempt the calculation of corrosion rates using electrochemical noise current data. This requires correlating the morphology of pit or crevice propagation to the current signals, which is demanding, and then applying deep learning techniques for predictive modeling. Such an approach could lead to more accurate real-time assessments and enhance predictive capabilities in corrosion monitoring systems.

- The effects of corrosion inhibitors, coatings, cathodic protection, and other experimental conditions, such as fluid pressure and pH, on the corrosion behavior of the flanges could be considered for future studies. These remain as gaps that could be addressed in further research.

ANNEX I

MANUFACTURING DRAWING OF FIXTURE

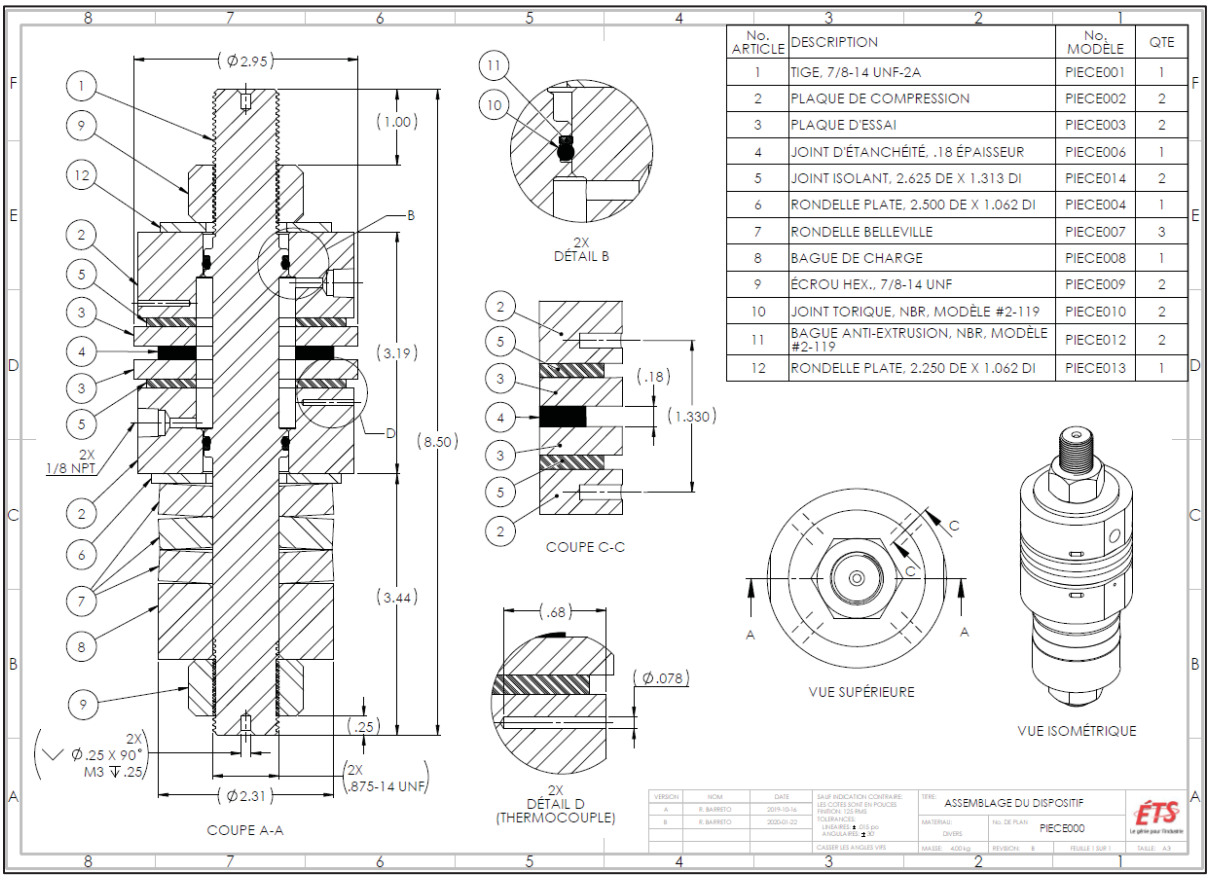

No. ARTICLE	DESCRIPTION	No. MODÈLE	QTE
1	TIGE, 7/8-14 UNF-2A	PIECE001	1
2	PLAQUE DE COMPRESSION	PIECE002	2
3	PLAQUE D'ESSAI	PIECE003	2
4	JOINT D'ÉTANCHÉITÉ, .18 ÉPAISSEUR	PIECE006	1
5	JOINT ISOLANT, 2.625 DE X 1.313 DI	PIECE014	2
6	RONDELLE PLATE, 2.500 DE X 1.062 DI	PIECE004	1
7	RONDELLE BELLEVILLE	PIECE007	3
8	BAGUE DE CHARGE	PIECE008	1
9	ÉCROU HEX., 7/8-14 UNF	PIECE009	2
10	JOINT TORIQUE, NBR, MODÈLE #2-119	PIECE010	2
11	BAGUE ANTI-EXTRUSION, NBR, MODÈLE #2-119	PIECE012	2
12	RONDELLE PLATE, 2.250 DE X 1.062 DI	PIECE013	1

VERSION	NOM	DATE	TITRE: ASSEMBLAGE DU DISPOSITIF
A	F. BARRETO	2019-10-16	
B	F. BARRETO	2020-01-22	MATÉRIAU: DIVERS — No. DE PLAN: PIECE000

SAUF INDICATION CONTRAIRE: LES COTES SONT EN POUCES FINITION: 125 RMS TOLÉRANCES: LINÉAIRES: ± .005 po ANGULAIRES: ± 1° CASSER LES ANGLES VIFS

MASSE: 4.00 kg — RÉVISION: B — FEUILLE 1 SUR 1 — TAILLE: A3

ÉTS Le génie pour l'industrie

Figure-A I-1 The general arrangement of fixture

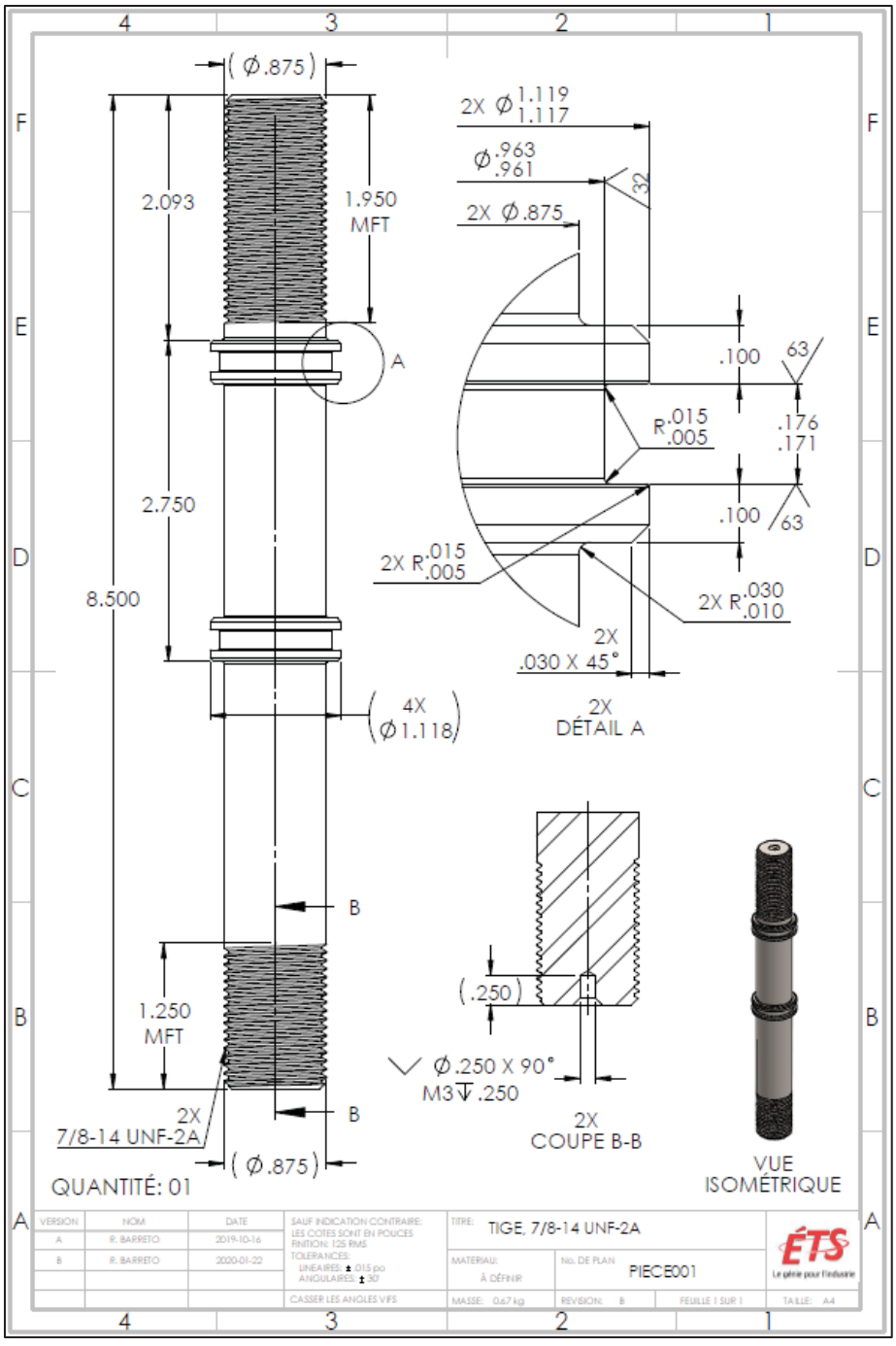

Figure-A I-2 Drawing of the central stud

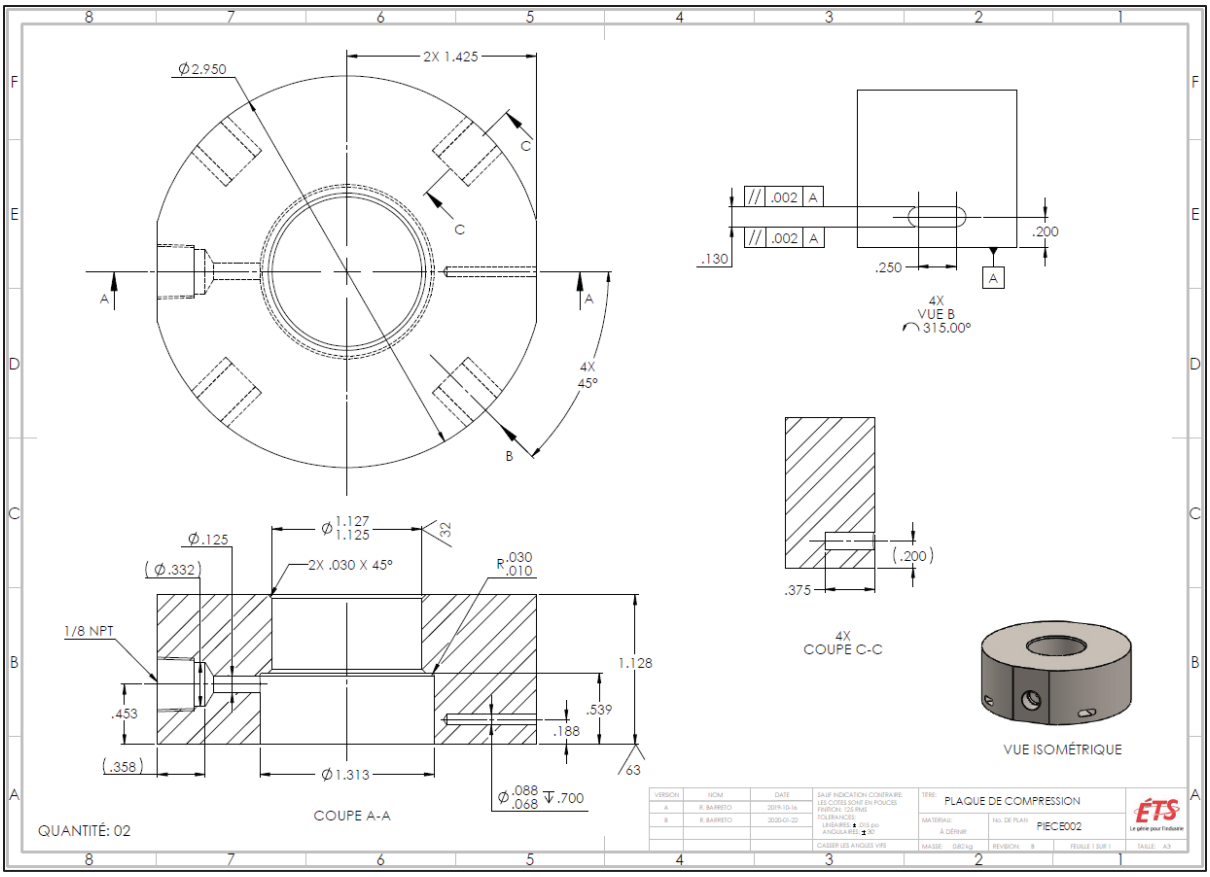

Figure-A I-3 Drawing of the compression plate

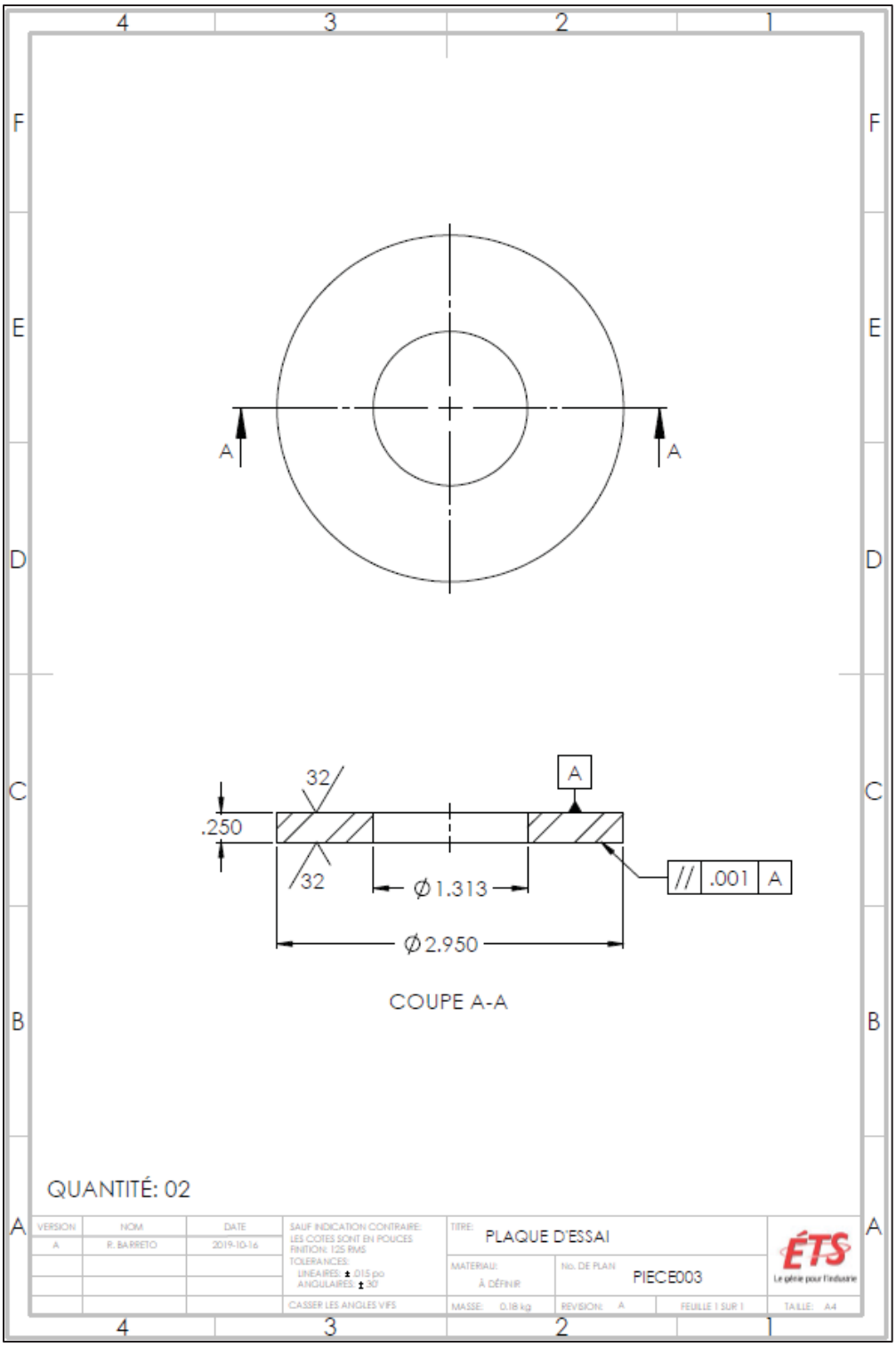

Figure-A I-4 Drawing of the flange sample plate

ANNEX II

DATA ACQUISITION SYSTEM

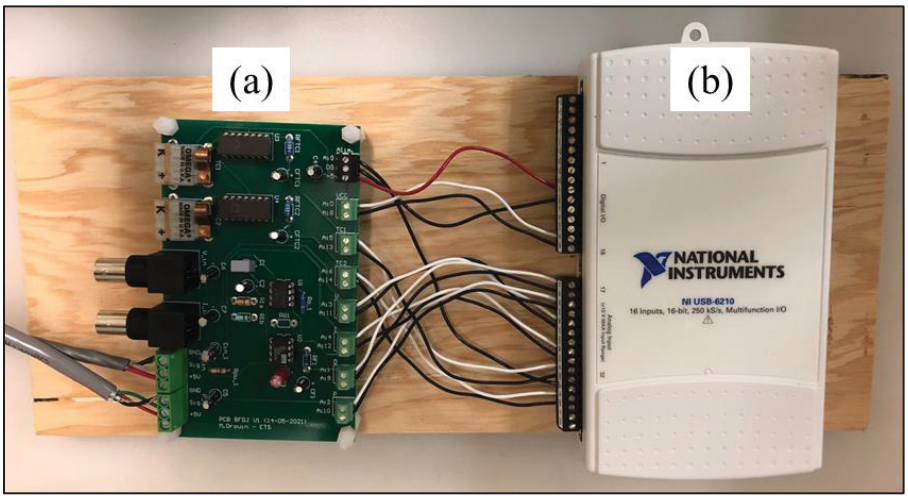

Figure-A II-1 a) The printed circuit board (PCB) that receives the analog signals from the sensors and acts as a hub for signal transmission. b) The data acquisition card (DAQ) that converts the analog signals into digital values for further processing.

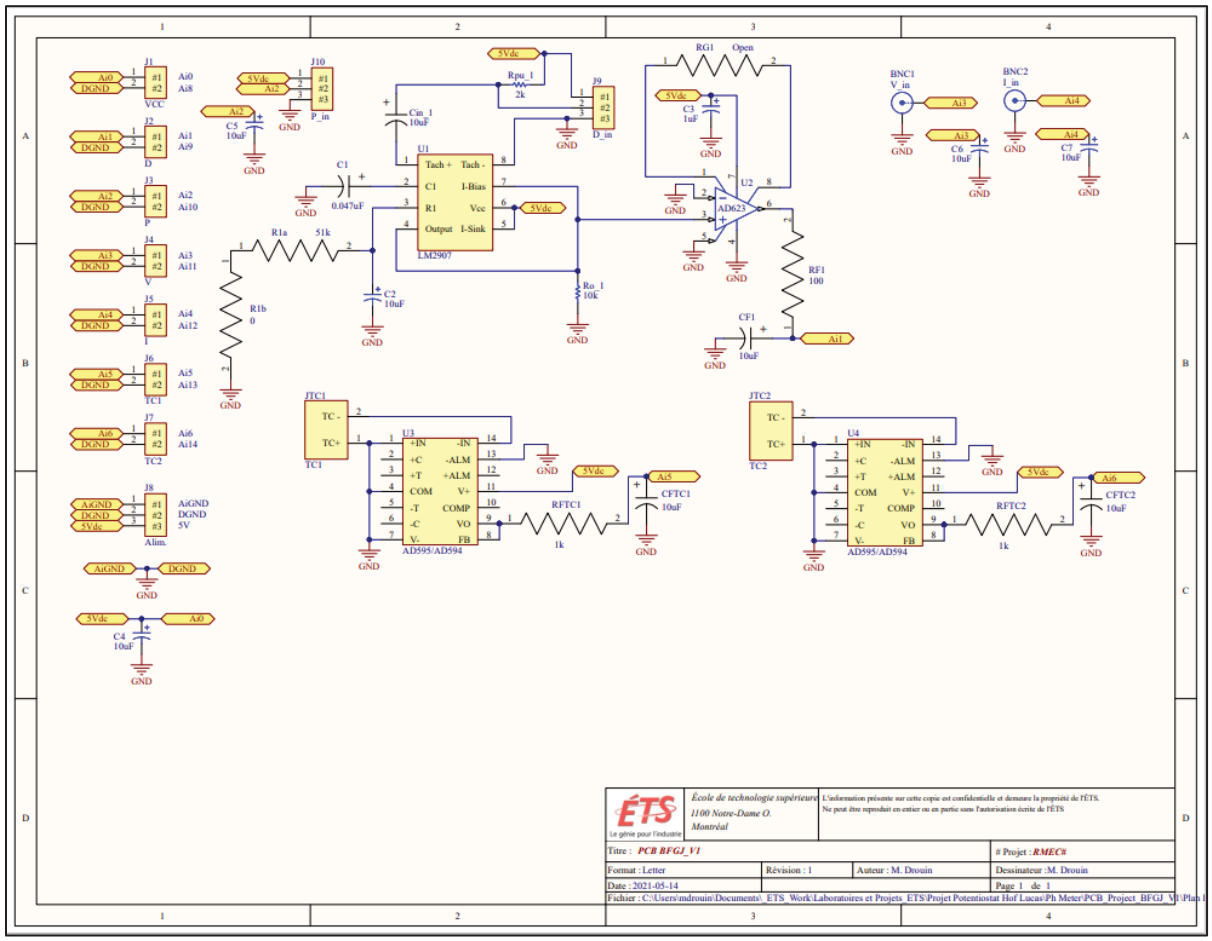

Figure-A II-2 Schematic of the electrical circuit

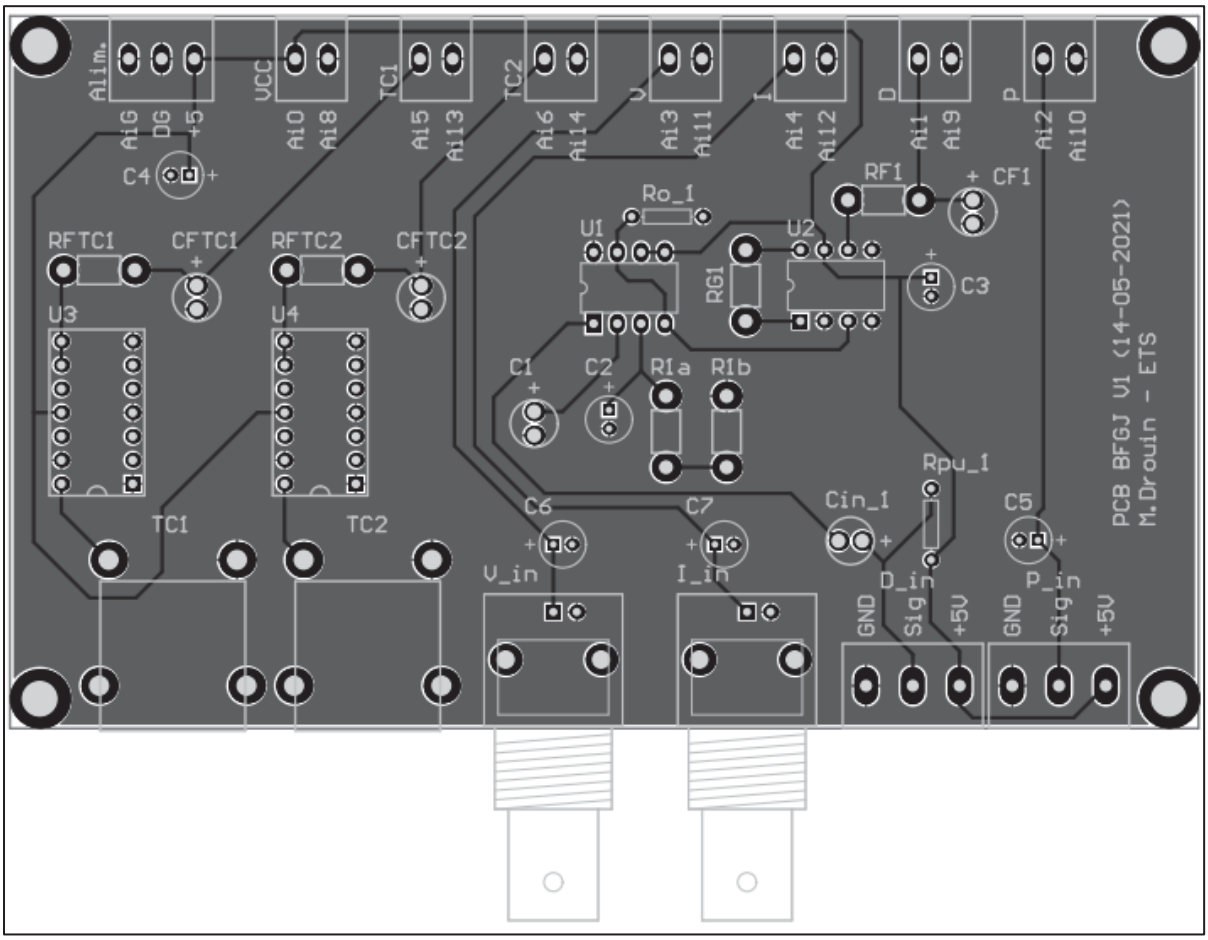

Figure-A II-3 Printed circuit board (PCB) design

Table-A II-1 Component list for the printed circuit board (PCB)

Comment	Description	Designator	Quantity
V_in	BNC Elbow Connector	BNC1	1
I_in	BNC Elbow Connector	BNC2	1
0.047uF	Polarized Capacitor (Radial)	C1	1
10uF	Polarized Capacitor (Radial)	C2, C4, C5, C6, C7	5
1uF	Polarized Capacitor (Radial)	C3	1
10uF	Polarized Capacitor (Radial)	CF1, CFTC1, CFTC2, Cin_1	4
VCC	Screw Connector	J1	1
D	Screw Connector	J2	1
P	Screw Connector	J3	1
V	Screw Connector	J4	1
I	Screw Connector	J5	1
TC1	Screw Connector	J6	1
TC2	Screw Connector	J7	1
Alim.	Screw Connector	J8	1
D_in	Screw Connector	J9	1
P_in	Screw Connector	J10	1
TC1	TC Connector	JTC1	1
TC2	TC Connector	JTC2	1
51k	Resistor	R1a	1
0	Resistor	R1b	1
100	Resistor	RF1	1
1k	Resistor	RFTC1, RFTC2	2
Open		RG1	1
10k	Resistor	Ro_1	1
2k	Resistor	Rpu_1	1
LM2907	F to V converter	U1	1
AD623	Low-Drift, Low-Power Instrumentation Amp	U2	1
AD595/AD594	Amp Thermocouple	U3, U4	2

ANNEX III

ENVIRONMENT OF LABVIEW SOFTWARE DESIGNED FOR THIS PROJECT

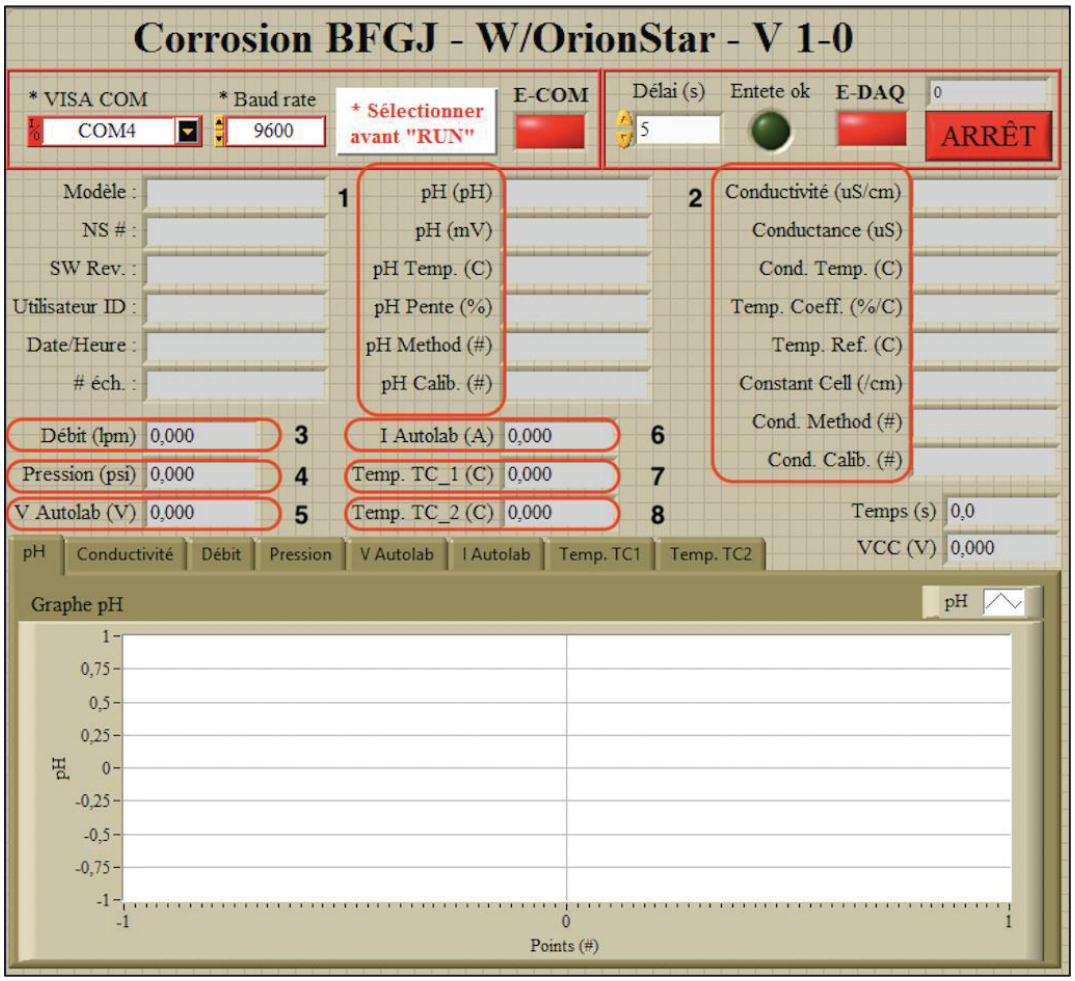

Figure-A III-1 Environment of LabVIEW software designed for this project: No.1 shows the data obtained from the pH sensor, No.2 shows the data obtained from the conductivity sensor, No.3 shows the flow rate, No.4 shows the pressure value, No.5 and 6 show the potential and current obtained from the potentiostat, No.7 shows the temperature of the solution, and No.8 shows the temperature of the fixture

APPENDIX

VITAE

Peer reviewed journal papers:

1. Soroosh Hakimian, Abdel-Hakim Bouzid, Lucas A. Hof, Effect of gasket material on flange face corrosion, *International Journal of Pressure Vessels and Piping*, Volume 209, 2024, 105207, ISSN 0308-0161, https://doi.org/10.1016/j.ijpvp.2024.105207.

2. Soroosh Hakimian, Abdel-Hakim Bouzid, Lucas A. Hof, Corrosion failures of flanged gasketed joints: A review, *Journal of Advanced Joining Processes*, Volume 9, 2024, 100200, ISSN 2666-3309, https://doi.org/10.1016/j.jajp.2024.100200.

3. Soroosh Hakimian, Abdel-Hakim Bouzid, Lucas A. Hof, An improved fixture to quantify corrosion in bolted flanged gasketed joints, ASME. *Journal of Pressure Vessel Technology*, Volume 146, 2024, 011302, https://doi.org/10.1115/1.4063975.

4. Soroosh Hakimian, Abdel-Hakim Bouzid, Lucas A. Hof, Effect of gap size on flange face corrosion, *Materials and Corrosion*, 2024, Pages 1–18, ISSN 0947-5117 https://doi.org/10.1002/maco.202414367.

5. Soroosh Hakimian, Shamim Pourrahimi, Abdel-Hakim Bouzid, Lucas A. Hof, Application of machine learning for the classification of corrosion behavior in different environments for material selection of stainless steels, *Computational Materials Science*, Volume 228, 2023, 112352, ISSN 0927-0256, https://doi.org/10.1016/j.commatsci.2023.112352.

6. Soroosh Hakimian, Shamim Pourrahimi, Abdel-Hakim Bouzid, Lucas A. Hof, Corrosion type identification in flanged joints using a novel recurrent neural network technique applied to electrochemical noise measurements, Submitted to *Engineering Applications of Artificial Intelligence.*

7. Mohammad Maroufkhani, Soroosh Hakimian, Alireza Khodabandeh, Iulian Radu, Lucas A. Hof, Mohammad Jahazi, Influence of oxygen content in the protective gas on pitting corrosion resistance of a 316L stainless steel weld joint, *Materials*, Volume 16, 2023, 5968, https://doi.org/10.3390/ma16175968.

8. Shamim Pourrahimi, Soroosh Hakimian, Abdel-Hakim Bouzid, Lucas A. Hof, On the use of machine learning algorithms to predict the corrosion behavior of stainless steels in lactic acid, *Metals*, Volume 13, 2023,1459, https://doi.org/10.3390/met13081459.

Conferences:

Peer reviewed papers:

1. Soroosh Hakimian, Lucas A. Hof, Hakim A. Bouzid, Effect of Temperature on the Crevice Corrosion Propagation on Flange Faces, ASME. Pressure Vessels and Piping Conference, 2024.

2. Soroosh Hakimian, Lucas A. Hof, Hakim A. Bouzid, The effects of fluid working conditions on flange face corrosion, ASME. Pressure Vessels and Piping Conference, Volume 87455, 2023, V002T02A004, https://doi.org/10.1115/PVP2023-106923.

3. Soroosh Hakimian, Abdel-Hakim Bouzid, Lucas A. Hof, An improved fixture to quantify corrosion in bolted flanged gasketed joints subjected to service conditions, ASME. Pressure Vessels and Piping Conference, Volume 86151, 2022, V002T02A004, https://doi.org/10.1115/PVP2022-82668.

Peer reviewed abstracts:

1. Soroosh Hakimian, Hakim A. Bouzid, Lucas A. Hof, Predicting crevice corrosion of flange faces using recurrent neural networks and electrochemical techniques, European Corrosion Congress, 2024.

2. Soroosh Hakimian, Lucas A. Hof, Hakim A. Bouzid, Application of recurrent neural networks to electrochemical noise data to predict flange face corrosion rates of bolted joints, 76th Annual Meeting of the International Society of Electrochemistry, 2024.

3. Soroosh Hakimian, Shamim Pourrahimi, Lucas A. Hof, Electrowinning of printed circuit boards (PCB) waste: electrochemical study of copper recovery, Congrès de recherche du LaCIME, April 2024.

4. Soroosh Hakimian, Lucas A. Hof, Hakim A. Bouzid, Investigation of the corrosion behavior of SA-105 material using a developed experimental bolted joint test fixture, Canadian Society for Mechanical Engineering International Congress, Volume 6, 2023, https://doi.org/10.17118/11143/21083.

5. Soroosh Hakimian, Hakim A. Bouzid, Lucas A. Hof, A study on the influence of operational factors on the flange face corrosion using a novel experimental test bench, ASME Bolted Joint Reliability Symposium, Houston, TX, USA, October 2022.

6. Soroosh Hakimian, Hakim A. Bouzid, Lucas A. Hof, Investigation of corrosion in bolted flanged joints using a novel experimental setup, Congrès de recherche du DYNAMO, September 2022.

7. Soroosh Hakimian, Lucas A. Hof, Hakim A. Bouzid, Investigation of corrosion in bolted flanged joints using a novel experimental setup, Electrochemical Society Meeting Abstracts 241, Volume MA2022-01, 2022, 990-990, https://doi.org/10.1149/MA2022-0116990mtgabs.

8. Soroosh Hakimian, Shamim Pourrahimi, Lucas A. Hof, Application of machine learning algorithms to classify and predict corrosion behavior of stainless steels in lactic acid, Electrochemical Society Meeting Abstracts 241, Volume MA2022-01, 2022, 1002-1002, https://doi.org/10.1149/MA2022-01161002mtgabs.

Patent:

- Declaration of invention (DOI), Identifying corrosion types using electrochemical noise data and recurrent neural networks (RNNs) during real-time corrosion monitoring, Number of declaration: VAL-429 - DI_20241107

Awards:

- Research Dissemination Substance Award - École de technologie supérieure (ÉTS), September 2024.
- First Runner-Up in the PhD Category, Student Paper Competition, ASME Pressure Vessels and Piping Conference, July 2024.
- Research Dissemination Substance Award - École de technologie supérieure (ÉTS), August 2023.
- Certificate of Appreciation for Co- Authoring the Outstanding Technical Paper at the 2022 ASME Pressure Vessels & Piping Conference - ASME Pressure Vessels & Piping Division, June 2023.

- Travel Grant Recipient for the 241st ECS Meeting (Global competition) - The Electrochemical Society, April 2022.

Bursary/Grants:

- Mitacs Business Strategy Internship Award for one session in Summer 2024. On the exploration of the origin of failure modes of photovoltaic modules in marine environments, CAPSolar.
- Bourse Colloque CIRODD for participation in European Corrosion Congress (EUROCORR2024), École de technologie supérieure (ÉTS), May 2024.
- Bourse Colloque CIRODD for participation in 75th Annual Meeting of the International Society of Electrochemistry, École de technologie supérieure (ÉTS), May 2024.
- Mitacs Business Strategy Internship Award for one session in Fall 2024. Developing and optimizing a novel eco-friendly binder for multi-material binder-jetting additive manufacturing system, Nanogrande Inc.
- The Québec Circular Economy Research Network (RRECQ) discovery grant, Electrowinning of Printed Circuit Boards (PCBs) waste - an AI-based approach for process optimization, winter 2024.
- Mitacs Business Strategy Internship Award for one session in Fall 2023. Developing and optimizing a novel multi-material binder-jetting additive manufacturing system, Nanogrande Inc.
- Circular Economy Seed Funding, Re-utilization of powders for nano additive manufacturing, University of British Columbia, March 2022.

BIBLIOGRAPHY

Abadi, M., Agarwal, A., Barham, P., Brevdo, E., Chen, Z., Citro, C., Corrado, G. S., Davis, A., Dean, J., Devin, M., Ghemawat, S., Goodfellow, I., Harp, A., Irving, G., Isard, M., Jia, Y., Jozefowicz, R., Kaiser, L., Kudlur, M., … Research, G. (n.d.). *TensorFlow: Large-Scale Machine Learning on Heterogeneous Distributed Systems*. Retrieved October 22, 2024, from www.tensorflow.org.

Abd El Meguid, E. A., Mahmoud, N. A., & Abd El Rehim, S. S. (2000). Effect of some sulphur compounds on the pitting corrosion of type 304 stainless steel. *Materials Chemistry and Physics*, *63*(1), 67–74. https://doi.org/10.1016/S0254-0584(99)00206-0

Abdulmutaali, A., Hou, Y., Aldrich, C., & Lepkova, K. (2024). An Online Monitoring Approach of Carbon Steel Corrosion via the Use of Electrochemical Noise and Wavelet Analysis. *Metals 2024, Vol. 14, Page 66*, *14*(1), 66. https://doi.org/10.3390/MET14010066

Abdulsalam, M. I. (2007). The role of electrolyte concentration on crevice corrosion of pure nickel. *Materials and Corrosion*, *58*(7), 511–513. https://doi.org/10.1002/MACO.200604037

Abid, M., & Nash, D. H. (2003). Comparative study of the behaviour of conventional gasketed and compact non-gasketed flanged pipe joints under bolt up and operating conditions. *International Journal of Pressure Vessels and Piping*, *80*(12), 831–841. https://doi.org/10.1016/J.IJPVP.2003.11.013

Abid, M., Nash, D. H., Javed, S., & Wajid, H. A. (2018). Performance of a gasketed joint under bolt up and combined pressure, axial and thermal loading – FEA study. *International Journal of Pressure Vessels and Piping*, *168*, 166–173. https://doi.org/https://doi.org/10.1016/j.ijpvp.2018.10.014

Al-Abbadi, S., Aoudi, H., AlShouly, W., Saeed, W., AlSafatli, K., & Toubar, A. (2017). Crevice Corrosion Effect on Alloy 625 in Untreated Seawater Environment. *Society of Petroleum Engineers - SPE Abu Dhabi International Petroleum Exhibition and Conference 2017*, *2017-January*. https://doi.org/10.2118/188302-MS

Al-Mazeedi, H. A. A., & Cottis, R. A. (2004). A practical evaluation of electrochemical noise parameters as indicators of corrosion type. *Electrochimica Acta*, *49*, 2787–2793. https://doi.org/10.1016/j.electacta.2004.01.040

Alves, L. M., Cotta, R. A., Ciarelli, P. M., Salles, E. O. T., Côco, K. F., & Samatelo, J. L. A. (2019). Identification of Corrosive Substances and Types of Corrosion Through Electrochemical Noise Using Signal Processing and Machine Learning. *Journal of Control, Automation and Electrical Systems*, *30*(1), 16–26. https://doi.org/10.1007/S40313-018-00423-0/TABLES/4

Alvino, A., Ramires, D., Tonti, A., & Lega, D. (2014). Influence of chemical composition on microstructure and phase evolution of two HP heat resistant stainless steels after long term plant-service aging. *Http://Dx.Doi.Org/10.1179/0960340913Z.0000000001*, *31*(1), 2–11. https://doi.org/10.1179/0960340913Z.0000000001

Arellano-Pérez, J. H., Ramos Negrón, O. J., Escobar-Jiménez, R. F., Gómez-Aguilar, J. F., & Uruchurtu-Chavarín, J. (2018). Development of a portable device for measuring the corrosion rates of metals based on electrochemical noise signals. *Measurement*, *122*, 73–81. https://doi.org/https://doi.org/10.1016/j.measurement.2018.03.008

Aslam, R., Mobin, M., Zehra, S., & Aslam, J. (2022). A comprehensive review of corrosion inhibitors employed to mitigate stainless steel corrosion in different environments. *Journal of Molecular Liquids*, *364*, 119992. https://doi.org/10.1016/j.molliq.2022.119992

ASME B16.5. (2021). Pipe Flanges and Flanged Fittings: NPS 1/2 through NPS 24, Metric/Inch Standard. *ASME International*. https://www.asme.org/codes-standards/find-codes-standards/b16-5-pipe-flanges-flanged-fittings-nps-1-2-nps-24-metric-inch-standard

ASME B16.21. (2022). Nonmetallic Flat Gaskets for Pipe Flanges. *ASME International*. https://www.asme.org/codes-standards/find-codes-standards/b16-21-nonmetallic-flat-gaskets-pipe-flanges

ASTM International. (2014). *ASTM G5 - 14e1 Standard Reference Test Method for Making Potentiodynamic Anodic Polarization Measurements*. https://www.astm.org/Standards/G5

ASTM International. (2015a). *ASTM G102 - 89(2015)e1 Standard Practice for Calculation of Corrosion Rates and Related Information from Electrochemical Measurements*. https://www.astm.org/Standards/G102

ASTM International. (2015b). ASTM G102-89 (2015) Standard Practice for Calculation of Corrosion Rates and Related Information from Electrochemical Measurements. In *Astm* (Vol. 89, Issue Reapproved 2015). https://doi.org/10.1520/G0102-89R15E01.2

ASTM International. (2017a). *ASTM A276 / A276M - 17 Standard Specification for Stainless Steel Bars and Shapes*. https://doi.org/10.1520/A0276_A0276M-17

ASTM International. (2017b). *ASTM G1 - 03(2017)e1 Standard Practice for Preparing, Cleaning, and Evaluating Corrosion Test Specimens*. https://www.astm.org/Standards/G1

ASTM International. (2017c). *ASTM G1-03 (2017) Standard Practice for Preparing, Cleaning, and Evaluating Corrosion Test Specimens*.

ASTM International. (2018a). *ASTM A105 / A105M - 18 Standard Specification for Carbon Steel Forgings for Piping Applications*. https://www.astm.org/Standards/A105

ASTM International. (2018b). *ASTM A350 / A350M - 18 Standard Specification for Carbon and Low-Alloy Steel Forgings, Requiring Notch Toughness Testing for Piping Components*. https://www.astm.org/Standards/A350.htm

ASTM International. (2018c). *ASTM G61 - 86(2018) Standard Test Method for Conducting Cyclic Potentiodynamic Polarization Measurements for Localized Corrosion Susceptibility of Iron-, Nickel-, or Cobalt-Based Alloys*. https://www.astm.org/Standards/G61.htm

ASTM International. (2018d). *ASTM G61-86(2018) Standard Test Method for Conducting Cyclic Potentiodynamic Polarization Measurements for Localized Corrosion Susceptibility of Iron-, Nickel-, or Cobalt-Based Alloys*.

ASTM International. (2018e). *ASTM G150-18 Standard Test Method for Electrochemical Critical Pitting Temperature Testing of Stainless Steels and Related Alloys*.

ASTM International. (2019). *ASTM G71-81(2019)- Standard Guide for Conducting and Evaluating Galvanic Corrosion Tests in Electrolytes*.

ASTM International. (2020a). *ASTM A182 / A182M - 20 Standard Specification for Forged or Rolled Alloy and Stainless Steel Pipe Flanges, Forged Fittings, and Valves and Parts for High-Temperature Service*. https://www.astm.org/Standards/A182.htm

ASTM International. (2020b). *ASTM A240/A240M − 20a Standard Specification for Chromium and Chromium-Nickel Stainless Steel Plate, Sheet, and Strip for Pressure Vessels and for General Applications*. https://doi.org/10.1520/A0240_A0240M-20A

ASTM International. (2020c). *ASTM G48-11(2020)e1, Standard Test Methods for Pitting and Crevice Corrosion Resistance of Stainless Steels and Related Alloys by Use of Ferric Chloride Solution*.

ASTM International. (2020d). *ASTM G59 - 97(2020) Standard Test Method for Conducting Potentiodynamic Polarization Resistance Measurements*. https://www.astm.org/Standards/G59

ASTM International. (2020e). *ASTM G78 - 20 Standard Guide for Crevice Corrosion Testing of Iron-Base and Nickel-Base Stainless Alloys in Seawater and Other Chloride-Containing Aqueous Environments*. https://www.astm.org/Standards/G78.htm

ASTM International. (2020f). *ASTM G192-08(2020)e1 Standard Test Method for Determining the Crevice Repassivation Potential of Corrosion-Resistant Alloys Using a Potentiodynamic-Galvanostatic-Potentiostatic Technique*.

Baboian, R. (n.d.). *Corrosion Tests and Standards: Application and Interpretation (2nd Edition): (MNL 20)*. ASTM International. https://app.knovel.com/hotlink/toc/id:kpCTSAIEM9/corrosion-tests-standards/corrosion-tests-standards

Baboian, R. (2005). *Corrosion tests and standards: application and interpretation* (Vol. 20). ASTM international.

Beguería, S. (2006). Validation and evaluation of predictive models in hazard assessment and risk management. *Natural Hazards*, *37*(3), 315–329. https://doi.org/10.1007/S11069-005-5182-6/METRICS

Belgiu, M., & Drăgu, L. (2016). Random forest in remote sensing: A review of applications and future directions. *ISPRS Journal of Photogrammetry and Remote Sensing*, *114*, 24–31. https://doi.org/10.1016/J.ISPRSJPRS.2016.01.011

Bengtsson, M. (2015a). *Investigation of Galvanic Corrosion between Graphite Gaskets and Stainless Steel Flanges*. http://www.teknat.uu.se/student

Bengtsson, M. (2015b). *Investigation of galvanic corrosion between graphite gaskets and stainless steel flanges*. Uppsala University.

Bernard, S., Heutte, L., & Adam, S. (2009). On the selection of decision trees in Random forests. *Proceedings of the International Joint Conference on Neural Networks*, 302–307. https://doi.org/10.1109/IJCNN.2009.5178693

Betova, I., Bojinov, M., Hyökyvirta, O., & Saario, T. (2010). Effect of sulphide on the corrosion behaviour of AISI 316L stainless steel and its constituent elements in simulated Kraft digester conditions. *Corrosion Science*, *52*(4), 1499–1507. https://doi.org/10.1016/J.CORSCI.2009.12.034

Betts, A. J., & Boulton, L. H. (1993). Crevice corrosion: review of mechanisms, modelling, and mitigation. *British Corrosion Journal*, *28*(4), 279–296.

Bond, S., Lattimer, A., & Welsford, P. (2018). Flange face corrosion in seawater and hydrocarbon environments related to gasket material selection. *Corrosion and Prevention 2018*. https://www.engineeringvillage.com/share/document.url?mid=cpx_Mc6ce3d816991d2d0b2M6a5810178163167&database=cpx

Bond, S., & Yi Li. (2020). A Novel Gasket Design for an Isolating Gasket to Solve Common Sealing Problems. *CORROSION 2020*.

Bouzid A.; Chaaban A.; Bazergui A. (1994, June). The influence of the flange rotation on the leakage performance of bolted flanged joints. *Canadian Society for Mechanical Engineering*.

Bouzid, A., Chaaban, A., & Bazergui, A. (1994). *The influence of the flange rotation on the leakage performance of bolted flanged joints*.

Bouzid, A., Chaaban, A., & Bazergui, A. (1995). The Effect of Gasket Creep-Relaxation on the Leakage Tightness of Bolted Flanged Joints. *Journal of Pressure Vessel Technology*, *117*(1), 71–78. https://doi.org/10.1115/1.2842093

Bouzid, A. H. (2009). On the effect of external bending loads in bolted flange joints. *Journal of Pressure Vessel Technology, Transactions of the ASME*, *131*(2). https://doi.org/10.1115/1.3006895/474944

Bouzid, A. H., Derenne, M., El-Rich, M., & Birembaut, Y. (2004). Effect of flange rotation and gasket width on the leakage behavior of bolted flanged joints. *Welding Research Council Bulletin*, *496*.

Bouzid, A.-H., & Das, S. K. (2023). Long-Term Performance of Semimetallic Gaskets. *Journal of Nuclear Engineering and Radiation Science*, *9*(3). https://doi.org/10.1115/1.4056260

Bouzid, H., Derenne, M., & El-Rich, M. (2004). *Effect of flange rotation and gasket width on leakage behavior of bolted flanged joints*.

Bradford, S. A. (2003). Corrosion. In R. A. Meyers (Ed.), *Encyclopedia of Physical Science and Technology (Third Edition)* (pp. 761–778). Academic Press. https://doi.org/https://doi.org/10.1016/B0-12-227410-5/00148-4

Brondel, D., Edwards, R., Hayman, A., Hill, D., Mehta, S., & Semerad, T. (1994). Corrosion in the oil industry. *Oilfield Review*, *6*, 4–18.

Cai, B., Liu, Y., Tian, X., Wang, F., Li, H., & Ji, R. (2010). An experimental study of crevice corrosion behaviour of 316L stainless steel in artificial seawater. *Corrosion Science*, *52*(10), 3235–3242. https://doi.org/10.1016/j.corsci.2010.05.040

Cai, Y., Zhao, Y., Ma, X., Zhou, K., & Wang, H. (2019). Application of hierarchical linear modelling to corrosion prediction in different atmospheric environments. *Corrosion Engineering Science and Technology*, *54*(3), 266–275. https://doi.org/10.1080/1478422X.2019.1578067/FORMAT/EPUB

Carvalho, T. P., Soares, F. A. A. M. N., Vita, R., Francisco, R. da P., Basto, J. P., & Alcalá, S. G. S. (2019). A systematic literature review of machine learning methods

applied to predictive maintenance. *Computers and Industrial Engineering*, *137*(September), 106024. https://doi.org/10.1016/j.cie.2019.106024

Cashell, K. A., & Baddoo, N. R. (2014). Ferritic stainless steels in structural applications. *Thin-Walled Structures*, *83*, 169–181. https://doi.org/10.1016/J.TWS.2014.03.014

Cavanaugh, M. K., Buchheit, R. G., & Birbilis, N. (2010a). Modeling the environmental dependence of pit growth using neural network approaches. *Corrosion Science*, *52*(9), 3070–3077. https://doi.org/10.1016/j.corsci.2010.05.027

Cavanaugh, M. K., Buchheit, R. G., & Birbilis, N. (2010b). Modeling the environmental dependence of pit growth using neural network approaches. *Corrosion Science*, *52*(9), 3070–3077. https://doi.org/10.1016/j.corsci.2010.05.027

Chawla, S. L. (1959). Factors Influencing Corrosion. *Corrosion*, *15*(9), 23–36. https://doi.org/10.5006/0010-9312-15.9.23

Cheng, M., He, P., Lei, L., Tan, X., Wang, X., Sun, Y., Li, J., & Jiang, Y. (2021). Comparative studies on microstructure evolution and corrosion resistance of 304 and a newly developed high Mn and N austenitic stainless steel welded joints. *Corrosion Science*, *183*. https://doi.org/10.1016/J.CORSCI.2021.109338

Chicco, D., & Jurman, G. (2020). The advantages of the Matthews correlation coefficient (MCC) over F1 score and accuracy in binary classification evaluation. *BMC Genomics*, *21*(1), 1–13. https://doi.org/10.1186/S12864-019-6413-7/TABLES/5

Chico, B., Díaz, I., Simancas, J., & Morcillo, M. (2017). Annual Atmospheric Corrosion of Carbon Steel Worldwide. An Integration of ISOCORRAG, ICP/UNECE and MICAT Databases. *Materials*, *10*(6), 601. https://doi.org/10.3390/ma10060601

Costa, E. M., Dedavid, B. A., Santos, C. A., Lopes, N. F., Fraccaro, C., Pagartanidis, T., & Lovatto, L. P. (2023). Crevice corrosion on stainless steels in oil and gas industry: A review of techniques for evaluation, critical environmental factors and

dissolved oxygen. *Engineering Failure Analysis*, *144*, 106955. https://doi.org/10.1016/J.ENGFAILANAL.2022.106955

Cox, A., & Lyon, S. B. (1994). An electrochemical study of the atmospheric corrosion of mild steel-I. Experimental method. *Corrosion Science*, *36*(7), 1167–1176. https://doi.org/https://doi.org/10.1016/0010-938X(94)90141-4

Dastgerdi, A. A., Brenna, A., Ormellese, M., Pedeferri, M., & Bolzoni, F. (2019a). Experimental design to study the influence of temperature, pH, and chloride concentration on the pitting and crevice corrosion of UNS S30403 stainless steel. *Corrosion Science*, *159*, 108160.

Dastgerdi, A. A., Brenna, A., Ormellese, M., Pedeferri, M. P., & Bolzoni, F. (2019b). Experimental design to study the influence of temperature, pH, and chloride concentration on the pitting and crevice corrosion of UNS S30403 stainless steel. *Corrosion Science*, *159*. https://doi.org/10.1016/j.corsci.2019.108160

Deng, X., Liu, Q., Deng, Y., & Mahadevan, S. (2016). An improved method to construct basic probability assignment based on the confusion matrix for classification problem. *Information Sciences*, *340–341*, 250–261. https://doi.org/10.1016/J.INS.2016.01.033

Dey, R., & Salemt, F. M. (2017). Gate-variants of Gated Recurrent Unit (GRU) neural networks. *Midwest Symposium on Circuits and Systems*, *2017-August*, 1597–1600. https://doi.org/10.1109/MWSCAS.2017.8053243

Dhanumalayan, E., & Joshi, G. M. (2018). Performance properties and applications of polytetrafluoroethylene (PTFE)—a review. *Advanced Composites and Hybrid Materials 2018 1:2*, *1*(2), 247–268. https://doi.org/10.1007/S42114-018-0023-8

Diao, X., Chi, Z., Jiang, J., Mebarki, A., Ni, L., Wang, Z., & Hao, Y. (2020). Leak detection and location of flanged pipes: An integrated approach of principle component

analysis and guided wave mode. *Safety Science*, *129*, 104809. https://doi.org/https://doi.org/10.1016/j.ssci.2020.104809

Diao, Y., Yan, L., & Gao, K. (2021). Improvement of the machine learning-based corrosion rate prediction model through the optimization of input features. *Materials and Design*, *198*, 109326. https://doi.org/10.1016/j.matdes.2020.109326

Durstewitz, D., Koppe, G., & Thurm, M. I. (2023). Reconstructing computational system dynamics from neural data with recurrent neural networks. *Nature Reviews Neuroscience 2023 24:11*, *24*(11), 693–710. https://doi.org/10.1038/s41583-023-00740-7

Efremov, A. I. (2005). Creep limitation of bolted fasteners and gaskets. *2005 ASME Pressure Vessels and Piping Conference, PVP2005, July 17, 2005 - July 21, 2005*, *3*, 167–171. https://doi.org/10.1115/PVP2005-71130

Esmailzadeh, S., Aliofkhazraei, M., & Sarlak, H. (2018). Interpretation of Cyclic Potentiodynamic Polarization Test Results for Study of Corrosion Behavior of Metals: A Review. *Protection of Metals and Physical Chemistry of Surfaces*, *54*(5), 976–989. https://doi.org/10.1134/S207020511805026X

Farfan-Cabrera, L. I., Rodríguez-Bravo, G. A., Godínez-Salcedo, J. G., Resendiz-Calderon, C. D., Salgado-Sviercovich, J. S., & Moreno-Ríos, M. (2021). A crevice corrosion assessment method for joints of mechanical components sealed with composite structure gaskets – The case of the engine cylinder head/mono-block joint. *Engineering Failure Analysis*, *119*. https://doi.org/10.1016/j.engfailanal.2020.104981

Fargas, G., Anglada, M., & Mateo, A. (2009). Effect of the annealing temperature on the mechanical properties, formability and corrosion resistance of hot-rolled duplex stainless steel. *Journal of Materials Processing Technology*, *209*(4), 1770–1782. https://doi.org/10.1016/j.jmatprotec.2008.04.026

Farrel J. Martin; Paul M. Natishan; Steven H. Lawrence; Elizabeth A. Hogan; Keith E. Lucas; Elvin Dail Thomas. (2004, March). Fluoroelastomeric gasket peculiarities influence the seawater crevice corrosion susceptibility of NiCrMo alloys. *CORROSION 2004*.

Fischer, C., & Zitter, H. (1960). Korrosion an Dichtflächen von Flanschverbindungen. *Materials and Corrosion*, *11*(1), 17–22.

Francis, R. (1994a). Galvanic Corrosion of High Alloy Stainless Steels in Sea Water. *British Corrosion Journal*, *29*(1), 53–57. https://doi.org/10.1179/000705994798268033

Francis, R. (1994b). Galvanic corrosion of high alloy stainless steels in sea water. *British Corrosion Journal*, *29*(1), 53–57.

Francis, R., & Byrne, G. (n.d.). FACTORS AFFECTING GASKET SELECTION FOR STAINLESS STEELS IN SEAWATER. In *rolledalloys.ca*. Retrieved November 30, 2020, from https://www.rolledalloys.ca/shared/library/technical-papers/corrosive/Factors-Affecting-Gasket-Selection-For-Stainless-Steels-In-Seawater.pdf

Gedge, G. (2008). Structural uses of stainless steel — buildings and civil engineering. *Journal of Constructional Steel Research*, *64*(11), 1194–1198. https://doi.org/10.1016/J.JCSR.2008.05.006

Gore, P., Sujata, M., & Bhaumik, S. K. (2014). Stress corrosion cracking of ring type joint of reactor pipeline of a hydrocracker unit. *Journal of Failure Analysis and Prevention*, *14*(3), 307–313. https://doi.org/10.1007/S11668-014-9820-8/TABLES/2

Graves, A., Mohamed, A. R., & Hinton, G. (2013). Speech recognition with deep recurrent neural networks. *ICASSP, IEEE International Conference on Acoustics, Speech and Signal Processing - Proceedings*, 6645–6649. https://doi.org/10.1109/ICASSP.2013.6638947

GRU — PyTorch 2.5 documentation. (n.d.). Retrieved October 22, 2024, from https://pytorch.org/docs/stable/generated/torch.nn.GRU.html#

Guo, D., Chen, J., Chen, X., Shi, Q., Cristino, V. A. M., Kwok, C. T., Tam, L. M., Qian, H., Zhang, D., & Li, X. (2021). Pitting corrosion behavior of friction-surfaced 17-4PH stainless steel coatings with and without subsequent heat treatment. *Corrosion Science*, *193*. https://doi.org/10.1016/j.corsci.2021.109887

Habib, K. (2010). Failure analysis of cracked reducer flange. *Journal of Failure Analysis and Prevention*, *10*(6), 480–485. https://doi.org/10.1007/S11668-010-9389-9/FIGURES/14

Habibzadeh, S., Li, L., Shum-Tim, D., Davis, E. C., & Omanovic, S. (2014). Electrochemical polishing as a 316L stainless steel surface treatment method: Towards the improvement of biocompatibility. *Corrosion Science*, *87*, 89–100. https://doi.org/10.1016/J.CORSCI.2014.06.010

Hack, H. P. (2016). Galvanic Corrosion. *Reference Module in Materials Science and Materials Engineering*. https://doi.org/10.1016/B978-0-12-803581-8.01594-0

Hakimian, S., Bouzid, A. H., & Hof, L. A. (2024a). An Improved Fixture to Quantify Corrosion in Bolted Flanged Gasketed Joints. *Journal of Pressure Vessel Technology, Transactions of the ASME*, *146*(1). https://doi.org/10.1115/1.4063975/1169913

Hakimian, S., Bouzid, A.-H., & Hof, L. A. (2023). An Improved Fixture to Quantify Corrosion in Bolted Flanged Gasketed Joints. *Journal of Pressure Vessel Technology*, 1–27. https://doi.org/10.1115/1.4063975

Hakimian, S., Bouzid, A.-H., & Hof, L. A. (2024b). Corrosion failures of flanged gasketed joints: A review. *Journal of Advanced Joining Processes*, *9*, 100200. https://doi.org/10.1016/J.JAJP.2024.100200

Hakimian, S., Bouzid, A.-H., & Hof, L. A. (2024c). Effect of gap size on flange face corrosion. *Materials and Corrosion*. https://doi.org/10.1002/MACO.202414367

Hakimian, S., Bouzid, A.-H., & Hof, L. A. (2024d). Effect of gasket material on flange face corrosion. *International Journal of Pressure Vessels and Piping*, *209*, 105207. https://doi.org/10.1016/j.ijpvp.2024.105207

Hakimian, S., Hof, L., & Bouzid, H. A. (2022). Investigation of Corrosion in Bolted Flanged Joints Using a Novel Experimental Setup. *Electrochemical Society Meeting Abstracts 241*, *16*, 990.

Hakimian, S., Pourrahimi, S., Bouzid, A.-H., & Hof, L. A. (2023). Application of machine learning for the classification of corrosion behavior in different environments for material selection of stainless steels. *Computational Materials Science*, *228*, 112352. https://doi.org/10.1016/J.COMMATSCI.2023.112352

Hamblin, M., & Finch, P. (2001). Dealing with some troublesome flanges. *2001 ASME Pressure Vessels and Piping Conference, July 23, 2001 - July 26, 2001*, *426*, 121–129.

He, X., Dunn, D. S., & Csontos, A. A. (2007). Corrosion of similar and dissimilar metal crevices in the engineered barrier system of a potential nuclear waste repository. *Electrochimica Acta*, *52*, 7556–7569. https://doi.org/10.1016/j.electacta.2006.12.077

Hladky, K., & Dawson, J. L. (1981). The measurement of localized corrosion using electrochemical noise. *Corrosion Science*, *21*(4), 317–322. https://doi.org/10.1016/0010-938X(81)90006-8

Homborg, A. M., Oonincx, P. J., & Mol, J. M. C. (2018). Wavelet Transform Modulus Maxima and Holder Exponents Combined with Transient Detection for the Differentiation of Pitting Corrosion Using Electrochemical Noise. *Corrosion*, *74*(9), 1001–1010. https://doi.org/10.5006/2788

Homborg, A. M., Tinga, T., Van Westing, E. P. M., Zhang, X., Ferrari, G. M., De Wit, J. H. W., & Mol, J. M. C. (2014). A Critical Appraisal of the Interpretation of Electrochemical Noise for Corrosion Studies. *Corrosion*, *70*(10), 971–987. https://doi.org/10.5006/1277

Homborg, A. M., Van Westing, E. P. M., Tinga, T., Ferrari, G. M., Zhang, X., De Wit, J. H. W., & Mol, J. M. C. (2014). Application of transient analysis using Hilbert spectra of electrochemical noise to the identification of corrosion inhibition. *Electrochimica Acta*, *116*, 355–365. https://doi.org/10.1016/J.ELECTACTA.2013.11.084

Homborg, A. M., van Westing, E. P. M., Tinga, T., Zhang, X., Oonincx, P. J., Ferrari, G. M., de Wit, J. H. W., & Mol, J. M. C. (2013). Novel time–frequency characterization of electrochemical noise data in corrosion studies using Hilbert spectra. *Corrosion Science*, *66*, 97–110. https://doi.org/10.1016/J.CORSCI.2012.09.007

Homborg, A., Mol, A., & Tinga, T. (2024). Corrosion classification through deep learning of electrochemical noise time-frequency transient information. *Engineering Applications of Artificial Intelligence*, *133*, 108044. https://doi.org/10.1016/J.ENGAPPAI.2024.108044

Hornus, E., Wang, K., Pabbruwe, M., Kop, A., Jones, C., Salleh, A., Salasi, M., & Iannuzzi, M. (2021). A new experimental method to simulate dynamic crevice corrosion in modular hip arthroplasty. *Corrosion Science*, *190*. https://doi.org/10.1016/j.corsci.2021.109704

Hou, Y., Aldrich, C., Lepkova, K., Machuca, L. L., & Kinsella, B. (2016). Monitoring of carbon steel corrosion by use of electrochemical noise and recurrence quantification analysis. *Corrosion Science*, *112*, 63–72.

Hou, Y., Aldrich, C., Lepkova, K., Machuca, L. L., & Kinsella, B. (2017). Analysis of electrochemical noise data by use of recurrence quantification analysis and

machine learning methods. *Electrochimica Acta*, *256*, 337–347. https://doi.org/10.1016/J.ELECTACTA.2017.09.169

Hu, Q., Liu, Y., Zhang, T., & Wang, F. (2020). Corrosion failure analysis on the copper alloy flange by experimental and numerical simulation. *Engineering Failure Analysis*, *109*, 104276. https://doi.org/10.1016/J.ENGFAILANAL.2019.104276

Hu, Q., Qiu, Y. B., Guo, X. P., & Huang, J. Y. (2010). Crevice corrosion of Q235 carbon steels in a solution of NaHCO3 and NaCl. *Corrosion Science*, *52*(4), 1205–1212. https://doi.org/10.1016/J.CORSCI.2010.01.006

Hu, Q., Zhang, G., Qiu, Y., & Guo, X. (2011a). The crevice corrosion behaviour of stainless steel in sodium chloride solution. *Corrosion Science*, *53*(12), 4065–4072. https://doi.org/10.1016/j.corsci.2011.08.012

Hu, Q., Zhang, G., Qiu, Y., & Guo, X. (2011b). The crevice corrosion behaviour of stainless steel in sodium chloride solution. *Corrosion Science*, *53*(12), 4065–4072. https://doi.org/10.1016/J.CORSCI.2011.08.012

Hussein Khalaf, A., Xiao, Y., Xu, N., Wu, B., Li, H., Lin, B., Nie, Z., & Tang, J. (2024). Emerging AI technologies for corrosion monitoring in oil and gas industry: A comprehensive review. *Engineering Failure Analysis*, *155*, 107735. https://doi.org/https://doi.org/10.1016/j.engfailanal.2023.107735

Ibrahim, M. A. M., Abd El Rehim, S. S., & Hamza, M. M. (2009). Corrosion behavior of some austenitic stainless steels in chloride environments. *Materials Chemistry and Physics*, *115*(1), 80–85. https://doi.org/10.1016/J.MATCHEMPHYS.2008.11.016

Jamali, S. S., Wu, Y., Homborg, A. M., Lemay, S. G., & Gooding, J. J. (2024). Interpretation of stochastic electrochemical data. *Current Opinion in Electrochemistry*, *46*, 101505. https://doi.org/10.1016/J.COELEC.2024.101505

Ji, N., Li, C., Wang, P., Zhu, L., & Feng, C. (2023). Corrosion Cause Analysis of a Surface Pipeline Flange. *Journal of Physics: Conference Series*, *2468*(1), 012171. https://doi.org/10.1088/1742-6596/2468/1/012171

Jian, L., Weikang, K., Jiangbo, S., Ke, W., Weikui, W., Weipu, Z., & Zhoumo, Z. (2013). Determination of Corrosion Types from Electrochemical Noise by Artificial Neural Networks. *International Journal of Electrochemical Science*, *8*(2), 2365–2377. https://doi.org/10.1016/S1452-3981(23)14315-X

Jiménez-Come, M. J., de la Luz Martín, M., & Matres, V. (2019). A support vector machine-based ensemble algorithm for pitting corrosion modeling of EN 1.4404 stainless steel in sodium chloride solutions. *Materials and Corrosion*, *70*(1), 19–27. https://doi.org/10.1002/maco.201810367

Jun, K., Lee, D. W., Lee, K., Lee, S., & Kim, M. S. (2020). Feature Extraction Using an RNN Autoencoder for Skeleton-Based Abnormal Gait Recognition. *IEEE Access*, *8*, 19196–19207. https://doi.org/10.1109/ACCESS.2020.2967845

Kain, R. M. (1998a). *Gasket Materials and Other Factors Influencing the Crevice Corrosion Resistance of Stainless Steel Flanges*. OnePetro. https://dx.doi.org/

Kain, R. M. (1998b, March). Gasket materials and other factors influencing the crevice corrosion resistance of stainless steel flanges. *CORROSION 98*.

Kamrunnahar, M., & Urquidi-Macdonald, M. (2010). Prediction of corrosion behavior using neural network as a data mining tool. *Corrosion Science*, *52*(3), 669–677. https://doi.org/10.1016/j.corsci.2009.10.024

Kang, D. H., & Lee, H. W. (2013). Study of the correlation between pitting corrosion and the component ratio of the dual phase in duplex stainless steel welds. *Corrosion Science*, *74*, 396–407. https://doi.org/https://doi.org/10.1016/j.corsci.2013.04.033

Kanthabhabha Jeya, R. P., Zhao, Z., & Bouzid, A.-H. (2020). Creep-Relaxation Modeling of HDPE and Polyvinyl Chloride Bolted Flange Joints. *Journal of Pressure Vessel Technology, Transactions of the ASME*, *142*(5). https://doi.org/10.1115/1.4047211

Karimi, S., Fraser, N., Roberts, B., & Foulkes, F. R. (2012). A review of metallic bipolar plates for proton exchange membrane fuel cells: Materials and fabrication methods. *Advances in Materials Science and Engineering*, *2012*. https://doi.org/10.1155/2012/828070

Kazeminia, M., & Bouzid, A.-H. (2016). Predicting leakage in packed stuffing boxes. *23rd International Conference on Fluid Sealing 2016, March 2, 2016 - March 3, 2016*, 45–59.

Kearns, J. R., Scully, J. R., Roberge, P. R., Reichert, D. L., & Dawson, J. L. (1996). The identification of pitting and crevice corrosion spectra in electrochemical noise using an artificial neural network. *Electrochemical Noise Measurement for Corrosion Applications*, *1277*, 157.

Kelly, R. G., & Lee, J. S. (2018). Localized Corrosion: Crevice Corrosion. *Encyclopedia of Interfacial Chemistry: Surface Science and Electrochemistry*, 291–301. https://doi.org/10.1016/B978-0-12-409547-2.13420-1

Kennell, G. F., Evitts, R. W., & Heppner, K. L. (2008). A critical crevice solution and IR drop crevice corrosion model. *Corrosion Science*, *50*(6), 1716–1725. https://doi.org/10.1016/J.CORSCI.2008.02.020

Koch, G. (2017). Cost of corrosion. *Trends in Oil and Gas Corrosion Research and Technologies: Production and Transmission*, 3–30. https://doi.org/10.1016/B978-0-08-101105-8.00001-2

Kölblinger, A. P., Tavares, S. S. M., Della Rovere, C. A., & Pimenta, A. R. (2022). Failure analysis of a flange of superduplex stainless steel by preferential corrosion of

ferrite phase. *Engineering Failure Analysis*, *134*, 106098. https://doi.org/10.1016/J.ENGFAILANAL.2022.106098

Kritzer, P., Boukis, N., & Dinjus, E. (1999). Factors controlling corrosion in high-temperature aqueous solutions: A contribution to the dissociation and solubility data influencing corrosion processes. *Journal of Supercritical Fluids*, *15*(3), 205–227. https://doi.org/10.1016/S0896-8446(99)00009-1

Kruger, J., & Begum, S. (2016). Corrosion of Metals: Overview. *Reference Module in Materials Science and Materials Engineering*. https://doi.org/10.1016/B978-0-12-803581-8.02708-9

Lachowicz, M. B., & Lachowicz, M. M. (2021). Influence of Corrosion on Fatigue of the Fastening Bolts. *Materials 2021, Vol. 14, Page 1485*, *14*(6), 1485. https://doi.org/10.3390/MA14061485

Larché, N., & Dézerville, P. (2012). Review of material selection and corrosion in seawater reverse osmosis desalination plants. *New Pub: Balaban*, *31*(1–3), 121–133. https://doi.org/10.5004/DWT.2011.2362

Larché, N., Thierry, D., Boillot, P., Cassagne, T., Blanc, J., Dézerville, P., Johansson, E., & Lardon, J. M. (2016). Crevice corrosion performance of high grade stainless steels and Ni-based alloys in natural and treated seawater. *CORROSION 2016*.

Lavigne, O., Gamboa, E., Costin, W., Law, M., Luzin, V., & Linton, V. (2014). Microstructural and mechanical factors influencing high pH stress corrosion cracking susceptibility of low carbon line pipe steel. *Engineering Failure Analysis*, *45*, 283–291. https://doi.org/10.1016/J.ENGFAILANAL.2014.07.011

Li, D. G., Wang, J. D., Chen, D. R., & Liang, P. (2014). Influences of pH value, temperature, chloride ions and sulfide ions on the corrosion behaviors of 316L stainless steel in the simulated cathodic environment of proton exchange membrane fuel cell.

Journal of Power Sources, *272*, 448–456. https://doi.org/10.1016/J.JPOWSOUR.2014.06.121

Li, S. Z., Li, H., Zhou, X. H., Wang, Y. H., Li, X. H., Gan, D., & Zhu, R. H. (2023). Damage detection of flange bolts in wind turbine towers using dynamic strain responses. *Journal of Civil Structural Health Monitoring*, *13*(1), 67–81. https://doi.org/10.1007/S13349-022-00622-Z/FIGURES/26

Liashchynskyi, P., & Liashchynskyi, P. (2019). *Grid Search, Random Search, Genetic Algorithm: A Big Comparison for NAS*. https://arxiv.org/abs/1912.06059v1

Likas, A., Vlassis, N., & J. Verbeek, J. (2003). The global k-means clustering algorithm. *Pattern Recognition*, *36*(2), 451–461. https://doi.org/10.1016/S0031-3203(02)00060-2

Lillard, R. S., & Scully, J. R. (1994). Modeling of the Factors Contributing to the Initiation and Propagation of the Crevice Corrosion of Alloy 625. *Journal of The Electrochemical Society*, *141*(11), 3006–3015. https://doi.org/10.1149/1.2059273/XML

Little, B. J., Ray, R. I., & Pope, R. K. (2000). Relationship Between Corrosion and the Biological Sulfur Cycle: A Review. *Corrosion*, *56*(04).

Liu, X., Sui, Y., Zhang, H., Liu, Y., Li, X., & Hou, J. (2024). Study on the passive behavior of 304 stainless steel under temperature variation. *Materials and Corrosion*. https://doi.org/10.1002/MACO.202414280

Lo, K. H., Shek, C. H., & Lai, J. K. L. (2009). Recent developments in stainless steels. *Materials Science and Engineering R: Reports*, *65*(4–6), 39–104. https://doi.org/10.1016/J.MSER.2009.03.001

Long, Y., Luo, J., Yue, M., Wu, G., Zhao, M., Ji, N., Song, W., Jin, Q., Kuang, X., & Fan, Y. (2022). Investigation on leakage cause of 13Cr pipe flange used for a Christmas tree in a high-pressure and high-temperature gas well. *Engineering*

Failure Analysis, *142*, 106793. https://doi.org/10.1016/J.ENGFAILANAL.2022.106793

Luo, B., Hu, Q., Liu, J., & Huang, F. (2022). Effect of crevice gap on crevice corrosion initiation and development of 2205 duplex stainless steel in NaCl solution. *Journal of Materials Research and Technology*, *21*, 2584–2597. https://doi.org/10.1016/J.JMRT.2022.10.059

Lv, Y. jun, Wang, J. wei, Wang, J. J. liang, Xiong, C., Zou, L., Li, L., & Li, D. wang. (2020). Steel corrosion prediction based on support vector machines. *Chaos, Solitons and Fractals*, *136*. https://doi.org/10.1016/j.chaos.2020.109807

Ma, C., Wang, Z., Behnamian, Y., Gao, Z., Wu, Z., Qin, Z., & Xia, D. H. (2019a). Measuring atmospheric corrosion with electrochemical noise: A review of contemporary methods. *Measurement*, *138*, 54–79. https://doi.org/10.1016/J.MEASUREMENT.2019.02.027

Ma, C., Wang, Z., Behnamian, Y., Gao, Z., Wu, Z., Qin, Z., & Xia, D.-H. (2019b). Measuring atmospheric corrosion with electrochemical noise: A review of contemporary methods. *Measurement*, *138*, 54–79. https://doi.org/https://doi.org/10.1016/j.measurement.2019.02.027

Malki, B., Berthomé, G., Souier, T., Boissy, C., Guillotte, I., & Baroux, B. (2021). A Combined Experimental and Computational Approach to Study Crevice Corrosion of Stainless Steels. *Journal of The Electrochemical Society*, *168*(10), 101504. https://doi.org/10.1149/1945-7111/ac2975

Mameri, N., Bouzid, A., Derenne, M., Marchand, L., & Piron, D. L. (1999). *Quantification of corrosion in bolted gasketed joints*.

Mameri, N., Piron, D. L., Bouzid, A., Derenne, M., Marchand, L., & Birembaut, Y. (2000). Corrosion quantification test for flanges with graphite-based gaskets. *Materials Performance*, *39*(4).

Marchand, L., Bazergui, A., & Derenne, M. (1992a). *Recent developments in elevated temperature gasket evaluation*. 209–223. https://doi.org/10.1007/978-94-011-2412-6_14/COVER

Marchand, L., Bazergui, A., & Derenne, M. (1992b). Recent Developments In Elevated Temperature Gasket Evaluation. In B. S. Nau (Ed.), *Fluid Sealing* (pp. 209–223). Springer Netherlands. https://doi.org/10.1007/978-94-011-2412-6_14

Marchand, L., Derenne, M., & Bazergui, A. (1992a). Weight loss correlation for sheet gasket materials. *Journal of Pressure Vessel Technology, Transactions of the ASME*, *114*(1), 1–7.

Marchand, L., Derenne, M., & Bazergui, A. (1992b). Weight Loss Correlation for Sheet Gasket Materials. *Journal of Pressure Vessel Technology*, *114*(1), 1–7. https://doi.org/10.1115/1.2929007

Martin, F. J., Lawrence, S. H., Natishan, P. M., Hogan, E. A., Lucas, K. E., & Thomas, E. D. (2004). Paper 04309 Crevice Corrosion Susceptibility of Ni-Cr-Mo Alloys. *Corrosion 2004*, *04309*, 1–16.

Martin, F. J., Natishan, P. M., Lawrence, S. H., Hogan, E. A., Lucas, K. E., & Thomas, E. D. (2004). *Fluoroelastomeric Gasket Peculiarities Influence the Seawater Crevice Corrosion Susceptibility of NiCrMo Alloys*. OnePetro. /NACECORR/proceedings-abstract/CORR04/All-CORR04/115699

Mathiesen, T., & Andersen, A. (2013). Challenges in Pre-Qualification Corrosion Testing of CRAs based on ASTM G48. *NACE Corrosion 2014*.

Mathiesen, T., & Bang, H. (2011). *Accelerated crevice corrosion testing of 6Mo stainless steel flanges with different gasket materials in seawater*.

Mazille, H., Rothea, R., & Tronel, C. (1995). An acoustic emission technique for monitoring pitting corrosion of austenitic stainless steels. *Corrosion Science*, *37*(9), 1365–1375. https://doi.org/10.1016/0010-938X(95)00036-J

McGuire, M. F. (2001). Austenitic Stainless Steels. *Encyclopedia of Materials: Science and Technology*, 406–410. https://doi.org/10.1016/B0-08-043152-6/00081-4

Mehmanparast, A., Lotfian, S., & Vipin, S. P. (2020). A Review of Challenges and Opportunities Associated with Bolted Flange Connections in the Offshore Wind Industry. *Metals*, *10*(6). https://doi.org/10.3390/met10060732

Mienye, I. D., Swart, T. G., & Obaido, G. (2024). Recurrent Neural Networks: A Comprehensive Review of Architectures, Variants, and Applications. *Information 2024, Vol. 15, Page 517*, *15*(9), 517. https://doi.org/10.3390/INFO15090517

Mohammadreza Tavakkolizadeh, B., Member, S., & Saadatmanesh, H. (2001). Galvanic Corrosion of Carbon and Steel in Aggressive Environments. *Journal of Composites for Construction*, *5*(3), 200–210. https://doi.org/10.1061/(ASCE)1090-0268(2001)5:3(200)

Murali Krishna, M., Shunmugam, M. S., & Siva Prasad, N. (2007). A study on the sealing performance of bolted flange joints with gaskets using finite element analysis. *International Journal of Pressure Vessels and Piping*, *84*(6), 349–357. https://doi.org/10.1016/J.IJPVP.2007.02.001

Nadarajah, C. (2004). A Parametric Study of ASME B16.5 Flanges Which Has Experienced Flange Face Corrosion. *Proceedings of the ASME/JSME 2004 Pressure Vessels and Piping Conference. Pressure Vessel and Piping Codes and Standards*, 157–163.

Nazarnezhad-Bajestani, M., … J. N.-J. of, & 2019, undefined. (n.d.). Determination of SS321 pitting stage in FeCl3 solution based on electrochemical noise measurement data using artificial neural network. *Elsevier*. Retrieved June 25, 2024, from https://www.sciencedirect.com/science/article/pii/S1572665719303935

Nazarnezhad-Bajestani, M., Neshati, J., & Siadati, M. H. (2019). Determination of SS321 pitting stage in FeCl3 solution based on electrochemical noise measurement data using artificial neural network. *Journal of Electroanalytical Chemistry*, *845*, 31–38.

Nechache, A., & Bouzid, A. H. (2007). Creep analysis of bolted flange joints. *International Journal of Pressure Vessels and Piping*, *84*(3), 185–194. https://doi.org/10.1016/J.IJPVP.2006.06.004

Nechache, A., & Bouzid, A. H. (2008). On the use of plate theory to evaluate the load relaxation in bolted flanged joints subjected to creep. *International Journal of Pressure Vessels and Piping*, *85*(7), 486–497. https://doi.org/10.1016/J.IJPVP.2008.01.005

Nelson, N. R., Prasad, S., & Sekhar, A. S. (2023). Structural integrity and sealing behaviour of bolted flange joint: A state of art review. *International Journal of Pressure Vessels and Piping*, *204*, 104975. https://doi.org/10.1016/j.ijpvp.2023.104975

Nguyen, H. D., Tran, K. P., Thomassey, S., & Hamad, M. (2021). Forecasting and Anomaly Detection approaches using LSTM and LSTM Autoencoder techniques with the applications in supply chain management. *International Journal of Information Management*, *57*, 102282. https://doi.org/10.1016/J.IJINFOMGT.2020.102282

Nicolas Larché; Dominique Thierry; Pauline Boillot; Thierry Cassagne; Jéréme Blanc; Philippe Dézerville; Elisabeth Johansson; Jean Marc Lardon. (2016, March). Crevice corrosion performance of high grade stainless steels and Ni-based alloys in natural and treated seawater. *CORROSION 2016*.

Nilsson, J. O. (2013). Super duplex stainless steels. *Http://Dx.Doi.Org/10.1179/Mst.1992.8.8.685*, *8*(8), 685–700. https://doi.org/10.1179/MST.1992.8.8.685

Nishimoto, M., Ogawa, J., Muto, I., Sugawara, Y., & Hara, N. (2016a). Simultaneous visualization of pH and Cl − distributions inside the crevice of stainless steel. *Corrosion Science*, *106*, 298–302. https://doi.org/10.1016/j.corsci.2016.01.028

Nishimoto, M., Ogawa, J., Muto, I., Sugawara, Y., & Hara, N. (2016b). Simultaneous visualization of pH and Cl− distributions inside the crevice of stainless steel. *Corrosion Science*, *106*, 298–302. https://doi.org/10.1016/J.CORSCI.2016.01.028

Noble, W. S. (2006). What is a support vector machine? *Nature Biotechnology 2006 24:12*, *24*(12), 1565–1567. https://doi.org/10.1038/nbt1206-1565

Nurhadiyanto, D. (2014a). *Influence of surface roughness on leakage of the corrugated metal gasket* [Yamaguchi University]. https://ci.nii.ac.jp/naid/500000932452/

Nurhadiyanto, D. (2014b). *Influence of surface roughness on leakage of the corrugated metal gasket*. Yamaguchi University.

Nyby, C., Guo, X., Saal, J. E., Chien, S.-C., Gerard, A. Y., Ke, H., Li, T., Lu, P., Oberdorfer, C., Sahu, S., Li, S., Taylor, C. D., Windl, W., Scully, J. R., & Frankel, G. S. (2021). Electrochemical metrics for corrosion resistant alloys. *Scientific Data*, *8*(1), 58. https://doi.org/10.1038/s41597-021-00840-y

Odahara, M., Tsuchiya, H., Fujimoto, S., Salgado, D. M., Lillard, S., Lillard, R. S., Mehrazi, S., & Miller, D. M. (2020). Quantifying Alloy 625 Crevice Corrosion Using an Image Differencing Technique: Part I. Initiation and Propagation. *Journal of The Electrochemical Society*, *167*(2), 021511. https://doi.org/10.1149/1945-7111/AB6EE6

Okonkwo, B. O., Ming, H., Meng, F., Wang, J., Xu, X., & Han, E.-H. (2021). Galvanic corrosion study between low alloy steel A508 and 309/308 L stainless steel dissimilar metals: A case study of the effects of oxide film and exposure time.

Journal of Nuclear Materials, *548*. https://doi.org/10.1016/j.jnucmat.2021.152853

Oldfield, J. W. (1987). Test techniques for pitting and crevice corrosion resistance of stainless steels and nickel-base alloys in chloride-containing environments. *International Materials Reviews*, *32*(1), 153–172. https://doi.org/10.1179/095066087790150313

Oldfield, J. W., & Sutton, W. H. (1978a). Crevice Corrosion of Stainless Steels: I. A Mathematical Model. *British Corrosion Journal*, *13*(1), 13–22. https://doi.org/10.1179/000705978798358671

Oldfield, J. W., & Sutton, W. H. (1978b). Crevice Corrosion of Stainless Steels: II. Experimental studies. *British Corrosion Journal*, *13*(3), 104–111. https://doi.org/10.1179/000705978798276258

One-class SVM with non-linear kernel (RBF) — scikit-learn 1.5.2 documentation. (n.d.). Retrieved November 16, 2024, from https://scikit-learn.org/stable/auto_examples/svm/plot_oneclass.html

Orlikowski, J., & Darowicki, K. (2011). Investigations of pitting corrosion of magnesium by means of DEIS and acoustic emission. *Electrochimica Acta*, *56*, 7880–7884. https://doi.org/10.1016/j.electacta.2010.12.021

Orlikowski, J., Jazdzewska, A., Mazur, R., & Darowicki, K. (2017). *Determination of pitting corrosion stage of stainless steel by galvanodynamic impedance spectroscopy*. https://doi.org/10.1016/j.electacta.2017.09.047

Park, C.-J., & Lee, Y.-H. (2004). Initiation and Repassivation of Crevice Corrosion of Type 444 Stainless Steel in Chloride Solution. *METALS AND MATERIALS International*, *10*(5), 447–451.

Pascanu, R., Mikolov, T., & Bengio, Y. (2012). On the difficulty of training Recurrent Neural Networks. *30th International Conference on Machine Learning, ICML 2013*, *PART 3*, 2347–2355. https://arxiv.org/abs/1211.5063v2

Pedregosa FABIANPEDREGOSA, F., Michel, V., Grisel OLIVIERGRISEL, O., Blondel, M., Prettenhofer, P., Weiss, R., Vanderplas, J., Cournapeau, D., Pedregosa, F., Varoquaux, G., Gramfort, A., Thirion, B., Grisel, O., Dubourg, V., Passos, A., Brucher, M., Perrot andÉdouardand, M., Duchesnay, andÉdouard, & Duchesnay EDOUARDDUCHESNAY, Fré. (2011). Scikit-learn: Machine Learning in Python. *Journal of Machine Learning Research*, *12*(85), 2825–2830. http://jmlr.org/papers/v12/pedregosa11a.html

Pei, Z., Zhang, D., Zhi, Y., Yang, T., Jin, L., Fu, D., Cheng, X., Terryn, H. A., Mol, J. M. C., & Li, X. (2020). Towards understanding and prediction of atmospheric corrosion of an Fe/Cu corrosion sensor via machine learning. *Corrosion Science*, *170*(March), 108697. https://doi.org/10.1016/j.corsci.2020.108697

Pickering, H. W. (1989). The significance of the local electrode potential within pits, crevices and cracks. *Corrosion Science*, *29*(2), 325–341. https://doi.org/https://doi.org/10.1016/0010-938X(89)90039-5

Pourrahimi, S., Hakimian, S., Bouzid, A.-H., & Hof, L. A. (2023). On the Use of Machine Learning Algorithms to Predict the Corrosion Behavior of Stainless Steels in Lactic Acid. *Metals*, *13*(8), 1459. https://doi.org/10.3390/met13081459

Pourrahimi, S., & Hof, L. A. (2024). On the Post-Processing of Complex Additive Manufactured Metallic Parts: A Review. *Advanced Engineering Materials*, 2301511. https://doi.org/10.1002/ADEM.202301511

Powers, D. M. W., & Ailab. (2020). *Evaluation: from precision, recall and F-measure to ROC, informedness, markedness and correlation*. https://arxiv.org/abs/2010.16061v1

Pruksawan, S., Lambard, G., Samitsu, S., Sodeyama, K., & Naito, M. (2019). Prediction and optimization of epoxy adhesive strength from a small dataset through active learning. *Science and Technology of Advanced Materials*, *20*(1), 1010. https://doi.org/10.1080/14686996.2019.1673670

Qiu, J., Wu, A., Li, Y., Xu, Y., Scarlat, R., & Macdonald, D. D. (2020). Galvanic corrosion of Type 316L stainless steel and Graphite in molten fluoride salt. *Corrosion Science*, *170*, 108677. https://doi.org/10.1016/J.CORSCI.2020.108677

Quinlan, J. R. (n.d.). *Bagging, Boosting, and C4.5*.

R. Francis; G. Byrne. (2007, March). Factors affecting gasket selection for stainless steels in seawater. *CORROSION 2007*.

Ramírez-Platas, M., Morales-Cabrera, M. A., Rivera, V. M., Morales-Zarate, E., & Hernandez-Martinez, E. (2021). Fractal and multifractal analysis of electrochemical noise to corrosion evaluation in A36 steel and AISI 304 stainless steel exposed to MEA-CO2 aqueous solutions. *Chaos, Solitons & Fractals*, *145*, 110802. https://doi.org/10.1016/J.CHAOS.2021.110802

Rice, D. A., & Waterland, A. F. (2014). Environmental Considerations for Gasket Selection and the Development of an Emissions Calculator for Gasket Materials. *American Society of Mechanical Engineers, Pressure Vessels and Piping Division (Publication) PVP*, *2*. https://doi.org/10.1115/PVP2014-28024

Ringnér, M. (2008). What is principal component analysis? *Nature Biotechnology 2008 26:3*, *26*(3), 303–304. https://doi.org/10.1038/nbt0308-303

Rodríguez-Pérez, R., & Bajorath, J. (2022). Evolution of Support Vector Machine and Regression Modeling in Chemoinformatics and Drug Discovery. *Journal of Computer-Aided Molecular Design*, *36*(5), 355–362. https://doi.org/10.1007/S10822-022-00442-9/FIGURES/5

Rogne, T., Drugli, J. M., Solem, T., Salbu, H., & Skjellevik, H. (1998). Crevice corrosion properties of weld overlays of nibased alloys compared to 6Mo stainless steels for seawater applications. *Corrosion*, *1998-March*.

Safavian, S. R., & Landgrebe, D. (1991). A Survey of Decision Tree Classifier Methodology. *IEEE Transactions on Systems, Man and Cybernetics*, *21*(3), 660–674. https://doi.org/10.1109/21.97458

Sak, H. H., Senior, A., & Google, B. (2014). *Long Short-Term Memory Recurrent Neural Network Architectures for Large Scale Acoustic Modeling*. https://doi.org/10.21437/Interspeech.2014-80

Salehinejad, H., Sankar, S., Barfett, J., Colak, E., & Valaee, S. (2017). *Recent Advances in Recurrent Neural Networks*. https://arxiv.org/abs/1801.01078v3

Salleh, S. H., Thomas, S., Yuwono, J. A., Venkatesan, K., & Birbilis, N. (2015). *Enhanced hydrogen evolution on Mg (OH) 2 covered Mg surfaces*. https://doi.org/10.1016/j.electacta.2015.02.079

Santos, M. S., Abreu, P. H., Japkowicz, N., Fernández, A., Soares, C., Wilk, S., & Santos, J. (2022). On the joint-effect of class imbalance and overlap: a critical review. *Artificial Intelligence Review 2022 55:8*, *55*(8), 6207–6275. https://doi.org/10.1007/S10462-022-10150-3

Sawa, T., Takagi, Y., & Torii, H. (2015). Effect of material properties of gasket on the sealing performance of pipe flange connections at elevated temperature. *ASME 2015 Pressure Vessels and Piping Conference, PVP 2015, July 19, 2015 - July 23, 2015*, *2*, Pressure Vessels and Piping Division. https://doi.org/10.1115/PVP2015-45177

Schindelin, J., Arganda-Carreras, I., Frise, E., Kaynig, V., Longair, M., Pietzsch, T., Preibisch, S., Rueden, C., Saalfeld, S., Schmid, B., Tinevez, J. Y., White, D. J., Hartenstein, V., Eliceiri, K., Tomancak, P., & Cardona, A. (2012). Fiji: an open-

source platform for biological-image analysis. *Nature Methods 2012 9:7*, *9*(7), 676–682. https://doi.org/10.1038/nmeth.2019

Schmidt, J., Marques, M. R. G., Botti, S., & Marques, M. A. L. (2019). Recent advances and applications of machine learning in solid-state materials science. *Npj Computational Materials 2019 5:1*, *5*(1), 1–36. https://doi.org/10.1038/s41524-019-0221-0

Schmidt, R. M. (2019). *Recurrent Neural Networks (RNNs): A gentle Introduction and Overview*. https://arxiv.org/abs/1912.05911v1

Schmitt, G., Moeller, K., & Plagemann, P. (2004). Online monitoring of crevice corrosion with electrochemical noise. *Materials and Corrosion*, *55*(10), 742–747. https://doi.org/10.1002/maco.200403812

scikit-learn: machine learning in Python — scikit-learn 1.0.1 documentation. (n.d.). Retrieved November 17, 2021, from https://scikit-learn.org/stable/

Shi, N., Liu, X., & Guan, Y. (2010). Research on k-means clustering algorithm: An improved k-means clustering algorithm. *3rd International Symposium on Intelligent Information Technology and Security Informatics, IITSI 2010*, 63–67. https://doi.org/10.1109/IITSI.2010.74

Shojaei, E., Mirjalili, M., & Moayed, M. H. (2019). The influence of the crevice induced IR drop on polarization measurement of localized corrosion behavior of 316L stainless steel. *Corrosion Science*, *156*, 96–105. https://doi.org/10.1016/J.CORSCI.2019.04.030

Shorts, M. (2017). *Gasket Handbook* (1st ed.). Fluid Sealing Association, and European Sealing Association.

Simonton, J., & Barry, L. (2006). Evolution of New Gasket Type Increases Reliability in HF Alkylation Unit . *Proceedings of the ASME 2006 Pressure Vessels and*

Piping/ICPVT-11 Conference. Volume 7: Operations, Applications, and Components, 431–433.

Simonton, J. L., & Barry, L. K. (2006). Evolution of a more reliable gasket for HF alkylation units. *Sealing Technology*, *2006*(11), 12–14. https://doi.org/https://doi.org/10.1016/S1350-4789(06)71457-X

Speiser, J. L., Miller, M. E., Tooze, J., & Ip, E. (2019). A comparison of random forest variable selection methods for classification prediction modeling. *Expert Systems with Applications*, *134*, 93–101. https://doi.org/10.1016/J.ESWA.2019.05.028

Sridhar, N. (2022). Localized Corrosion in Seawater: A Bayesian Network-Based Review. *Corrosion*, *79*(3), 268–283. https://doi.org/10.5006/4215

Sridhar, N., & Cragnolino, G. A. (1993). Applicability of Repassivation Potential for Long-Term Prediction of Localized Corrosion of Alloy 825 and Type 316L Stainless Steel. *Corrosion*, *49*(11).

Standard Specification for Forged or Rolled Nickel Alloy Pipe Flanges, Forged Fittings, and Valves and Parts for Corrosive High-Temperature Service. (n.d.). Retrieved April 6, 2022, from https://www.astm.org/b0462-18e01.html

Stephen Bond; Yi Li. (2020, June). A novel gasket design for an isolating gasket to solve common sealing problems. *CORROSION 2020*.

Sun, B., Zuo, X., Cheng, X., & Li, X. (2020). The role of chromium content in the long-term atmospheric corrosion process. *Npj Materials Degradation 2020 4:1*, *4*(1), 1–9. https://doi.org/10.1038/s41529-020-00142-5

Sun, D., Jiang, Y., Tang, Y., Xiang, Q., Zhong, C., Liao, J., & Li, J. (2009). Pitting corrosion behavior of stainless steel in ultrasonic cell. *Electrochimica Acta*, *54*, 1558–1563. https://doi.org/10.1016/j.electacta.2008.09.056

Sun, J., Tang, H., Wang, C., Han, Z., & Li, S. (2022). Effects of Alloying Elements and Microstructure on Stainless Steel Corrosion: A Review. *Steel Research International*, *93*(5), 2100450. https://doi.org/10.1002/SRIN.202100450

Sun, X., & Yang, L. (2006). *Real-Time Monitoring of Crevice Corrosion Propagation Rates in Simulated Seawater using Coupled Multielectrode Array Sensors*. OnePetro. https://dx.doi.org/

Takahiro Tsuda; Nozomi Satake; Manabu Itoki. (2021, April). Mitigation of flange face corrosion during plant construction. *CORROSION 2021*.

Talha, M., Behera, C. K., & Sinha, O. P. (2013). A review on nickel-free nitrogen containing austenitic stainless steels for biomedical applications. *Materials Science and Engineering C*, *33*(7), 3563–3575. https://doi.org/10.1016/J.MSEC.2013.06.002

Tavares, S. S. M., Pardal, J. M., Almeida, B. B., Mendes, M. T., Freire, J. L. F., & Vidal, A. C. (2018). Failure of superduplex stainless steel flange due to inadequate microstructure and fabrication process. *Engineering Failure Analysis*, *84*, 1–10. https://doi.org/10.1016/J.ENGFAILANAL.2017.10.007

Tawancy, H. M. (2019). Failure Analysis of 304 Stainless Steel Components Used in Petrochemical Industry Applications. *Metallography, Microstructure, and Analysis*, *8*(5), 705–712. https://doi.org/10.1007/s13632-019-00578-5

Thyssen Edelstahlwerke AG. (1992). *Chemical resistance of the stainless REMANIT steel*.

Troels Mathiesen; Henrik Bang. (2011, September). Accelerated crevice corrosion testing of 6Mo stainless steel flanges with different gasket materials in seawater. *EUROCORR 2011*.

Trond Rogne; John M. Drugli; Tone Solem; Hakon Salbu; Helge Sljellevik. (1998, March). Crevice corrosion properties of weld overlays of Ni-based alloys compared to 6Mo stainless steels for seawater applications. *CORROSION 98*.

Tsuda, T., Satake, N., & Itoki, M. (2021). *Mitigation of Flange Face Corrosion during Plant Construction*. OnePetro.

Turnbull, A. (1998). Prevention of crevice corrosion by coupling to more noble materials? *Corrosion Science*, *40*(4), 843–845. https://doi.org/https://doi.org/10.1016/S0010-938X(97)00169-8

Turnbull, A. (1999). Impact of Graphite Gasket/Duplex Stainless Steel Couples on Crevice Chemistry and the Likelihood of Crevice Attack in Seawater. *Corrosion*, *55*(02).

Vasilescu, E., Drob, P., Raducanu, D., Cinca, I., Mareci, D., Calderon Moreno, J. M., Popa, M., Vasilescu, C., & Mirza Rosca, J. C. (2009). Effect of thermo-mechanical processing on the corrosion resistance of Ti6Al4V alloys in biofluids. *Corrosion Science*, *51*, 2885–2896. https://doi.org/10.1016/j.corsci.2009.08.014

Victoria, A. H., & Maragatham, G. (2021). Automatic tuning of hyperparameters using Bayesian optimization. *Evolving Systems*, *12*(1), 217–223. https://doi.org/10.1007/S12530-020-09345-2/FIGURES/7

Wang, A. Y. T., Murdock, R. J., Kauwe, S. K., Oliynyk, A. O., Gurlo, A., Brgoch, J., Persson, K. A., Persson, K. A., & Sparks, T. D. (2020). Machine Learning for Materials Scientists: An Introductory Guide toward Best Practices. *Chemistry of Materials*, *32*(12), 4954–4965. https://doi.org/10.1021/acs.chemmater.0c01907

Wang, J., Su, H., Chen, K., Du, D., Zhang, L., & Shen, Z. (2019). Effect of δ-ferrite on the stress corrosion cracking behavior of 321 stainless steel. *Corrosion Science*, *158*, 108079. https://doi.org/https://doi.org/10.1016/j.corsci.2019.07.005

Wang, Z., Zhang, L., Zhang, Z., & Lu, M. (2018). Combined effect of pH and H2S on the structure of passive film formed on type 316L stainless steel. *Applied Surface Science*, *458*, 686–699. https://doi.org/10.1016/J.APSUSC.2018.07.122

Wasim, M., Shoaib, S., Mubarak, · N M, Inamuddin, ·, & Asiri, A. M. (2018). *Factors influencing corrosion of metal pipes in soils*. *16*, 861–879. https://doi.org/10.1007/s10311-018-0731-x

Weijtjens, W., Stang, A., Devriendt, C., & Schaumann, P. (2020). *Bolted ring flanges in offshore-wind support structures-in-situ validation of load-transfer behaviour*. https://doi.org/10.1016/j.jcsr.2020.106361

Wen, Y. F., Cai, C. Z., Liu, X. H., Pei, J. F., Zhu, X. J., & Xiao, T. T. (2009). Corrosion rate prediction of 3C steel under different seawater environment by using support vector regression. *Corrosion Science*, *51*(2), 349–355. https://doi.org/10.1016/j.corsci.2008.10.038

Westin, E. M., & Hertzman, S. (2014). Element distribution in lean duplex stainless steel welds. *Welding in the World*, *58*(2), 143–160. https://doi.org/10.1007/s40194-013-0108-5

Wong, T. T., & Yeh, P. Y. (2020). Reliable Accuracy Estimates from k-Fold Cross Validation. *IEEE Transactions on Knowledge and Data Engineering*, *32*(8), 1586–1594. https://doi.org/10.1109/TKDE.2019.2912815

Worden, K. (2014a). Flange corrosion: Prevention and mitigation through better gasketing. In *Fuels and Petrochemicals Division 2014 - Core Programming Area at the 2014 AIChE Spring Meeting and 10th Global Congress on Process Safety* (Vol. 2, pp. 1000–1008).

Worden, K. (2014b). Flange corrosion: Prevention and mitigation through better gasketing. *17th Topical on Refinery Processing 2014 - Topical Conference at the 2014 AIChE Spring Meeting and 10th Global Congress on Process Safety*, 551–559. https://www.engineeringvillage.com/share/document.url?mid=cpx_M2cc27161 4be6b666a4M7cbd1017816338&database=cpx

Wu, J., Chen, X. Y., Zhang, H., Xiong, L. D., Lei, H., & Deng, S. H. (2019). Hyperparameter Optimization for Machine Learning Models Based on Bayesian Optimization. *Journal of Electronic Science and Technology*, *17*(1), 26–40. https://doi.org/10.11989/JEST.1674-862X.80904120

Xia, D.-H., Song, S., Behnamian, Y., Hu, W., Cheng, Y. F., Luo, J.-L., & Huet, F. (2020). Review—Electrochemical Noise Applied in Corrosion Science: Theoretical and Mathematical Models towards Quantitative Analysis. *Journal of The Electrochemical Society*, *167*(8), 081507. https://doi.org/10.1149/1945-7111/ab8de3

Xu, J., Wu, X., & Han, E. H. (2011). Acoustic emission during pitting corrosion of 304 stainless steel. *Corrosion Science*, *53*(4), 1537–1546. https://doi.org/10.1016/J.CORSCI.2011.01.030

Yan, L., Diao, Y., Lang, Z., & Gao, K. (2020). Corrosion rate prediction and influencing factors evaluation of low-alloy steels in marine atmosphere using machine learning approach. *Science and Technology of Advanced Materials*, *21*(1), 359–370. https://doi.org/10.1080/14686996.2020.1746196

Yin, W., Kann, K., Yu, M., SchützeSch, H., & Munich, L. (2017). *Comparative Study of CNN and RNN for Natural Language Processing*. https://arxiv.org/abs/1702.01923v1

Yu, T., & Zhu, H. (2020). *Hyper-Parameter Optimization: A Review of Algorithms and Applications*. https://arxiv.org/abs/2003.05689v1

Yu, Y., Si, X., Hu, C., & Zhang, J. (2019). A Review of Recurrent Neural Networks: LSTM Cells and Network Architectures. *Neural Computation*, *31*(7), 1235–1270. https://doi.org/10.1162/NECO_A_01199

Zaffora, A., Di Franco, F., & Santamaria, M. (2021). Corrosion of stainless steel in food and pharmaceutical industry. *Current Opinion in Electrochemistry*, *29*, 100760. https://doi.org/10.1016/j.coelec.2021.100760

Zhang, J., Heng, J., Dong, Y., Baniotopoulos, C., & Yang, Q. (2024). Coupling multi-physics models to corrosion fatigue prognosis of high-strength bolts in floating offshore wind turbine towers. *Engineering Structures*, *301*, 117309. https://doi.org/10.1016/j.engstruct.2023.117309

Zhang, J., Li, B., Li, Y., Lu, J., Wang, K., & Zhang, H. (2021). Effect of sulfide on corrosion behavior of stainless steel 316SS and Hastelloy C276 in sub/supercritical water. *International Journal of Hydrogen Energy*, *46*(42), 22222–22233. https://doi.org/10.1016/J.IJHYDENE.2021.04.031

Zhou, H. F., Zhang, J. W., Zhou, Y. Q., Guo, X. J., & Ma, Y. M. (2021). A feature selection algorithm of decision tree based on feature weight. *Expert Systems with Applications*, *164*, 113842. https://doi.org/10.1016/J.ESWA.2020.113842